IMPERIAL

Engineering the Cathode Catalyst Layer Architecture for Fuel Cells

Simon Kellner

Department of Chemical Engineering

Imperial College London

A thesis submitted in partial fulfilment of the requirements for the degree of Doctor of Philosophy in Chemical Engineering

2024

Statement of Originality

I, Simon Kellner, hereby declare that the work reported in this thesis is original and has not been submitted for the requirements of any other degree. This thesis originates from my own work, contributions of others are acknowledged at the beginning of each experimental chapter, and all used references are appropriately cited.

Copyright declaration

The copyright of this thesis rests with the author. Unless otherwise indicated, its contents are licensed under a Creative Commons Attribution-NonCommercial 4.0 International Licence (CC BY-NC).

Under this licence, you may copy and redistribute the material in any medium or format. You may also create and distribute modified versions of the work. This is on the condition that: you credit the author and do not use it, or any derivative works, for a commercial purpose.

When reusing or sharing this work, ensure you make the licence terms clear to others by naming the licence and linking to the licence text. Where a work has been adapted, you should indicate that the work has been changed and describe those changes.

Please seek permission from the copyright holder for uses of this work that are not included in this licence or permitted under UK Copyright Law.

Acknowledgement

First and foremost, I would like to thank Prof. Magda Titirici for supervising my PhD studies. I appreciate that she gave me the freedom to explore my own curiosities and ideas in the research projects, and also her patience to wait for the fruits, which we reaped at the end. I take her most important advice to “keep it simple” with me into the future.

I am also grateful for the advice and guidance of my co-supervisors Prof. Sandrine Heutz and Prof. Ifan Stephens.

I would like to thank all Titirici Group members and specifically the Oxygen Reduction Reaction colleagues including Dr. Mengnan Wang, Dr. Silvia Favero, Dr. Angus Pedersen, Dr. Jingyu Feng as well as the electrocatalysis research fellow Dr. Jesús Barrio and his student Jingie Zhu, for their valuable insights and support. In addition, I acknowledge the contributions in the lab from the Master students, who I had the chance to supervise, Aqeeb Dange and Ying Wang, and especially the great experimental outcomes from UROP student, Ziyang Liu.

Each project came with its specific set of challenges, which could not all be solved alone. With regards to the GDE design, I am grateful for Prof. Ifan Stephens to establish the connection to Prof. Mathias Arenz and Dr. Gustav Wiberg, who one year before submission helped me to design the new setup, which solved all the issues from previous measurements. Special thanks to the Gavin Barnes from the workshop, who implemented all the changes in the GDE always precisely and quickly. After spending half a year without any progress in the etching of AAO, Dr. Heather Au gave me a new perspective for approaching the etching differently, which lead to final success in that project. I am grateful for Dr. Silvia Favero’s idea to prescreen the oxygen limiting current by scanning the current, prompting the breakthrough for the oxygen limiting current measurements.

I am grateful for the diverse and smart cohort of PhD students I met in the Department in my role as departmental representative and representative in the safety committee. I am grateful for the department of chemical engineering for providing the financial support in form of the departmental scholarship.

Lastly, I am deeply grateful for my brother’s and my parents loving support from the cradle to the graduation.

“Probleme kann man niemals mit derselben Denkweise lösen, durch die sie entstanden sind.”

“The significant problems we have cannot be solved at the same level of thinking with which we created them.”[1]

Albert Einstein (1879-1955)

Table of Contents

Statement of Originality 2
Copyright declaration 3
Acknowledgement 4
List of Abbreviations 9
Abstract 11
List of Publications 12
Outlines of the chapters 13
1. Introduction 15
1.1. Fuel cell electric vehicles history 15
1.2. Fuel cell electric vehicles today 15
1.3. Platinum – the price to be paid for commercialization 16
2. Literature review 18
2.1. The origins of performance losses in platinum group metal free cathode based fuel cells 18
2.2. Proton exchange membrane fuel cell vs. alkaline exchange membrane fuel cell 20
2.3. Fe-N-C catalyst development: Increase volumetric activity 22
2.4. Density Functional Theory (DFT) modelling to predict activities of active sites 24
2.5. Cathode catalyst layer design 28
2.6. Design of catalysts with inherent mass transport 29
2.7. Model Simulation To Meet Transport Performance Targets 30
2.8. Vertically-aligned carbon tube catalyst layers 35
2.9. Inverse opal macroporous catalyst layers 35
2.10. Gas-Diffusion-Electrodes: The intermediate technique between Rotating Disk Electrode and Membrane Electrode Assembly 36
2.11. The optimized small Gas-Diffusion-Electrode setup 39
3. Experimental 42
Details of the materials preparation in Chapter 4 42
Details of the materials preparation in Chapter 5 43
Details of the experiment preparation in Chapter 6 45
Characterization techniques 47
Electrochemical characterization 51
Rotating Disc Electrode 51
Gas Diffusion Electrode Half Cell 52

4. AAO template for Fe-N-C tubular catalysts for the cathode in PEMFCs 54
4.1. Background of vertically aligned cathodes 54
4.2. Goal: PGM-free VACNTs 59
4.3. Characterization of the steps towards VACNTs in AAO 62
4.4. Review of the etching protocols in literature 65
4.5. Detailed Analysis of the etching progress 68
4.6. Oxygen Reduction Reaction Performance of FeN_4-C_{tubes} electrodes 71
4.7. Conclusive remarks 75
4.8. Potential future work 76
4.9. Ideas for further improvement of the project 76
5. Engineering Macroporous Carbon Films as Freestanding Fe-N-C cathode Catalyst Layer for Fuel Cells 78
5.1. Abstract 78
5.2. Introduction Text 79
5.3. Results and Discussion 81
5.3.1. Replacing SiO_2 template with Polystyrene (PS) spheres 81
5.3.2. The preparation of macroporous carbon films 83
5.3.4. Adjusting the PS content for interconnected macropore network 84
5.3.5. The effect of heating protocol and carbonization atmosphere on the film properties 86
5.3.6. RDE study of the ORR performance of the ball-milled film 87
5.3.7. ORR performance at high current densities of the macroporous carbon film cathode in GDE 90
5.4. Conclusion 94
5.5. Future work: Introducing mesopores 95
6. Combinations of Commercial Alkaline Ionomers and Membranes for the Oxygen Reduction Reaction in Half-Cell Studies in Gas-Diffusion-Electrodes 97
6.1. Abstract 97
6.2. Introduction 98
6.3. Results and Discussion 101
6.3.1. Rotating Disc Electrode (RDE) study of AEIs and SAXS measurement of RDE inks 101
6.3.2. Preparation of the catalyst layer for Gas-Diffusion-Electrode (GDE) testing – from ink to morphology 104

6.3.4. Effect of the AEI type on the oxygen reduction reaction performance of Fe-N-C catalyst in alkaline gas-diffusion-electrode 107

6.3.5. Effect of the AEI on the water vapor sorption capabilities of Fe-N-C catalyst layers 109

6.3.6. Effect of the membrane on the ORR overpotential in the GDE 111

6.3.7. The effect of AEI on O_2 mass-transport in the catalyst layer 112

6.4. Conclusion 113

7. Conclusive remarks 115

7.1. Value generated in this thesis 115

7.2. Retrospective blind spots of the research in this thesis 116

7.3. Prospective research directions outgoing from this thesis 117

7.4. The destiny of PGM-free Fe-N-C catalysts 118

Appendix 120

Appendix Chapter 4 120

Appendix Chapter 5 121

Appendix Chapter 6 125

References 129

List of Abbreviations

3DOHP = 3D ordered hierarchical porous

AAO = anodic aluminium oxide

AEI = alkaline exchange ionomer

AEM = alkaline exchange membrane

AEMFC = alkaline exchange membrane fuel cell

AFC = alkaline fuel cell

ALD = atomic layer deposition

BET = Brunauer-Emmett-Teller theory

CCL = cathode catalyst layer

CCM = catalyst coated membrane

CFC = carbon film cathode

CL = catalyst layer

CVD = chemical vapor deposition

DFT = density functional theory

DLS = dynamic light scattering

EDX = energy dispersive X-ray analysis

FCEV = fuel cell electric vehicle

FT-IR = fourier-transform infrared spectroscopy

GDE = gas diffusion electrode

GDL = gas diffusion layer

HOR = hydrogen oxidation reaction

I/C = ionomer to catalyst ratio

ICP-MS = inductively coupled plasma mass spectrometry

MCND = mesoporous carbon nano dendrites

MEA = membrane electrode assembly

MP = mesophase pitch

OCV = open circuit voltage

ORR = oxygen reduction reaction

PEMFC = proton exchange membrane fuel cell

PGM = platinum group metal

PPD = peak power density

PS = polystyrene

PVA = polyvinyl alcohol

RDE = rotating disk electrode

SACs = single atom catalysts

SAXS = small angle X-ray scattering

SD = site density

SEM = scanning electron microscopy

TEM = transmission electron microscopy

TGA = thermogravimetric analysis

TOF = turnover frequency

TPD = temperature programmed desorption

VACNT = vertically aligned carbon nanotubes

Abstract

Approaches to improve the performance and durability of fuel cells range from system level engineering down to the atomic level engineering of the catalyst's active sites. In the length scales, catalyst design focuses on the sub-nanometer and nanometer range, whereas the integration of the catalyst into the catalyst layer concerns agglomerates within length scales between 50 nm and 10 µm. This thesis focuses on the interface between catalyst design and cathode catalyst layer structure of platinum-group-metal (PGM) free catalysts. The intrinsic lower volumetric activity of PGM-free catalysts necessitates increased loading of the cathode. The structure of thick conventional PGM-free catalyst layers lacks a defined order of pores, ionomer paths and catalyst agglomerates, and therefore faces the risk of mass-transport limitation at high current densities. In the thesis, two freestanding carbon film supports with precisely defined pores within the length scale between 5 and 500 nm are proposed with the goal to facilitate mass transport and to increase the active site utilization. The first concept is based on vertically aligned carbon tubes, which are grown by chemical vapor deposition of a nitrogen-rich organic precursor 2-methylimidazole on anodic aluminium oxide (AAO). The second concept relies on polystyrene (PS) nanospheres molding the carbon precursors, mesophase pitch and polyvinyl alcohol, to create a conductive inverse opal macroporous carbon film support. The performances of the cathode film architectures with anchored Fe-N_x sites are characterized at high current densities in a half-cell gas-diffusion-electrode (GDE) setup. Furthermore, three commercial alkaline exchange ionomers are combined with a commercial PGM-free catalyst to establish a benchmark alkaline ionomer. The investigation also evaluated the performance of commercial alkaline exchange membranes. In addition, an oxygen limiting current measurement protocol is introduced to characterize the mass transport of cathode catalyst layers in the GDE half-cell.

List of Publications

Simon Kellner, Mengnan Wang, Ying Wang, Jesús Barrio, Guangmeimei Yang, Sandrine E. M. Heutz, Ifan E. L. Stephens, Magda Titirici, Engineering Macroporous Carbon Films as Freestanding Fe-N-C Cathode Catalyst Layer for Fuel Cells
Chapter 5 / Manuscript ready for submission

Simon Kellner, Ziyang Liu, Silvia Favero, Francesco D'Acierno, Angus Pedersen, Jesús Barrio, Sandrine E. M. Heutz, Ifan E. L. Stephens, Magda Titirici, Combinations of Commercial Alkaline Ionomers Membranes for the Oxygen Reduction Reaction in Half-Cell Studies in Gas-Diffusion-Electrodes
Chapter 6 / Manuscript ready for submission

Jesús Barrio, Angus Pedersen, Silvia Favero, Hui Luo, Mengnan Wang, Saurav Ch Sarma, Jingyu Feng, Linh Tran Thi Ngoc, Simon Kellner, Alain You Li, Ana Belén Jorge Sobrido, Magda Titirici, 2022, Bioinspired and bioderived aqueous electrocatalysis, *Chem. Rev.*, **123**, 2311-2348

Nattaphon Hongrutai, Saurav Ch Sarma, Yuxiang Zhou, Simon Kellner, Angus Pedersen, Kari Adourian, Helen Tyrrell, Mary P. Ryan, Joongjai Panpranot, Jesús Barrio, 2023, Sequential deposition of FeNC-Cu tandem CO2 reduction electrocatalysts towards the low overpotential production of C2+ alcohols, *JPhys Materials*, **7**, 015007

Lorenzo Mazzoli, Angus Pedersen, Simon Kellner, Robert D. Hunter, Rongsheng Cai, Mengnan Wang, Kevin Sivula, Sarah J. Haigh, Jesús Barrio, 2024, Inducing porosity in xylose-derived FeNC electrocatalysts for alkaline oxygen reduction, *Green Chem.*, **26**, 3271-3280

Outlines of the chapters

Chapter 1: Introduction

The general topic is introduced by presenting the current status of fuel cell light duty vehicles. The main inhibitor for the commercialization of PEMFCs is identified as the high price of platinum, which is used as catalyst in commercial fuel cells. Alternative platinum-free catalysts composed of the elements iron, nitrogen and carbon (Fe-N-C) are introduced as a potential substitute for platinum at the cathode.

Chapter 2: Literature review

The performance losses in platinum group metal-free cathode based fuel cells are illustrated directing the focus on mass transport losses in thick Fe-N-C cathodes. The technologies of low temperature fuel cells types, proton exchange membrane fuel cells and alkaline exchange membrane fuel cell are explained. General approaches to increase the volumetric activity of synthesized Fe-N-C catalyst are complemented by theoretical models. The parameters of influence in conventional cathode catalyst layer preparation are outlined. Numerical models of ordered PGM catalyst layers motivate the transfer of the concept of vertical tubular carbon structure and inverse opal macroporous catalyst layer to Fe-N-C catalyst layers. The main testing platform, a half cell setup gas-diffusion-electrode is introduced by illustrating the gap between existing testing setups of rotating disk electrode and membrane electrode assembly.

Chapter 3: Experimental

The materials preparation, characterization methods and electrochemical testing are described.

Chapter 4: AAO template for Fe-N-C tubular catalysts for the cathode in PEMFCs

Tubular channelled supports with large pore diameter perpendicular to the membrane and gas-diffusion-layer are explored as an idea to enhance mass transport within a Fe-N-C catalyst layer. Vertically aligned large diameter (300 nm) carbon tubes are prepared with chemical vapour deposition of a nitrogen-rich carbon precursor onto anodic aluminum oxide template. The formation of the tubes is tracked with FT IR and SEM imaging. After hot pressing of the samples onto a Nafion membrane, the etching process of AAO template to release the tubes is characterized by XRD and SEM imaging with EDX. The ORR performance of the tubes with

coordinated iron is tested in acidic electrolyte and compared to a commercial Fe-N-C benchmark.

Chapter 5: Engineering macroporous carbon films as freestanding Fe-N-C cathode catalyst layer for fuel cells

A carbon film support with interconnected macropore network based on inverse opal technique is designed for improved mass transport. Carbon precursors are mixed in an optimized ratio with macropore template polystyrene spheres to form a carbon film. The formation of the pore network is confirmed with SEM imaging and Mercury Intrusion Porosimetry. Model FeN_4 active sites are attached on the macroporous film and compared with a catalyst layer based commercial particle support equipped with the same FeN_4 active sites in GDE configuration. The effect of the thickness of the catalyst layers is investigated for the film cathodes and classic particle cathodes. Initial results of future work, which aims to expand the surface area of the film by introducing a compatible mesopore templating agent, are presented.

Chapter 6: Combinations of Commercial Alkaline Ionomers and Membranes for Oxygen Reduction Reaction in Half-Cell Studies in Gas-Diffusion-Electrodes

Three commercial alkaline exchange ionomers are compared with Nafion ionomer as binder in an RDE study on a commercial Fe-N-C catalyst complemented by SAXS measurements. The effect of the type of alkaline ionomer in a catalyst layer of Fe-N-C catalyst on the oxygen reduction reaction performance in a gas-diffusion-electrode half-cell is investigated by taking water adsorption capability and BET surface area retention of the catalyst upon interaction with the anion exchange ionomer into account. The effect of the choice of the membrane is elaborated by cross-combining three commercial alkaline exchange membranes with the catalyst layers. Finally, oxygen limiting current measurement of the catalyst layers reveals the oxygen transport properties of the catalyst layers with different alkaline ionomers.

Chapter 7: Conclusive remarks

The valuable outcomes of each chapter in this thesis are emphasized. In addition, future directions for research are proposed, finalising with a short perspective on Fe-N-C catalysts status and future potential.

1. Introduction

1.1. Fuel cell electric vehicles history

In 1966, the first fuel cell electric vehicle (FCEV) named "Electrovan" was released by General Motors (Figure 1). The car could reach a top speed of 70 mph and had a driving range of 150 miles.[2] The vehicle was powered by liquid hydrogen and liquid oxygen in an alkaline fuel cell (AFC) developed by Union Carbide Corp (UCC).[3] Interestingly, UCC produced porous baked carbon plate and also tubular carbon electrodes yielding excellent power densities already in the early 1960s.[4] In the article authored by Karl Kordesch, who was involved in the development of the Union Carbide AFCs, it is described that "the electrodes were made by mixing a filler, petroleum coke flour, with binder coal-tar pitch, then baking to carbonize the pitch, and finally firing at high temperatures up to 1700°C. The pore structure was determined by the size of the filler particles. The electrodes were brittle and had to be relatively thick (3 to 4 mm) to be sufficiently strong." Despite being unaware of this pioneering research, similar concepts for freestanding carbon electrodes based on mesophase pitch were conceived in the following thesis. This demonstrates that sometimes ideas ahead of their time, are re-invented.

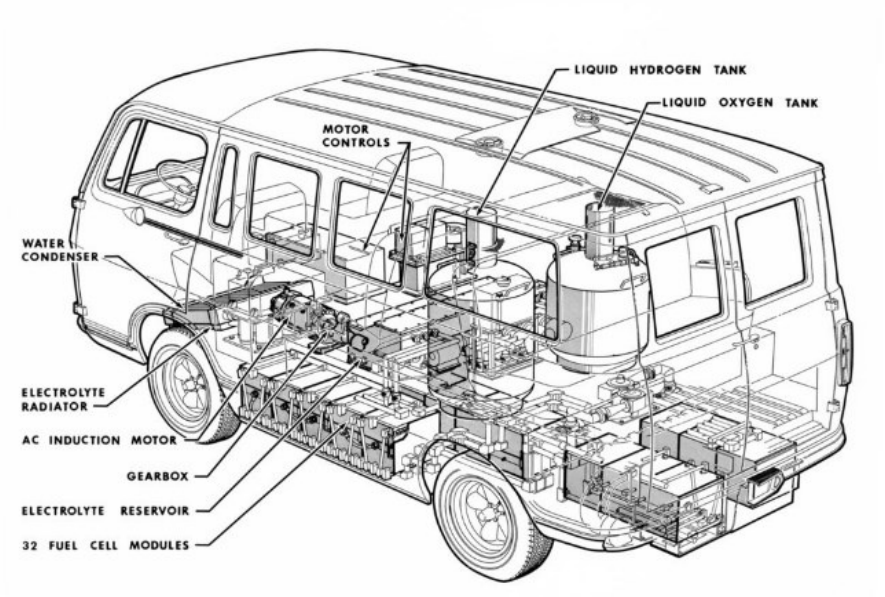


Figure 1. The General Motors Electrovan in 1966. Image reproduced from: GM Archive [5].

1.2. Fuel cell electric vehicles today

According to the 2023 Global EV Outlook report of the International Energy Agency (IEA), there are 72 000 FCEV globally on the roads.[6] The FCEV are composed of 80% cars, 10%

trucks and almost 10% buses. Speaking in numbers, in the context of total 26 000 000 electric light duty vehicles, the contribution of FCEV is rather irrelevant. In 2023, only two available series models in light duty vehicle sector, including the Toyota Mirai and Hyundai Nexo, were available on the market. Besides, a lot of car manufacturers are presenting or are about to present their concept cars and pilot fleets. The main issues for the large scale commercialization of FCEVs is the lack of refueling infrastructure. Currently, there are 93 hydrogen refueling station in Germany, leading in Europe, and 10 in the UK.[7] The existing refueling infrastructure seem to be rather contracting with Shell recently closing down their share of 7 out of 55 hydrogen fueling stations across California, the only state in USA with public accessible hydrogen infrastructure.[8,9]

1.3. Platinum – the price to be paid for commercialization

The primary fuel cell technologies used in the automotive sector are low temperature fuel cells (< 120 °C).[10] The fuel cell stacks in the two commercialized vehicles are assembled of single proton-exchange-membrane fuel cells (PEMFC).[11,12] Since a single PEMFC creates a relatively low voltage (usually 0.6 – 1 V, depending on the operation point), it is necessary to stack cells in series to increase the total power output.[13] For commercialization of PEMFC stacks being economically feasible and accelerated, the price set by the internal combustion engine with < 30 $/kW is targeted. In the last decades, PEMFCs advanced technologically accompanied with a considerable decrease of their cost. While the power density improved by factor of ~3 from 2002 to 2022 (Figure 1 a): Green), the system costs decreased by a factor of ~4 from 2008 to 2022 to a current value of 60 $/kW (Figure 1 a): Orange).[14] For light-duty vehicles, the goal is set below 30 $/kW for the system costs and below 15 $/kW for the fuel cell stack.[14] In the breakdown of the stack costs, the platinum cathode catalyst contributes up to 40% at high manufacturing volume of 500 000 per year.[15,16] Therefore, a reduction of platinum loading from 0.2 g/kW to ultralow loadings of less than 0.05 g/kW could decrease the stack costs by 9 $/kW.

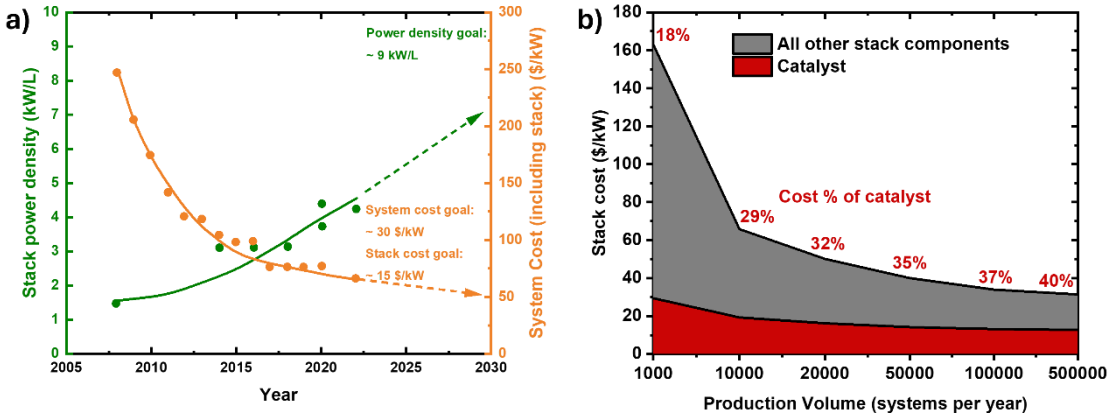


Figure 2. a) Development trend of PEMFC stack power density (blue) and PEMFC system cost for light-duty vehicles (orange). b) The proportion of catalyst cost in the stack cost. Replotted with data from US DOE [17].

Since the deployment of the first mass-produced FCEV, Tucson ix35 by Hyundai in 2013, the platinum content in the stack has been reduced from 78 g to 56 g in the Nexo launched in 2018.[18] Toyota allegedly reduced the platinum in the second generation of Mirai down to 10 g.[19] Mesoporous carbon nano dendrites (MCND) with small mesopores house 80% of the Pt inside MCND preventing direct contact between the Pt and the ionomer and suppressing sulfonic acid cover poisoning. This new carbon support combined with a platinum-cobalt (PtCo) alloy catalyst enabled a boost of the catalytic activity by 50%. In addition, a new highly oxygen-permeable ionomer with an oxygen diffusion performance three times greater than the previous ionomer was implemented into the catalyst layer.[20] In academia, the new goals of the DOE to reduce the Pt loading further to 0.1 mg_{Pt}/cm^2 with ultra-low platinum loading catalyst are met, even demonstrating PEMFC stability after 30000 test cycles.[21] Apart from downsizing the platinum loading, the elimination of platinum (Pt) is considered. As the oxygen reduction reaction (ORR) at the cathode is kinetically six orders of magnitude slower than the hydrogen oxidation reaction (HOR) at the anode[22], the larger share of the Pt is required at the cathode to catalyse the ORR. Therefore, a substitution of Pt at the cathode with alternative abundant materials has motivated research. Experimental screening for alternative catalysts has focused on the transition metals coordinated by nitrogen in a carbon matrix (M-N-C). In the vast majority of these studies, Fe was identified as the most active metal for M-N-C catalysts in both acid and alkaline electrolytes[23,24], followed by Co with satisfactory activity.[25] To conclude, the most promising platinum group metal free (PGM-free) catalysts for the ORR are materials containing the elements iron, nitrogen and carbon (Fe-N-C). [26,27,28]

2. Literature review

2.1. The origins of performance losses in platinum group metal free cathode based fuel cells

The nature of active sites with highest activity in Fe-N-C type catalyst is distinct from Pt-based catalysts. The preferentially atomically dispersed iron sites versus the mandatory minimal size of Pt nanoparticles[29] lead to differences in the respective volumetric activity of the catalysts. As a consequence of the lower volumetric activity of Fe-N-C catalysts, the thickness of Fe-N-C cathode catalyst layers is increased up to 100 µm to produce comparable PEMFC performances as 10 µm thick Pt/C cathode catalyst layers.[30] In order to understand the performance losses in PEMFCs with Fe-N-C catalysts and especially the losses due to the thick cathode catalyst layers, the theory about the causes of losses in PEMFCs is introduced (Figure 3 a)).

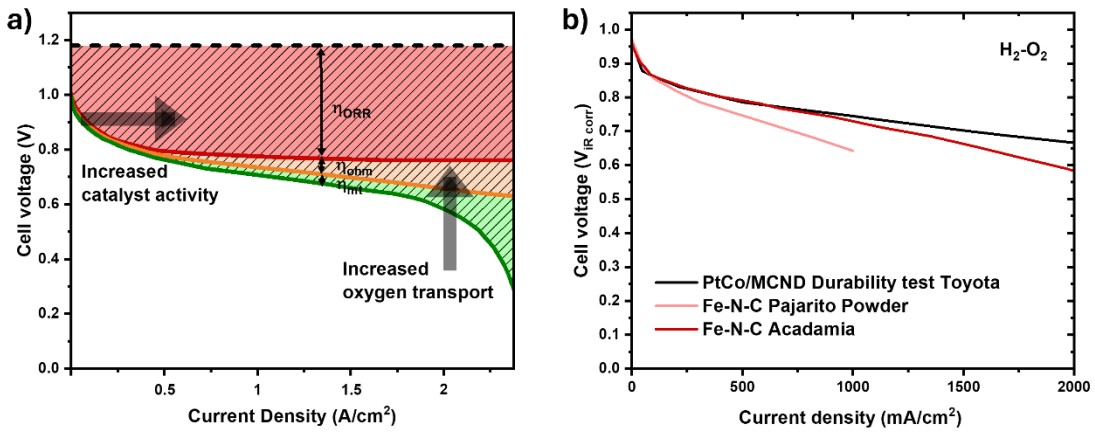


Figure 3. a) Theoretical illustration of a PEMFC polarization curve and the composition of losses. Based on theoretical considerations from [31]. b) PEMFC polarization curves recorded in H_2-O_2 for PEMFC with cathode catalysts of industrial and academic relevance. Replotted with data from [30,32,33].

In theory, the fuel cell potential at 25°C and atmospheric pressure would be expected to be the thermodynamic equilibrium potential at 1.23 V as calculated with the Nernst equation. As fuel cells are commonly operated at 80°C to improve the performance in terms of reaction kinetics, the temperature-dependence of the Nernst equilibrium potential would give an ideal cell reversible potential (E_{rev}) of 1.18 V, as represented by the horizontal black dashed line (Figure 3 a)). The open circuit voltage (OCV), the voltage measured while zero current is drawn from the cell, in a proton exchange membrane fuel cell (PEMFC) is typically approximately 300 mV lower.[34] At low current densities, the prevailing losses are caused by kinetic

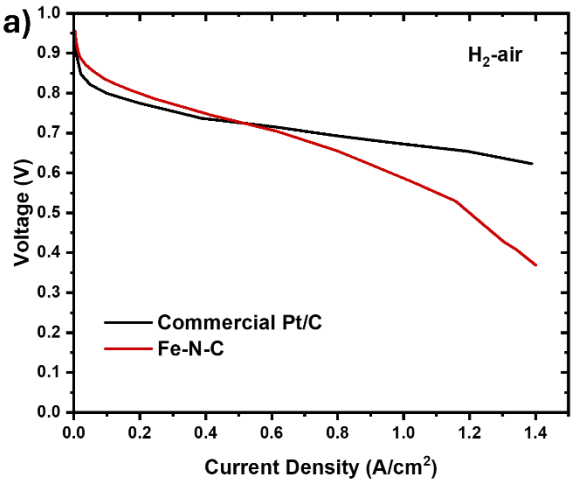
overpotential.[35] Due to ultrafast HOR kinetics on the Pt-catalysts at the anode, the HOR only contributes negligibly to the kinetic overpotential.[36] Therefore, kinetic losses are mainly attributed to the sluggish ORR, and referred to as ORR overpotential (η_{ORR}).[37] The ohmic losses (η_{ohm}) result from electronic contact resistances and limitations in the proton transport in the membrane and ionomer in the catalyst layer, and are proportional to the current density. At high current densities, the transport of oxygen through the diffusion medium and the catalyst layer to the active sites becomes limited. Additionally, poor water removal may cause flooding of the pores in the catalyst layer, and thus, inhibiting the oxygen transport. The inefficient oxygen reactant supply translates to mass-transport overpotential ($\eta_{mass\text{-}transport} = \eta_{mt}$). In summary, the relative impact of these overpotentials with respect to the deviation of the actual cell voltage E_{cell} at a certain current density from the reversible potential can then be described as:

$$E_{cell} = E_{rev} - \eta_{ORR} - \eta_{ohm} - \eta_{mass\text{-}transport} \quad \text{(Equation 1)}$$

The polarization curve of an actual fuel cell with the same PtCo/MCNT catalyst at the cathode as in the Toyota Mirai II (black line) is shown (Figure 3 b)) corresponding to the expected η_{ORR} and η_{ohm} as described by theory and with η_{mt} expected at higher current densities.[38] In that industrial research study, a Pt loadings of 0.17 mg_{Pt}/cm^2 for the cathode and of 0.025 mg_{Pt}/cm^2 for the anode were chosen. The thickness of the tested cathode catalyst layer was approximately 10 µm. In order to meet the DOE 2025 ORR activity target for PGM-free catalysts set at 44 mA/cm^2 at 0.9 $V_{iR\text{-}free}$ at oxygen pressure of 1.0 bar[39], higher Fe-N-C loadings between 4.0 to 4.5 mg/cm^2 are used at the cathode to compensate for the lower intrinsic volumetric activity. Recently, an MEA generated a current density of 50.8 mA/cm^2 exceeding the activity target.[40] As the entire polarization curve for that particular Fe-N-C catalyst is not displayed in the article, the MEA polarization curves with cathodes prepared with commercial Fe-N-C catalyst from Pajarito Powder[30] (pink) and a Fe-N-C Academia catalyst based on ZIF8 with high iron loading of 7 wt%[33] (dark red) tested in oxygen 1 bar are re-plotted (Figure 3 b)). The mass transport losses are evident in both cases, with the potential for the Pajarito Powder based MEA drops below 0.65 V at 1 A/cm^2 and the Fe-N-C Academia catalyst, initially overlapping with the polarization curve of the Pt-based MEA, starts to deviate from it around 1 A/cm^2. At 2 A/cm^2 the potential loss for Fe-N-C Academia compared with Pt-based MEA is almost 100 mV. The ultimate goal is to use air instead of oxygen in fuel cells, for which the mass-transport losses in MEAs incorporating present-day Fe-N-C cathodes are far more pronounced. The Fe-N-C catalyst, which meets the activity target, does not meet either of the mass transport performance targets in air. The current density of 191 mA/cm^2 at 0.8 V fails to meet the 300 mA/cm^2 target.

Despite adjustment of the relative humidity to 75% to mitigate water flooding within the thick Fe-N-C cathode, the improvement of the mass transport marks a power density of 501 mW/cm^2 at 0.67 V. Especially the electrode structure has potential for the improvement with regards to increase the utilization and reduction of thickness to meet the automotive target of 1000 mW/cm^2.[41] In contrast to the Pt/C cathode, the voltage losses at high current densities take off rapidly and grow to approximately 250 mV at 1.4 A/cm^2. The overview of this section emphasizes the additional performance losses in PEMFCs with Fe-N-C cathodes due to mass transport limitations of the thick catalyst layers.

a)



b)

Performance at 0.9 $V_{iR\text{-}free}$ H_2-O_2, 1 bar O_2	> 44 mA/cm^2
Performance at 0.8 V H_2-air, 1 bar air	> 0.3 A/cm^2
MEA power density H_2-air, 1 bar air	> 1000 mW/cm^2

Figure 4. a) PEMFC polarization curves recorded in H_2-air for PEMFC with cathode catalysts based on reference Pt/C (0.1 mg$_{Pt}$/cm^2) and Fe-N-C (4.0 – 4.5 mg/cm^2) with intrinsic activity above DOE 2025 target. Replotted with data from [40]. b) Overview of the DOE 2025 activity and mass transport targets [39,41].

2.2. Proton exchange membrane fuel cell vs. alkaline exchange membrane fuel cell

While the development of mature PEMFC technology plateaued in the last decade, breakthroughs in alkaline ionomer[42] and membrane[43] technology accelerated progress in anion exchange membrane fuel cells (AEMFCs).[44] Therefore, the two types of low temperature fuel cells based on polymer electrolyte membranes are briefly introduced and their reaction chemistries are compared (Figure 5). Both fuel cells consist of the same core components, which are arranged in a sandwich configuration. The main component is the membrane-electrode assembly (MEA) comprising anode catalyst layer, membrane, and cathode catalyst layer. On both sides, bipolar plates distribute the gas supply via gas-diffusion-layers to the respective electrodes. Technically, AEMFCs are similar to PEMFCs, with the main difference

being that the solid membrane is an hydroxide ion conducting anion exchange membrane (AEM) instead of an acidic proton conducing proton exchange membrane (PEM). Electricity is generated through a hydrogen oxidation reaction (HOR) at the anode and an oxygen reduction reaction (ORR) reaction at the cathode, with the electrons moving from anode to cathode in an external circuit. While in PEMFCs, hydrogen is oxidized at the anode to form two protons, the oxidation in an AEMFC involves two hydroxide ions and produces two water molecules as byproduct. The ORR in PEMFC produces two water molecules per oxygen molecule. In contrast, in the ORR in the AEMFC two water molecules in the roles of reactants are producing four hydroxide ions. To balance the charges and reactants, hydroxide ions are transported from the cathode to the anode in an AEMFC, opposite to the proton conduction direction in a PEMFC. In contrast to PEMFCs, water management plays a crucial role in AEMFC to achieve high power densities, as the amount of water generated in the anode is two times faster than the electrochemical consumption of water in the cathode.[45]

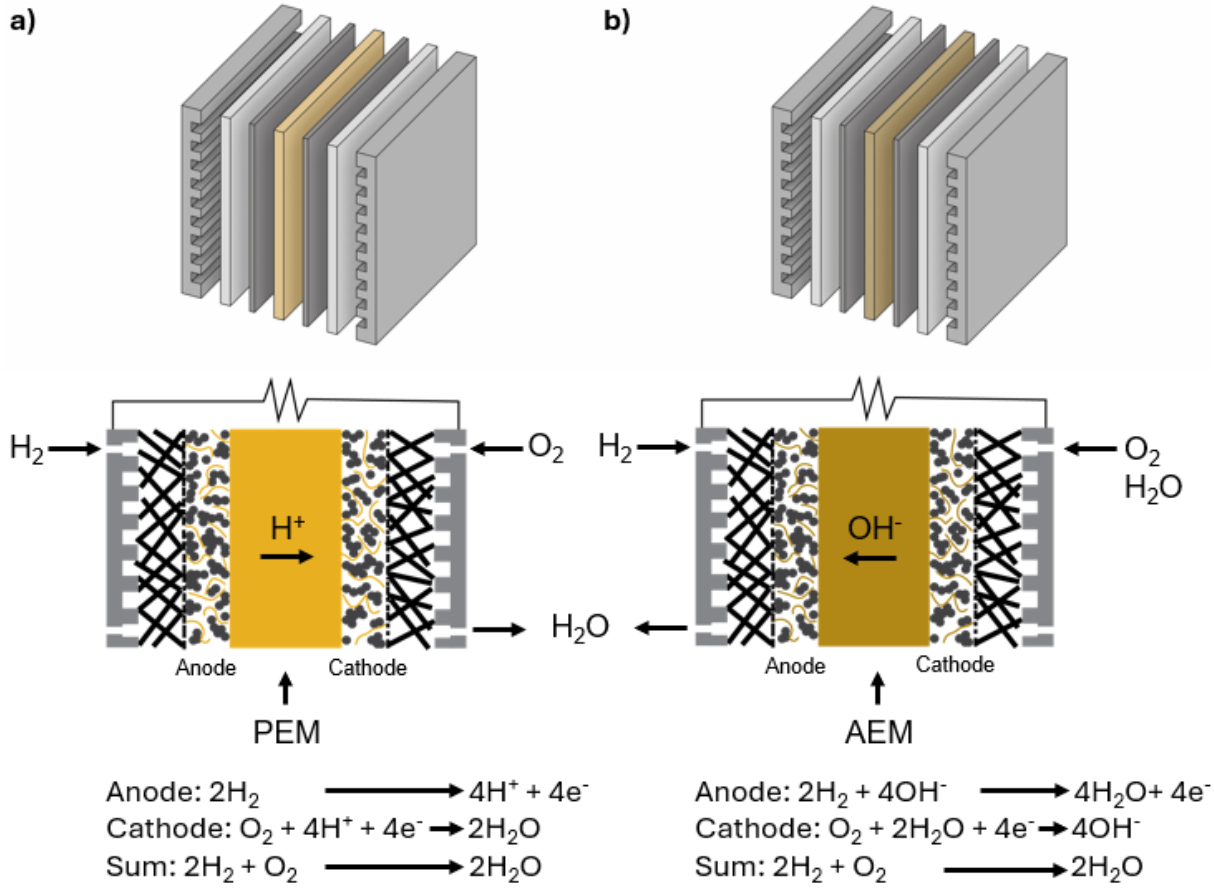


Figure 5. Schematics and reactions in a) PEMFC (left) and b) AEMFC (right).

AEMFCs benefit from the catalysts superior ORR kinetics in alkaline media. Generally, Fe-N-C catalysts have demonstrated superior activity in alkaline pH compared to acidic pH.[46,47,48] Therefore, the cathode loading in AEMFCs can be reduced to 1-1.2 mg/cm^2.[49] Recently, the performance of an AEMFCs (H_2-O_2) with commercial Fe-N-C catalyst at the cathode exceeded 2 W/cm^2.[50]

2.3. Fe-N-C catalyst development: Increase volumetric activity

Originally, Fe-N-C catalysts were prepared by high temperature heat treatments (> 700°C) of a mixture of nitrogen-rich carbon precursors and iron-containing precursors.[51,52] However, the inherent lack of control of molecular processes occurring in the pyrolysis step, which is required for the formation of a conductive porous carbon network, leads to a heterogeneous composition of iron species in the product. As a result, it is difficult to disentangle the individual contribution of various active sites to the ORR activity. In addition, a large proportion of active sites may be buried in the carbon matrix and not participating at ORR at the triple phase boundary. More rational design of Fe-N-C catalysts followed with focus on improving the activity (Figure 6 b)). The activity of Fe-N-C is recommended to be reported as mass activity from RDE studies.[53] However, in MEA testing the volumetric activity is a more fair measure as it takes the cathode thickness into account.[22,54] Cleverly, the loading of the catalyst can be increased to meet the areal activity targets at high potentials. Thicker catalyst layers (> 100 μm) can suffer from mass-transport limitation due to increasing path lengths for O_2, protons and electrons to reach the active sites. The volumetric activity of a Fe-N-C catalyst in a cathode catalyst layer is governed by the turnover frequency (TOF), site density (SD) and utilization of the catalyst[55] (Figure 6 a)). The TOF describes the intrinsic activity of a specific type of active site characterized by its electronic structure regulated by the metal center, coordinated atoms, guest groups and environmental atoms.[56] The site density (SD) can be modified by maximizing the number of active sites per surface area. Theoretically, it was proposed that a maximum of 7.5 x 10^{20} sites/g can be achieved on a catalyst with high surface area, 1000 m^2/g, and a high iron content, 7 wt%, assuming a spatial separation of 1.1 nm between surface iron atoms.[33] Experimentally, the iron sites can be determined electrochemically with nitrite adsorption followed by reductive NO electrostripping.[57] Due to their specific and strong interaction with FeN_x sites, nitrite anions NO_2^- adsorb onto electrolyte exposed FeN_x sites to form an additional nitrosyl ligand at the iron. In the subsequent reductive scan, each adsorbed NO is reduced in a five-electron process to ammonia. However, as nitrite is prone to disproportionation into NO and NO_2 at low pH, a

pH of 5.2 is chosen to avoid any interference with the stripping protocol. This moderately acidic pH value does not represent the more acidic pH regime at PEMFC cathodes. In addition, only 70% of the ORR-active sites are blocked by NO adsorption, as a decrease of the ORR current density shows. The rest of the ORR activity may either be attributed to nitrogen doped carbon active sites or types of FeN_x sites, which can not be targeted by NO.

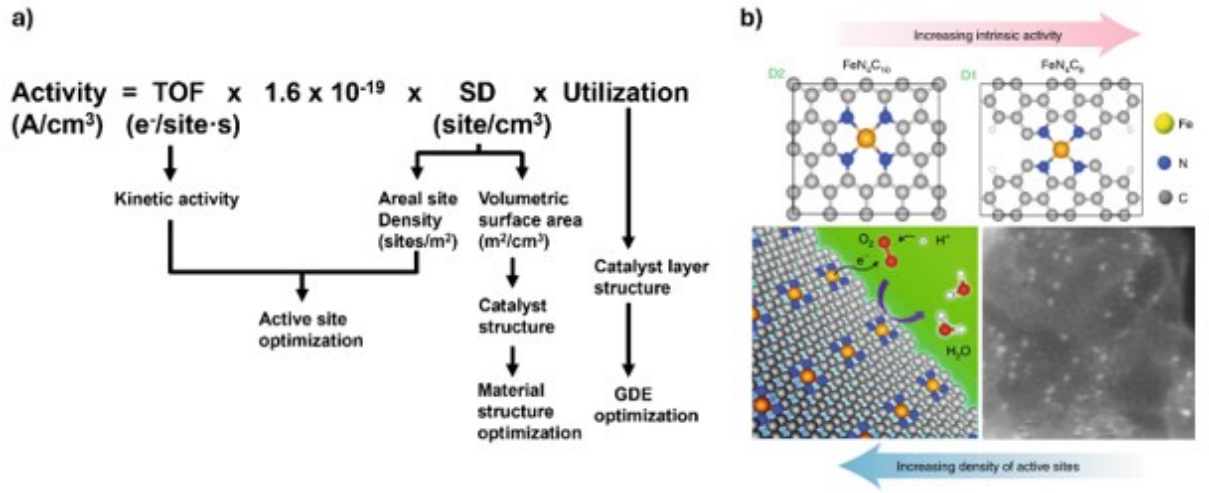


Figure 6. a) Overview of the factors to increase volumetric activity of Fe-N-C catalysts. Replotted based on scheme in [58]. b) Two strategies to improve the catalytic activity of Fe-N-C electrocatalysts. Reproduced from [59].

There is a second option to probe the number of FeN_x sites in a non-electrochemical environment. This ex situ method involves CO chemisorption at -80°C from the gas phase followed by temperature-programmed CO desorption (TPD) during heating ramps to 600°C.[60] The experimentally determined FeN_4 SD with both techniques are of the same order of magnitude of 10^{19} sites/$g_{Catalyst}$.[61] Regarding the SD values obtained from both methods, the detailed SD(CO) values derived from gaseous CO cryo chemisorption exceeded the SD(NO_2^-) by factor of 2 to 8. This discrepancy between the two methods might originate from different accessibilities of the probes, gas-phase accessibility in case of the CO cryo-adsorption method and liquid-phase electrochemical accessibility in the nitrite stripping method. Gaseous CO might even have access to FeN_4 located in micropores of the dry solid catalyst, whereas NO_2^- adsorption takes place in liquid electrolyte with potential blocked access to micropores. In PEMFC, a large-amplitude Fourier-transform alternating current voltammetry (FTacV) has been demonstrated to quantify the electrochemically active site density of Fe-N-C catalyst in the cathode catalyst in situ during fuel cell operation.[62] An active site density was extracted from the simulation with $6.3 \cdot 10^{18}$ sites/$g_{Catalyst}$ comparable to the number measured with the

nitrite stripping method. The electrochemical utilization of the total amount of iron ($Utilization_{Nitrite/ICP}$) reveals the accessibility of the active sites. Despite a reported maximum of 52% electrochemical utilization of FeNx sites[63], the surface iron content might be potentially further increased in future catalyst development. Several approaches are being explored using different chemical precursors and synthesis paths, at the forefront single atom catalysts (SACs) with maximum Fe utilization efficiency have guided the research in Fe-N-C catalysts in recent years. Synthesis methods with the goal to increase the number of active sites avoid the presence of iron in the pyrolysis step, which is required for the preparation of the conductive carbon support. Post-coordination of the iron, a process called metalation is carried out either in liquid or gas phase for anchoring single iron sites on the support. A prominent example of the liquid phase metalation is refluxing of an iron salt in methanol.[64] Alternatively, a chemical vapour deposition (CVD) process can deposit iron sites by flowing an iron chloride (anhydrous) vapor over the nitrogen-doped carbon support.[65] While modifying the structure of active sites and their density are main approaches in catalysis, it is also important to offer efficient porosity to enable accessibility of the active sites and mass transport of the reactants and products to and from the active sites. Otherwise, active sites, even though they might be on the surface of the catalyst material, might not be electrochemically accessible or not continuously supplied with reactant to operate at maximum TOF. These considerations gain importance for Fe-N-C cathode catalyst layers due to their increased thickness.

2.4. Density Functional Theory (DFT) modelling to predict activities of active sites

Theory has developed models that predict the ORR activity and selectivity of a catalyst according to binding strength, a measure of binding free energy, of the intermediates to the active sites. The four electron ORR may proceed through an associative or dissociative mechanism. In the SACs community, there is agreement on ORR proceeding according to an associative mechanism due to spatial isolation of the active site and the end-on oxygen adsorption, corresponding to the Pauling model.[66,67] The associative mechanism involves three intermediate binding oxygen species including *OH, *O, and *OOH. First, the O_2 diffuses and adsorbs to the active site (*). The adsorbed O_2 is reduced to water in four sequential electron transfers.

Associative mechanism:

In acidic pH:

$$* O_2 + * + e^- + H^+ \rightarrow * OOH \text{ (Equation 2)}$$

$$* OOH + e^- + H^+ \rightarrow * O + H_2O \text{ (Equation 3)}$$

$$* O + e^- + H^+ \rightarrow * OH \text{ (Equation 4)}$$

$$* OH + e^- + H^+ \rightarrow H_2O + * \text{ (Equation 5)}$$

In basic pH:

$$* O_2 + * + H_2O + e^- \rightarrow * OOH + OH^- \text{(Equation 6)}$$

$$* OOH + e^- \rightarrow * O + OH^- \text{ (Equation 7)}$$

$$* O + H_2O + e^- \rightarrow * O + OH^- \text{(Equation 8)}$$

$$* OH + e^- \rightarrow OH^- + * \text{ (Equation 9)}$$

For alkaline pH, H_2O acts as the proton donor.

Theorists present ORR activity and selectivity trends in volcano-type correlations as a function of the binding energy of oxygen intermediates to the catalyst.[68] Catalytic activity of SACs is influenced by the selection of the metal center and the coordination configuration, specifically the coordination number and the electronegativity of the coordinating atoms and the local environment.[69,70] The onset potential U(V), equivalent to the thermodynamic limiting potential meaning the highest theoretical potential at which all reduction reaction steps are still energetically downhill for SACs with MN_4C active site with pyridinic structure were both calculated with DFT and determined experimentally with RDE measurements (|current density| > 0.2 mA/cm^2)[71,72,73] (Figure 7). As the binding free energies of the three reaction intermediate oxygen species to the active site of the catalyst correlate with each other linearly in a scaling relationship, the relationship between activity and binding free energies of the intermediates can be simplified by choosing one representative intermediate such as *OH as descriptor.[74] According to the Sabatier principle, the catalyst with balanced binding energy, neither too weak nor too strong, to the ORR intermediates *OH, *O, *OOH is located at the peak of the volcano and achieves the best catalytic activity.[75] The FeN_4C site is closest to the top of the volcano and has the lowest onset potential and thus, the highest activity for the ORR. The binding strength

of the *OOH intermediate determines whether the ORR proceeds along the four electron pathway to H_2O or along the two electron pathway to H_2O_2. In case of Fe, relatively strong binding of *OH and correspondingly *OOH, is directing towards the four electron ORR. In contrast, the weaker binding energy of *OH and linearly dependent *OOH to Co, predicts a predominant two electron ORR towards H_2O_2, as the O-O bond is not cleaved.

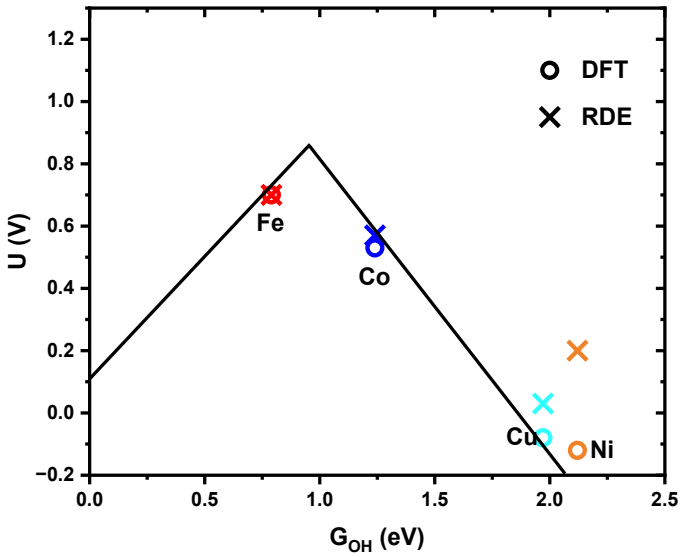


Figure 7. Volcano activity plot of the onset potential for ORR calculated with DFT (O) and experimentally determined for single M-N_4 sites with pyridinic structures versus the *OH binding free energy (G_{*OH}). Replotted with data from [73].

Apart from the metal center, the coordination configuration is influencing the catalytic activity of FeN_4C sites. The most prominent and intensely debated example is coordination configuration of FeN_4C sites, either pyrrolic type or pyridinic type, because of its implication on activity and stability of the active site.[76] In the case of the pyrrolic type, each coordinating nitrogen is integrated into a five-membered ring with carbon atoms (Figure 8 b)). Alternatively, in the pyridinic type, each nitrogen is part of a six-membered ring with carbon atoms (Figure 8 d)). In the free energy path, the rate determining step (RDS) for ORR is the most the endothermic step at equilibrium potential (U = 1.23 V). The RDS also depends on the structure on the FeN_4 active, it is predicted to be the fourth reduction step from *OH to H_2O for a model based on planar molecular FePc.[77] The RDS restricts the overall ORR kinetics. The potential at which all steps become exothermic is called the onset potential or thermodynamic limiting potential. The difference between onset potential and equilibrium potential is the overpotential. The free energy diagrams for ORR steps on the pyrollic N-coordinated FeN_4C_{12} and the

pyridinic N-coordinated FeN_4C_{10} change with applied voltage. The pyrrolic N-coordinated FeN_4C_{12} site is predicted to have higher catalytic activity with an onset potential of 0.73 V compared to the pyridinic N-coordinated FeN_4C_{10} with an onset potential of 0.65 V.

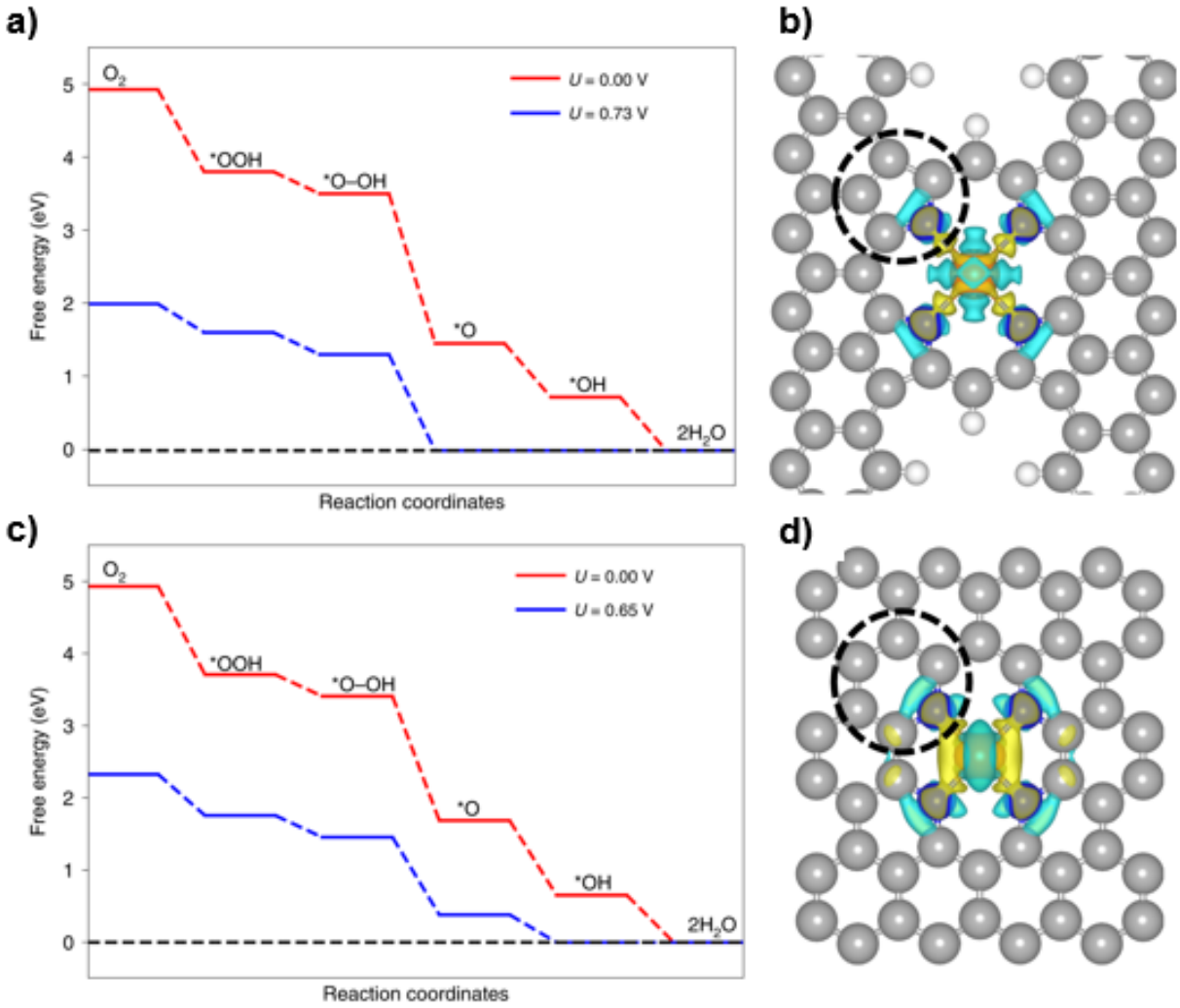


Figure 8. Predicted free energy evolution for the ORR through 4 electron associative pathway on pyrrolic N-coordinated FeN_4C_{12} (a)) and on pyridinic N-coordinated FeN_4C_{10} (c)) under electrode potentials of U = 0.00 V (red) and their corresponding limiting potential (blue). Charge density on pyrrolic N-coordinated FeN_4C_{12} (b)) and on pyridinic N-coordinated FeN_4C_{10} (d)). Cyan and yellow represent charge accumulation and depletion in the region, respectively. Reproduced from [76].

2.5. Cathode catalyst layer design

The abundant literature about synthesis and measuring the kinetic activity of Fe-N-C catalyst in the RDE and MEA is opposed by the scarce literature about the optimizing of the cathode catalyst layer design. However, in PGM-free cathode catalyst layers, the thickness has a more pronounced effect on charge and mass transfer resistances.[78] A conventional catalyst layer is composed of a disordered distribution of agglomerated catalyst particles, ionomer and pores. The three components form a network of transport channels for the reactants, comprising electron, ion, and oxygen transfer to the active sites in the catalyst and repulsion of produced water out of the catalyst layer. Electrode composition and structure optimization offer the opportunity to minimize transport resistances, and as a result to increase the fuel cell performance. The goal is to maximize the triple-phase boundary of electron, ion, and oxygen at the active sites.[79] Since the performance of a MEA is not only dictated by the intrinsic activity of the catalyst, as determined by aqueous half-cell studies in RDE, it is challenging to translate the intrinsic activity into real devices. In MEAs, solid electrolyte ionomer and thicker catalyst layers inhibit the transport of oxygen and protons compared to experiments in liquid electrolyte. However, widespread catalyst deposition methods such as spray coating at research lab scale or doctor blade coating at industrial manufacturing scale, lack the accurate nanoscale control of the final CL structure.[80] Generally, parameters such as catalyst loading[30] to increase the number of active sites in the CL and ionomer / catalyst (I/C) ratios[30,81] are adjusted when implementing a new catalyst into a CL. The ionomer proportion has to be delicately balanced between maximizing activity by spreading as much ionomer as possible in proximity of the active sites for efficient proton supply, and minimizing oxygen diffusion through excessive ionomer film coverage on the catalyst and filling of the meso- and macropores in the bulk catalyst layer.[82] Simply phrased, it is a trade off between oxygen mass transport resistance and proton transport resistance.[83] Recently, nanoscale resolution X-ray computed tomography (nano-CT) (resolution of ~ 50 nm) was used to resolve solid and pore morphology as well as the Nafion distribution in PGM-free cathodes with different ionomer loading[82] (Figure 9). However, due to the unique blueprint with regards to pore structure and surface chemistry of each individual catalyst, the optimal I/C ratio may be different in each study. Smaller sized catalyst particles improve the mass transport properties after down-sizing with ball milling[84,85] Additionally, the choice of solvent and the evaporation temperature can impact the pore structure of the CL.[86]

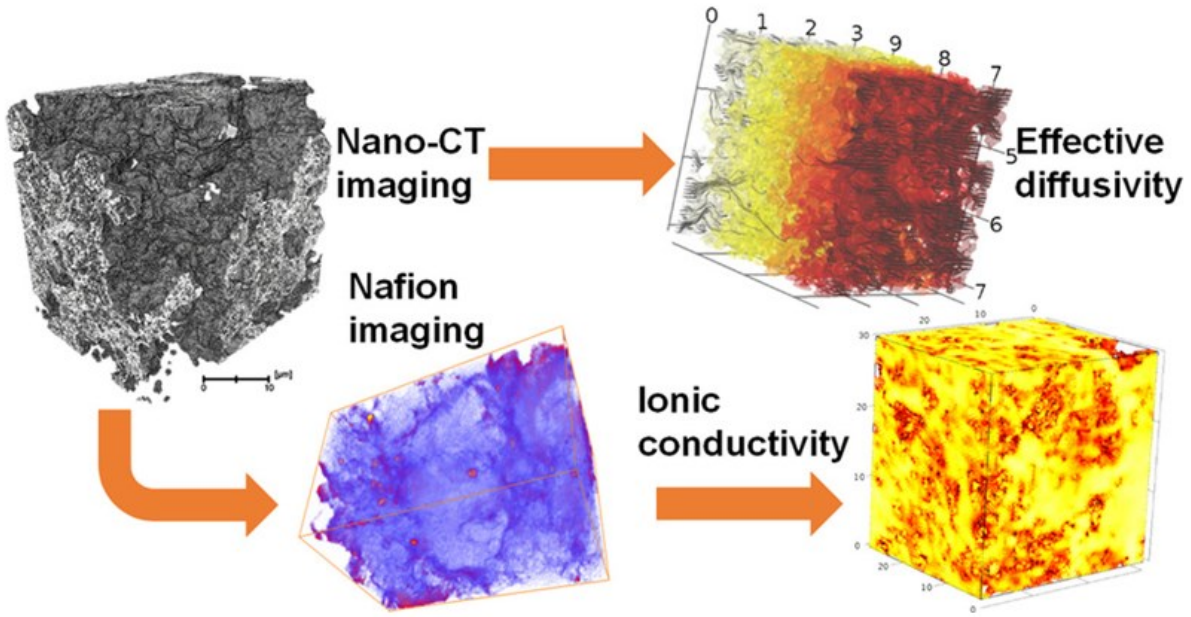


Figure 9. Nano-CT of Pore and Ionomer Distribution in PGM-free particle-based CL. Reproduced from [82].

In summary, the fuel cell performance is dependent on more factors beyond the intrinsic activity of the PGM-free catalyst, including accessibility of the active sites, local and bulk oxygen transport, and proton transport properties of the cathode CL. The transport properties become especially relevant at high current densities, and limit the PGM-free cathode CL from accessing high power density (> 1.0 W/cm^2) required for the application in the transportation sector.

2.6. Design of catalysts with inherent mass transport

Approaches to promote the mass transport properties at catalyst structure level have been mainly focusing on electrospun electrodes, since the fiber connectivity is expected to be beneficial for electron and proton transport, and in addition the macropores may improve oxygen and water transport. The electrospinning of ZIF-8 and polyacrylonitrile produced a fiber, which was carbonized at elevated temperatures.[87] The disadvantage of introducing the Fe precursor into the electrospinning solution is that the high voltage applied during electrospinning causes the formation of metallic Fe nanoparticles, as observed in the analysis after pyrolysis. The electrospun web was ground and mixed with Nafion dispersion to prepare a catalyst layer. The fiber catalyst outperformed the particle based reference catalyst in MEA testing confirming the theory of enhanced mass transport in the macroporous voids between the

fibers. To simplify the process, a pyrolyzed Fe-N-C catalyst, Nafion and carrier polymer were electrospun in a single step. [88] The power density of this fiber electrode was 50% increased compared to traditionally prepared electrodes in H_2 - air fuel cell testing due to reduced bulk oxygen transport resistances.

2.7. Model Simulation To Meet Transport Performance Targets

In industrial settings, fuel cells operate at cell voltages between 0.6 V and 0.7 V, where the power output is maximized.[31] To operate fuel cells more efficiently and reduce the amount of electrochemically generated heat, an operating voltage of 0.67 V is chosen. Thus, a MEA has to produce a current density of at least 1.493 A/cm^2 for PGM catalysts to obtain a power density of 1 W/cm^2. Although a Mirai stack conveys 1.85 A cm^{-2} @ 0.67 V, a value that exceeds the rated power density target, the MEA PGM loading is still high with 0.33 mgPt/cm^2 compared to the 0.125 mg$_{Pt}$/cm^2 DOE target for both electrodes.[89,90,91] The 2020 DOE performance target for non-PGM catalysts was set to 500 mA/cm^2 at E_{cell} = 0.675 V and has been reached recently.[92,93] Nevertheless, the commercial Fe-N-C catalyst (Pajarito Powder) has not lived up to that target yet[94] (Figure 10 a)). In contrast to the activity target of DOE at E_{cell} = 0.9 V, which a lot of PGM-free catalysts met recently, the limiting processes for the performance target at 0.675 V are different. Thicker catalyst layers impacts the transport resistance for oxygen diffusion, electron and proton conductivity to the catalyst active sites due to tortuosity, and as well as water removal, especially at high current densities.[94,95] The order of magnitude of cathode catalyst layer thickness difference between Toyota Mirai with PGM-catalyst, and PGM-free catalysts Fe-C-N 1000 C (4 mg/cm^2) and Pajarito Powder (4 mg/cm^2) (Figure 10 a)) emphasizes the challenge for PGM-free catalysts to reach high performance in H_2-air fuel cells. A modelling project based on data of CM-PANI-Fe catalyst suggests that the mass transport losses can be reduced by reducing the thickness of the catalyst layer, while the current in the activation region (E_{cell} = 0.9 V) is reduced at the same time[96] (Figure 10 b)). These findings were confirmed by a second study based on data of iron nircarbazin (Fe-NCB) catalyst by resorting to low humidity conditions.[97] PGM-free cathodes with varying mass loadings from 0.5 to 4 mg/cm^2 have been simulated (Figure 10 c), d)). The assumption of the thickness of the PGM-free electrode is referred to the experimental observation of a thickness of 100 μm with a 3 mg/cm^2 loading, concluding that a loading of 1 mg/cm^2 of Fe-NCB corresponds to 33.3 μm in thickness.[98] The higher cathode catalyst loading increases the performance at low current density (E_{cell} = 0.9 V), and in this way enables the activity target to be reached. For the Fe-NCB

the optimal loading seems to be 3 mg/cm^2, as the improvement in the fuel cell operation activation region is not accompanied with improved performance at higher current densities. In addition, the authors of this model study concluded that the main limiting factor for that particular Fe-N-C catalyst is not gas transport resistance, but also electric and low proton conductivity, as they observed compressing the thickness with a fixed catalyst mass loading improved the performance.[98] An ideal model was established which requires a Fe-N-C with the DOE activity target performance, optimized phase composition and a cathode thickness of 45 μm, to fulfil the US DOE catalytic activity target at 0.9 V and the ultimate fuel cell target (1.5 A/cm^2 at 0.675 V). [96] Another model derived the oxygen transport resistances for 100 μm thick PGM-free electrodes based on atomically dispersed Fe-N-C[99] taking Knudsen diffusion (pressure-independent) and solid-state diffusion processes (pressure-dependent) into account.[41] Depending on the conditions the oxygen transport resistance varied between 1.0 and 1.8 s/cm, 2-3 times compared to a PGM-electrode with 0.1 mg$_{Pt}$/cm^2 loading with 0.5 s/cm (at 80°C, 100% RH).

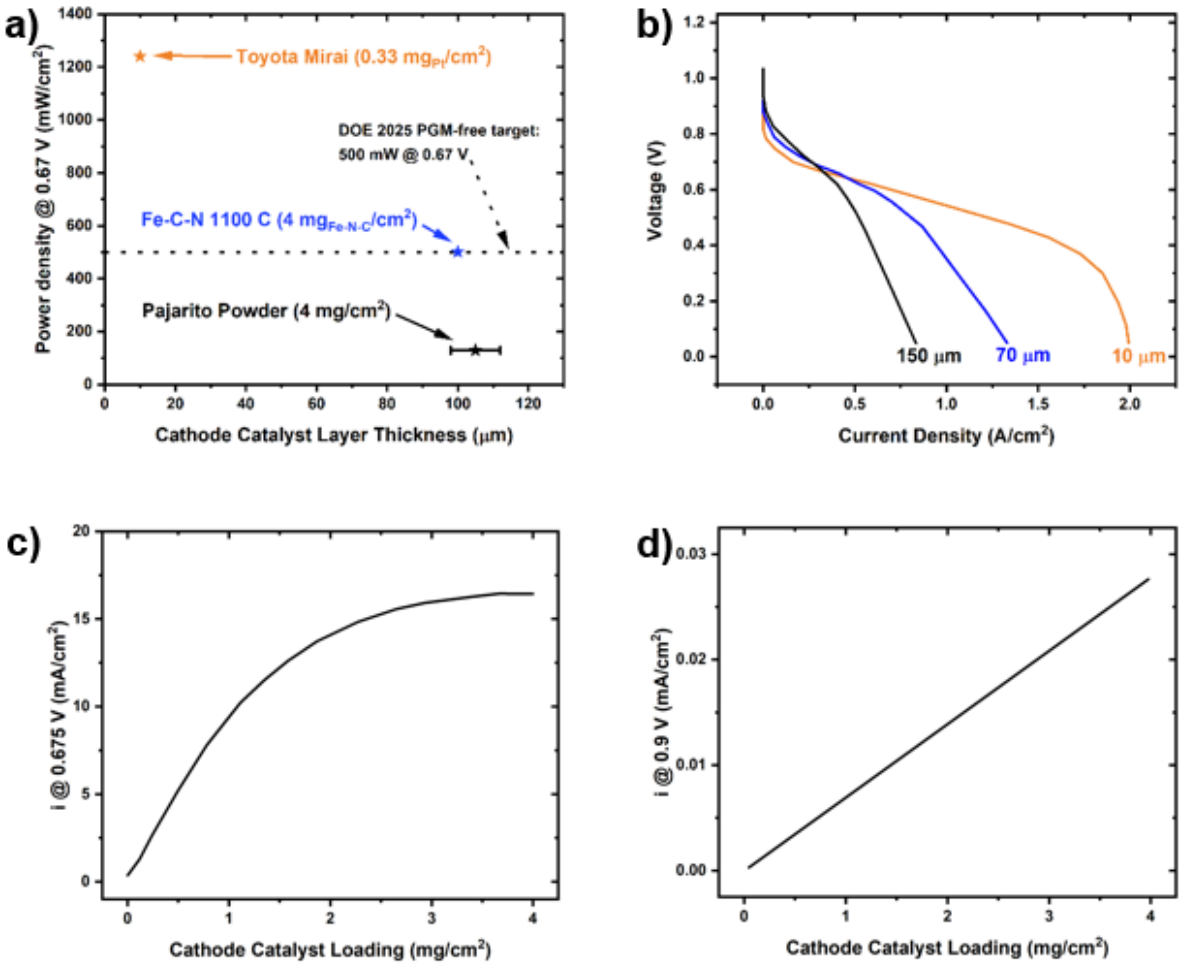


Figure 10. a) Extracted power densities at 0.67 V of H_2-air fuel cells versus thicknesses of cathode catalyst layers comparing commercial Toyota Mirai based on a Pt catalyst[89], commercial PGM-free Pajarito powder[94] and target surpassing Fe-N-C catalyst[40] (Fe-C-N 1100 C, estimated thickness of 100 µm at a reported loading of 4 mg/cm^2). b) Modelling of PGM-free catalyst layer thickness[96]: Effect of thickness on the 50 wt% Nafion loading cyanamide-polyaniline-iron salt (CM-PANI-Fe) electrode on the MEA performance. The simulation was run at 80°C and 100% RH H_2 and air feed gas at 1 atm partial pressure. c) Towards the fuel cell performance target: Relationship between the current density at E_{cell} = 0.675 V and the cathode catalyst loading. d) Towards the activity target: Relationship between the current density at E_{cell} = 0.9 V and cathode catalyst loading. c) and d) are based on the iron nircarbazin (Fe-NCB) catalyst prepared with sacrificial support method. Data replotted from [94].

The structure of classical PGM-free cathode catalyst layers is inherently disordered due to a random distribution and agglomeration of catalyst particles, ionomer and pores. As a result of that morphology, poor transport pathways and low utilization of the catalyst, the power output is restricted. Therefore, it is hypothesized that ordered architectures of the catalyst layer may be beneficial for mass transport and active site utilization. Owing to the lack of models for ordered PGM-free catalyst layer architectures, the assumptions are backed up by recent models developed for vertical aligned tubular and inverse opal structured PGM-based cathodes. An early numerical model for vertical aligned carbon nanotubes (VACNT) cathode catalyst with Pt uniformly deposited on them with tube outer / inner diameter of 50 nm / 40 nm, determined that a spacing of 400 nm between the individual tubes leads to the best mass transport among the spacings studied.[100] The optimal thickness of the Nafion in an ordered nanostructured catalyst layer based on VACNTs was found to be 10 nm and suggested that carbon tube spacing of 50 nm would be optimal for mass transport when taking a tube length of 3 μm.[101] However, these two models oversimplified mass transport processes, considering water only in vapor phase. In addition, the macroscale transport behaviour in the pores and channels was neglected. Recently, a multiscale model unified both macroscopic and microscopic mass transfer. It consists of a PEMFC macroscopic model that describes the electrochemical and mass transport process and a local oxygen transport sub-model that reflects the transfer of oxygen molecule from the bulk pores to the catalyst surface.[102]

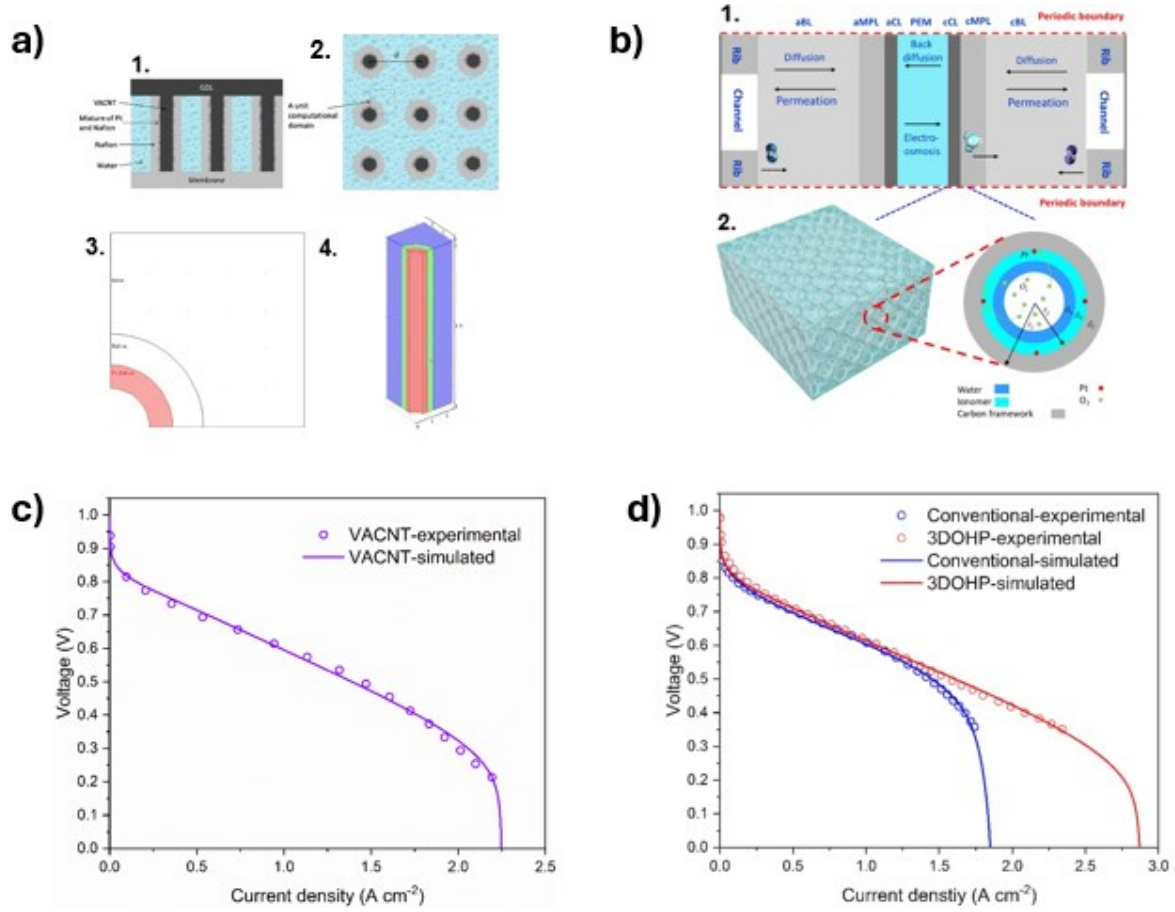


Figure 11. a) (1) Schematic of VACNT CCL with cross-section (2) top view of VACNT CCL, (3) top view of a quarter unit computational domain of VACNT CCL and (4) 3D unit computational domain. Reproduced from [103]. b) Schematic of the multiscale mode. (1) Computational domains of PEMFCs. (2) Representative unit of 3DOHP-based "inverse opal style" based CL in the local oxygen transport sub-model. c) Validation of the multiscale model against the experimental results of VACNT-based CLs. d) Validation of the multiscale model against the experimental results of 3DOHP based CLs. Reproduced from [102].

The multiscale model is validated by the experimental data, which is going to be discussed in the next section of the Literature in detail, for both the VACNT and 3D ordered hierarchical porous (3DOHP) "inverse opal style" based CL. Both models, for VACNTs and 3DOHP, suggest superior fuel cell polarization curve performance than a conventional particle-based CL, due to enhanced bulk and local oxygen transport. The numeric models clearly show that oriented electrodes and 3D-structured electrode may have better utilization of the Pt catalyst complemented by efficient mass transport to the catalytic sites. Based on the modelling results for PGM-based ordered architecture catalyst layer, the implementation of such catalyst layers represents a promising endeavour at least for PGM catalyst layers.

2.8. Vertically-aligned carbon tube catalyst layers

This section is part of the detailed introduction of Chapter 4 “AAO template for Fe-N-C tubular catalysts for the cathode in PEMFCs”

2.9. Inverse opal macroporous catalyst layers

Colloidal templates are a common method to prepare carbons with periodic ordered interconnected pore structure.[104] Besides, threedimensional periodic macroporous materials can be prepared by assembling colloid particles on a conductive substrate and subsequent electrodeposition to fill the voids between the template spheres.[105] Platinum macroporous film can be prepared by galvanostatic-pulse electrodeposition of Pt onto GDL coated with monodispersed polystyrene (PS) spheres.[106] The produced 3DOHP-based CL with interconnected pore network proved to increase the utilization and mass transfer of the Pt catalyst. A PEMFC with a 3DOHP cathode catalyst of 0.12 mg_{Pt}/cm^2 loading exhibited a rated power density of 0.84 W/cm^2. In comparison to a conventional reference with the same Pt loading, the power density of 3DOHP PEMFC is 17% higher. In the PGM-free field, PS also served as a template for assembling Fe-doped ZIF precursors (Figure 12). After dissolution of the PS, the structure was carbonized to prepare atomically dispersed FeN_4-doped hierarchical ordered porous carbon (FeN_4/HOPC).[107] Coating 4 mg/cm^2 of the macroporous PGM-free catalyst powder on a GDL and testing in PEMFC demonstrates a great performance with a peak power density of 0.42 W/cm^2 surpassing the cathode of the same material synthesized without the PS template with a PPD 0.35 W/cm^2.

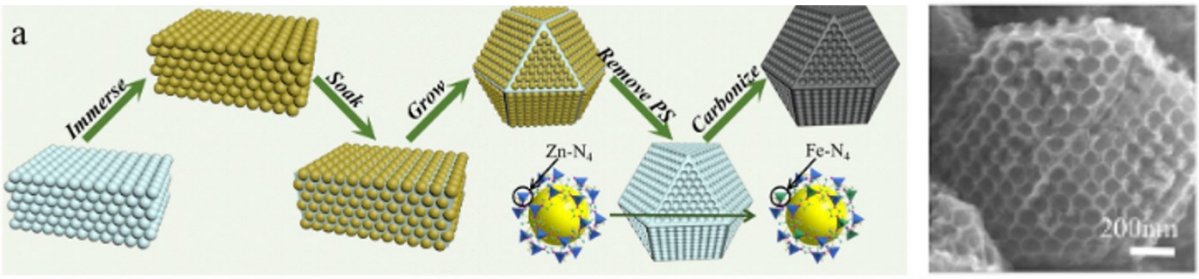


Figure 12. Illustration of the synthesis of FeN_4/HOPC catalysts. Figure reproduced from [107].

In order to move from ZIF particle to freestanding film structure, innovative preparation methods are necessary. Long-range macro-microporous metal-organic framework films over an area of 12 cm^2 can be prepared by electrochemical deposition of zinc acetate and 2-methylimidazole on PS coated FTO substrates.[108] The thicknesses of multilayered films were 2-5 μm, and the pore diameter was controlled by the diameter of the PS template.

2.10. Gas-Diffusion-Electrodes: The intermediate technique between Rotating Disk Electrode and Membrane Electrode Assembly

The activity of catalysts for the ORR can be evaluated in different testing configurations, among which the rotating disk electrode (RDE) and membrane electrode assembly (MEA) are the most widely implemented standard techniques. Each setup has its capabilities and limitations[109,110], which are addressed in the following segment. At an early stage of the catalyst development, the activity is benchmarked with the RDE. With respect to the heavy material losses in the synthesis protocols, with pyrolysis and washing steps, the minimal yields of a few micrograms are sufficient to be tested in the RDE. The benefit of the method at this stage is the low Fe-N-C loading required per sample tested varying between 200 and 800 μg/cm^2 drop casted on a Ø = 5mm electrode tip.[53,111] However, two issues originate from the rather high Fe-N-C loadings on the RDE. First, the film quality and uniformity affects the activity determination. Second, the theoretical foundation of the RDE is a thin film associated with the assumption that the mass transport only takes place from the bulk electrolyte to outer surface of the catalyst, but not within the catalyst layer. Due to a well-defined relationship between the homogeneous convective-diffusive flux of dissolved oxygen controlled by the electrode rotation rate, electrode potential-dependent current densities can be corrected for mass transport contributions.[112] The Koutecky-Levich equation is commonly used for the correction of mass transport effects in RDE testing to obtain kinetic current densities.

Koutecky-Levich equation: $\frac{1}{i_{measured}} = \frac{1}{i_{kinetic}} + \frac{1}{i_{mass-transport}}$

The main drawback of RDE concerns the transport of the oxygen in the liquid phase. The limited oxygen solubility in electrolyte (bulk concentration of O_2 in 0.1 M $HClO_4$: $1.26 \cdot 10^3$ mol/L, and in 0.1 M KOH: $1.2 \cdot 10^{-3}$ mol/L) and diffusion coefficient ($1.93 \cdot 10^{-5}$ cm^2/s in 0.1 M $HClO_4$ and $1.93 \cdot 10^{-5}$ cm^2/s in 0.1 M KOH) leads to a diffusion-convection limited plateau in RDE with maximum current density values of approximately 6 mA/cm^2 at 1600 rpm.[113] Theoretical limiting current density: $i_{lim} = 0.62nFCD^{\frac{2}{3}}\nu^{-\frac{1}{6}}\omega^{\frac{1}{2}}$

This oxygen transport limitation restricts the extraction of the kinetic activity to a narrow potential window (0.80 - 0.90 V) in the RDE. Activities and mass-transport properties of the catalyst at high current densities (1.5 – 2.0 A/cm^2), not accessible with the RDE, can be characterized in the MEA. For the MEA testing, larger electrodes (5 cm^2) are prepared by coating either an ink of catalyst and ionomer onto the membrane (CCM) or onto the gas-diffusion layer (GDL). In addition, a anode catalyst layer is coated onto the catalyst-free side membrane or an additional gas-diffusion-layer. The MEA is assembled to form a five-layered sandwich in the order of GDL-Anode-Membrane-Cathode-GDL. Instead of oxygen transport over the liquid phase, in the MEA the oxygen or air is supplied over the gas phase from the gas-diffusion-layer to the cathode CL. In contrast to liquid electrolyte as proton source, a solid polymer electrolyte transports the protons to the active sites through an ionomer network. The oxygen transport takes place in the pores of the catalyst/ionomer network. The presence of ionomer agglomerates limit the O_2 transport, as oxygen diffusion in the ionomer is reduced compared to the pores, leading to oxygen transport resistance.[114] The oxygen transport resistance is amplified at the high current densities, in which MEAs operate in.[115] However, due to the different environments, the catalyst utilization in the MEA is lower due to fewer triple phase boundaries, where the ORR is taking place. In an MEA, to achieve high current densities more active sites are required resulting in Fe-N-C cathode catalyst loading of 1-4 mg$_{Cat}$/cm^2, an order of magnitude higher than in RDE. Furthermore, the operating temperature of MEA is usually between 60°C and 80°C in contrast to ambient temperature for standard RDE setups. The additional components in the MEA including membrane and anode catalyst layer also affect the measured polarization curve. Consequently, the polarization curve is not a direct measure of the performance of the cathode catalyst and cathode CL individually.

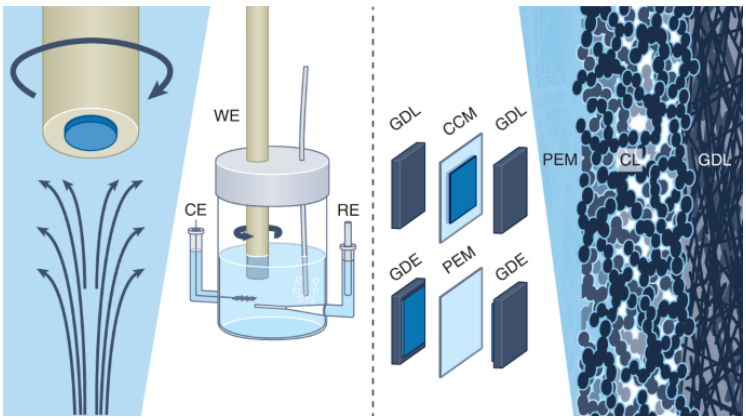


Figure 13. Illustrative comparison of the RDE and the five-layer MEA set-up. Five-layer MEA set-ups consisting either of a catalyst-coated membrane (CCM) sandwiched between two gas diffusion layers (GDLs) or a PEM between two GDEs. Figure reproduced from [109].

The progress in the development of Fe-N-C ORR catalysts has been restricted by the divergent results of ORR mass activities measured in RDE and compared with results in actual MEA tests.[116,117] Therefore, alternative setups for benchmarking the performance of electrocatalysts have been developed. A pioneering example is the floating electrode, which allows screening of tiny amount of catalyst applied onto a porous Au-coated polycarbonate membrane floating on the electrolyte.[118] While this method is valuable for investigating intrinsic activities of electrocatalysts at mass transport-free conditions, the small loading and catalyst spot does not reflect real fuel cell catalyst layers. In the following years, other groups presented gas-diffusion-electrodes (GDE) half-cell setups that enable the isolated testing of cathode catalyst layers without anode and membrane at technically relevant conditions applied in fuel cells (Figure 14). The GDE half cells combine the advantages from RDE and MEA setups. First, cathode catalyst layers with thicknesses and compositions relevant for fuel cells can be investigated as opposed to the none application-representative thin film on the RDE tip. Second, the gas flow is provided from the back side of the electrode across a gas-diffusion-layer mimicking the gas supply in a fuel cell. Third, highly concentrated liquid electrolyte is the proton or hydroxide source, enabling a testing platform with reduced components in comparison with MEA, and allowing focus on the characterization on a single catalyst layer. As a result, the GDE half cells are conceived to benchmark the activity of catalysts and to analyse the mass transport properties of catalyst layers in potential ranges found in operating fuel cells. The abbreviations for the different GDE cells were chosen according to the size ranking of their geometric working electrode area: L = large ($S_{geo,L}$ = 2.01 cm^2) M = medium ($S_{geo,M}$ = 0.385 cm^2), and S = small ($S_{geo,S}$ = 0.0707 cm^2). The origin of the L-GDE half cell from Wilkinson's group[119] has been further modified in Cherevko's group.[120] The L-GDE cell is composed of a gas and electrolyte compartment. A flow field presses the gas compartment against the electrolyte compartment. The PTFE cell has an electrolyte compartment with a chamber for the reference electrode. To minimize the uncompensated resistance between working electrode and reference electrode, Luggin capillaries with proximity to the working electrode are crucial components in the cell design. In the L-GDE, the reference electrode compartment is connected to the electrolyte compartment with a fine channel, acting as a Luggin capillary. The end of the channel in the electrolyte compartment is located 1 mm apart from the electrode-electrolyte interface ensuring a minimal uncompensated resistance (R_u ~ 0.5 Ω). The M-GDE is a commercial cell from with the brand name FlexCell® PTFE (Gaskatel GmbH).[121] It also features a Luggin capillary to a separate reference electrode compartment. The S-GDE consists of a stainless steel flow flied and a PEEK cell body.[122] The initial setup

had no separate chamber for the reference electrode. Owing to different distances between the working and reference electrode in each experiment, the resistance between working and reference electrode varied and, usually above 10 Ω.[123] Nevertheless, the S-GDE is designed to insert a membrane between catalyst layer and liquid electrolyte. When implementing a GDE half cell, the cell is first benchmarked with Pt/C catalyst layers with different loadings. A standardized protocol based on galvanostatic steps coupled with impedance spectroscopy to determine the uncompensated resistance (R_u) at each step has been established.[124] The universal applicability of the protocol has been demonstrated in an interlab comparison. Polarization curves in O_2 up to -2 A/cm^2 without systematic mass transport limitations for the suggested benchmark Pt/C GDE with 0.3 mg$_{Pt}$/cm^2 for all the GDE half cell setup deviated negligibly from each other despite different cell designs (Figure 14 D)).

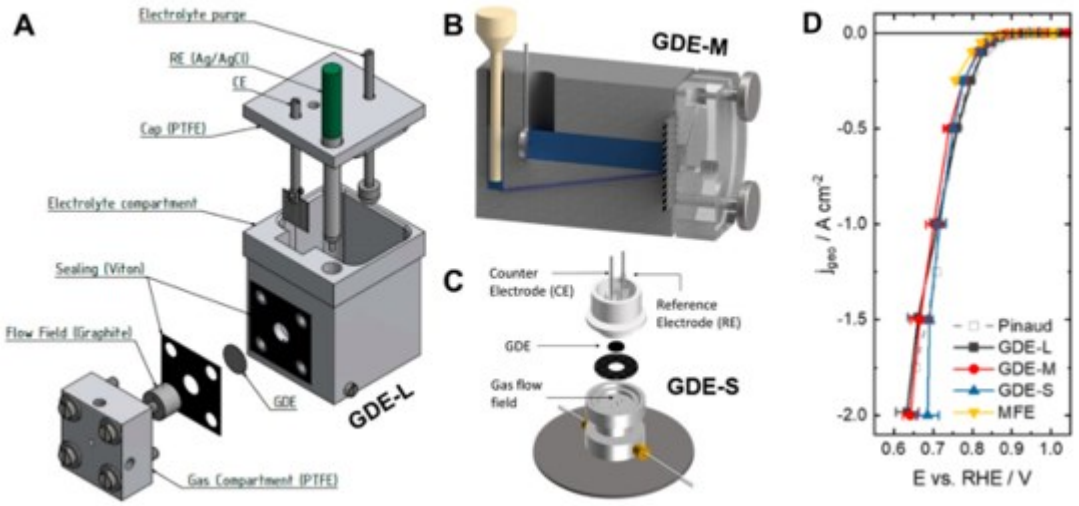


Figure 14. Different GDE half-cell setups: A) GDE-L (Wilkinson and Cherevko groups), B) GDE-M (Gaskatel cell), C) GDE-S (Arenz and Escudero-Escribano groups). D) Interlab comparison of a commercial Pt/C GDE (0.3 mg$_{Pt}$/cm^2, 40 wt% Pt on Vulcan, FuelCellsEtc). Figure reproduced from [124].

2.11. The optimized small Gas-Diffusion-Electrode setup

The design of the S-GDE half-cell, which is the main electrochemical characterization technique in this PhD thesis, has been steadily improved by the team around G. K. H. Wiberg and M. Arenz to reduce the impact of gas bubble formation and to minimize the solution resistance.[125] The updated version of S-GDE half-cell comprises two parts (Figure 15). The lower compartment for the gas supply is a flow field with gas lines extruded from titanium. The

gas supply is connected to a simple gas bubbler filled with water to adjust the humidity of the reactant gas. The upper compartment for the liquid electrolyte is divided into a chamber for the reference electrode and a chamber for the counter electrode. The circular opening (Ø = 3 mm) at the bottom of counter electrode chamber defines the working electrode area. A Luggin capillary (Ø = 1 mm) is connecting the bottom of the reference electrode chamber with the membrane positioned 2 mm next to the large opening for the working electrode. Hereby, the solution resistance is reduced to less than 0.1 Ω. The samples, a catalyst on a GDL is sandwiched between the lower and upper compartment with the catalyst side facing towards the liquid electrolyte and is electrically contacted via the conductive titanium flow field. Optional a membrane can be inserted above the GDE.

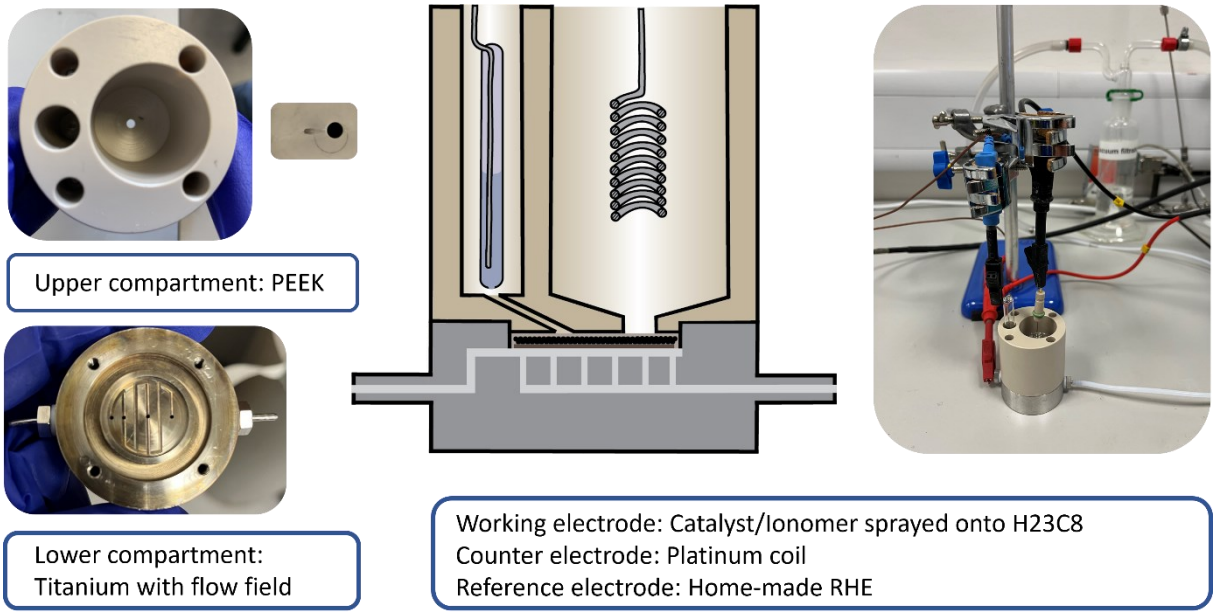


Figure 15. Home-made version of the S-GDE cell in the Titirici lab. a) Upper part, b) Lower part, c) Overview cross section scheme, d) S-GDE in operation.

The S-GDE half-cell has several advantages over the other GDE half cell designs. The smaller geometric working electrode area is beneficial, because less catalyst is needed to prepare an electrode for testing at high current densities. Thus, quick screening of a low-yield new catalyst can be carried out without having to invest all of the material for this particular characterization step. Besides, the small geometric working electrode is more cost-saving to implement with regards to lab equipment, as the absolute current of 0.1414 A for measuring the highest current density at 2 A/cm^2 is accessible with a standard potentiostat. In contrast to the GDE half cells with large geometric working electrode areas may need a booster to access the high current density region. Owing to the high reaction rates at high current densities, the primary source of

uncertainty in activity determination originated from the uncompensated resistance between working and reference electrode. Generally, the larger the working electrode area, the more precise the iR drop needs to be determined. S-GDE is also most forgiving with errors in the iR correction. Due to the small absolute currents in the S-GDE cell, a single frequency at 5 kHz can determine the uncompensated resistance. For example, operating the 3 mm diameter working electrode at 2 A/cm^2 requires an absolute current of 0.14 A. The uncompensated resistance is usually between 0.1 to 1 Ω in the S-GDE, giving an iR drop of 0.014 to maximal 0.14 V. Even if there is an error of in determining the solution resistance of ±10%, the maximal error introduced amounts to ±14 mV. Cyclic voltammetry with non-steady-state condition during cycling distort the results, as the scan rate affects the measured ORR activity. The faster the scan, the higher the measured ORR activity. Therefore, in the thesis, all polarization curves are based on galvanostatic steps. Electrochemical impedance spectroscopy measured at each step increases the accuracy of the reported data in this thesis, as the uncompensated resistance may change during experiments. The main drawback of small geometric working electrode areas concerns the amplified impact of inhomogeneous catalyst layers on the measured polarization curves. Therefore, it is recommended to use automated spray coaters for the preparation of the GDE instead of hand spray coating. The homogeneity of the catalyst layer should be verified using SEM cross-sectional imaging. To minimize errors and validate reproducibility, the measurement on each new catalyst film is repeated at least once. Finally, the conditions by covering the catalyst layer with a membrane resemble realistic conditions in fuel cells. Distinct from the GDE exposed to liquid electrolyte, the addition of a membrane creates the same proton and ionomer reactant transport rates in the solid electrolyte phase as in fuel cells. While the exposure to liquid electrolyte risks flooding of the catalyst layer, the catalyst layer is more inclined to dry out at presence of the membrane. In the thesis, Nafion membranes, which are hot-pressed on the electrode, in acidic electrolyte, and several alkaline exchange membranes (AEMs), which have been placed manually on top of the GDE, are utilized in alkaline conditions. The fragility of AEM is a major drawback when creating an efficient GDE / membrane interface.[126] Despite, the aim to be the first to report Fe-N-C catalysts tested in S-GDE configuration, others identified this gap as well.[127]

3. Experimental

Details of the materials preparation in Chapter 4

AAO membrane SmartPor180-50-A2 with a lattice constant of 480 nm, pore diameter of 300 nm and 50 μm thickness have been supplied by SmartMembranes GmbH.

Firstly, the commercial AAO membranes were lasercut into 3 mm and 5 mm pieces. Then the AAO pieces were cleaned by ethanol and deionized water, afterwards dried by nitrogen.

1. Deposition of the ZnO onto AAO membrane (AAO → ZnO/AAO)

ZnO was prepared inside the AAO template using a sol-gel method. 0.45 g (0.1 M) zinc acetate dehydrate (Zn $(CH_3COO)_2x2H_2O$) (Fisher Chemical, 98%) was dissolved in 20 ml methanol and 0.25 ml acetyl acetone (Sigma-Aldrich, 99%) mixture at room temperature. The prepared solution was mixed with a magnetic stirrer for 4 h at 50°C until a transparent solution was obtained. Then the solution was aged for 24 h. For ZnO deposition into AAO, AAO template was immersed in prepared sol-gel ZnO at 65°C for 12 h. Then deposited sol-gel ZnO in AAO template was annealed at 600°C for 30 min. (Heating rate: 5 C/min; atmosphere: air).[174]

2. Deposition of 2-methylimidazole onto AAO membrane (ZnO/AAO → N-$C_{tubes,CVD}$/AAO)

The nitrogen-doped carbon tube membrane (N-$C_{tubes,CVD}$) was fabricated by a chemical vapour deposition (CVD) described before.[169,128] 1.5 g of 2-methylimidazole and AAO were put into a glass test tube 3 centimetres distance apart. The glass test tube was sealed with aluminum and a tiny hole with a metal wire was pricked into the aluminum foil for pressure relief. The samples were placed into a furnace (OTF-1200X, MTI) to heat to 350°C with a heating rate of 10°C / min, held for 30 minutes, and then heated to 550°C and kept for 4 h in nitrogen atmosphere.

3. Carbonization of the nitrogen-doped carbon tubes (N-$C_{tubes,CVD}$/AAO → N-$C_{tubes,T}$/AAO)

N-$C_{tubes,CVD}$/AAO membrane was heated in a furnace to T = 800, 900, or 1000°C for 1 hour in N_2 atmosphere to yield N-$C_{tubes,T}$/AAO. The heating rate in the ramp is 3°C / min.

4. Transfer of the carbonized nitrogen-doped carbon tubes onto Nafion membrane (N-$C_{tubes,T}$/AAO → N-$C_{tubes,T}$/AAO/Nafion)

The N-$C_{tubes,T}$/AAO was hotpressed onto Nafion at 135°C and a pressure of 340 N/cm^2 for 10 minutes.

Aquivion ionomer (0.05 wt%, 11μL) was dropcast onto the N-$C_{tubes,T}$/AAO/Nafion.

5. Removal of the AAO (N-$C_{tubes,T}$/AAO/Nafion → N-$C_{tubes,T}$/Nafion)

The AAO was etched in 6 M NaOH at 80°C for 72 hours (unless stated otherwise) in a Teflon container with a 1 mm hole in the top lid cover.

6. Fe metalation onto N-doped carbon tubes (N-$C_{tubes,T}$/Nafion → Fe-N-$C_{tubes,T}$/Nafion)

The active site coordination step was carried out by refluxing of the N-$C_{tubes,T}$/Nafion in $FeCl_2$ x4H_2O ($25x10^{-3}$ M) (Sigma-Aldrich) solution in refluxing methanol for 24 h.[64]

7. Reprotonation of Nafion (Fe-N-$C_{tubes,T}$/Nafion→ Fe-N-$C_{tubes,T}$/NafionH^+

Subsequent, the samples were washed in 0.5 H_2SO_4 (12 h) and DI water (3 h) to remove physisorbed Fe and to re-protonated the Nafion membrane.[146]

Details of the materials preparation in Chapter 5

Chemicals

Styrene (ReagentPlus®, with 4-tert-butylcatechol as stabilizer, ≥ 99%), potassium persulftate (≥ 99%), 1-butanol (99.9%), 1,3-propanediol (98%) and LUDOX® CL colloidal silica (30 wt% suspension in H_2O) were obtained from Sigma-Aldrich. Polyvinyl alcohol (87-89% hydrolyzed, low molecular weight) was purchased at VWR. Mesophase pitch (MP) was obtained from Bonding Chemical USA.

Synthesis of the polystyrene nanospheres

Styrene was washed two times with 0.5 M sodium hydroxide solution (1:1 vol/vol ratio of NaOH solution : styrene) and subsequently one time with distilled water (1:1 vol/vol ratio) to remove polymerization inhibitors. The purified styrene was added to 180 mL of argon-degassed DI water at 80°C, prior to the dropwise addition of 20 mL (0.08 g) argon-degassed potassium persulfate aqueous solution during 300 rpm agitation. After 22 h, the colour of the solution turned white due to the formation of polystyrene colloidal nanospheres, which were recovered by centrifugation at 10000 rpm for 10 minutes. After two further centrifugation steps with water exchange between the steps, the resulting powder was dried at 80°C for 12 hours and finally ground into a fine powder in a mortar and pestle for use as a macropore-directing hard template.

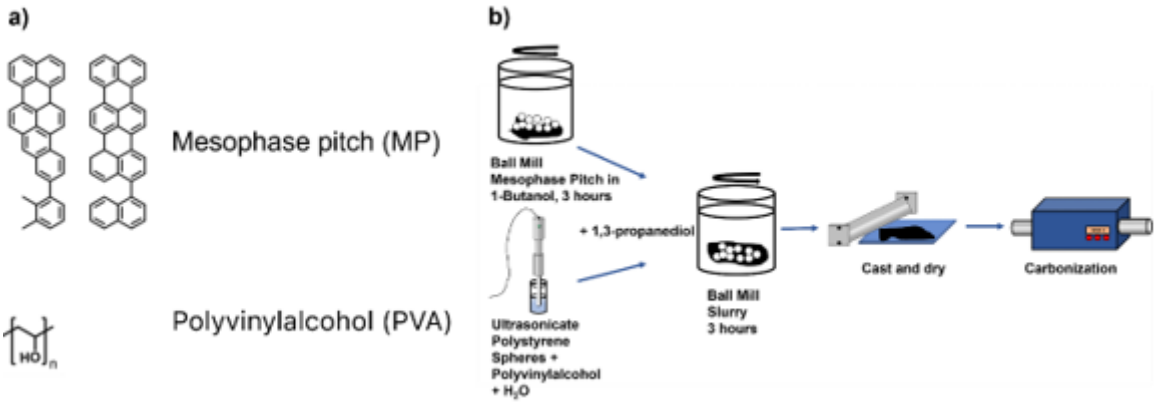


Figure 16. a) Representative molecular structure of mesophase pitch and PVA. b) Preparation sequence of the macroporous carbon film.

Synthesis of the macroporous carbon film

a) Slurry preparation

0.1 g mesophase pitch and 0.25 mL n-butanol are ball milled (TOB-YXQM-4L, 600 rpm, 5 min forward, 5 min backward, 5 min waiting, total time of active milling: 2 hours) using 20 g of zirconia balls (diameter: 3 mm) in a zirconia jar (volume: 50 mL). 0.5 g polyvinyl alcohol (PVA, 86-89% hydrolyzed, low molecular weight) and polystyrene nanospheres (PS, 0 g/ 0.25 g/ 0.63 g/ 1.05 g / 1.25 g / 1.64 g) are ultraprobesonicated (Fisherbrand) in 5 mL DI water for 10 minutes (5 seconds – 5 seconds break). Then the PVA/PS suspension is added to the mesophase pitch in the ball mill jar, and ball milled (TOB-YXQM-4L, 600 rpm, 5 min forward, 5 min backward, 5 min waiting, total time of active milling: 3 hours). For the last 30 minutes of active ball milling time 0.47 mL 1,3-propanediol (PD) is added to the jar. The slurry and the balls are poured into a centrifuge tube with a 2 mm hole at the bottom, to separate the slurry from the balls. The slurry drops are collected in a vial below the centrifuge tube.

b) Macroporous carbon film preparation

The slurry was cast on the backside of the BLODLÖNN mirror (IKEA) using a doctor blade with a 500 µm and 1000 µm gap between doctor blade and substrate. Subsequently, the film is dried for 12 hours. Then, the films are peeled of, cut into 2 cm x 4 cm pieces, and stored in plastic petri dishes in nitrogen atmosphere for the next steps. The films are sandwiched between two carbon papers (H23, Freudenberg), which are themselves sandwiched between two carbon felts for the oxidative stabilization step. (MTI OTF-1200X , Compressed Air, Flowrate: 0.5 L/min, RT – Heating Rate: 10°C/min – Temperature Target: 130°C – Heating rate: 0.2°C/min – Temperature Target: 210°C – Dwell Time: 600 min – Temperature after Dwell Time 210°C). The stabilized films are transferred into vials with toluene for 30 minutes. This extraction

protocol was repeated four times to achieve complete removal of the polystyrene hard template. Then the films are sandwiched again in the same sandwich layer combination as for the oxidative stabilization and carbonized. (MTI OTF-1200X, Nitrogen, Flowrate: 0.5 L/min, RT – Heating Rate 1°C/min – Temperature Target: 200°C – Heating rate: 0.1 / 0.5 / 1.0 °C/min – Temperature Target: 900°C – Dwell Time: 30 min).

Details of the experiment preparation in Chapter 6

Materials

The commercially available products are used without modification.

Fe-N-C catalyst: Pajarito Powder PMFD14401 (Abbreviation: Pajarito Powder or Fe-N-C)

All AEI and AEM materials are supplied from Fuel Cell Store (USA):

Ionomers:

Fumasep® Fumion FAA-3-SOLUT-10 (10wt% in NMP) (Abbreviation: FI)

PiperION® Anion Exchange Dispersion (5 wt% in ethanol) (Abbreviation: PI)

Sustainion® XA-9 Alkaline Ionomer (5 wt% in ethanol) (Abbreviation: SI)

Nafion™ D-521 (5 wt% in H_2O and isopropanol)

Nafion™ D-1021 (10 wt% in H_2O)

Membranes:

Fumasep® FAA-3-50: 45-55 µm (dry thickness) (Abbreviation: FM)

PiperION® AEM: 40 µm (dry thickness) (Abbreviation: PM)

Sustainion® X37-50 Grade 60: 50µm (dry thickness) (Abbreviation: SM)

GDE spraycoating

A typical ink composition for the GDE was 20wt% Ionomer / 80wt% Fe-N-C catalyst with a catalyst content of 2 $mg_{Fe\text{-}N\text{-}C}$/mL. The detailed ink formulation contained 10 mg Fe-N-C (Pajarito Powder PMFD14401) and 50.7 µL AEI (Sustainion (5 wt% in ethanol), or Piperion (5 wt% in ethanol)) or 19.4 µL AEI (Fumion (10 wt% in NMP). The reference sample contained 10 mg Fe-N-C , 25 µL Nafion™ D-1021 (10 wt% in H_2O) and the solvents 2.475 mL DI H_2O and 2.5 mL isopropanol (99.5% Honeywell™). The inks are subjected to sonication in an ice bath for 1 hour, and are stirred overnight. The GDEs are prepared via an Exactacoat (Sonotek) ultrasonic spraycoater with a 48 kHz nozzle at 0.15 mL/min (air shaping 0.3 psi) with an offset

serpentine spray pattern on a 5 cm^2 gas diffusion layer (Freudenberg H23C8) while heated at 40°C on a vacuum plate. The gas diffusion layer is weighed pre and post-cathode spraying to determine the cathode catalyst loading.

Membrane activation

The membranes are stored and pre-treated as recommended by the respective manufacturer.

Fumasep FAA-3-50: The membrane is delivered in bromide form (Br^-) and dry form. Prior to the GDE application, the membrane is converted into the OH^- by treating it in aqueous 1.0 M KOH (99.995% Suprapur) for 24 hours at room temperature in a sealed PET bottle.[129]

PiperION® AEM: The membrane is delivered in the bicarbonate form. Prior to the GDE application, the membrane is placed into an aqueous solution of 0.5 M KOH (99.995% Suprapur) for 1 hour at room temperature. Then, it is transferred to a fresh aqueous solution of 0.5 M KOH (99.995% Suprapur) for an additional 1 hour at room temperature. Subsequently, the membrane is rinses with DI water, and transferred into fresh 0.5 M KOH (99.995% Suprapur) solution in a sealed PET bottle.[130]

Sustainion® X37-50 Grade 60: The membrane arrived soaked in a ethylene glycol plasticizer to prevent cracking. Prior to the GDE application, the membrane is activated for 3 hours in 1 M KOH at 55°C, and then transferred into a fresh 1.0 M (99.995% Suprapur) solution in a sealed PET bottle.[131]

Characterization techniques

Dynamic light scattering (DLS)

DLS measurements on the GDE inks (with ink formulation described in Electrochemical Measurement part) were performed using a Malvern Zetasizer MicroV. Before the measurements, the inks were diluted by a factor of 100. The analyzed inks contained 0.02 mg/mL catalyst and 0.005 mg/mL ionomer. The inks are sonicated in the quartz cuvette for 10 minutes before the measurement. The program carried out 60 runs for 10s each and is repeated three times.

The size of the synthesized polystyrene particles is measured with DLS in a Malvern Zetasizer MicroV. The samples are dispersed for 10 minutes in a ultrasonicated bath. The program carried out 60 runs for 10s each and is repeated three times.

Fourier-transformed infrared (FT-IR)

FT-IR spectra were collected in attenuated total reflectance mode in an Agilent Cary 630 FTIR Spectrometer by performing 32 sample scans.

Electron microscopy

a) Scanning electron microscopy (SEM)

The GDE samples were cut with a razor blade to prepare the cross-section samples. Cross-section samples were stuck with carbon tape on a special stub with a vertical edge with the cross-section of the sample facing to the top. The top-view samples were prepared with carbon tape on top of a regular stub. A film of chromium (40 nm) was sputtered onto the specimen. The images were taken on a Zeiss Leo Gemini 1525.

b) Energy dispersive X-ray (EDX)

EDX data were recorded with a x-act detector (Oxford instruments) at a working distance of 10 mm and an acceleration voltage of 10 kV.

c) Transmission electron microscopy (TEM)

The ground powder samples were dispersed in iso-propanol for 15 minutes. The solution was dropped onto TEM grids (Holey Carbon Films on 300 Mesh Copper Grids, Agar Scientific) and dried. The images were taken in a JEOL JEM-2100F at 200 kV.

Inductively Coupled Plasma – Mass Spectrometry (ICP-MS)

The Fe content of the catalysts was measured with ICP-MS. The samples (5 mg) were digested in aqua regia 25 v/v% HNO_3 (70%, Certified AR, Eur. Ph. , for analysis Fisher Chemical, Fisher Scientific and 75 v/v% HCl (37%, Certified AR, Eur. Ph., for analysis Fisher Chemical, Fisher Scientific) using a MARS 6 microwave system at 215°C for 15 minutes. The solutions were further filtered (0.22 µm) and diluted with 2% HNO_3 to prepare samples with Fe concentrations below 500 ppb. The diluted samples were submitted to the Agilent 7900 ICP-MS spectrometer referring to the internal scandium standard and calibration solutions with Fe concentrations of 0, 5, 50, 100, 200 and 500 ppb. Two measurements were taken for each sample to demonstrate accuracy and reproducibility.

Mercury intrusion porosimetry (MIP)

Macropores in carbon materials and catalyst layers can be resolved with mercury intrusion porosimetry (MIP). MIP measurements were performed using an AutoPore IV Servies (Micromeritics) in the pressure range of $2.5x10^{-2}$ to $2.28x10^{3}$ bar. The cumulative mercury intrusion volume can be translated to a cumulative pore volume as a function of the pore diameter using the analysis software AutoPore IV (version 9500).

Resistivity measurements

The conductivity of the film at different stages in the preparation protocol was calculated from the resistivity by a four-probe-measurement along the measured thickness obtained.

Rheology

The shear stress and viscosity data were measured with an Anton Paar MCR 302 Rheometer. A volume of 20 mL of the GDE inks (with ink formulation described in Electrochemical Measurement part), reference ink of Pajarito Powder with same concentration as in GDE inks in ethanol and ethanol only are poured into the rotational cylinder cup and temperature is adjusted to 25°C. The data is collected at steady state stepping the shear rate from 1 to 2510 s^{-1} with logarithmic spacing.

Sorption measurements

GDE inks (with ink formulation described in Electrochemical Measurement part) were sprayed manually with an airbrush set (Paasche) powered by an Iwata Smart Jet Pro Airbrush compressor onto aluminum foil. The CL covers an area of 20 cm^2 with a loading of 1.0 $mg_{Fe\text{-}N\text{-}}$

$_C$/cm^2 and the weight of loading is determined by pre- and post-spray weighing. Spraying onto aluminum foil has the advantage over catalyst coated membranes (CCM) that the correction for the high membrane water adsorption is eliminated from the water sorption measurement.[132]

a) Nitrogen sorption

Nitrogen sorption experiments of the CLs on Al foil were conducted on a 3Flex (Micromeritics) adsorption analyzer at 77 K within a relative pressure range from 10^{-5} to 0.99 p/p_0. Before the measurement, the samples were degassed at 10^{-6} bar, 453 K for 24 hours, using the micromeritics VacPrep. The BET surface area was obtained with the linearized BET equation, in the region where Roqouerol plot increases monotonically.[133] The pore size distribution was calculated using slit geometry and heterogeneous surface-2D-NLDFT model in-built with 3Flex software.

b) Water vapor sorption

Water sorption isotherms of the CLs on Al foil were recorded on a 3Flex (Micromeritics) adsorption analyzer at 298 K within a relative pressure range from 1^{-3} to 0.86 p/p_0. Before the measurements the CLs are dried at 453 K for 24 hours in vacuum and the water was purified by performing three freeze-thaw cycles to remove any air and dissolved gases.

Thermogravimetric analysis (TGA)

Thermogravimetric analysis was performed using a Perkin-Elmer TGA8000. The samples were heated in a nitrogen atmosphere with a heating rate of 1°C/min from 30°C to 1000°C in case of the film components. The carbon burn-off for the SiO_2 templated films was carried out in compressed air with a heating rate of 10°C/min and a constant temperature holding step at 900°C for 10 minutes.

Ultra-small angle X-ray scattering (USAXS)

The USAXS/SAXS study of particle and agglomerate size for dispersed RDE catalyst inks (with ink formulation described in Electrochemical Measurement part) was conducted at BL11 – BCD-SWEET beamline at ALBA synchrotron. Freshly sonicated ink samples are transferred into a glass capillary tube (1 mm diameter) with the help of a syringe and sealed with an epoxy resin for transport. Before the measurement the capillary tubes are immersed into an ultrasonic bath for 10 minutes. The background scattering data from the glass capillary tube filled with the solvent solutions (Ethanol/H_2O) were recorded and subtracted from the scattering data for each sample. The samples were exposed to a monochromatic X-ray beam in the operational energy range from 6.5 to 20 keV (including WAXS). The scattered X-ray intensity was

measured with a Pilatus3 S 1M detector. The X-ray intensity data were collected in scattering angle ranges from $4x10^{-3}$ A^{-1} to 0.75 A^{-1} (SAXS), 0.4 A^{-1} to 10.8 A^{-1} (WAXS). The scattering data were analyzed in the data analysis software SASView with simulations of scattering fitting functions.

X-ray photoelectron spectroscopy (XPS)

XPS analysis was performed with a Thermo Fisher K-Alpha XPS system to probe the elemental surface composition of the supports and catalysts. The spectra were measured at pressures below $5 \cdot 10^{-8}$ bar with a monochromatic Al-K_α excitation source, and analysed using Avantage software. The C1s peak at 284.8 eV was used for spectrometer calibration.

X-ray diffraction (XRD)

X-ray diffraction patterns were obtained with a PANalytical X'PERT PRO poweder X-ray diffractometer using a Cu K_α source operating at 40 kV and 15 mA. The scan step size was 0.010866° within a 2Θ range from 30° to 70°.

Electrochemical characterization

Rotating Disc Electrode

Electrochemical characterization was performed in a standard three-electrode cell using a potentiostat Multi AUTOLAB/M101 (Metrohm). The working electrode was a glassy carbon disk (Ø = 5 mm). Inks contained 4 mg of the Fe-N-C catalyst, 480 µg ethanol (99.5%, Sigma Aldrich), 480 µg 18.2 MΩ deionized water and 40 µg of ionomer dispersion (Nafion™, or Piperion, or Sustainion) or 20 µg of ionomer dispersion (Fumion). The choice of the ionomer / catalyst weight ratio of 0.5 is consistent with the literature[46,312], corresponding to 33wt%/66wt% I/C. After sonication in an ice bath for 30 minutes, the ink is dropcast (10 µL) on a freshly polished circular area glassy carbon disk to load 200 $\mu g_{Fe\text{-}N\text{-}C}/cm^2$. The ink was dried under rotation (300 rpm). A glassy carbon rod served as counter electrode. A Hg/HgO (30 mm, Redox.me) reference electrode was calibrated against a H_2 (1 bar) purged Pt RDE tip (Ø = 3 mm, Metrohm) working electrode (1000 rpm) and platinum wire counter electrode in 0.1 M KOH (99.995% Suprapur).[134] After purging N_2 (99.9998%, Ultrapure Plus), 50 cyclic voltammograms were recorded at 50 mV/s and 1600 rpm in the potential range of 0.20 V_{RHE} to 1.05 V_{RHE} to precondition the catalyst. Subsequently, 3 cyclic voltrammgramms were recored at 10 mV/s and 0 rpm across the potential range of 0.20 V_{RHE} to 1.10 V_{RHE} to evaluate the capacitive current. After purging O_2 (99.99998% BIP® Plus) for 15 minutes, three cyclic voltammograms at 10 mV/s and 1600 rpm were recorded in the potential range from 0.25 V_{RHE} to 1.10 V_{RHE}. The pseudocapacitance was corrected by subtracting the current obtained previously in N_2 from the cyclic voltammograms in O_2. The ohmic drop was calculated for each measurement by means of electrochemical impedance measurements from 10^5 to 10^{-1} Hz at 0.85 V at 1600 rpm by taking the first intercept of the real impedance axis in the Nyquist plot.
The kinetic current densities (j_{kin}) were calculated at 0.85 V_{RHE} using the geometric disk current density (j_d) at 0.85 V_{RHE} and the limiting current density (j_{lim}) at 0.25 V_{RHE} following equation:

$$j_{kin} = \frac{j_d \cdot j_{lim}}{j_d - j_{lim}} \qquad \text{(Eq. 1)}$$

The mass activity (MA) can be calculated with the following equation:

$$MA = \frac{j_{kin}}{Catalyst\ Loading} \text{ (Eq. 2)}$$

Gas Diffusion Electrode Half Cell

Cell cleaning

Before each experiment the upper cell compartment was boiled two times in a glass beaker with 18.2 MΩ deionized water and rinsed with 18.2 MΩ deionized water. To avoid contamination, the cell was stored in 18.2 MΩ deionized water in a sealed glass container between the experiments. When changing to a new catalyst layer composition, the cell was soaked into Nochromix® overnight, then extensively rinsed in 18.2 MΩ deionized water before being transferred into a beaker for the boiling procedure.

GDE Setup

Electrochemical characterization was performed in a updated small gas-diffusion-electrode[125] (GDE) cell using a potentiostat PGSTAT204 with FRA32M Module (Metrohm) in combination with a BOOSTER10A. For the working electrode preparation, a piece (Ø = 3 mm, Boehm) was cut out of the GDE, and inserted into a hole (Ø = 3 mm, Boehm) of a H23C8 GDL (Freudenberg). The AEM membrane (Ø = 20 mm) was positioned between the upper cell body and the H23C8 GDL with its hydrophobic coating facing the AEM and with the GDE catalyst layer facing the membrane exactly located underneath the hole in the upper cell body. The lower cell body with a flow-field facing towards the H23C8 GDL was connected to a bubbler and gas flow meter (Bronkhorst) with a flow rate of 300 mL/min unless stated otherwise. The counter electrode was a platinum coil. The hydrogen reference electrode (RHE) was manufactured in-house and the hydrogen in the capillary is prepared before each single sample. The compartment of the RHE is contact with the AEM via a Luggin capillary. The upper cell compartment of the GDE was filled with as 1 M aqueous KOH (99.995% Suprapur). The measurement protocols with the GDE half-cell are described into detail in Table 1 and 2.

Electrochemical Protocol

For each data GEIS polarization curve at least two samples were tested. The electrochemical protocol for the GDE ORR testing was adapted from the community standard protocol.[124] The last data point of each galvanostatic step was iR-compensated by taking a EIS at each galvanostatic step. The value for uncompensated resistance was the magnitude of the impedance, for which the phase angle is closest to 0 in the high frequency region > 1000 Hz. Typically the solution resistance was below 1 Ω.

Table 1. Electrochemical protocol for the GDE ORR testing

	Step	Electrochemical Technique		Parameters
1	Preconditioning (N_2)	Cyclovoltammograms	Gas purge (Flow rate) Purge duration Potential limits Scan rate Number of cycles	N_2 (300 mL/min) 15 min 0.06 – 1.1 V vs. RHE 50 mV/s, 500 mV/s 10 each
2	Polarization Curve (O_2)	Galvanostatic steps coupled with impedance spectroscopy (GEIS)	Gas purge (Flow rate) Purge duration Current steps (hold time) EIS frequency range iR-compensation	O_2 (300 mL/min) 10 min - 0.1 mA/cm^2 (90 s), - 1/-2.5/-5/-10 mA/cm^2 (30 s), - 25/-50/-10/-250 mA/cm^2 (5 s) - 0.5/-1.0/-1.5/-2.0 A/cm^2 (5 s) f = 10 kHz – 1 Hz 100% post-correction

The electrochemical protocol for the GDE O_2 mass transport measurements was adapted from an established protocol.[135] For each type of CL at least 2 samples were tested. A concentration of 2.5 vol% O_2 were mixed into N_2. The total flow is set to 500 mL/min. Using the limiting current i_{lim}, the mass transport resistance R_T can be calculated:

$$R_T = \frac{4\,F\,x_0^{dry-in}}{i_{lim}} \frac{p - p_w}{RT} \quad \text{(Eq. 3)}$$

with the Faraday constant F = 96485 C/mol, the concentration of O_2 regulated to the dry mole fraction x_0^{dry-in}, p denotes total gas pressure which is atm in the small GDE setup, p_w is the water vapor pressure, T is the absolute cell temperature and R is the universal gas constant.

The average value of the mass transport resistance R_T and error is reported.

Table 2. Electrochemical protocol for the O_2 mass transport measurements

	Step	Electrochemical Technique		Parameters
1	Oxygen Mass Transport (2.5% O_2)	Galvanostatic Staircase with Electrochemical Impedance Spectroscopy	Gas purge composition Gas purge flowrates Total flowrate Purge duration Scan rate EIS frequency	2.5% O_2 / 97.5% N_2 12 mL/min O_2 / 488 mL/min N_2 500 mL/min 15 min 20 mA/cm^2 / 5 s = 5 mAcm^{-2}s^{-1} f = 5 kHz

4. AAO template for Fe-N-C tubular catalysts for the cathode in PEMFCs

4.0. Contributions

Laser cutting of the AAO samples at the initial stages was carried out by Mengjun Gong and Andrés Parra Puerto. Heather Au helped to design a safe etching cell and environment.

4.1. Background of vertically aligned cathodes

The spraying of catalyst ink onto a membrane or gas-diffusion-layer (GDL) is the conventional preparation route for catalyst layers. Even though the ink composition can be adjusted to roughly optimize the catalyst layer structure, the method inherently lacks control to precisely define pore structure, ionomer phases and catalyst distribution. The resulting catalyst layers are composed of randomly distributed catalyst particle agglomerates (Figure 16 left side), ionomer phases, and voids. Each component makes up a network, for different purposes. The connected network of conductive support particles is responsible for the electron transfer, the ionomer network for proton or anion movements, and the void pores for supply of oxygen and transport of water. This disorganized catalyst layer structure in particle based cathodes limits charge and mass transport due to long pathways and lack of integration of particle agglomerates into the network.[136] As a result, the catalyst utilization ratio is low due to active sites buried in the interior of the carbon support agglomerates, oftentimes below 30%[101], and the operation at high current densities is limited. Especially, the intrinsically low site density of Fe-N-C catalysts requires thick catalyst layers, causing mass transport limitations.[54] Therefore, parallel to the research which aims to design and maximize the active sites and local catalyst structure, research into the design of overall catalyst layer architecture is expected to improve the overall fuel cell performance. In the field of platinum group metal (PGM)-based catalyst, there has been research devoted to the preparation of ordered nanostructured catalyst layers.[137, 138] In contrast to PGM based catalyst layers, which are in the thickness dimension of 5-15 µm, PGM-free based Fe-N-C catalyst layers are at least one order of magnitude thicker, in the range of 100-150 µm.[95,139] Therefore, Fe-N-C catalyst layers might profit even more from an ordered nanostructured catalyst layer design. However, so far there are only few reports on rationally designed PGM-free catalyst layers. [97,140,141] In the following, after deep diving into carbon supported PGM-based catalyst layer structures, a design concept for PGM-free catalyst layers is developed.

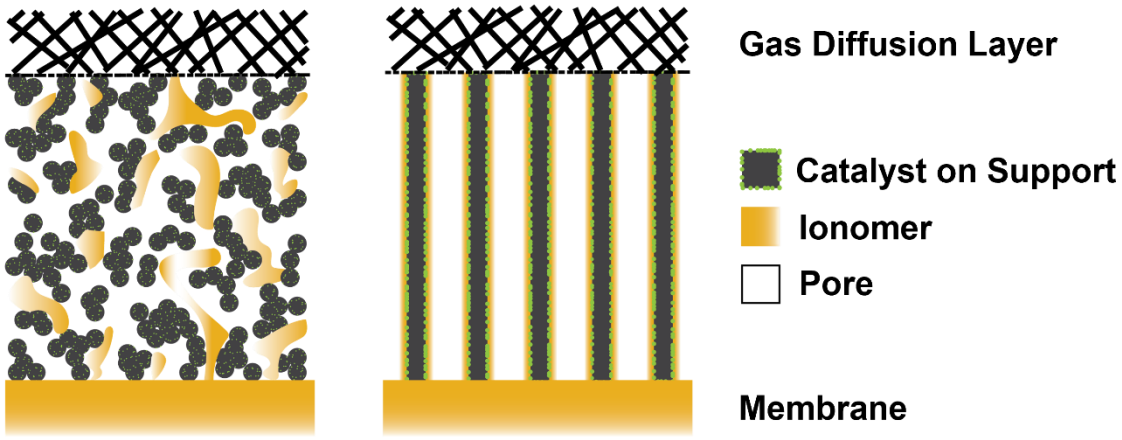


Figure 16. Left side: Sprayed particle based catalyst layers. Right side: The ideal electrode of ordered 1D nanostructured catalyst layers proposed by Middleman[142].

The first theoretical concept for 1D nanostructured catalyst layers dates back to 2002.[142] Middleman describes the ideal catalyst layer as a vertically oriented columnar electron conductor containing catalyst on the outside. (Figure 16, right side) A thin film of ionomer is covering the areas around the catalyst particles. The columns with > 10^9 units per cm^2 are equally separated by void space. This electrode structure has efficient mass transport paths and high catalyst utilization. Inspired by the ideal electrode model, various ordered nanostructured cathode catalyst layer have been developed for PGM fuel cells. Two different approaches are pursued to bring the theoretical model into existence, either as support-free self-standing vertically aligned catalyst structures, or by deposition of catalyst on vertically aligned support.

Support-free Pt nanotube arrays have been prepared by depositing Pt on the pore walls of sacrificial anodic alumina oxide (AAO) template by either electron beam evaporation (EBE)[143] or atomic layer deposition (ALD)[144,145]. Hot pressing of Pt-coated AAO template onto a Nafion membrane lead to full adhesion of the AAO/Pt_{tubes}-array on the Nafion membrane. After removal of the AAO template with NaOH (1 M, 2 M[145]), Pt tubes are still anchored on the membrane. Short tubes with length of 150 and 200 nm[143] are straight (100 $\mu g_{Pt}\ cm^{-2}{}_{geo}$), whereas long Pt tube structures produced via ALD method tended to form small bundles.[144] Maximum length of the Pt tube with ALD of 17 µm has been achieved with ALD.[145] When Pt nanotube array electrodes are tested without ionomer, overhumidified conditions of 120% RH lead to a significant performance increase.[145]

As support-free PGM tubes require high amount of PGM, vertically-aligned carbon nanostructures were used as support for PGM catalysts to reduce the PGM content. In 2006, a research team of Toyota scientists reported a MEA based on vertically aligned CNTs (VACNTs)

(length before hotpressing: 40 µm, after hotpressing 8 µm).[146] The MEA with VACNTs shows excellent mass transport properties due to the vertically oriented structure in combination with continuous straight pore structure leading to higher voltages at high current densities than with conventional carbon black. Nevertheless, due to the large size of Pt nanoparticles (2-6 nm), the Pt mass activity of catalyst layer with VACNTs does not outperform the conventional catalyst layer. As the surfaces of pristine VACNTs are chemically inert for anchoring Pt sites, plasma-treatment and attachment of functional groups based on poly(diallyldimethylammonium) (PDDA) facilitate the anchoring of Pt nanoparticles on the VACNTs.[147] A sandwich-structure MEA of Pt-VACNT/Nafion/Pt-VACNT (length of 4 µm) has been constructed via the attachment of two sets of VACNTs array electrode structures to opposite sides of a Nafion membrane.[148] The Pt utilization and the mass specific power density of the VACNTs MEA exceeded the conventional catalyst layer MEA. In another work, the control of area density of VACNTs was accomplished by controlling the amount of FeCo bimetallic catalyst on the Al foil substrate by spraying different volume of FeCo acetate solution.[149] The ideal Nafion loading in this study was determined to be 10.8 $\mu g/cm^2$. Impregnation of Nafion into Pt/VACNTs composite cathode architecture improves proton transportation capability and promotes the availability of active sites, and also adjusts the hydrophobic and hydrophilic properties of Pt/VACNTs film to form channels for the transport of O_2 and H_2O to and from the catalysts active site, which result in an improvement in the performance of PEMFC at high current densities. However, the overload of Nafion impregnation lead to a decrease of the performance of the Pt/VACNTs cathode. The optimized MEA with a Pt loading of 35 $\mu g_{Pt}/cm^2$ (Figure 17 c) : dark blue) reached equal performance to the conventional MEA with a Pt loading of 400 $\mu g_{Pt}/cm^2$.[149] Another approach to reduce the PGM loading was to deposit alloys of Pt with Co as catalyst on VACNT.[150] Dual functionality of the VACNTs film is enabled by its bifunctional properties. The hydrophobic properties of the VACNTs favouring water management and the hydrophilic layer of the segment along the length of VACNTs with covering metal catalyst makes the hydrophobic gas-diffusion-layer redundant.[150,151]

In 2014, Toyota pioneered a 236 cm^2 large Pt/VACNTs cathode for a MEA for vehicular use.[152] The polarization curve of this gigantic MEA composed of VACNTs with a 100 $\mu g_{Pt}/cm^2$ is compared with a Ketjen Black cathode of equal loading. (Figure 17 a)) The VACNTs outperform the Ketjen black in the kinetic and mass transport region. The mass transport capability, a rarely reported performance metric, of both MEAs is investigated by recording the limiting current density in 1% O_2. (Figure 17 b))[152] The total gas diffusion resistance $R_{diffusion}$

including catalyst layer and GDL can be obtained with $R_{diffusion} = \frac{p_{O_2}}{RT}\frac{4F}{i_{lim}}$.[152] The values for the VACNTs of 43.6 s/m and Ketjen Black of 65.5 s/m substantiate the superior gas transport properties of VACNTs electrodes. In this study, the coil-shaped VACNTs prevented agglomeration during the manufacturing process and maintained the continuous pore structure. The density of the VACNTs impedes ionomer impregnation and influences the cell performance, if the ionomer does not reach and covers the CNT along its entire length. A VACNTs with a 200 nm distance between the 20 nm CNTs (40 – 60 µm length) was found to enable ionomer penetration in the void. The diameters of ionomer colloids in solution are usually between hundreds and thousands nanometers.[153,154] As the transfer from the substrate for VACNTs growth to the membrane is a delicate step with potentially destructive impact on the structures, Pt/CNT structures have been directly grown on carbon paper (Pt/CNTs/Carbon Paper) and carbon fiber composites.[155,156,157] The Pt/CNTs/Carbon paper cathodes outperformed the commercial available Pt/C electrode in MEA testing.[155] In another study, CNTs grown on GDL were treated with active screen plasma nitriding (ASPN) to increase the activity of CNTs. Subsequently, Pt nanorods were grown on the N-CNT arrays.[158] The Pt/N-CNT/GDL achieved 1.23-fold power density over Pt/C with less than half of the Pt loading.

The peak power densities normalized to mass of platinum are an indicator for the performance and utilization, whereas the geometrical peak power density is an effectiveness indicator with regards to the electrode area in the actual device. The cathode catalyst layer Pt mass-specific peak power density are plotted versus the geometrical peak power densities of representative Pt catalysts. (Figure 17 c)) The best cathode choice for a fuel cell would have both high Pt mass-specific peak power density and geometrical peak power density and thus be closest to the right upper corner of the plot. A transition from random distributed CNT with 50$\mu g_{Pt}/cm^2$ (brown hexagon)[159] to VACNTs with 50 $\mu g_{Pt}/cm^2$ increases the Pt mass-specific peak power density from 20.3 kW/g_{Pt} to 32.2 kW/g_{Pt}.[151] From that, it can be concluded that ordered nanostructuring of the cathode can increase the Pt utilization. An increase of the Pt loading on VACNTs from 10 $\mu g_{Pt}/cm^2$ to 30 $\mu g_{Pt}/cm^2$ leads to an 80% increase of the maximum power density (bright blue triangle).[151] However, further stepwise increase of the platinum loading to 50 $\mu g_{Pt}/cm^2$ (bright blue triangle) only leads to minor improvements of 18% of the maximum power density. At the lowest mass loading of 10 $\mu g_{Pt}/cm^2$ the VACNTs (bright blue triangle)[151] outperform the 20 wt% Pt/C (ochre circle).[160] Similar performance enhancement has been observed for a 100 $\mu g_{Pt}/cm^2$ loading of VACNT (red triangle) compared to Ketjen Black (red circle).[152] To summarize the advantages of vertically-oriented carbon nanostructure supports, which are

evident for PGM-based cathodes: The mass transfer resistance decreases in the catalyst layer by 33% (Figure 1 b)), the utilization of catalyst is increased (Figure 17 c)), resulting in significantly enhanced Pt-mass (35%-49%) and geometrical performance (35%-49%).

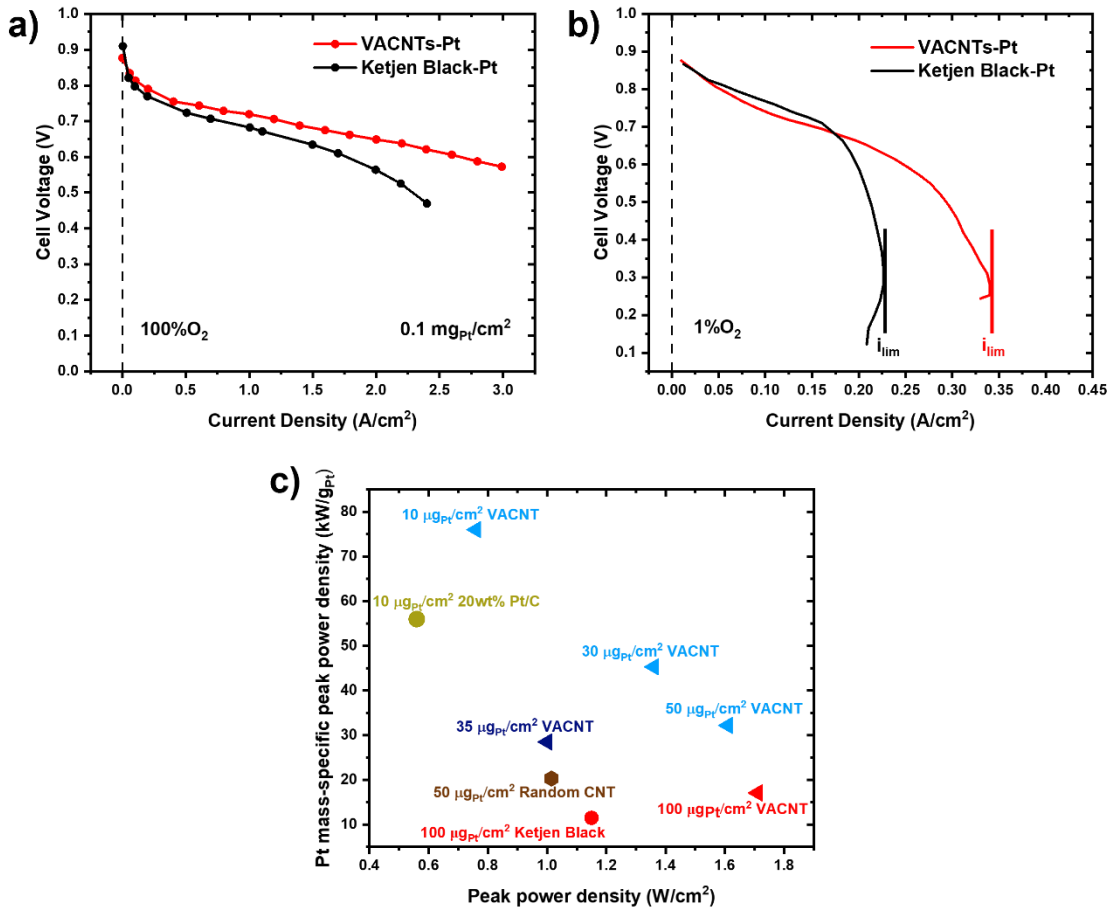


Figure 17. a) Polarization curves of large MEA with 236 cm^2 Pt/VACNTs vs. Ketjen Black-Pt as cathode catalyst layer in 100% O_2. Replotted from [152]. b) Polarization curves of VACNT electrodes and conventional electrodes on limiting current density measurement under oxygen-depleted test conditions (Cathode: 1% O_2 / 99% N_2, RH 80%, 80°C). Replotted from [152]. c) Cathode catalyst layer Pt mass-specific peak power density vs. geometrical peak power density of random CNT, VACNT and commercial powder catalysts. Values taken from [149,151,152,159,160].

Beyond the carbon-tube 1D nanostructured catalyst layers, a recent review summarises the progress in electrode design based on one-dimensional nanostructure arrays for PGM-based catalysts proton exchange membrane fuel cell applications.[138]

While 1D carbon structures have been operated as cathode in PGM-based fuel cells, there is no demonstration for non-PGM on ordered carbon structures as cathodes catalyst layers in fuel cells. The PGM-free 1D tubular carbon structures to date have been tested only in the rotating

disk electrode in liquid electrolyte.[161,162,163] From the RDE testing setup, no conclusion about the mass transport properties of the 1D carbon structure as catalyst layers can be drawn. Among them, there are VACNTs of small diameters and AAO-templated Fe-N-C carbon tubes with larger diameters.

VACNTs with nitrogen doping have been reported as metal-free ORR catalysts.[164,165] However, as the preparation involved iron phthalocyanine or iron ferrocene as catalyst during the chemical vapour deposition (CVD) growth, there might be even a tiny amount remaining and distorting the activity measured. It is doubtful that the electrochemical purification method has removed all iron from the catalyst. The diameter of the of VACNTs grown by chemical vapour synthesis on flat substrates is limited to smaller diameters (< 5 nm), as the dimension of the metal catalyst determines the diameter of the carbon nanotubes. AAO template allows creation of carbon nanotube structures with larger diameters. The AAO pore channels can be filled with a Fe salt as source to form Fe-N-C in a subsequent CVD process of acetonitrile.[162]

4.2. Goal: PGM-free VACNTs

The literature on PGM-free VACNTs is sparse. However, the recent tremendous advances in Fe-N-C catalysts is on the verge to spill over into nanostructured channel catalyst layers due to necessity of thick Fe-N-C catalyst layers in fuel cells. These Fe-N-C catalyst layers suffer even more from mass transport limitations at high current densities as discussed in the introduction chapter. Therefore, tubular structures with integrated Fe-N-C sites have a high degree of active site exposure and highly efficient mass transfer paths, which could offer a breakthrough solution for this emerging catalyst class.

The goal of the work presented in this chapter is to prepare a cathode catalyst layer with vertically aligned large diameter carbon tubes, which have an orientation perpendicular to the membrane (Figure 18). Catalytically active sites for the ORR in the form of Fe-N-C sites are distributed in high density on the carbon tube walls on the inside and outside. The tube diameter and inter tube distance is chosen to allow for mass transport to and away from the active sites on inner and outer surface of the tubes.

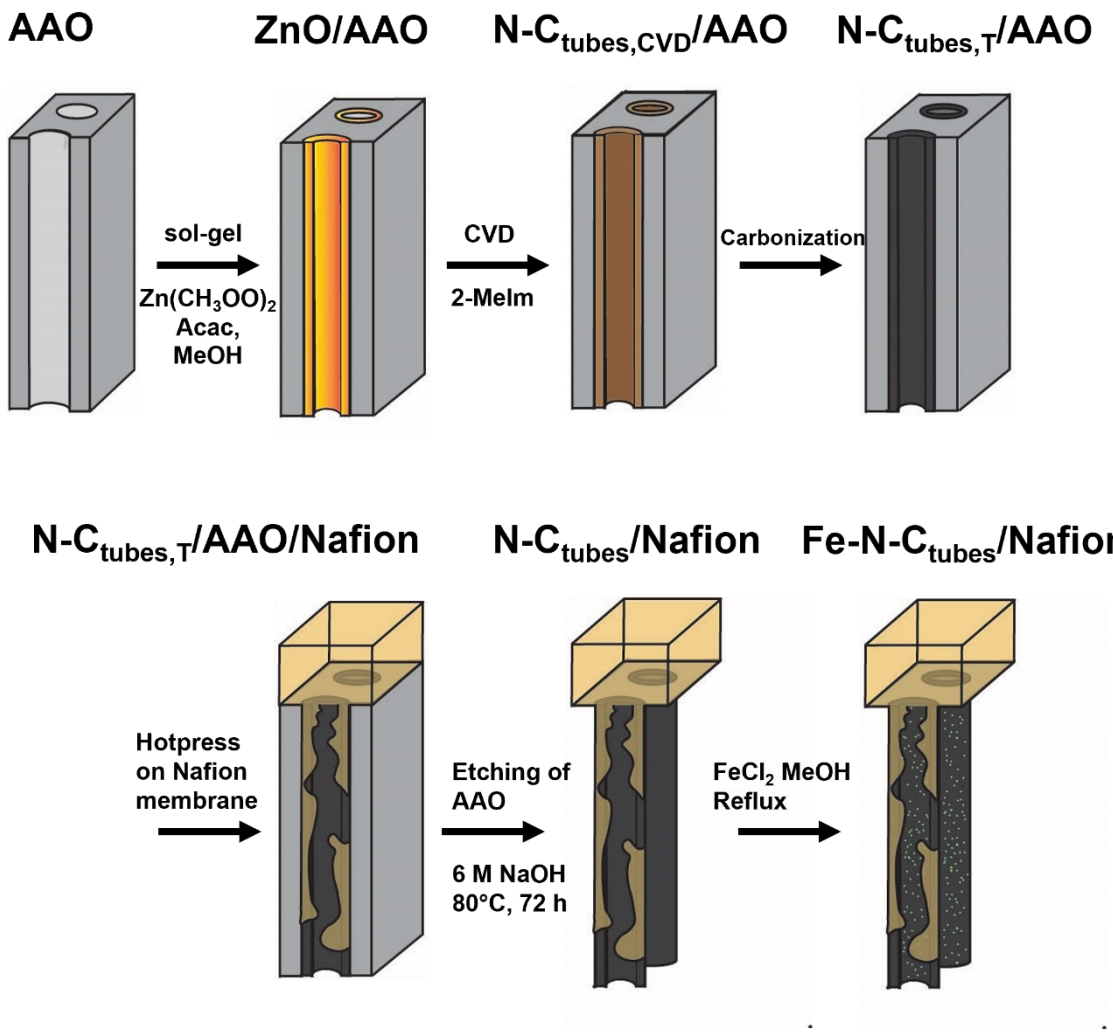


Figure 18. Preparation steps of iron containing nitrogen-doped carbon tubes anchored on Nafion (Fe-N-C_{tubes}/Nafion) with the AAO template approach.

Templates offer a starting basis to create defined and controlled dimensions and morphology of the final tubular catalyst layer. Anodic alumina oxide (AAO) is the ideal choice to guide the vertical alignment of CNTs arrays, because of their parallel and straight channels. The uniform pores in AAO define the outer diameter of the created open-ended CNTs. The disadvantage of AAO template includes the costs and the additional etching step to remove the template. Since the discovery of the self-ordering mechanism of pores in AAO through the use of a two-step anodization by Masuda and Fukuda in 1995, several anodization conditions with different electrolytes have been found to create highly-ordered close-packed hexagonal cells of nanopores.[166] The basic mechanism of anodization can be explained by taking into consideration that the aluminum oxidation leads to an expansion by a factor of about two, because the density of alumina is only half that of metallic aluminum.[167] The entire metal/oxide interface is oxidized by the electrolyte and will be under compressive stress, limiting the pore wall expansion only in the upward direction. A balance between dissolution and growth of the

oxide layer leads to the growth of pores. The repulsive forces between neighbouring pores due to mechanical stress allows for the formation of hexagonally ordered pores. The applied voltage and electrolyte concentration are the factors to determine the volume expansion. Nowadays, the availability of AAO membranes with different thicknesses, interpore distances and pore diameters opens up a huge tool box in template and nanoscience. The thermal stability of AAO membrane at a high temperature of 900°C and the uniform pores are two important parameters for the preparation of vertically aligned carbon tube (VACT) arrays.

Instead of creating a randomly located Fe-N-C on the carbon tubes such as in the chemical vapour deposition processes discussed above[162], it is also striven for maximization of the site density. Preferably, the Fe-N-C sites are dispersed on the inside and outside of the tubes, as mass flow limitations within the tubes might occur during oxygen reduction reaction.

Zeolitic-imidazolate-framework-8 (ZIF-8) has been widely utilized as a precursor for Fe-N-C catalysts. The volatility of Zn at high temperatures can be capitalized for anchoring Fe. Either the Fe precursor is doped into ZIF-8 during carbonization to create Fe-N-C sites[52] or the available N-C after Zn evaporation are used for post-coordination of Fe.[33,168] Recently, the chemical vapour deposition of 2-methyl imidazole onto Fe-doped ZnO powders at 350°C lead to the creation of atomically dispersed nitrogen-coordinated Fe sites.[169] In this procedure, 2-MeIm (0.75 g) and Fe-ZnO nanosheets (0.15 g) were placed in two separate alumina combustion boats in a furnace with two temperature zones, respectively. The temperatures for the up and downstream zones are heated to 280°C and 350°C, respectively. As a result, the evaporated gaseous 2-MeIm flows with the argon gas and subsequently deposits onto Fe-ZnO nanosheets. After 30 minutes at constant temperature, the temperature is increased to 1000°C with a heating rate of 30°C / min and held for 1 hour to yield the catalyst.

ZnO/AAO based tubes would be a great precursor material for vertical aligned carbon tube arrays with high Fe-N-C site density. One approach to prepare ZIF-8 tubes in AAO membranes is electrophoretic deposition (1 V, 20 min / 40 min / 60 min, molar ratio of zinc ion to 2-methylimidazole: 1:75). However, no continuous filling of the pores, but rather separated ZIF-8 particle are produced until the tube clogs at the opening. [170,171,172] In another study, a vapor-phase technique has been used to synthesize ZIF-8 membranes.[173] In a first step, ZnO is coated on AAO pore walls via atomic layer deposition (ALD). This ZnO layer is exposed to 2-methyl imidazole vapour, which converts the ZnO layer to ZIF-8. As no ALD for ZnO deposition is available in our laboratory, zinc oxide films in tubular shape on the AAO walls are prepared by

the sol-gel method [174,175] Vertical ZnO tubes with 40 nm inner diameter and 3.2 µm length of area across a geometric area of 6 cm^2 were fabricated.[174]

The calcinated ZnO/AAO is exposed to vapour phase deposition with 2-methyl imidazole to form nitrogen-doped carbon films on the pores walls of AAO (N-$C_{tubes,CVD}$/AAO). Previously, ALD zinc oxide films with 3 – 15 nm thickness were transformed to ZIF-8 film by exposure to 2-methylimidazole vapour at 100°C for 30 min.[176] The transformation of dense zinc oxide to highly porous ZIF-8 is accompanied with an expansion in film thickness.

The N-$C_{tubes,CVD}$/AAO are carbonized at 800, 900, 1000°C for 1 hour in nitrogen atmosphere to obtain N-$C_{tubes,T}$/AAO. The N-$C_{tubes,T}$/AAO are transferred onto a Nafion membrane with hotpressing. The Nafion membrane provides the platform for the tubular structure. In the subsequent etching step, the AAO template structure around the tubes dwindles, and N-$C_{tubes,T}$/AAO are anchored on the Nafion membrane (N-$C_{tubes,T}$/AAO/Nafion). Finally, according to widely used active site imprinting protocol, atomically-dispersed Fe sites can be introduced via (trans-)metalation with $FeCl_2$ in anhydrous methanol solution.[168] Thereby, the uncontrolled formation of various iron species potentially less active Fe species at high temperature carbonization can be circumvented, yielding the final Fe-N-C_{tubes}/Nafion structure.

As VACNTs with Fe-N-C active sites have only been characterized in ex-situ rotating disc electrode (RDE) experiments, the nanotubes are usually dispersed without forming an ordered array.[161,162,163] Gas-diffusion-electrode setup enables the testing of the VACNTs with their directionally aligned structures intact. Finally, the oxygen reduction reaction performance of the Fe-N-C_{tubes}/Nafion is compared with a commercial Fe-N-$C_{Pajarito\ Powder}$ catalyst in acidic electrolyte.

4.3. Characterization of the steps towards VACNTs in AAO

Anodic aluminum oxide (AAO) with its porous channels of 300 nm diameter is the starting template (Figure 19 a)). A sol-gel method is applied to grow zinc oxide tubes on the pore walls (AAO/ZnO_{tubes}). The sol consists of a methanol solution containing zinc acetate and acetyl acetone.[174] Zinc acetate has the advantage over other zinc salts such as $Zn(NO_3)_2$ for example that it forms uniform and smooth ZnO films, whereas $Zn(NO_3)_2$ forms small crystallites of ZnO.[177] Acetylacetone acts as stabilizing agent and can form chelate complexes in the ZnO sol.[178] Because of the lower viscosity of obtained solution than that of traditional sol, this solution impregnates more easily the AAO template. The sol-gel method consists of two steps.

The first step is the hydrolysis, which is initiated by heating to 50°C to form zinc ions and acetate ions.[179] Water from the hydration shell of the Zn precursor reacts with Zn ions to form $Zn(OH)_2$ sol. During the 24 h aging, the sol particles form by the aggregation of ZnO molecules. If the aging time goes beyond 24 hours, larger sol particles form, which would produce larger grains in the final film.[180] After the preparation of an aged sol, the AAO is dipped into the sol for the growth of the ZnO film. In the second step, $Zn(OH)_2$ colloid cluster condense to form ZnO.[181] (Figure 19 b))

Hydrolysis: $Zn(CH_3COO)_2x2H_2O \rightarrow Zn(OH)_2 + 2\ CH_3CH_3COOH$

Condensation: $Zn(OH)_2 \rightarrow ZnO + H_2O$

After calcination at 600°C in air, ZnO tubes with uniform thickness along the pore length are formed. From top view, the wall thickness of the ZnO tubes is approximately 20 nm. (Figure 19 c)) However, it has to be pointed out that EDX cross section analysis only detected Zn very close to signal to noise ratio (not shown). It is probably due to sputtering of an additional layer of 40 nm chromium, superimposing the Zn signal.

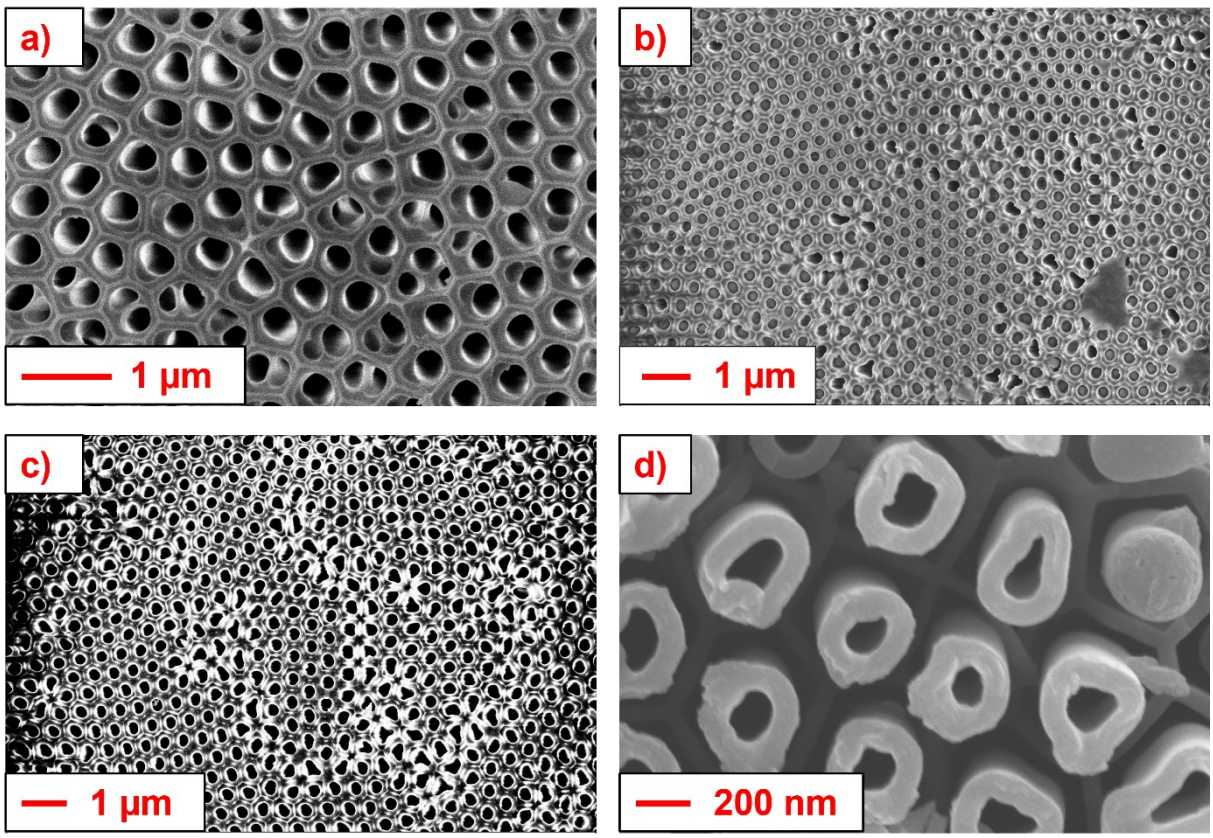


Figure 19. SEM: Topview of (a) pristine AAO, b) AAO filled with $Zn(CH_3COO)_2$, c) AAO with ZnO tubes after treatment at 600°C, d) with nitrogen-doped carbon tubes.

In the next step, the AAO samples are exposed to 2-Methylimidazole (2-MeIm) vapour at 350°C to deposit a nitrogen-doped carbon film in the channels of AAO (Figure 19 d)). In literature the deposition of nitrogen-rich carbon precursors into the pore channels of AAO in liquid phase [182,183] and gas phase[184,185] has been reported. A nitrogen-rich precursor such as 2-MeIm is chosen to maximize the nitrogen-content in the final carbon tubes for Fe coordination. Imidazole has been reported to produce a nitrogen doping content from 12.1 to 25.7% in a chemical vapour deposition processes (700 – 900°C) when deposited together with the catalysing ferrocene.[184] The original AAO sample shows the common absorption band below 1000 cm^{-1} to 600 cm^{-1} associated to the longitudinal mode of the Al-O stretching vibration consistent with previous reported FT-IR spectra of AAO (Figure 20 : grey line).[186] The FT-IR spectrum of the 2-MeIm powder sample contains methyl groups (CH_3) as evident by the peaks at 3146 and 3008 cm^{-1}, which originates from the C-H stretch of the methyl group (CH_3) and the peak at 1436 cm^{-1}, which can be assigned methyl group bending.[187] The broad band reaching from 2300 to 3400 cm^{-1} can be assigned to intermolecular hydrogen bond derived from the hydroxyl group and N-H in the protonated imidazole rings.[188] The band around 1675 cm^{-1} arises from the C=C stretch mode.[189] The signals between 1300 and 1460 cm^{-1} stem from the entire ring stretching, whereas the band at 1150 cm^{-1} can be assigned to aromatic C-N stretching mode.[190] The peaks at 993 and 740 cm^{-1} could be attributed to C-N bending vibration and C-H bending.[189] The signal at 1591 cm^{-1} for N-H bending and 1843cm^{-1} for N-H···N bending indicate that the 2-MeIm in its protonated form.[191] However, after the CVD process the features associated with N-H-bond disappear.[176] A similar vanishing of the peaks is also observed when looking at the spectrum of commercial Basolite® Z1200 ZIF8, in which the deprotonated N moiety is coordinated to zinc. Therefore, it might be concluded that the N moiety is coordinated to Al or Zn deposited in the AAO channels for the AAO/CVD 2-MeIm sample.

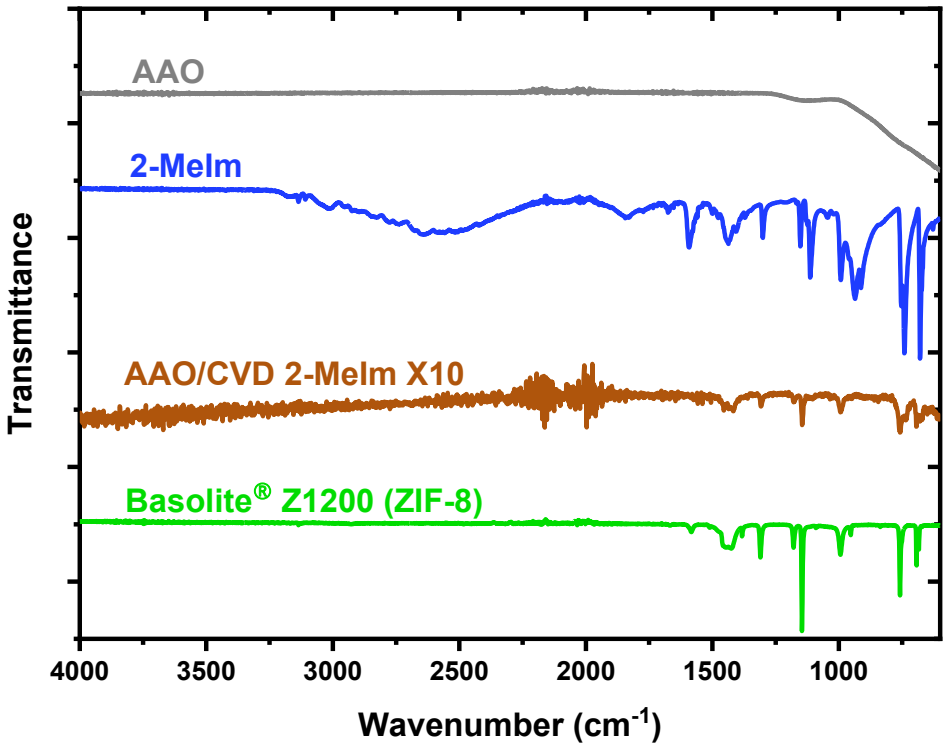


Figure 20. The formation of 2-MeIm tubes after CVD at 350°C. Transmittance of ATR FT-IR of AAO (grey), 2-MeIm powder (blue), AAO/CVD 2-MeIm with signal processing of factor 10, and commercial Basolite® Z1200 powder.

The physical appearance of the AAO membrane turned from transparent white to brown. After the chemical vapour deposition, the 2-MeIm/AAO samples are carbonized with a heating rate of 3°C/min and a 30 minutes constant temperature hold step at 800, 900 and 1000°C respectively, yielding N-doped $C_{tubes,T}$/AAO with T representing the final temperature of the carbonization step. The resulting samples are shiny black. The preparation of the carbon tubes is completed and the template function of the AAO to bestow the shape of the pores onto the carbon is no longer needed. Therefore, the AAO is etched in the next step.

4.4. Review of the etching protocols in literature

Due to initial difficulties in the etching process of heat treated AAO samples, the reported etching procedures of AAO membranes in literature for AAOs containing carbon structures are reviewed. Various bases and acids are reported in literature to etch AAO membranes. The

pristine AAO membrane can be etched with 3 M NaOH within 8 minutes.[192] However, the chemical resistance of the AAO changes as a result of heat treatment. After thermal treatment of pristine AAO for 3 hours at 900°C, the corrosion reaction rate in acid and alkaline solution is diminished.[193] The reason is a phase transition from amorphous anodic oxide to crystalline structure.

The majority of publications which use low carbonization temperature < 800°C to prepare carbon 1D structures in the pore of AAO, are able to etch the AAO with milder etching solutions based on phosphoric acid (H_3PO_4) and sodium hydroxide (NaOH). [194,195,196,197]

AAO membranes were placed on top of a PAN solution to wet the membrane by drawing PAN solution into the pores due to capillary force. The carbonization was carried out at 600°C for an hour. The AAO template was removed by dissolving in 1 M NaOH aqueous solution.[194] Nitrogen-doped carbon tubes in AAO were prepared by using ethylenediamine and carbon tetrachloride precursor solution, in which the AAO were immersed. After carbonization (600° C, 5 hours, N_2 atmosphere), the nitrogen-doped carbon tubes were obtained by removing AAO membranes with 2 M NaOH for 4 hours at 40°C.[195] A graphitic structure was synthesized by catalyst-free chemical vapor deposition on an anodized aluminum oxide (AAO) template using acetylene as the carbon source at a temperature of 620°C (50 min). The AAO template was removed by chemical etching, which yielded a three-dimensional structure featuring planar layers seamlessly joined together by nanotube pillars via continuous carbon-carbon bonding. After growth, the AAO template was removed by etching in 5 M NaOH for approximately 48 h.[196] The removal of the AAO template after carbonization of a AAO-hydrothermal carbon composite (4 h, 350°C, 550°C, 750°C in N_2) has been reported with concentrated phosphoric acid under stirring at 65 °C.[197]

In almost all experimental procedure, involving carbonization temperatures > 800°C, harsh etching agent hydrofluoric acid (HF) applied to remove the AAO from the carbon structure.[162,185,198,199,200,201,202,203]

In 1996, pyrolytic carbon deposition with propylene at 800°C in the pores of AAO created carbon tubes and compared with carbonized polyfurfurylalcohol tubes.[198] The tubes were released from the template with 46% HF solution. Different N-containing precursors were used to adjust the nitrogen doping in the carbon tubes in this study at a temperature of 850°C. 5 wt% HF solution was used to obtain liberated CNTs.[185] Wen et al. fabricated open-ended HTC-derived CNTs using AAO as template and glucose as carbon source.[199] In the first step, glucose

has been polymerized in the pores of the AAO template resulting in the uniform coating of the inner surfaces of the AAO nanochannels with carbonaceous film. The carbonaceous films on the AAO template have then been carbonized at 900°C for hours under a flow of N_2. The authors observed a shrinkage of the carbon polymers and the formation of a gap between the CNTs and the AAO walls. Subsequently, Pt nanoparticles have been deposited by immersing the AAO/CNT membranes several times in a H_2PtCl_6 and $NaBH_4$ solution after pyrolysis. The Pt-CNT-Pt hybrid composites have been liberated by dissolving the AAO template with HF.[199] Core–multishell Fe@C NWs–AAO nanocomposites were synthesized via electrodeposition of Fe and low-pressure chemical vapour deposition (CVD) at 900°C.[200] The Al_2O_3 from the nanocomposite was not chemically etchable after CVD at 900 °C. Even harsh etching conditions with 10 M NaOH (80°C), 0.5% HF (wt%), and 1,8% H_2CrO_4 + 6% H_3PO_4 (wt%) (65°C) did not lead to removal of the AAO membrane.[200] Nanotubes grown by propylene gas on the membrane at different temperatures (500, 600, 700, 800, 900, 1000°C) have been released from the AAO membrane in concentrated HF.[201] The nanotubes formed at 500°C and 600°C did not survive HF treatment. Hexa(4-dodecylphenyl)-peri-hexabenzocoronene has been drop-infiltrated into AAO channels and carbonized at 900°C for 5 hours. The template have been partially dissolved in NaOH (3 M), exposing the upper tips of the carbon tubes.[202] In the case of the Fe-N-C carbon tubes in AAO, a CVD process of acetonitrile was deposited on AAO membrane, which pores have been filled with $Fe(NO_3)_3$.[162] Excess Fe nanoparticles and the AAO template were removed in a mixture of HF and HCl at 70°C for 12 hours. Among the studies of carbon tube preparation at 900°C, one can be found which uses 6 M NaOH to remove the alumina template.[203] This study prepared N-doped carbon tubes from a variety of polymer precursors.

In the case, that the complete AAO is covered by a thin carbon film, even the most aggressive etchants are not able to dissolve the AAO.[204,205,206] A plasma-enhanced CVD process of methane and hydrogen on nanoporous AAO at 900°C lead to complete coverage of the AAO substrate with a thin layer of graphene. The full coverage of the graphene layer over AAO was confirmed by inserting the sample in HF (40 %) for 22 hours. As the sample remained the same, it was concluded that the graphene/AAO is completely covered by a protective graphene layer.[204] Even a short CVD process of 10 min methane and hydrogen (920°C) can coat the internal pore surface and external area of AAO membrane with a ultrathin homogenous carbon layer. As the carbon layer is so thin that it cannot be resolved with SEM, the chemical resistance has been analysed in saturated NaOH, saturated KOH solution, 40% HF in H_2O and 25% $HClO_4$ in ethanol, for 24 hours, and compared to pristine AAO membranes. The AAO covered with the

thin carbon film proved stable in all of the 4 harsh chemical environments.[205] Same coverage has been observed recently by Nishihara and coworker.[206] A nanoporous membrane electrode based on ordered array of hollow giant carbon nanotubes inside the pores of AAO has been electrochemically characterized without etching of the AAO. The thin layer of carbon film is normally formed on the top surface of the AAO template during the CNT growth easily verified by resistance measurement and would have to be removed before the wet etching step. It was found that by dry-etching, either with ion milling or reactive ion etching (RIE), a uniform and clean surface can be obtained.[207,208]

In table A1, an overview of the temperature for carbonization and the chosen wet etching agent is given.

The conclusion from this section is that two factors might render the removal of the AAO template more arduous. First, heat treatment at higher temperature (> 800°C) increases the etching resistance of AAO. Secondly, potentially a thin protecting carbon film enveloping the AAO, denying access of the wet etching agent to the AAO. The carbon film covering the top surface AAO and not the inside the pores can be removed with oxygen plasma.[207]

4.5. Detailed Analysis of the etching progress

As HF is a toxic chemical, 6 M H_3PO_4 is chosen as the etching agent. After 24 hours in 6 M H_3PO_4 at 80°C, the AAO template is completely removed from the N-doped $C_{tubes800}$/AAO yielding vertically aligned N-doped $C_{tubes800}$ (Figure 21 a), b)). In contrast, the etching process of N-doped $C_{tubes900}$/AAO is more sluggish, and only minor etching progress is observed after 24 hours (Figure 21 c)). The EDX spectrum indicates that the N-doped $C_{tubes800}$ does not contain any Al anymore after 24 hours of etchings; whereas in the EDX spectrum of the N-doped $C_{tubes900}$ sample an Al signal is still present at around 1.5 keV. The etching of N-doped $C_{tubes900}$/AAO sample is completed after 72 hours (Figure 21 f)).

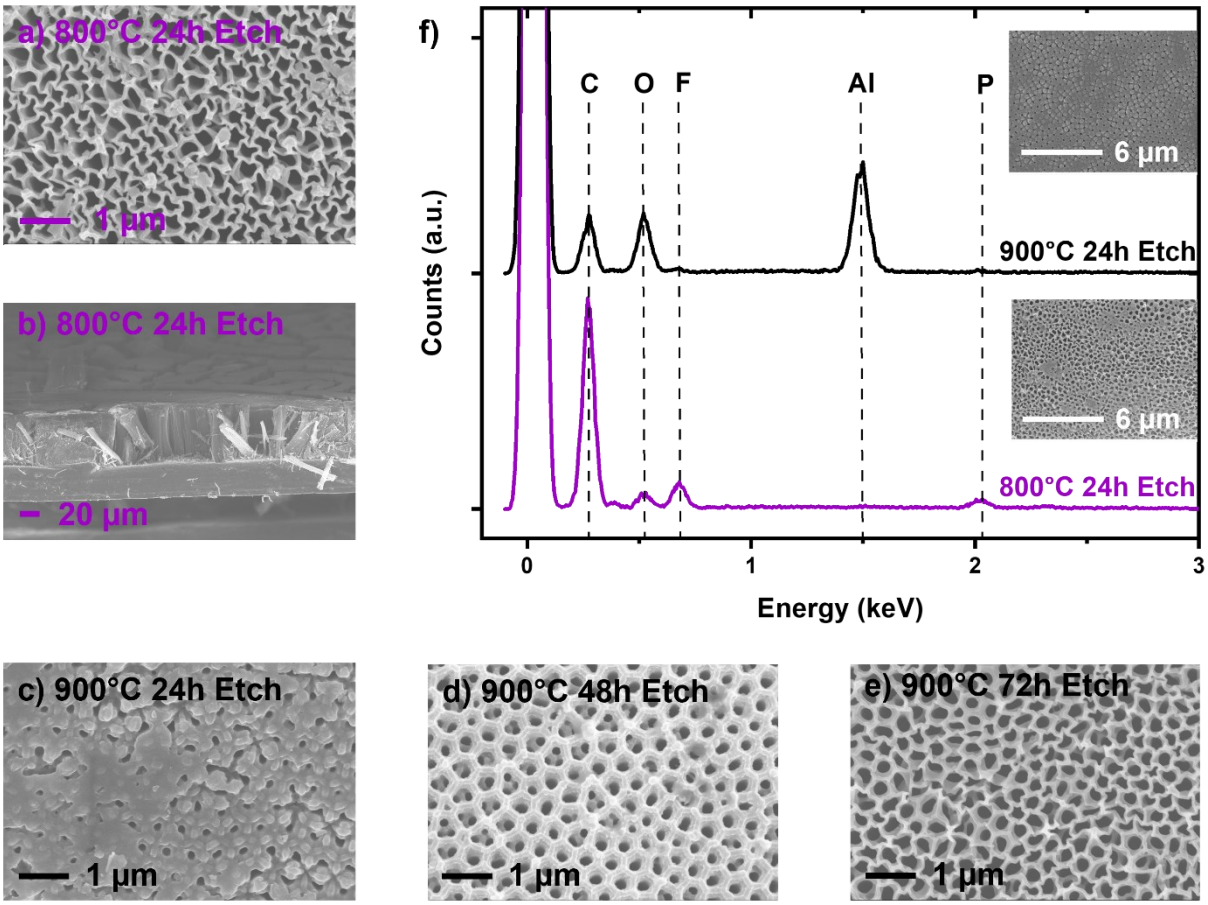


Figure 21. The etching process in 6 M H_3PO_4: Tracking AAO dissolution of $C_{tubes800}$/AAO for 24 hours (a) and b)) and $C_{tubes900}$/AAO for 24 (c), 48 (d) and 72 hours (e) with SEM. f) EDX comparing the progress etching of AAO from $C_{tubes800}$ and $C_{tubes900}$ after 24 hours.

The effect of annealing of AAO on its chemical stability is studied with XRD on the AAO without any ZnO and carbon chemical vapour deposition. The annealing of AAO enhances its etching resistance.[209] The chemical resistance can be significantly improved by annealing of the porous films in the temperature range of 800-1000°C. A sequence of phase transformation from amorphous alumina to a mixture of γ-Al_2O_3 and θ-Al_2O_3 changing to γ-Al_2O_3, δ-Al_2O_3 and θ-Al_2O_3 and finally to α-Al_2O_3 with increasing temperature has been reported for AAO.[210] The phase composition of the AAO samples annealed at 800°C corresponds to a mixture of the γ-Al_2O_3 and α-Al_2O_3 (Figure 22: golden line), consistent with previous data.[211] Identification of the X-ray diffraction pattern for the AAO annealed at a temperature of 900°C indicates the formation of θ-Al_2O_3 phase and δ-Al_2O_3 phase (Figure 22: red line). The presence of polymorphs states of of θ-Al_2O_3 phase and δ-Al_2O_3 phase simultaneously depend on the

temperature and the time, as the transitions are gradually evolving through a combination of of θ-Al_2O_3 phase and δ-Al_2O_3 phases.[212]

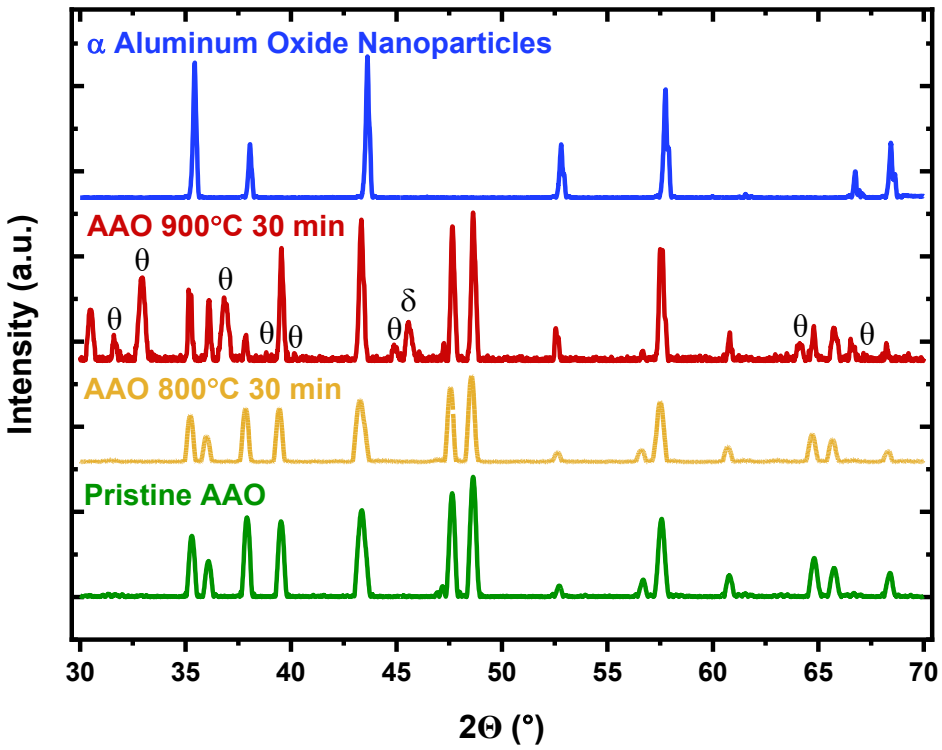


Figure 22. XRD of pristine AAO (green), AAO heat treated at 800°C for 30 minutes (gold), AAO heat treated at 900°C for 30 minutes (red) and α aluminum oxide nanoparticles (blue).

For the determination of the carbon loading, a TGA of the AAO/C_{tubes} samples has been carried out to determine the carbon loading, as the carbon is burned off in air, whereas the AAO remains unaffected. The sample size was 0.28 cm^2, four times larger area than for the GDE testing to minimize the error. The bare AAO before CVD of carbon tubes is heat treated at 1000°C for 2 hours to prevent any phase transitions of AAO with concomitant weight losses, which could distort the measured value for the carbon weight loss. Before the start of the TGA experiments the samples were stored in oven at 80°C for 48 hours to remove any ambient moisture. The TGA curves show weight losses of < 0.01% in the range from 30°C to 120°C confirming the absence of moisture in the sample. The sample colour change from black, N-doped C_{tubes} in AAO, to white, carbon-free AAO confirms the successful oxidative burn off of carbon. The weight % loss of N-doped carbon tubes in the AAO amounts to 2.01% for the carbon tubes carbonized at 800°C and 1.70% for the carbon tubes carbonized at 900°C (Table 3). In other works, typical yield of carbon nanotubes growth in AAO has been reported to be about 1% by

weight.[213] Overall, the carbon tubes have ultralow loadings of 15.7 µg for N-doped $C_{tubes800}$ and 19.8 µg for N-doped $C_{tubes900}$.

	N-doped $C_{tubes800}$/AAO	**N-doped $C_{tubes900}$/AAO**
Weight % loss	2.01 %	1.70 %
Mass weight loss of 0.28 cm^2	0.0629 mg	0.0793 mg
Mass weight loss of ORR sample size (0.0707 cm^2)	15.7 µg	19.8 µg

Table 3. Carbon mass loading in AAO: TGA of N-doped C_{tubes} in compressed air (10°C/min) from 30°C to 900°C to determine weight% loss.

4.6. Oxygen Reduction Reaction Performance of FeN_4-C_{tubes} electrodes

The planar N-doped C_{tubes}/AAO pieces are hotpressed onto Nafion membranes for 10 minutes at a temperature of 135°C and an applied pressure of 340 Ncm^{-2}. In literature, the common procedure is to impregnate VACNTs with diluted Nafion ionomer solutions prior to hotpressing.[147,148,149] Thus, the structure of alignment of the carbon tubes can be kept intact during the hotpressing. In addition, the cohesion of the nanotubes by capillary force in the liquid-air interface during drying could be prevented. Usually Nafion is a bulky polymer, so the infiltration into pores might be restricted.[214] Polybenzimidazole (PBI) and end-capped hyperbranched sulfonated macromolecules (HBM) are reported to wrap around randomly distributed carbon nanotubes in powder catalyst.[215,216] Therefore, such molecular ionomer could be employed in 1D VACNTs arrays with narrow tube distances. A commercially available short-chain proton ionomer is Aquivion. Recently, freestanding carbon web MEAs employed Aquivion to be able to deeply infiltrate the carbon structure with ionomer.[217] In contrast to the small diameter VACNTs in literature, which are prepared without the presence of a AAO template, it is decided to impregnate the ionomer post hotpressing to prevent formation of an ionomer layer on top of the N-doped C_{tubes} upon hotpressing. As the loading of 10.8 μgcm^{-2} of Nafion onto Pt/VACNTs showed the best performance[149], a 10 μgcm^{-2} loading of Aquivion is chosen. 11 µL of 0.05 wt% Aquivion in IPA was drop casted onto the carbon tube exposed site of N-doped C_{tubes}/AAO/Nafion samples. After slow drying at ambient atmosphere, the samples are immersed into 6 M H_3PO_4 at 80°C for 72 hours to etch the AAO template and yield N-doped C_{tubes}/Nafion. The etching process took place in a Teflon container with a lid and a 1 mm hole at the top lid. The volume of etching solution was tracked on a daily basis and no loss of etching solution was observed. After etching and washing the samples with DI water, the samples were dried in the oven at 80°C. The quick evaporation of residual solvent is crucial to prevent the formation of carbon tube bundles. The carbon tubes with 300 nm outer diameter and pore wall

thicknesses between 30 and 70 nm are embedded successfully into the ionomer matrix (Figure 23).

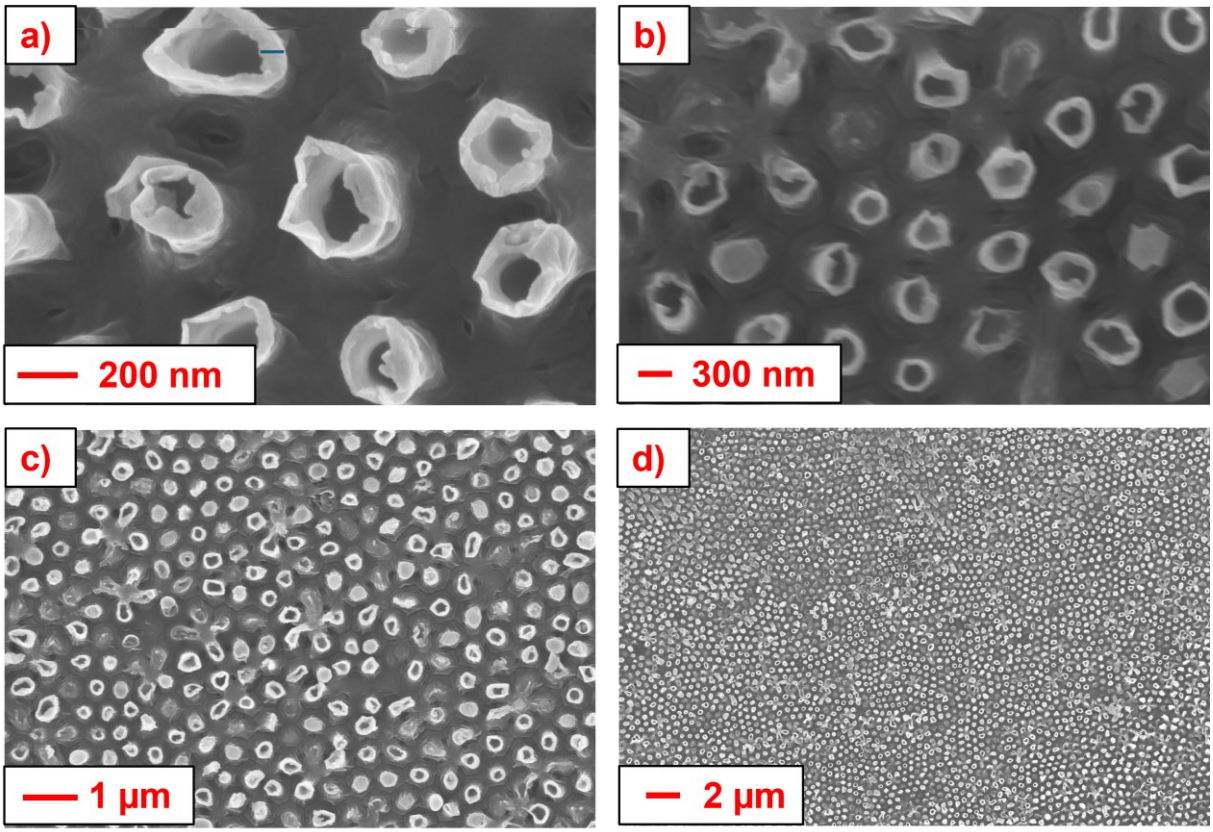


Figure 23. SEM images of the final FeN_4-C_{tubes} surrounded by ionomer polymer matrix at different magnifications.

The N-C_{tubes}/Nafion samples were treated in $FeCl_2$ reflux to coordinate Fe onto available N_x-sites. Consequently, the samples labelled Fe-N-$C_{tubes,T}$/Nafion were stored in 0.5 M H_2SO_4 solution until testing in gas-diffusion-electrode (GDE) setup. The samples for ORR testing were prepared very close to the end of the PhD and the ZnO step has been omitted for this, as the was no certain proof of Zn covering the pore channel uniformly in its entirety. Coating the AAO uniformly with ZnO in ALD process might be more reliable and worthy of investigation in the future [173,218], as the sol-gel liquid phase method can not be that precisely controlled as the cycled layer by layer deposition in ALD. In the low current density region, the 1000°C Fe-N-$C_{tubes,T}$/Nafion achieve higher current densities at lower overpotentials, whereas it shows lower current density values for potentials lower than 0.2 V. In contrast, the 800°C Fe-N-$C_{tubes,800}$/Nafion can reach higher current densities at lower overpotentials (Figure 24 a)). Several previous studies of nitrogen-doped carbon tube catalysts have reported decreasing nitrogen content with increasing carbonization temperature.[184,219,220,221] Lower nitrogen content is associated with poorer performance for metal-free nitrogen-doped carbon tubes

catalysts.[203,222,223] In addition, fewer nitrogen sites are available after higher temperature treatment for the coordination of iron atoms, leading to poorer performance at high current densities due to a smaller amount of active sites. In addition, the mass activity normalized to carbon tubular material is compared to commercial Fe-N-C catalyst of Pajarito Powder (PMF-D14401). Due to the ultralow carbon loadings < 0.25 $mg_C cm^{-2}$ as determined by ICP-MS, the value of 0.25 $mg_C cm^{-2}$ is assumed for the carbon mass loading for the Fe-N-C_{tubes} samples tested in gas-diffusion-electrode. The Pajarito Powder catalyst is elementally composed of 0.6 wt% Fe, 84.45 wt% C and 2.71 wt% N as measured with ICP-MS.[61] Based on that composition, a carbon mass loading of 1.02 $mg_C cm^{-2}$ is calculated for the comparison sample with a loading of 1.21 $mg_{Fe\text{-}N\text{-}C}$ Pajarito Powder catalyst (Figure 24 b)). The commercial catalyst outperforms the Fe-N-$C_{tubes,T}$/Nafion catalysts except the 1000°C Fe-N-$C_{tubes,T}$/Nafion at the second and third smallest current density steps. However, the lack of mesopores and micropores of the Fe-N-$C_{tubes,T}$/Nafion catalysts is suspected to reduce the overall surface area drastically. While this smaller surface area can not be verified from BET measurement due to the insufficient amount of sample available, morphology analysis with SEM and TEM indicate a smooth carbon tube surface (Figure 24 d)). Therefore, a theoretical approach is taken to estimate the surface area of the Fe-N-$C_{tubes,T}$ on 1 cm^2. From the lattice constant of 480 nm, a number of 434 027 777.8 Fe-N-$C_{tubes,T}$ are available on 1 cm^2. This is the order of magnitude of Middleman's model and corresponds to a fraction of 43.4% of 10^9 tubes described in his model.[142] The inner and outer diameter of 250 nm and 300 nm obtained from the average tube wall thickness of 50 nm, and a tube length of 50 µm yields a total specific surface area of 86.4 μm^2 per tube. Overall, a specific surface area of 0.0375 m^2/cm^2 is available on 1 cm^2 of loaded area. In contrast, for the BET specific surface area of the used Pajarito Powder catalyst 675 m^2/g is measured. A loading of 1.21 $mg_{Fe\text{-}N\text{-}C}$ Pajarito Powder catalyst gives a 0.8168 $m^2_{Catalyst\ Surface}/cm^2$. As a result, the surface area of Pajarito Powder per loaded area is larger by a factor of 22 compared to the carbon tube samples. After normalization of the ORR performance with regards to the BET surface area, the Fe-N-$C_{tubes,T}$ outperform the Pajarito Powder catalyst at low currents per catalyst surface area (Figure 24 c)). At the high currents per catalyst surface area, Pajarito Powder sample shows equal performance as the Fe-N-$C_{tubes,800}$, surpassing both the Fe-N-$C_{tubes,900}$ and Fe-N-$C_{tubes,1000}$.

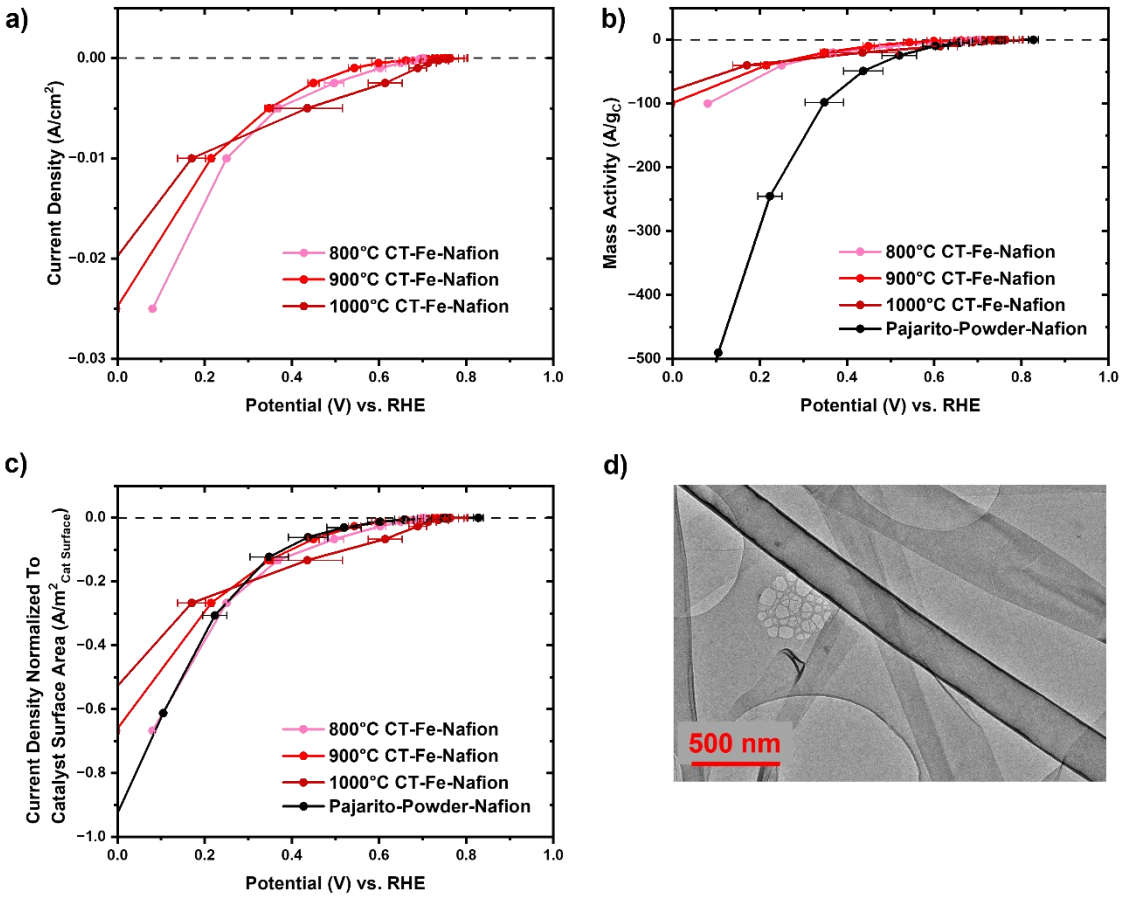


Figure 24. a) The ORR performance of CT-Fe-Nafion with CT supports prepared at 800°C, 900°C, 1000°C separated with Nafion membrane from 2 M $HClO_4$ in the upper cell compartment. b) Carbon mass activity of CT-Fe-Nafion samples compared with Pajarito Powder catalyst. c) Activity per BET specific surface area of catalyst. d) TEM image of N-$C_{tubes,900}$.

Here, it is repeatedly highlighted that the striking difference in performance between the Fe-N-$C_{tubes,T}$ prepared at different temperatures might be explained by the nitrogen content on the tube surfaces. The nitrogen content and graphitization is not only expected to affect the activity and number of active sites, but also to impact the wettability of the tubes.[224] Unfortunately, the X-ray photoelectron spectroscopy (XPS) setup at Imperial College does not allow the analysis of fluorine-containing samples. As the Fe-N-$C_{tubes,T}$ samples are anchored on a Nafion platform, Nafion is a tetrafluoroethylene polymer the analysis was not possible. Unfortunately, the etching of AAO without a platform only provides tiny amounts of particles which are hard to extract. Future work, with a suitable XPS setup could allow to gain further insight into the types of nitrogen sites and amount of nitrogen present in the samples.[223,225] Previous work on VA-

CNTs prepared with alumina template, correlates a greater number of pyridinic-type nitrogen sites in the carbon structure with improved ORR activity in acidic electrolyte in rotating disk electrode (RDE) testing setup.[203] This work represents a step forward towards PEMFC testing of Fe-N-$C_{tubes,T}$ or N-$C_{tubes,T}$ prepared by the AAO templating method. A comparable study demonstrated metal-free vertically aligned nitrogen-doped carbon nanotube (VA-NCNT) arrays prepared by the pyrolysis of iron phthalocyanine and purification to remove the iron arrays.[226] This VA-NCNT cathode catalyst exhibited a peak power density of 320 Wg^{-1} at a loading of 0.16 $mgcm^{-2}$ in a PEMFC.[226] However, doubt remains about negligible iron contents.

4.7. Conclusive remarks

1. The annealing **temperature** has a decisive influence on the phase composition and as a consequence the **chemical resistance of AAO**. The etching environment has to be chosen thoughtfully, as alkaline etching with high concentrations of NaOH would preferentially etch the glass instead of the AAO template. It is recommended to use Teflon containers with a lid that has a 1 mm diameter hole for pressure relief.

2. **Short side-chain ionomers** are required to fill the macropores of the carbon tubes. The main obstacle of Nafion entering into pores is the aggregation of Nafion molecules to large particle (> 500 nm) above a threshold concentration (1 g/L in H_2O).[214] Instead, Aquivion, a ionomer with shorter side chains allows easier penetration into the carbon tubes and spaces between the carbon tubes.

3. Even though **macroporous** carbon tubes offer transport high ways and great accessibility, the surface area is limited. The surface area is an important factor to increase the amount of electrochemical active surface area by exposure of more active sites. Thus, macroporosity by itself is not enough for the preparation of a highly active and functional freestanding Fe-N-C cathode catalyst. Further levels of smaller size porosity network, which is connected to the macropores is required.

4.8. Potential future work

1. Quantitative and qualitative analysis **nitrogen-content** on the surface of the carbon tube samples carbonized at different temperatures with X-ray photoelectron spectroscopy (**XPS**) would allow to draw further conclusion about the how many of which type of nitrogen sites are available for the oxygen reduction reaction by their own intrinsic activity[203] and also available for the metalation with iron. There is one sample of each carbonization temperature N-doped $C_{tubes,T}$/AAO hotpressed on Nafion left. Etching of the samples for three days in Teflon containers in H_3PO_4 at 80°C and subsequent washing in DI water could give samples for XPS. However, a XPS has to be found which allows the analysis of fluorine-containing samples, as the carbon tubes are going to be anchored on a Nafion membrane.

2. The **wettability** of the carbon tubes prepared at different temperatures could be investigated to explain the differences at low- and high current density performances. The differences might originate from water repulsion in case of hydrophobic properties or flooding in case of hydrophilic surface properties of the tubes.[224]

3. Control experiments: Control experiments could include to prepare samples **with ZnO** step and test them for the oxygen reduction reaction to assess whether this step is giving any improvement at all in the synthesis sequence. In addition, **iron-free** N-doped carbon tube samples could be tested for the oxygen reduction reaction to characterize the ORR-activity of the N-doped carbon tubes prior to iron metalation.

4.9. Ideas for further improvement of the project

1. Instead of the Sol-Gel method, which is not a reliably reproducible and controlled method to grow ZnO structures in the pore channels of AAO, atomic layer deposition (ALD) allows uniform gas phase deposition of ZnO onto AAO.[173,218] The company inredox sells **AAO with ZnO coatings**. Orders for AAO wafers with 200 nm pore diameter and 20 nm thick ZnO ALD coating have been placed in October 2023, but it has not been delivered yet.

2. **Additional meso- and microporosity** could be introduced into the carbon tubes to extend the electrochemically active surface area. An AAO membrane with straight macropores and mesopores in the range of 10-40 nm inside the pore wall can be obtained by immersing the membrane into 2wt% phosphoric acid and heat-treating it at 1400°C.[227] The BET surface area of the AAO increased from 3.5 m^2g^{-1} to 11.7 m^2g^{-1} after the introduction of mesopores. Those mesopores in the template could be transferred onto the carbon tube structure. Another way to

prepare three-dimensional carbon tube grid (3D-CTG) with interconnected and structurally integrated vertical and lateral carbon tubes has been reported.[228] Cu-contained nanoparticles are incorporated into the channel walls by anodization of Al foils with Cu impurity and subsequent selective wet-chemical etching of the nanoparticles opens wall the lateral connections. Single Pt atoms are anchored onto the 3D-CTG and tested as cathodes for hydrogen evolution achieving 1000 mA/cm^2.[229] Microporosity could be induced onto the carbon tubes by activation in NH_3.[162]

3. A **simultaneous CVD** process of anhydrous $FeCl_3$[65] and 2-Methylimidazole[169] onto the AAO at 350°C could produce more active sites Fe-N_x in situ. Those active sites would then be formed before the hotpressing onto Nafion membrane and thus, could be easier quantified with ICP-MS or nitrite stripping on RDE after ball milling of the Fe-N-C-AAO.

5. Engineering Macroporous Carbon Films as Freestanding Fe-N-C cathode Catalyst Layer for Fuel Cells

5.0. Contributions

Mengnan Wang instructed me in the polystyrene synthesis and took one of the two TEM images in the future directions part. Jesús Barrio carried out the XPS measurement and deconvoluted the spectra. Guangmeimei Yang determined the conductivity of the films with four point probe measurements. Koji Nakabayashi provided the TMA analysis. Ying Wang helped in the optimization of the slurry and the carbonization procedure.

5.1. Abstract

As the oxygen reduction reaction (ORR) kinetics account for the largest share of performance losses for fuel cells, most research in platinum group metal (PGM)-free catalysts prioritize on improving the activity of catalysts by maximizing the active site density and by engineering of the local coordination environment of the active site to meet the activity targets. Thereby, the mass-transport capabilities of the catalyst are usually neglected at early stages of catalyst development. In this work, the reverse approach is taken: a carbon film support with an interconnected macropore network is designed for improved mass transport. Carbon precursors mesophase pitch and polyvinylalcohol (PVA) are combined with the macropore template polystyrene (PS) spheres in a ball-milling process to form a slurry for casting the film. After a new rapid removal process of the PS template, the molded macroporous structure is carbonized for electron conductivity. The macroporous film support is characterized in a Gas-Diffusion-Electrode (GDE) half-cell, which can operate under high current density conditions, at which mass transport losses can be expected. Model FeN_4 active sites are attached on macroporous films, of which one variant was carbonized in nitrogen with macropores (Film-N_2), and the other type of films was carbonized in 1% oxygen / 99% nitrogen with macropores and micropores (Film-1%O_2). The Film-1%O_2 sample achieves a slightly lower overpotential at high current densities of 2 Acm^{-2} probably due to the presence of additional micropores. Adjusting the film support thickness from 30 µm to 70 µm only slightly reduces the ORR activity at low current densities. For comparison, a conventional powder catalyst layer is sprayed with Vulcan XC 72 powder support. Mercury intrusion porosimetry (MIP) reveals that the macropore size distribution in the range 40-60 nm of Vulcan XC 72 catalyst layer is distinct from the macroporous carbon film cathode (CFC) with 100-400 nm. The average overpotentials

at a high current density of 2 A/cm^2 are centered in the narrow range of 0.52 V ± 0.03 V irrespective of the type of catalyst support.

5.2. Introduction Text

The widespread commercialization of low temperature fuel cell technologies depends on the stack production and materials costs, to which the cathode catalyst contributes up to 40%.[230] Cheaper catalysts for the oxygen reduction reaction at the cathode are either obtained by a reduction of the platinum content with ultralow loading platinum group metal (PGM) catalysts[10], or by eliminating the PGM costs with platinum group metal free (PGM-free) catalysts.[59] The activity of Fe-N-C catalysts, the best performing representative of latter catalyst class, has improved tremendously in both acidic and alkaline pH environment.[231,232] Despite the progress, the volumetric activity of less bulk dense Fe-N-C catalysts is still significantly inferior to that of commercial Pt/C catalysts due to the low active site density of Fe-N-C catalysts.[26] Consequently, high loadings of Fe-N-C catalysts are applied compared to Pt/C cathodes. Typically, Fe-N-C catalysts show superior activity at high pH,[233] due to a change of ORR mechanism from proton-coupled electron transfer to outer-sphere electron transfer going from low pH to high pH affecting the electrochemical activity.[47] Therefore, when integrating Fe-N-C in cathode for AEMFCs loadings of 1 $mg_{Fe\text{-}N\text{-}C}/cm^2$ are sufficient[49,50], whereas in PEMFC loadings of around 3 – 4 $mg_{Fe\text{-}N\text{-}C}/cm^2$ are required[33,65,76] to meet the DOE targets (44 mA/cm^2 at 0.9 V (iR-free)) in the kinetics-controlled region. Consequently, the cathode catalyst layers (CL) for Fe-N-C catalysts are thicker than that of Pt-based catalysts, which manifests itself with 60-100 µm of CL for Fe-N-C in contrast to 10 µm for identical performance for Pt-based catalysts in PEMFC.[234] As a result, thick Fe-N-C CLs suffer from severe mass-transport losses at high current densities with reported of about 100 mV at a current density of 1 A/cm^2.[235] Two main strategies are pursued to improve the mass-transport in Fe-N-C CL including the tailoring of mesopores[63,236,237] in the catalyst structure for efficient mass-transport pathways and the fine tuning of hydrophilic/hydrophobic properties of catalysts to achieve better water management.[238,239] While these approaches focused on the material and structure design at catalyst level (< 100 nm) might benefit the actual fuel cell performance, the effect of morphology design at catalyst layer level (> 100 nm) on transport losses with limiting current measurements have rarely been investigated yet.[240,241] Most spatial inhomogeneities are found on the macroscale with three-dimensional micro X-ray computed tomography (CT).[242] The observation of large voids and catalyst aggregates with sizes up to 10 µm raise questions whether such isolated aggregates are conductively integrated into the CL and thus, are

participating in the ORR. Conventional methods for cathode preparation such as slurry casting and spraying lead to random packing of catalyst particles, ionomer and pores, and thus, are restricting the control of the final catalyst layer morphology for efficient mass transport and accessibility of all available active sites. Therefore, it is suggested to overcome these issues with a freestanding carbon film cathode (CFC) support with interconnected macropores penetrating the structure continuously (Figure 25).

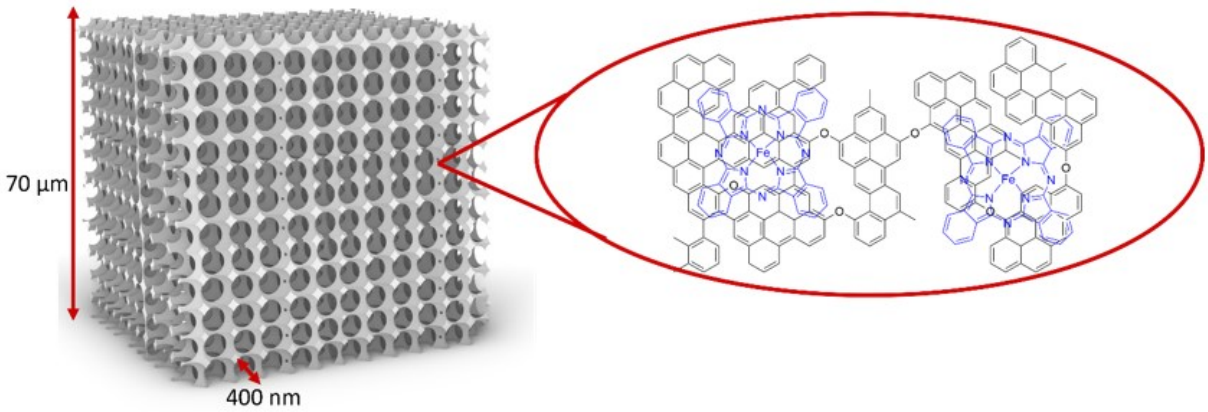


Figure 25. Macroporous carbon film cathode as a support for FeN_4 model catalyst sites of iron phthalocyanine.

Such a structure is expected to benefit the reactant accessibility to the active sites in the catalyst layer, guaranteeing electrical connectivity, and allowing continuous mass transport. Inspired by the development of porous freestanding CFC, onto which Pt nanoparticles are deposited, for PEMFC[243], the concept is extended to PGM-free electrode development. The CFC has to be increased from 12 µm, to match the thicknesses relevant for Fe-N-C CL. In addition, the spherical SiO_2 template is substituted by in-house synthesized polystyrene spheres in order to eliminate the time-consuming SiO_2 etching step involving harsh chemicals. Initially, the macroporous morphology of CFC support was characterized with SEM imaging complemented by detailed pore characterization with nitrogen adsorption mercury intrusion porosimetry to prove the successful creation of continuous macropore network. Adjusting the carbonization atmosphere to 1% oxygen in nitrogen affected the microporosity and changed surface composition as revealed with x-ray photoelectron spectroscopy (XPS). The freestanding film support was compared with a conventional powder support of Vulcan XC 72. For sake of simplicity, both supports are equipped with active sites of a model FeN_4 site, iron phthlocyanine

(FePc), to guarantee that powder and film catalysts have the same active sites and the performance of the catalyst layer morphology is not distorted by heterogeneous active site composition. The catalysts were first screened in RDE, followed by characterization of the mass transport performance at 2 Acm^{-2} for CFCs and powder based cathodes with different thicknesses in gas-diffusion-electrode (GDE) setup.

5.3. Results and Discussion

5.3.1. Replacing SiO_2 template with Polystyrene (PS) spheres

The carbon sources for the CFC include mesophase pitch, which can be obtained from pitch, a byproduct of crude oil and coal refining processes. This residue contains a heterogeneous mixture of polycyclic aromatic hydrocarbon structures with high C/H ratio, as shown in a representative molecular structure drawing (Experimental Section, Figure 16).[244] Mesophase pitches (MPs) are produced by thermal polymerization of aromatic rich fraction. Alternatively, AR mesophase pitch is produced by the catalytic treatment of aromatic molecules such as naphthalene.[245] Due to the orientational order adopted by the stacking of planar aromatic molecular structures to domains, optical anisotropy is observed under an optical microscope with polarized light, defining the intermediate liquid crystal structure as mesophase.[246] Hard templates are commonly used to endow structure on mesophase pitch-based carbons. Typical methods employed for the preparation of meso- and macroporous carbons from mesophase pitch such as colloid-imprinted carbon (CIC) method[247,248] or melt impregnation[249,250] rely on silica templates. These meso- and macroporous carbons are relevant for applications in electrocatalysis such as support for Pt for the ORR.[251] The commercial PGM-free catalyst of Pajarito Powder is also based on the so called sacrificial support method involving silica.[252] In most publications, the silica template is removed with hydrofluoric acid (HF) causing concerns due to its toxicity. A milder etching agent in the form of sodium hydroxide was found to successfully remove silica template and even improve the activity of Fe-N-C catalysts owing to carbon activation caused by treatment with sodium hydroxide.[253] The tedious waiting of up to three days reported for the completion of the etching process to remove SiO_2 in its entirety is not favourable for scalability. After reproduction of the preparation of freestanding CFC with SiO_2 CL LUDOX (12 nm average particle size) as recommended in the published protocol[243], the etching progress of the SiO_2 from the carbon film was tracked by burning off the carbon in air and the residual weight was measured (Figure 26 a)). The initial SiO_2 weight proportion

before starting the etching process of 72% decreased to 20-23% after 24 hours. After two days, the residual SiO_2 in the templated carbon was around 10% and remained in that range with no further etching between 48 and 72 hours. The residual SiO_2 is suspected to be isolated in the carbon matrix and not accessible for the etching solution. It is noteworthy that the low concentration 1 M NaOH (50 vol% EtOH) achieved a comparable etching as 3 M NaOH. The opening of the mesopores was confirmed with nitrogen adsorption measurement with six fold increase of mesopores with 10 nm pore width (Figure A1). Despite, the establishment of a more sustainable etching protocol of SiO_2, it would be even more time-saving to make the etching step redundant.

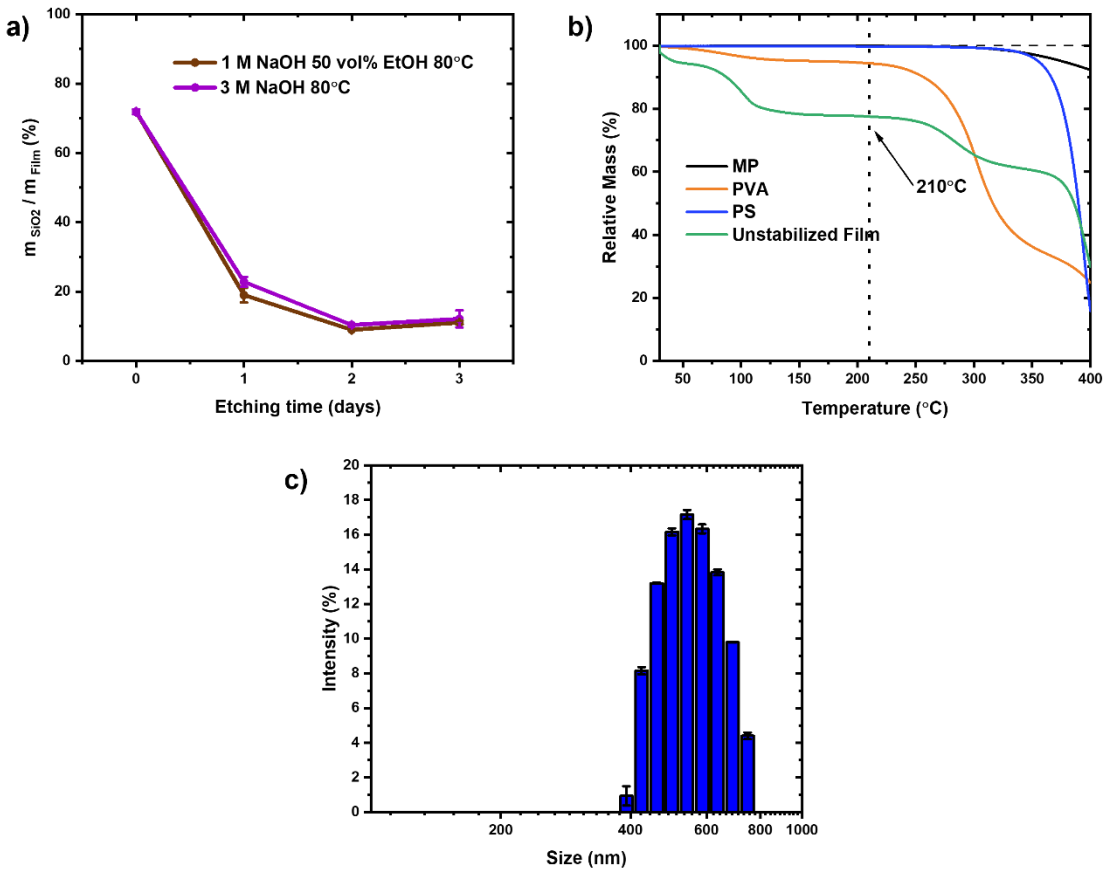


Figure 26. a) Tracking the etching of SiO_2 from the carbon support in alkaline solutions by measuring the residual SiO_2 after oxidative burn off of the carbon with TGA in compressed air (CA) atmosphere. b) TGA of MP, PVA, PS and unstabilized film in nitrogen (N_2) atmosphere. c) Particle size distribution of synthesized PS spheres.

5.3.2. The preparation of macroporous carbon films

Polystyrene (PS) is an alternative spherical hard template for the preparation of ordered interconnected porous carbon matrix of Fe-N-C powder catalysts.[254,255] PS nanospheres can be synthesized with diameter ranging from 15 nm to 1000 μm[256,257,258,259,260], allowing to tailoring pore structures of inverse opal carbon. The compatibility of the template and the carbon precursors is investigated, meaning that the carbon structure has to be solidified before the removal of the template. A common strategy to solidify the structure of MP fibers is oxidative stabilization. As pitch fibers cannot be directly carbonized without infusible stabilization treatments because they would melt at higher temperatures and lose their form[261], this might apply as well to templated carbon films after removal of the polystyrene template. During the oxidative stabilization step crosslinking of the functional groups of the various polycyclic aromatic hydrocarbons (PAHs) in the pitch takes place increasing its thermal stability and preventing it from melting at higher temperatures.[262] The oxidative stabilization of mesophase pitch is typically carried out at a temperature higher than the softening point of the mesophase pitch[263], but at a temperature lower than the onset of thermal decomposition of the PS template. Thermomechnical analysis (TMA) was used to determine the initial softening point of mesophase pitch at 175°C (Figure A2) and is expected to increase as the oxidation treatment progresses.[264] Thermogravimetric analysis (TGA) was used to identify the temperature of onsets of decomposition of the ingredients of the envisioned CFC. While MP and PS did not show any weight loss up to 300°C, the third carbon ingredient polyvinyl alcohol (PVA) showed a weight loss in the temperature region between 80°C and 110°C due to evaporation of water, which is expected (Figure 26 b)). In addition, the TGA curve of PVA indicates a second region of weight loss starting from 230°C. Therefore, 210°C has been chosen for the stabilization step of the CFC. The PS synthesis was carried out according to an additive-free emulsion polymerization method[265] and the size distribution of the product is analysed with dynamic light scattering (DLS). A broad distribution of PS particles sizes ranging from 400 to 800 nm was obtained (Figure 26 c)). The synthesized spherical PS with an average diameter of 557 nm were introduced as a macropore-directing hard template to substitute SiO_2 nanoparticles. The surface charge can be regulated in the synthesis process to facilitate the adsorption of positively charged Fe^{x+} onto the template surface[266] and thus, exposing the iron in pores after template removal. The mean zeta potential of the synthesized PS particles amounts to -41.8 mV. A general outline of the preparation of the conductive marcoporous film for the CFC support (Figure 27), is complemented by a detailed description in the Experimental section (Figure 16).

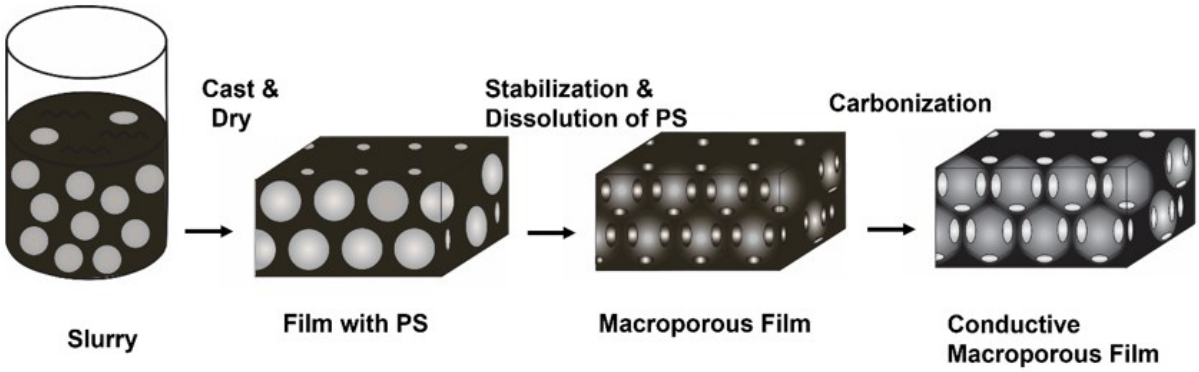


Figure 27. Preparation steps for the conductive macroporous carbon film.

The precursor ingredients have to be added together in a certain order to produce a slurry for the casting of the film. The mesophase pitch is ball milled in 1-Butanol, while an aqueous suspension of PS particles with PVA as a surfactant is probesonicated. Then, the two liquids are unified and the plasticizer 1,3-propanediol is added for a second round of ball milling. The slurry was casted, dried and peeled off for the oxidative stabilization step. During the oxidative stabilization, oxygen-containing functional groups are formed with simultaneous dehydrogenation, and polymerization reactions forming crosslinking bridges between PAHs.[267] The introduction of oxygen into the pitch usually leads to a minimal weight gain, whereas other reactions such as dehydrogenation, cyclization and cross-linking might compensate the weight gain by emitting CO, CO_2 and H_2O and low molecular weight hydrocarbons. As a result of the stabilization process, MP in the film changes from a thermoplastic solid to a thermosetting material, which maintains the morphology of carbon film, as it can effectively inhibit the deformation and melting of the pitch at high temperature heat treatment.[268] The oxidation condition are specific for each MP, as a large number of chemical reactions between the diverse molecular fragments can occur. Each reaction has its characteristic kinetics, products and mass change.[269]

5.3.4. Adjusting the PS content for interconnected macropore network

The film's PS volume ratio is optimized to endow a well-connected macroporous framework on the solid carbon precursor mixture of MP and PVA. After the stabilization step, the PS template is dissolved in toluene within 1 hour, leaving the molded carbon structure of MP and PVA intact (Figure 28 upper row). The films containing 64% (1.05 g) and 68% (1.25 g) PS

exhibit a lack of pore connectivity, particularly evident in the uppermost layer, despite having interconnected pores within the film bulk phase. Lower PS contents in the film are also studied (Figure A3). According to the theory of close-packing of equal spheres, 74% represents the maximum volume occupied by sphere of equal size. Remarkably, the film with 75% PS (1.64 g) confirms this theory, resulting in a macroporous network omnipresent in the film (Figure 28 c)).

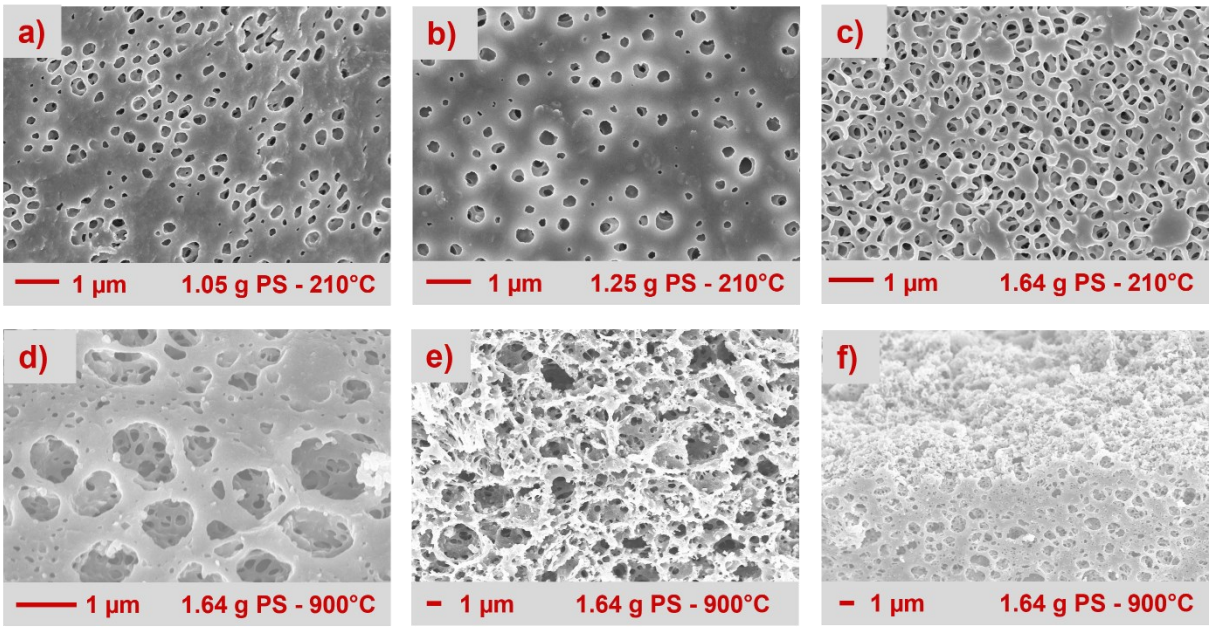


Figure 28. Upper row: Films with different proportions of PS a) 1.05 g, b) 1.25 g and c) 1.64 g after the oxidative stabilization step at 210°C and subsequent dissolution of the PS template. Bottom row: Film with 1.64 g PS carbonized at 900°C with d) top view, e) cross section view and f) edge view.

The pore structure is preserved after carbonization in nitrogen atmosphere at 900°C. Even though on the surface the macropores are coalescing to larger pores (Figure 28 d)), the interpenetrating channel network remains unaltered as can be seen from the cross-sectional and edge imaging analysis (Figure 28 e),f)). As a consequence of the carbonization step, the previously resistive film transforms into an electron conductive support with a value of 3.02 S/m (Table A4). An essential characteristic for the film suitability as cathode in actual MEA is flexibility. Notably, a lower stabilization temperature of 210°C resulted in carbon fibers with the highest modulus[261], a factor considered for the selection of the stabilization temperature.

5.3.5. The effect of heating protocol and carbonization atmosphere on the film properties

The heating rate has a decisive effect on the brittleness of the carbonized mesophase pitch carbon films.[270] While 0.5 C°/min and 1 C°/min limited the bendability of the film, the heating rate of 0.1 C°/min enabled greater flexibility (Figure A4).

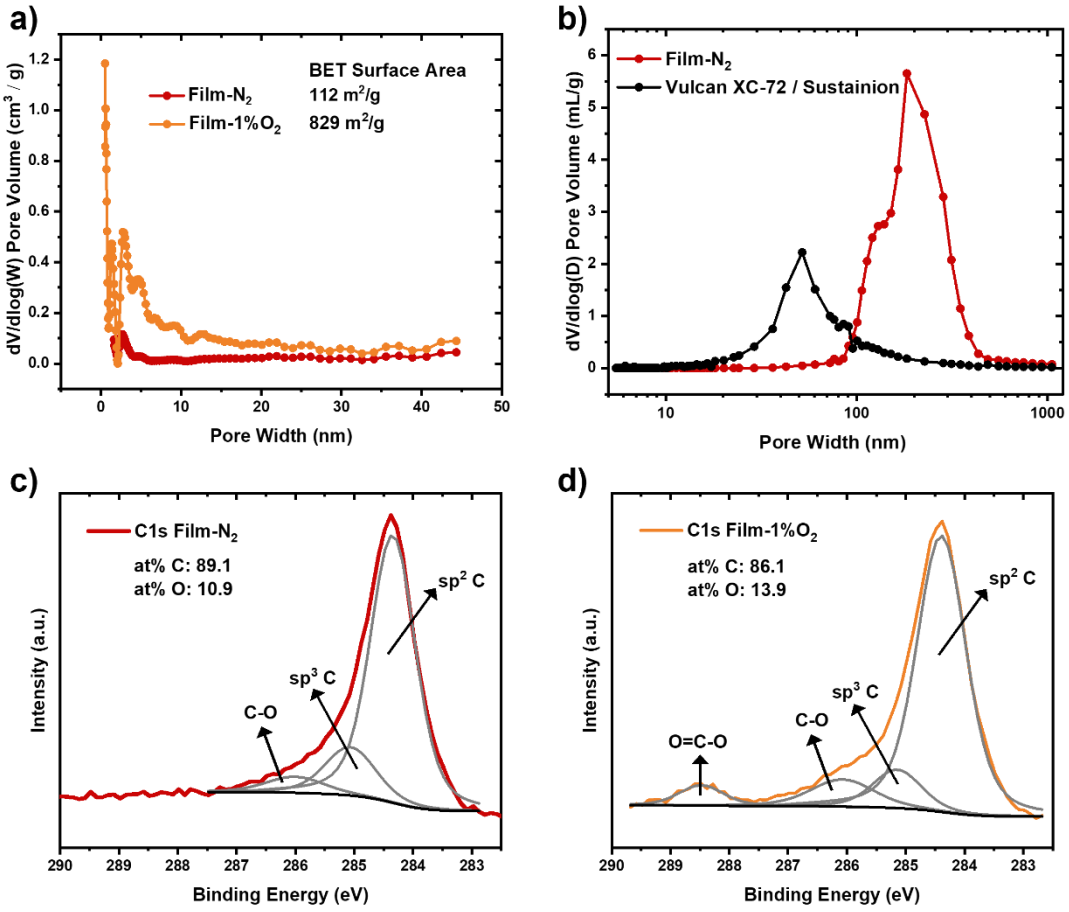


Figure 29. a) Pore size distribution in for micro- and mesopore range obtained by nitrogen adsorption. b) Pore size distribution for cathodes based on Film-N_2 and Vulcan XC-72 / Sustainion obtained by MIP. XPS spectra of the C1s for the film carbonized in c) N_2 and in d) 1% O_2 /99% N_2.

The composition of the carbonization atmosphere can modify the pore structure and elemental surface composition of the macroporous carbon film.[271] The microporosity of carbon materials can be expanded by the application of physical or chemical activation.[272] For physical activation, an oxidizing gas (O_2, CO_2) can be introduced in the temperature range of 600-1200°C to create microporosity. For chemical activation, KOH, H_3PO_4, $ZnCl_2$ are mixed with carbon material before carbonization. However, the purification of the products is required for

most chemical activation agents. Carbonization of the macroporous film under a nitrogen (N_2) atmosphere yielded a BET surface area of 112 m^2g^{-1}, primarily originating from macropores as evidenced by Mercury Intrusion Porosimetry (MIP) analysis (Figure 29 b)). The film had a porosity of 79% as determined with MIP. The nitrogen adsorption data indicated a lack of pores within the mesopore range (Figure 29 a)). Introducing a 1% O_2 dosage into the N_2 atmosphere during the carbonization led to a remarkable increase of the BET surface area to 829 m^2/g owing to a substantial rise of the micropore volume (Figure 29 a)). The high resolution C1s spectra for the film carbonized in nitrogen (Film-N_2) and the film carbonized with a 1% dosage of O_2 in N_2 atmosphere (Film-1%O_2) were deconvoluted.[273,274] (Figure 29 c), d)) Both spectra exhibit three common peaks. The peak centered at 284.5 eV corresponds to aromatic (sp^2) carbon bonds. The peak at 285 eV can be assigned to sp^3 carbon bonds, which is slightly decreased for the Film-1%O_2 compared to the aromatic peak, since aliphatic side chains are more reactive than the aromatic structures.[261] The peak at a binding energy of 286 eV is indicative of oxygen functional groups (C-O) on the carbon surface. An additional peak at 288.5 eV for carboxy fragments (O-C=O) is detected for the Film-1%O_2 sample (Figure 29 d)), which is absent in C1s spectrum of the Film-N_2. Quantitative analysis reveals that the Film-N_2 sample contained 89.1 at% carbon and 10.9 at% oxygen. As a consequence of the exposure to 1% oxygen during the carbonization, the degree of carbon oxidation for the Film-1%O_2 sample was higher, as reflected also by an increased proportion of oxygen of 13.9 at% besides the abovementioned additional peak at 288.5 eV.

5.3.6. RDE study of the ORR performance of the ball-milled film

The suitability of the carbon film as support for molecular catalysts in the oxygen reduction reaction was initially screened with the rotating disk electrode (RDE). Conventionally, inks are drop casted on a glassy carbon electrode tip for RDE measurements. For this purpose, the carbon film supports are ball-milled into a powder, which can be dispersed in an ink with Nafion binder. Unfortunately, the previous macroporous structure is destroyed in this process and the products are smaller carbon particles without any discernible macroporous structure in SEM imaging (Figure A5). The ball milled (BM) supports BM-Film-N_2 and BM-Film-1%O_2 are compared to a commercial reference support Vulcan XC 72 (BET surface area: 250 m^2/g). Metal macrocyclic compounds such as porphyrins and phthalocyanines are frequently used as molecular catalysts for the oxygen reduction reaction (ORR), as they can be readily solution-adsorbed onto supports. In a previous RDE study, of transition metal phthalocyanines on Vulcan

XC 72, iron centers outperformed the other transition metals.[275] While porphyrins and phthalocyanines mimic a pyrrolic active FeN_4 site, a model complex with a pyridinic FeN_4 site recently has been characterized for the ORR (Figure 30 a)).[276]

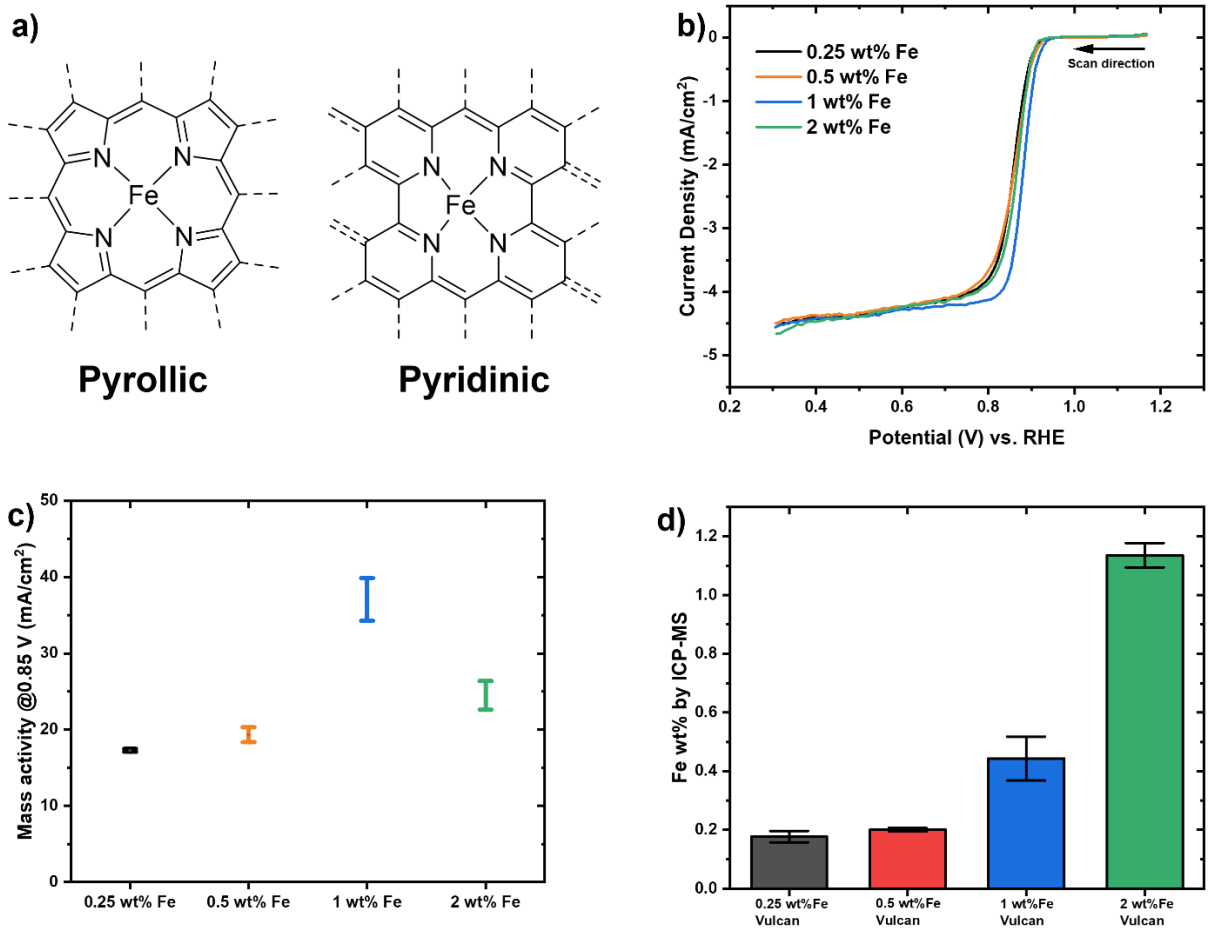


Figure A30. a) Pyrollic and pyridinic coordination structure of the active FeN_4 site. b) Optimization of the FePc loading on Vulcan XC 72 with LSV in RDE in oxygen-saturated 0.1 M KOH at 1600 rpm with a scan rate of 10 mV/s for Fe wt% loadings of 0.25 wt%, 0.5 wt%, 1 wt% and 2 wt%. c) Mass Activities at 0.85 V. d) Iron content measured by ICP-MS for the samples with different Fe wt% loading.

The disadvantage of molecular iron phthalocyanine (FePc) is its susceptibility to degrade in acidic environment.[277] Three demetallization processes of FePc were identified including the electrochemical oxidation of the ligand ring at high potentials (> 0.65 V vs. RHE), Fenton reagents (between 0.6 and 0.2 V vs. RHE) and hydrogen peroxide at lower potentials.[278] By heat treatment at temperatures (≥ 900°C) of FePc/C, a more stable catalyst can be obtained.[279] However, at high temperature FePc is converted to a heterogeneous mixture of active site structures including iron single sites coordinated to nitrogen (Fe-N_4), metallic iron, and iron oxide (Fe_3O_4) nanoparticles.[280,281] As a consequence of FePc's instability in acidic electrolytes,

the majority of studies with FePc are conducted at alkaline pH.[282] The effect of the support on the ORR performance can be easily elaborated with macrocyclic molecular catalyst, because the parameter of type of active sites can be kept constant due to their homogeneous nature.[283] It is important to quantify the FePc weight loading in order to take the effect of the number of active sites into account. The FePc loading on reference support Vulcan XC 72 was optimized (Figure 30 b)). Besides electron transport to the active sites, the main role of the carbon support is to disperse the molecular catalyst for increased availability of the active sites by preventing aggregation, a tendency that macrocyclic molecular catalysts without support show.[284] The 1 wt% Fe sample showed the highest mass activity, whereas the other iron loadings had mass activities below 30 Ag^{-1} (Figure 30 c)). The iron content of the sample with experimentally weighed FePc for 1 wt% Fe was verified as 0.45 ± 0.07 wt% Fe with ICP-MS (Figure 30 d)). It is suspected that for lower FePc loadings, the support is sparsely covered with FePc active sites. In contrast, at higher FePc loading (2 wt% Fe) active sites might be buried in molecular aggregates leading to reduced active site exposure.

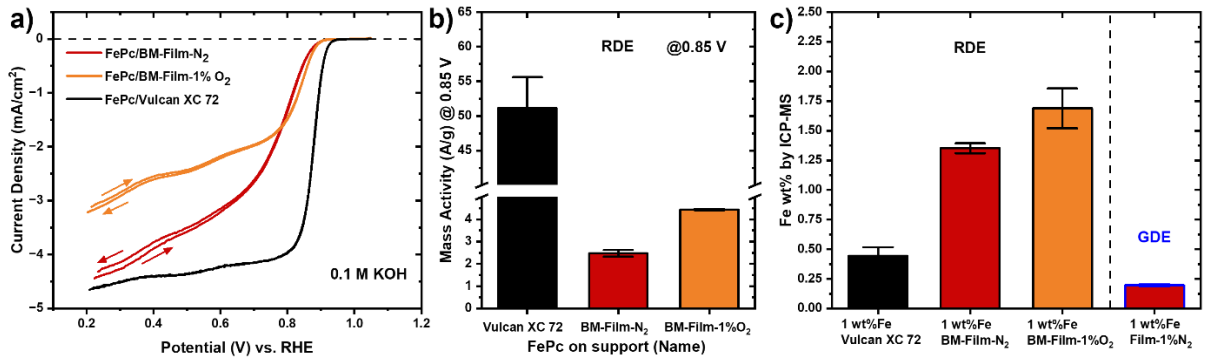


Figure 31. a) Cyclic voltammetry of ball milled film supports (BM-Film-N_2, BM-Film-1% O_2) with model active site FePc compared to Vulcan XC 72 in oxygen-saturated 0.1 M KOH at 1600 rpm. (Loading: 200 µg/cm^2) b) Overview of the mass activities at a potential of 0.85 V in the RDE configuration. c) Iron content measured with ICP-MS for the catalyst prepared by physisorption of FePc on the respective powders for RDE and the Film-1%N_2 for GDE.

The cyclic voltammograms (CVs) of FePc/BM-Film-N_2 and FePc/BM-Film-1%O_2 in oxygen-saturated 0.1 KOH are compared with FePc 1wt% CB (Figure 31 a)). In the kinetic region, FePc 1wt% CB had the lowest overpotential, followed by FePc/BM-Film-1%O_2 and slightly higher BM-Film-N_2. Minor improvement of FePc/BM-Film-1%O_2 compared to BM-Film-N_2 FePc 1wt% might be due to the slightly higher oxygen surface content. Axial coordination of FePc

to an oxygen group on the support enables better oxygen adsorption and activation abilities.[285] Vulcan XC 72 achieved the highest diffusion-limited current density, whereas the diffusion-limiting current density was low for FePc/BM-Film-1%O_2, presumably because of lack of porous structure after ball milling process. Furthermore, the mass-activity of the three supports at 0.85 V (vs. RHE) was evaluated. The mass activity at 0.85 V (vs. RHE) for FePc 1wt% Vulcan XC 72 with 51.15 $A g^{-1}$ was approximately ten times greater than FePc/BM-Film-N_2 and FePc/BM-Film-1%O_2 with both having values below 5 $A g^{-1}$ (Figure 31 b)). Despite twofold higher FePc loadings for the BM-Films as determined with ICP-MS (Figure 31 c)), the BM-Films failed to match the performance of the reference Vulcan XC 72 support. It can be concluded that the selection of the support for molecular catalysts is crucial for improving the ORR activity, which is in agreement with literature.[286] The surface chemical properties and electronic structure of the carbon support interact with the electronic structure of the molecular catalyst adsorbed, and thus modifying the adsorption energy of the ORR intermediates. While a detailed DFT study is beyond the scope of this work, the adsorption energies reaction participants in the ORR on FePc on Vulcan XC 72 have been calculated elsewhere.[287]

5.3.7. ORR performance at high current densities of the macroporous carbon film cathode in GDE

Even though non-heat-treated molecular catalysts with exceptional performance have been reported in the past, they were rarely tested in a fuel cell. In 2012, the performance of catalyst coated Tokuyama A901 membranes with phthlocyanines with different metal centers supported on Vulcan XC 72 were compared in an AEMFCs. While keeping the cathode loading constant at 2 mg/cm^2, it was found that FePc/Vulcan XC 72 showed the poorest performance with a peak power density (PPD) of 88 mW/cm^2.[275] An optimization of the catalyst layer mass loading in the cathode, utilizing FePc supported on Ketjenblack (KCB), demonstrated that the lowest loading of 1.0 mg/cm^2 lead to improved performance. In numbers, 1 mg/cm^2 loading with a PPD of 108 mW/cm^2 surpassed the loadings of 2.0 mg/cm^2 and 3.0 mg/cm^2.[283] Fluorinated iron phthalocyanine (FeFPc) supported on high surface area carbon BP2000 (FePPc@BP2000, 2 mg/cm^2) exhibited the highest PPD with 166 mW/cm^2 of molecular catalysts implemented on the cathode in AEMFCs.[288]

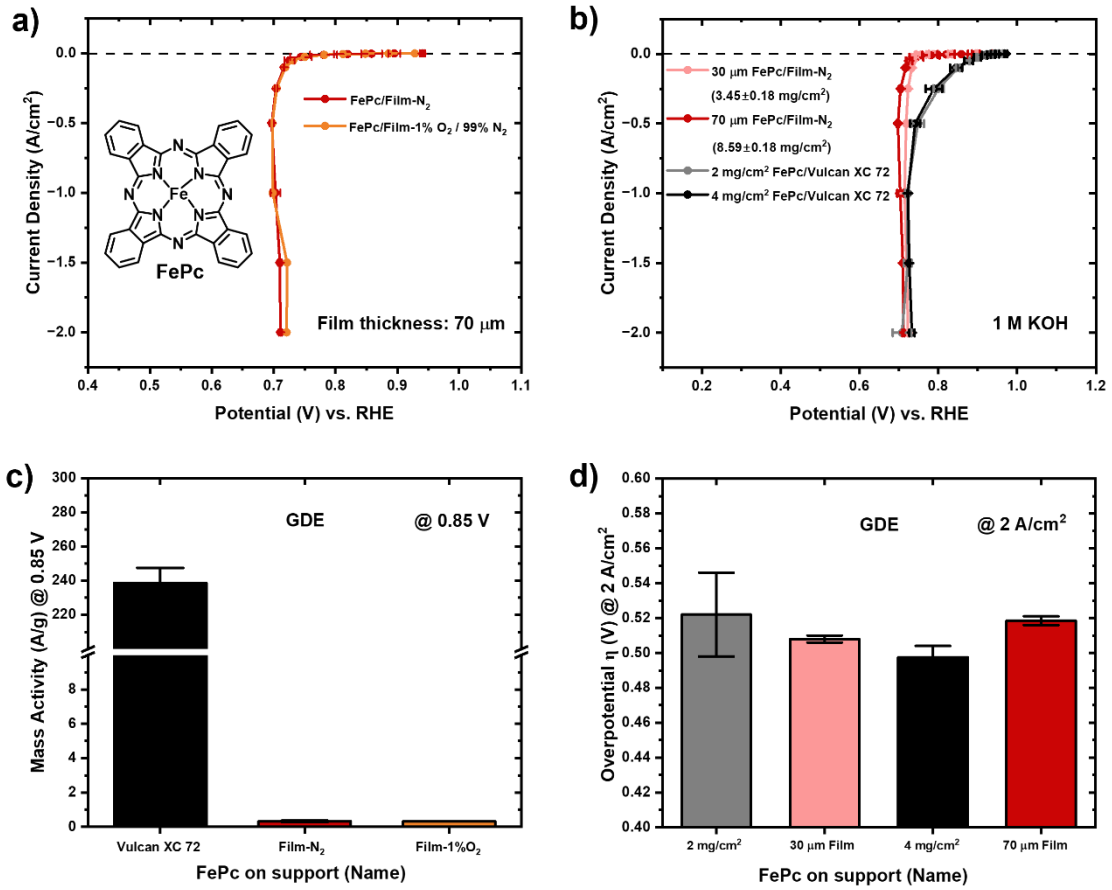


Figure 32. a) Oxygen reduction reaction polarization curves measured with the GEIS protocol for FePc supported on macroporous carbon films, Film-N_2 and Film-1%O_2/99%N_2, with the same thickness of 70 µm in 1 M KOH. b) Oxygen reduction reaction polarization curves measured for different powder and film catalyst layer loadings. c) Overview of the mass activities extracted from the polarization curve in the GDE half cell at 0.85 V. d) Overview of the overpotentials at 2 A/cm^2 for the catalyst layers tested in GDE configuration. Error bars are obtained by repeated measurements of a different sample from the same sample type.

The ORR activity study was extended from the ball-milled powder RDE study to ORR performance evaluation of the CFC equipped with FePc active sites in the small gas-diffusion-electrode (GDE) setup.[125] The advantage of the GDE setup is that much larger current densities (up to 2 A/cm^2) can be measured due to effective oxygen diffusion through the GDL. The GEIS curve of the FePc/Film-N_2 and FePc/Film-1%O_2 with the same thickness of 70 µm superimpose at low current densities. At high current densities (1.5 A/cm^2, 2.0 A/cm^2), FePc/Film-1%O_2 had a slightly lower overpotential than the FePc/Film-N_2 (Figure 32 a)). According to a modelling study, the thickness of the catalyst layer, proportional to the catalyst loading, is expected to be

a main determinant of mass transport losses in PGM-free catalyst layers.[96] The macroporous film supports have been designed with the intention to have the capability to increase the thickness of catalyst layers without suffering mass transport losses compared to conventional powder catalyst layers. The goal was to shift the pore size distribution of the macroporous pore structure for through catalyst layer mass transport toward larger pore sizes, broadening the transport channels from normal roads to highways. The macropore size distribution for the Vulcan XC 72 catalyst layer prepared with alkaline Sustainion ionomer is compared with the Film-N_2 with MIP (Figure 32 b)). The majority of macropores in the Vulcan XC 72 catalyst layer is between 40 nm and 60 nm, whereas macropores in the CFC fall into a range between 100 and 400 nm.

The effect of adjusting the thickness of the macroporous CFC (FePc/Film-N_2) for 30 µm and 70 µm was explored in GDE configuration. Notably, the 30 µm film outperformed the 70 µm slightly in all galvanostatic steps by approximately 10 mV lower overpotential (Figure 32 b)). To be able to determine the mass activities of the CFCs, catalyst layer mass loading was determined by weighing laser cut samples (Ø = 3 mm) and subsequent measuring of their geometrical electrode area in SEM (Figure 33).

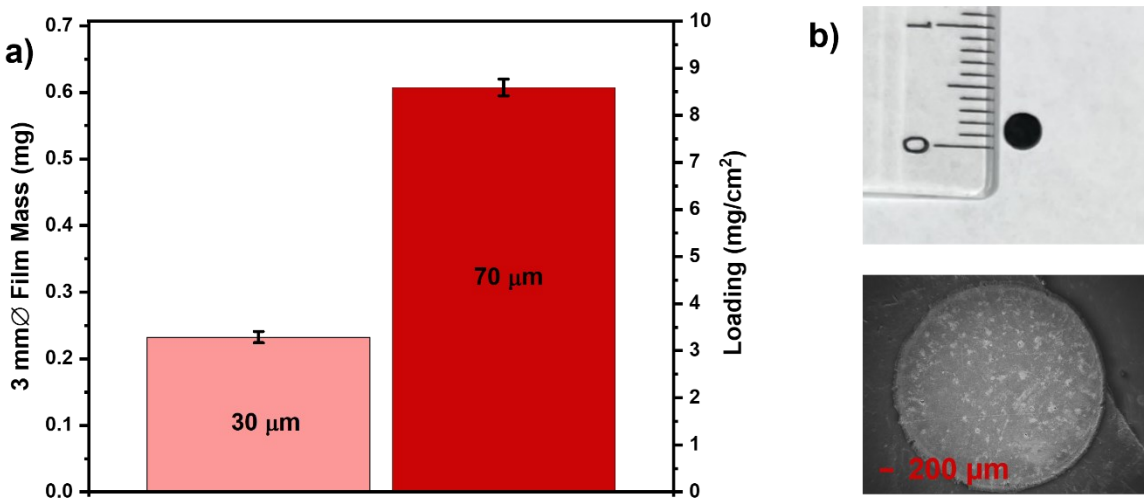


Figure 33. a) Determination of the catalyst layer mass loading of the film samples. b) Preparation of the Ø = 3 mm sample for the GDE testing with laser cutting.

Reference catalyst layers of conventional FePc/Vulcan XC 72 with loadings of 2mg/cm^2 and 4 mg/cm^2, corresponding to thicknesses of 50 µm and 100 µm, as determined with SEM cross section imaging, were prepared (Figure 34).

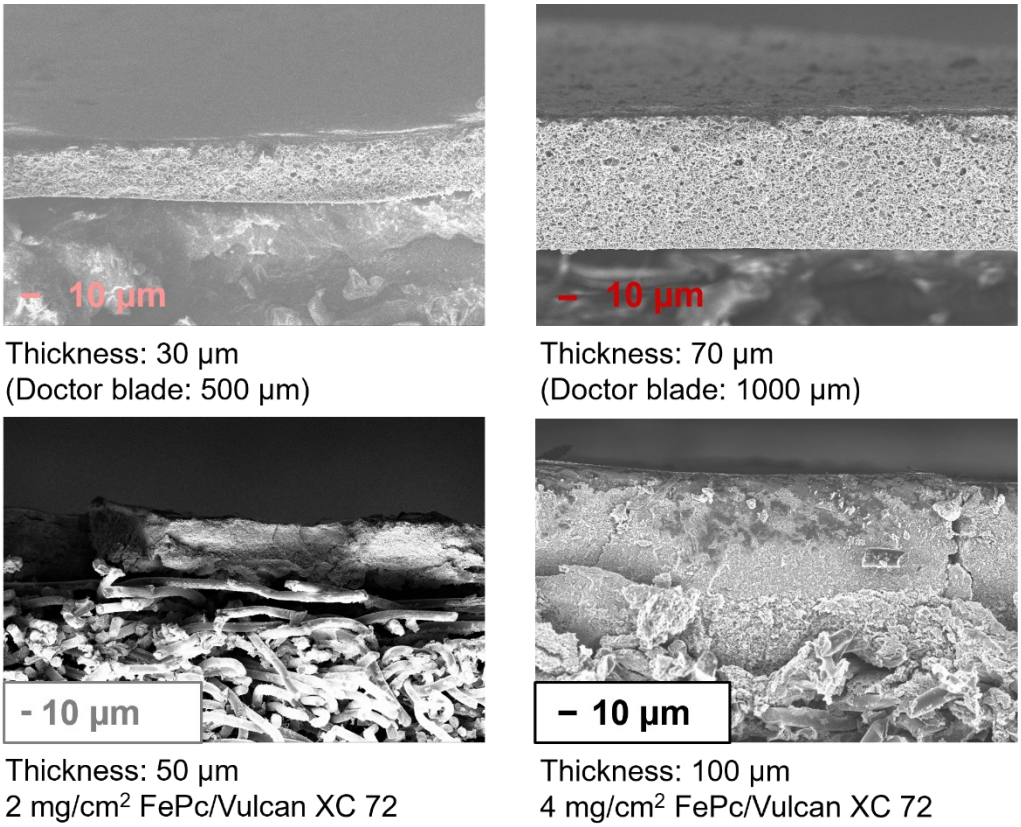


Figure 34. Determination of the catalyst thicknesses for the FePc/Film-N_2 (upper row) and FePc/Vulcan XC 72 (bottom row) cathode catalyst layers.

At low current densities, the 2 mg/cm^2 loading had lower overpotentials than the 4 mg/cm^2. At high current densities, the error in the overpotential of the 2 mg/cm^2 became large (± 24 mV), which can be potentially explained by inhomogeneous catalyst layer loadings due to hand spraying. In general, it was observed that the 4 mg/cm^2 catalyst with more active sites performed better at higher current densities above 1 A/cm^2. In the entire current range, the powder based catalysts layer of 4 mg/cm^2 outperformed the CFCs except for the data recorded for the 2 mg/cm^2. The mass activity for the samples tested in GDE were extracted at 0.85 V (vs. RHE), at which the current is mostly controlled by ORR kinetics (Figure 32 c)). The mass activities for the CFCs were below 1 A/g, surpassed by the FePc/Vulcan XC 72 catalyst layers with a mass activity averaging at 239 A/g by far. This stark difference is consistent with the results from RDE at a potential of 0.85 V (vs. RHE), even though the FePc/Vulcan XC 72 had a five times higher mass activity in GDE. Deviation of the mass activities between GDE in fuel cell studies and RDE measurements have been reported previously. At high current density of 2 A/cm^2, where mass transport losses are expected to be most significant due to highest oxygen consumption, the thickness of the catalyst layer seemed not to influence the mass transport for either sample class, Vulcan XC 72 and Film-N_2. The average overpotentials at 2 A/cm^2 for the

four types of samples fell into a range of 50 mV difference, which is within the error range (Figure 32 d)). It has to be noted that the established preconditioning protocol for powder catalysts might not be applicable to carbon films, as a repetition of the steps at high current densities in a second round lead to an improvement of 50 mV except for the 2 A/cm^2 value, which improved by 10 mV (Figure A6).

5.4. Conclusion

This study is a starting point when it comes to macropore engineering of freestanding PGM-free CFCs. The limitations of standard slurry casting and spraying with regards to the control of the macropore structure of the final catalyst layer can be overcome by engineering a film with interconnected pore network. The template for the pore network is chosen to be temperature compatible with the stabilization step and the decomposition of the film precursors. Polystyrene fulfilled the thermal compatibility and stands out due to rapid removal among the hard templates dominated by SiO_2 and Al_2O_3. The PS content is adjusted for interconnectivity of the macropores confirming the theory of closed packed spheres. Apart from SEM imaging, MIP is an essential tool, with little application in the field, to investigate the bulk phase porosity. Pore analysis investigation of nitrogen adsorption and MIP could be complemented with nano X-ray computed tomography in future work.[242] The conductivity of the carbon scaffold proves that all active sites in the film can be supplied by electrons. Oxygen activation during carbonization (1% O_2) can enhance the micropore structure and tune elemental surface composition for marginal improvement in ORR kinetics. The obvious lack of mesopores is worth to be addressed, despite recent findings that mesopores in Fe-N-C catalysts might not be necessary for efficient oxygen supply as the magnitude of decrease in current density when switching from O_2 to air is comparable for catalyst with marginal and with high mesopore volume content.[81] Nevertheless, mesopores might be beneficial for the macroporous carbon film developed, as the BET surface is quite low compared to most PGM-free powder catalysts.[289] Likewise, carbon supports with accessible mesopores are implemented in industrially PEMFC by GM[89] and Toyota[12]. It is expected that mesopores in the side wall of the macropores are going to increase the surface area to host a multitude of active sites. The selection of a second template for the creation of mesopores has to be compatible with the solvent system of the slurry and the temperature for the stabilization step of mesophase pitch. Among a huge library of soft templates, PS spheres with diameter of 10 nm or poly(isobutylene)-b-poly(ethylene oxide) polymer for 20 – 25 nm[290] are options for exploration. As model molecular FePc catalyst is restricted to studies in alkaline environment, a CFC can be designed with integrated FeN_4

sites on the carbon surface for the operation at acidic pH. Two concepts worthy for exploration for the deposition a nanometer thin nitrogen-rich carbon film on the carbon surface of the porous film. In liquid phase, aniline could be electrodeposited onto the porous carbon film.[291] Chemical vapour deposition of a carbon-nitrogen compound can also access the pores to cover the entire porous CFC with nitrogen doping. Subsequently, iron sites can be loaded to available nitrogen coordination via the methanol reflux method. These approaches are considered to prepare Fe-N-C CFC for testing in acidic electrolyte. Future electrochemical characterization could aim to specifically target the mass transport properties with oxygen limiting current measurement in GDE[135], electrochemical impedance spectroscopy (EIS) assessment of the mass transport resistance[292], and effective diffusivity measurement with help of sensor-integrated cell.[241]

5.5. Future work: Introducing mesopores

The option of introducing a second level of porosity was briefly investigated. A template with a smaller size than polystyrene was selected to expand the surface area of the macroporous structure with additional smaller sized pores in the macropore walls of the film. Diblock copolymer Poly(isobutylene)-b-poly(ethylene oxide) (PIB3000) (Figure 35 a)) self-assembles into micelles with an average size of 50 nm (Figure 35 c)) and is classified as mesopore template. Due to its micelle formation in aqueous solutions, it is a compatible ingredient to the aqueous dispersion of PS and PVA. In addition, the thermal decomposition of PIB3000 started above 290°C (Figure 35 b)) and therefore, its stability and templating function at the temperature of the oxidative stabilization (210°C) step is ensured.

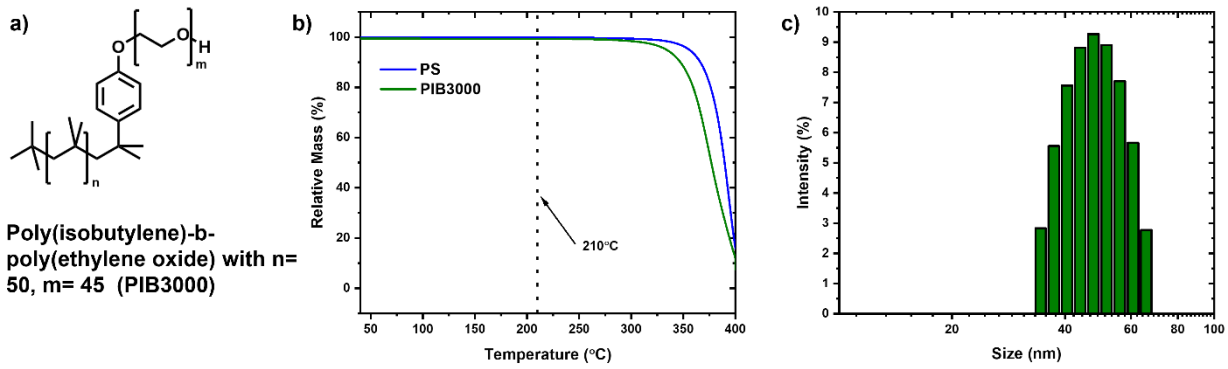


Figure 35. a) Molecular structures of PIB3000. b) TGA of PIB3000. c) Micelle size distribution of PIB3000.

For the preparation of macro- and mesoporous templated film, the template weight composition for the respective macropore templating agent PS and mesopore templating agent PIB3000 was set to 6:1. The established synthesis protocol was carried out and due to the limited amount of product, TEM was chosen instead of gas sorption to validate the presence of mesopores (Figure 36).

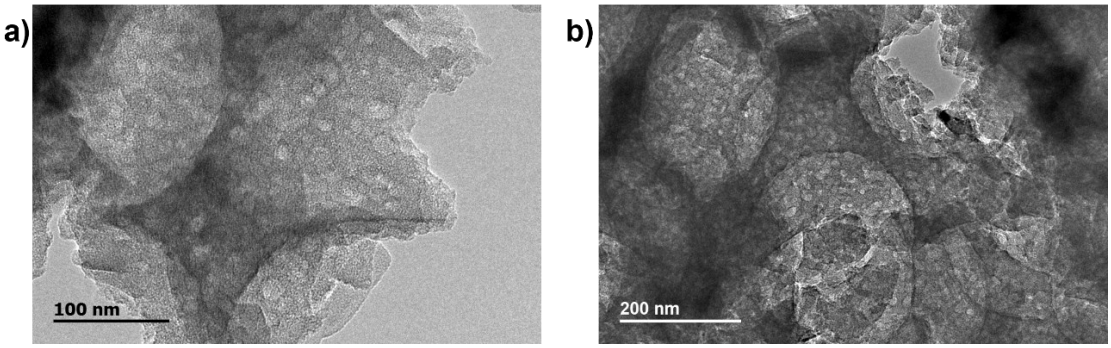


Figure 36. a) and b) TEM images of PS+PIB3000 templated macro+mesoporous carbon film.

The macroporous-mesoporous carbon film was tested as support for FePc for the ORR in the GDE. Remarkably, the FePc/Macro+Mesoporous film outperformed the FePc/Macroporous film at all galvanostatic steps (Figure 37). The reason for the improved performance is suggested to originate from the increased number of accessible active sites on the larger surface area. These initial results with a second smaller poresize level are an appealing foundation for future projects with the established carbon film structure.

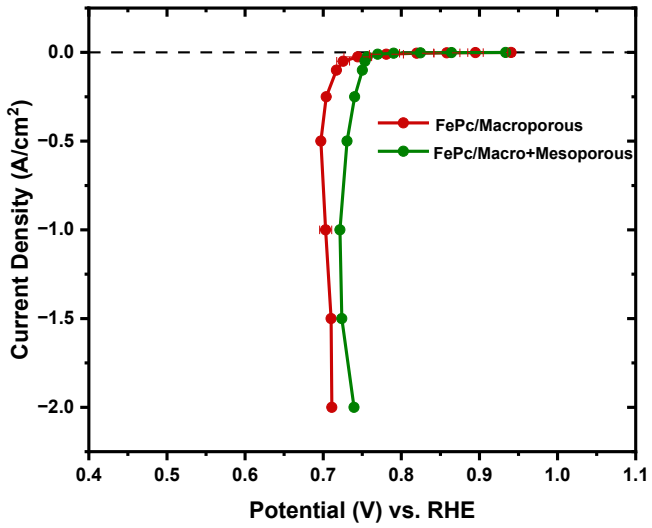


Figure 37. ORR polarization curves in GDE half cell of FePc supported on Macroporous and Macroporous+Mesoporous film.

6. Combinations of Commercial Alkaline Ionomers and Membranes for the Oxygen Reduction Reaction in Half-Cell Studies in Gas-Diffusion-Electrodes

6.0. Contributions

Ziyang Liu helped in the ink preparation, sprayed the catalyst layers for the sorption measurements, and contributed to the GDE measurements. Silvia Favero provided the data of the nitrogen and water sorption measurements. Angus Pedersen spray coated the GDE samples. Francesco D'Acierno recorded the USAXS/SAXS of the inks at the synchrotron.

6.1. Abstract

Hitherto, research into alkaline exchange membrane fuel cells (AEMFCs) lacks an accessible commercial benchmark anionomer and membrane such as a Nafion™ analogue in proton-exchange membrane fuel cells (PEMFCs). Three commercial alkaline exchange ionomers (AEI) are scrutinized for that role in combination with a commercial platinum-group-metal free (PGM-free) Fe-N-C (Pajarito Powder) catalyst for the cathode. Initial rotating disc electrode (RDE) benchmarking of the Fe-N-C catalyst's oxygen reduction reaction (ORR) activity using Nafion™ in alkaline electrolyte seems to neglect the restricted oxygen diffusion in the AEIs, and is recommended to be complemented by measurements with the same AEI as used in the AEMFC testing. Evaluation of the catalyst layer (CL) in a Gas-Diffusion-Electrode (GDE) setup prior to the integration of CLs into AEMFCs offers a technique to assess the performance without the interference of device-level water management. Blending of a porous Fe-N-C catalyst with different types of AEI yields CLs with different pore size distributions. The CL with Piperion® was retaining the highest proportion of the original BET surface area of Fe-N-C catalyst. The water adsorption capacity was also influenced by the AEI, with Fumion FAA-3® and Piperion® have equal high capabilities surpassing Sustainion®. Finally, the choice of the membrane influenced the ORR performance as well, where the low hydroxide conductivity of Fumion FAA-3® in the room temperature experiments mitigated the ORR performance irrespective of the AEI in the CL. The best overall performance at high current densities was shown by Piperion® AEI matched with Sustainion® X37-50 AEM.

6.2. Introduction

For the last sixty years research in low temperature fuel cells focused on the proton-exchange-membrane fuel cells (PEMFCs) benefiting from the development of high performance Nafion™ membranes by DuPont in 1961. Due to its excellent proton conductivity of 231 mS/cm (Nafion 117 at 80°C)[293], Nafion™ established itself as benchmark and membrane of choice in PEMFC research. However, Nafion™ is based on expensive perfluorinated polymer backbones functionalized with sulfonic acid groups. In 2023, the European Chemicals Agency (ECHA) proposed a ban for per- and polyfluoroalkyl substances, including Nafion™, in Europe.[294] This potential restriction on Nafion™ could benefit hydrocarbon-based anion conducting polyelectrolytes (ACP), which are cheaper and safer to produce.[44] The progress in ACP development over the past twenty years has accelerated research on alkaline exchange membrane fuel cells (AEMFC).[295] In contrast to PEMFC, AEMFCs benefit from catalysts higher oxygen reduction reaction (ORR) kinetics in alkaline medium.[48,296,297,298] Therefore, the catalysts can be chosen from a larger library of materials, without resorting to rare and expensive platinum-group-metals (PGMs). The critical component is the ACP applied as ionomer (AEI) in the catalyst layers (CLs) and as membrane (AEM) between anode and cathode.[299] However, the requirement on the ACP differs depending on the function as either AEI or AEM. The commonality is that both need to satisfy the ion conductivity for hydroxide ion (OH^-) transport. AEMs are positioned between anode and cathode, and also act as gas barrier to block hydrogen and oxygen cross-over, and should have low H_2 and O_2 permeabilities (<10 x 10^{-17} mol (cm s Pa)$^{-1}$).[300] In contrast, AEI are a component in anode and cathode catalyst layers acting as binder to attach the catalyst in the catalyst layer. In addition, AEIs create a triple-phase boundary (TPB) between catalyst (solid), water educt and product (liquid) and gaseous reactions (gas). AEMs require good gas barrier properties and limited water contents to minimize membrane swelling, while AEIs need high water permeability, fast oxygen transport, and minimal blocking of electrocatalysts active site accessibility. Nevertheless ionomers are produced by dissolving the respective ACP, often with the same molecular structure as the AEM, in a mixture of solvents.[301] Ideally, the development of AEIs and AEMs should take place separately to design the properties of the material for the specific function as either AEI and AEM.[302] The progress in materials development for AEIs[42] and for AEMs[303] has been reviewed recently. The rapid development lead to scale up and commercialization of ACP technologies. A few commercially available AEIs and AEMs can be obtained without the necessity to sign NDAs and therefore, are accessible for publishable unbiased academic studies. For this work, the AEI and AEMs products listed from the brands Fumasep®, Versogen™ and

Sustainion® with their specific molecular unit structures have been selected (Figure 38).

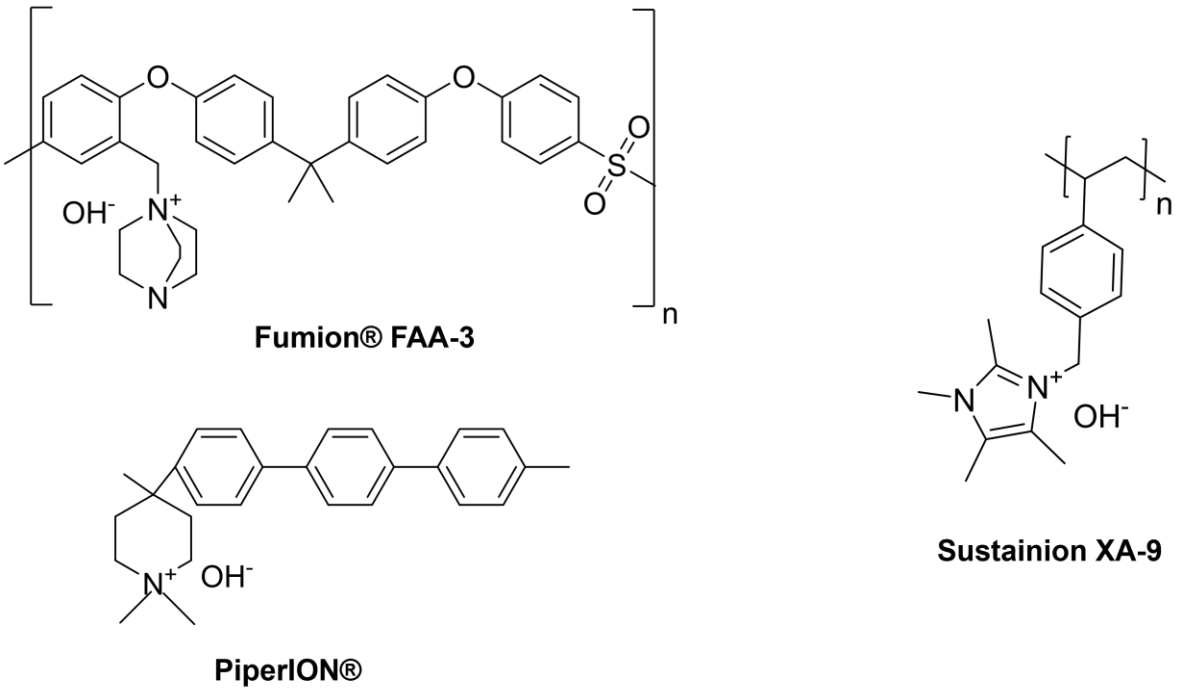


Figure 38. The molecular structures of commercial anion exchange ionomers (AEIs).

In AEMFCs, PtRu/C is usually used as the anode benchmark catalyst, while Pt/C is used at the cathode. As the ORR is more favorable with faster electrochemical kinetics in alkaline, a lower catalyst loading can be used in AEMFC. With the recent availability of highly anion conductive AEMs, PGM-based AEMFCs achieved a breakthrough into peak power densities (PPD) > 2 W/cm^2 (Table A3). A way for cost-cutting is to reduce the PGM loading by substituting the cathode PGM-catalyst with a PGM-free catalyst. The most prominent and best performing PGM-free catalysts in AEMFC are Fe-N-C catalysts.[232] Only a few Fe-N-C cathodes in AEMFCs exceeded PPD level of 1 W/cm^2 [50] (Table A4). The first commercially available and probably most investigated Fe-N-C catalyst is from Pajarito Powder. Successful water management addressing the anode flooding and cathode drying is the key to break through into high PPDs and long term cell stability. Typically, the prevention of flooding through water diffusion from anode to cathode is facilitated by adjusting external parameters such as asymmetric pressure[304], inlet relative humidities[305], and the anode and cathode dew points.[306] Despite being simple and effective, these engineering solutions only compensate for the lack of a systematic catalyst layer design. The ideal CL inherently controls the quantity, location and diffusion of water by a pore network and hydrophilic/hydrophobic domains of the AEI. Therefore, it would be valuable to optimize the CL in isolation before proceeding to the

integration of the CL into a MEA. Half-cell studies of CLs in gas-diffusion-electrodes (GDE) offer an intermediate opportunity to refine an isolated CL. The utilization of the catalyst can be maximized by tailoring the I/C composition, the efficiency of water and O_2 mass transport can be enhanced by fine-tuning the microstructure via the choice of solvents in the ink[307], and the optimal total loading of catalyst can be determined. The door towards alkaline studies in a GDE setup was opened with a study of commercial Aemion™ ionomer with Pajarito Powder with focus on the activation time of the CL and catalyst durability.[308] Several GDE setups have been established and benchmarked.[124] The updated version of the small GDE with Luggin capillary directly on the membrane reduces solution resistance less than 0.1 Ω.[125]As a result, the voltage error is minimal and can easily be corrected.

After introduction of the small GDE cell into our laboratory[309], an extensive study on cathode catalyst layers based on Fe-N-C from Pajarito Powder and the three AEIs Fumasep® Fumion FAA-3 (abbrev.: FI), PiperION® (abbrev.: PI), and Sustainion® (abbrev.: SI) is presented in this work. In contrast to the Aemion™ study, in the GDE employed in this work the CL is separated with a membrane from the liquid electrolyte compartment. The advantage of this configuration is that the flooding of the CL is prevented. In addition the effect of the membranes Fumasep® FA-3-50 (FumaTech) (abbrev.: FM), PAP-TP-85® (Piperion) (abbrev.: PM) and X37-50® (Sustainion) (abbrev.: SM) on the ORR performance is also elaborated by cross-combining the selected AEIs with the AEMs (Figure 39).

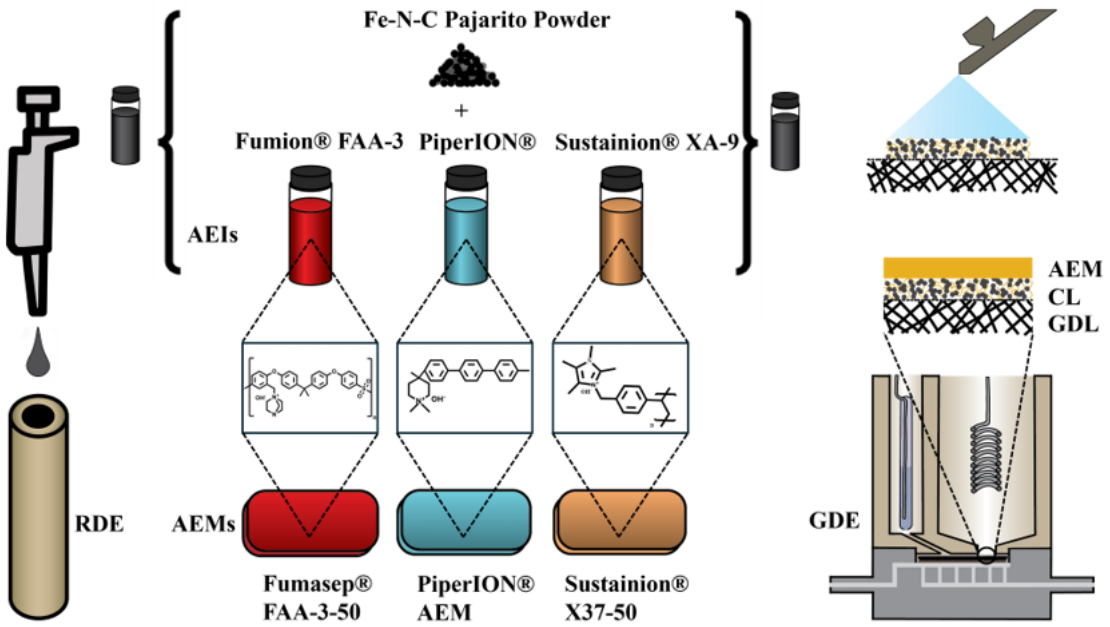


Figure 39. Inks based on commercial Fe-N-C Pajarito Powder and one of three types of commercial AEI respectively were either drop casted on the RDE or sprayed onto a gas-diffusion layer. The gas-diffusion-electrode is attached to a commercial AEM and tested in a gas-diffusion-electrode half-cell.

Initially, the effect of the ionomer interaction with Fe-N-C catalyst was characterized ex-situ in rotating disc electrode (RDE) study combined with SAXS study. Then, the sprayed catalyst layers were characterized for their ORR performance in the small gas-diffusion-electrode (GDE) cell, and correlations between the ORR performance and catalyst layer morphology in SEM, catalyst layer pore size distribution and water uptake were drawn. The gas-diffusion-properties were also characterized by O_2 limiting current measurements. The choice of membrane with its intrinsic hydroxide conductivity also impacted the performance.

6.3. Results and Discussion

6.3.1. Rotating Disc Electrode (RDE) study of AEIs and SAXS measurement of RDE inks

The RDE is the most conventional method to benchmark the catalytic activity in the kinetic region. Routinely, Fe-N-C catalyst are dispersed in an ink composed of ionomer and solvents and that ink is drop casted on glassy carbon electrode with a loading commonly in the range of 200 µg/cm^2 - 800 µg/cm^2. Recently, the analysis of RDE studies of Fe-N-C catalysts observed

that the metric of half-wave potential increases as the RDE catalyst loading is increased. It is concluded that the mass activity is the better metric for intrinsic activity than the half-wave potential.[53] Lower loadings are recommended, as the high loadings may diminish the mass activity due to transport losses. Therefore, a catalyst loading of 200 μg/cm^2 was chosen in this work. Despite, the original molecular structure of Nafion designed to be a proton conducting ionomer, Nafion ionomer is used in the majority of RDE studies in alkaline electrolyte.[310,311] The ionomer may not be necessary for hydroxide ion conduction in liquid electrolyte ex situ studies in RDE, but it is relevant for the testing of the catalyst in an MEA. Therefore, it is questionable whether the RDE experiments should not be carried out in an ionomer environment that partially simulate the catalyst layer in MEA to be able to translate the results from RDE to MEA more easily. Therefore, the Fe-N-C catalyst was investigated with three commercial available alkaline ionomers, including FI, PI, SI in the RDE and compared to Nafion (Figure 40 a)). Even though the catalyst loading and ink composition has been kept constant for all ionomers, the cyclic voltammograms in oxygen saturated 0.1 M KOH were quite different. In the kinetic region, the combination with Nafion had the best activity followed by Fumion, which was closely followed by Sustainion. The combination of the Fe-N-C catalyst with Piperion showed the worst kinetic performance. It has already been reported that the use of Fumion instead of Nafion in RDE lead to a lower kinetic current density with Fe-N-C and metal-free catalysts.[312,313] The mass activities (MA) at 0.85 V ranked from the highest with Nafion (30.35 A/g), to Fumion (10.90 A/g), to Sustainion (9.65 A/g) to the lowest with Piperion (2.05 A/g). A same trend was found for the limiting current density at 0.2 V, the highest limiting current was found with Nafion (5.18 mA/cm^2), then Fumion (3.78 mA/cm^2), then Sustainion (3.68 mA/cm^2) and last Piperion (2.98 mA/cm^2). Normally, the diffusion limiting currents at around the theoretical value of 5.97 mA/cm^2 at 1600 rpm on a 5mm diameter working electrode in 0.1 M KOH are expected.[314] Obviously, the AEI were blocking the transport of oxygen to the catalysts' active site, whereas in the case of Nafion the oxygen transport was not restricted.

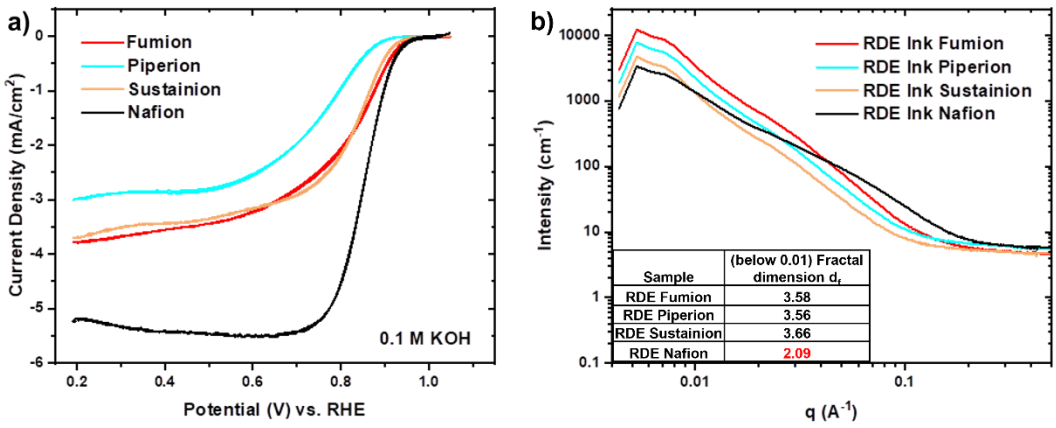


Figure 40. a) Cyclic voltammetry (CV) with a 10 mV/s scanrate of Fe-N-C Pajarito Powder catalyst with respective ionomer Fumion, Piperion, Sustainion and Nafion (33% Ionomer / 66% Catalyst) in oxygen-saturated 0.1 M KOH. Catalyst loading: 200 µg/cm^2. b) SAXS scattering curves of catalyst inks for RDE.

The RDE inks were investigated in SAXS to gain insights into the agglomerates of ionomer and catalyst in the ink. The scattered intensity (I(q)) was plotted versus the scattering vector (q) for the four different inks (Figure 40. b)). The power-law scaling exponent of the intensity at low q (< 0.01Å^{-1}) in $I(q) \sim q^{-d_f}$ is called fractal dimension d_f.[94] The fractal dimension represents the agglomerate structure, where a larger d_f indicates a higher level of agglomeration. As listed in the table, the d_f values for the AEI (3.58, 3.56, 3.66) were at least 70% larger than the one obtained for Nafion (2.09). These values suggest that the AEI inks contain larger agglomerates than the ink based on Nafion. Electrochemical impedance spectroscopy (EIS) recorded at 0.85 V in oxygen at 1600 rpm showed larger diameter semi-circles at low frequencies for the AEIs compared to Nafion (Figure 41).

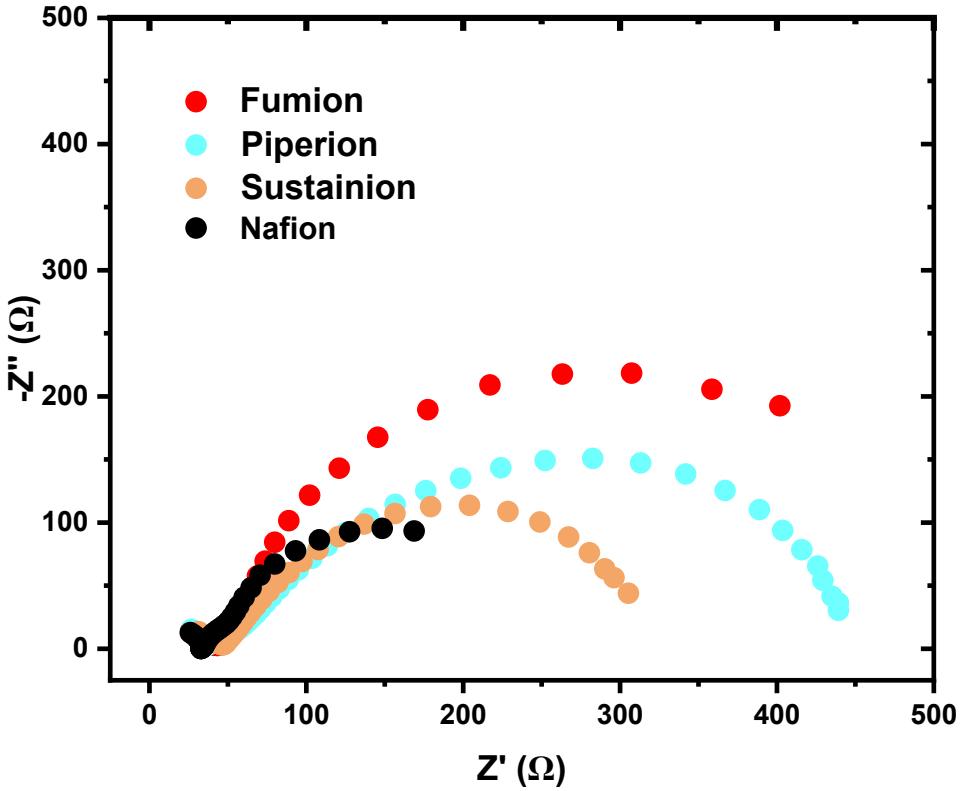


Figure 41. EIS in RDE at 0.85 V in oxygen saturated 0.1 M KOH at 1600 rpm.

An increased diameter of the low-frequency semi-circle is indicative for increased mass-transfer inhibition of oxygen from the bulk of the solution to the active sites.[315] Therefore, the EIS supported the assumption that the commercial AEIs have slower oxygen-diffusivities. The origin of lower local oxygen transport for the commercial AEIs is suspected to be found in the lack of oxygen-carrying properties of perfluorocarbons, which are present in Nafion. A comparison of an AEI, whose molecular structure is modified either with methyl ($-CH_3$) or trifluoromethyl ($-CF_3$) demonstrated that the RDE limiting current density is increased by 15% (from 4.5 to 5.3 mA/cm^2) for the fluorinated AEI.[316]

6.3.2. Preparation of the catalyst layer for Gas-Diffusion-Electrode (GDE) testing – from ink to morphology

For the GDE testing, inks with a composition (20wt% / 80wt% I/C) following the best reported performance of Fe-N-C Pajarito Powder in AEMFC with ETFE-based radiation-grafted benzyltrimethylammonium-type ionomer[50], distinct from the RDE ink (33wt% / 66wt% I/C)

composition were prepared. The GDE inks were characterized with rheology and dynamic light scattering (DLS) to gain insights of how the ink microstructure affects the catalyst layer structure. There are a lot of parameters to adjust in the ink composition including types of solvents[331], solvent ratio, concentration of catalyst and concentration of ionomer. For the sake of focus on the anionomer properties, all these parameters were kept constant and only the type of ionomer was changed. Ethanol was chosen as the solvent for the GDE ink as the technical data sheets of all AEIs state solubility in ethanol[317] or the AEI is supplied in ethanol dispersion, as it is the case for Piperion and Sustainion. In contrast to the RDE inks studied in the previous section, which can be ultrasonicated to re-disperse the ink fully before withdrawing a pipette from the ink, the dispersibility is of more importance for the inks in the GDE. The duration of the spraying of the electrode compared to RDE dropcasting is much longer, and precipitation of the ionomer or catalyst in the ink container of the spray gun should be avoided. The concentration of the catalyst in the ink is chosen to be 2 mg_{Cat}/mL (0.2 wt%), as higher concentrations caused frequent clogging of the spray gun needle.

The shear stress increased linearly with increasing with a constant slope for ethanol, slightly deviating from this linear increase at shear rates below 10 s^{-1} for the inks containing the AEIs and Pajarito Powder and the reference with Pajarito Powder in ethanol (Figure 42 a)). The straight line observed for ethanol is typical for Newtonian fluids such as this solvent without the addition of any particles. The presence of Pajarito Powder with and without ionomers in the inks caused weak shear thickening as can be seen from the minor increase of the shear stress at shear rates below 10 s^{-1}. The viscosity stayed constant in the shear rate window from 10 to 100 s^{-1} for all inks (Figure 42 b)). At lower and higher shear rates, the viscosity tended to increase. It can be concluded that the type of ionomer does not affect the viscosity of the ink. The Fe-N-C inks previously investigated rheologically investigated have been applied with a paint brush[94] instead of spray coating. The catalyst concentrations were 2 and 5 wt%[318], or ~ 2.7 wt%[94] (26 mg_{Cat}/mL with 82 wt% H_2O and 18 wt% IPA). As the listed inks are at least 10 times higher concentrated for the different method to prepare a catalyst layer, the 0.2 wt% of catalyst and 0.04 wt% AEI in the inks are very dispersed. In addition, there have been several works analyzing the influence of the dispersion solvents composition on the microstructure of the catalyst layers with the help rheology studies.[94]

Further dilution of the inks by a factor of 100 was required for the DLS measurement. The average aggregate sizes for the inks with Pajarito Powder and, FI and PI, were distributed between 300 and 700 nm (Figure 42 c)). Most aggregates for these two inks can be found between 400 an 500 nm. A shift of the aggregate distribution by 100 nm to larger aggregates is observed for the ink containing Pajarito Powder and SI AEI.

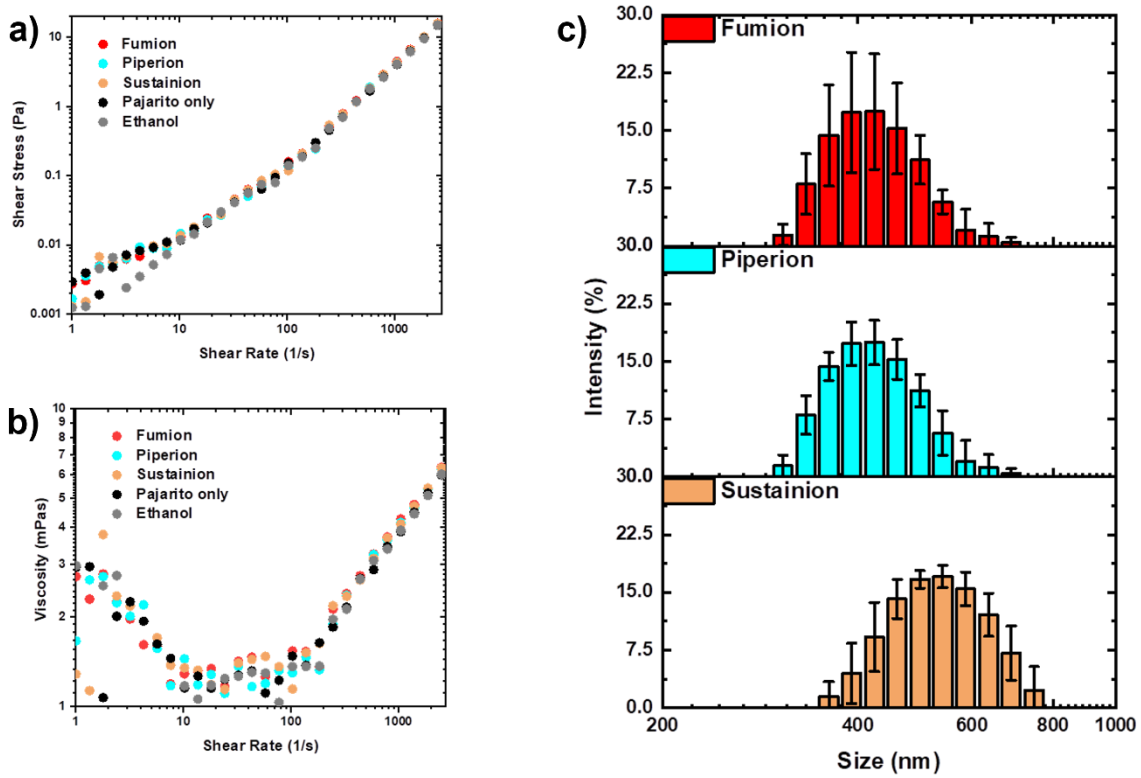


Figure 42. a) Shear stress and b) Viscosity for the AEI/Fe-N-C GDE inks and Fe-N-C only and solvent Ethanol only. c) Aggregate size distribution of the GDE inks.

After spraycoating onto the hydrophobic side of gas-diffusion-layer H23C8 (Freudenberg), the morphologies of the catalyst layers were inspected with scanning electron microscopy (SEM) (Figure 43). The loading of the catalyst layers was verified with cross section imaging. The catalyst loadings were determined with balance for FI as 1.31 $mg_{Fe\text{-}N\text{-}C}$, PI as 1.20 $mg_{Fe\text{-}N\text{-}C}$ and SI 1.28 $mg_{Fe\text{-}N\text{-}C}$. The thicknesses of the cross-section were measured from the SEM images to be 40 µm for FI/Fe-N-C, 35 µm for PI/Fe-N-C, and 40 µm for SI/Fe-N-C. The comparable catalyst loadings between the catalyst layers open up the way for studies of the ORR in the gas-diffusion-electrode. The catalyst layers showed different surface layers. The surface of the catalyst layer based on FI looked smooth with aggregates forming flat and dense island structures of catalyst aggregates. For the PI containing catalyst layer, a rough surface with rather

loose catalyst aggregates, which are occasionally protruding out of the surface plane can be observed. The SEM image of the SI based catalyst layer portrayed a homogeneous distribution of catalyst particles which are still somewhat distant from each other but at the same time not too loose.

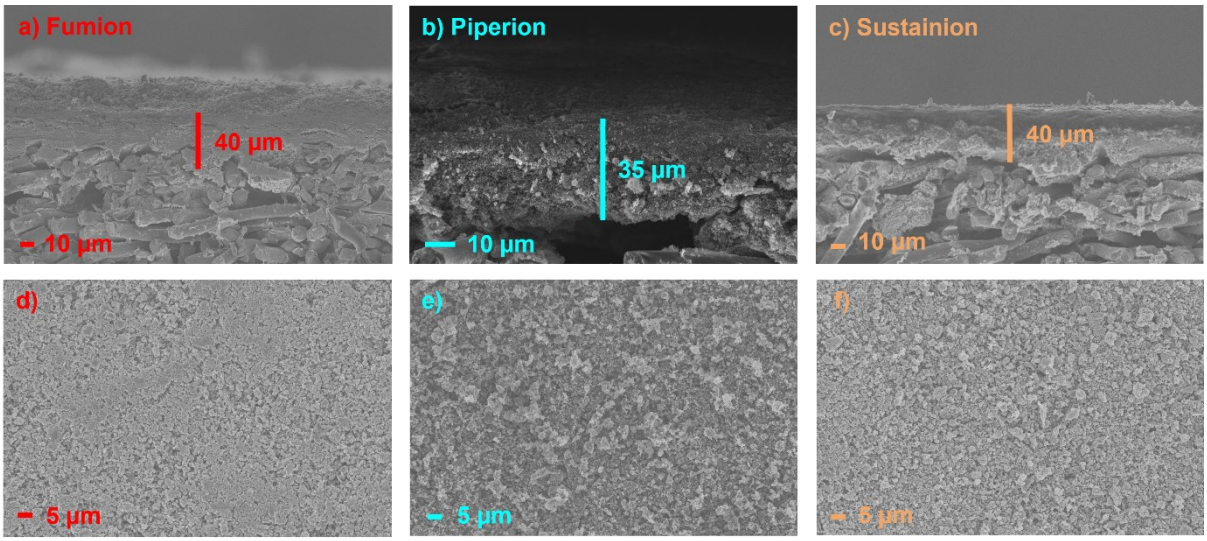


Figure 43. Cross section catalyst layers based of Pajarito Powder and a) Fumion (Loading: 1.31 mg/cm^2), b) Piperion (Loading: 1.20 mg/cm^2) and c) Sustainion (Loading: 1.28 mg/cm^2) and the topviews of catalyst layers with d) Fumion e), Piperion and f) Sustainion.

The macroscopic images (Figure A7) of the catalyst layers of the three AEIs on aluminum foil for the BET measurements also revealed their different surface properties. It has to be noted, that the SI catalyst layer on aluminum foil partially peels off, whereas the other two AEIs form rather smooth well-adhesive catalyst layers.

6.3.4. Effect of the AEI type on the oxygen reduction reaction performance of Fe-N-C catalyst in alkaline gas-diffusion-electrode

The first analysis of the AEIs combined with membrane in the oxygen reduction reaction (ORR) focuses on the type of ionomer. At high current densities (2 A/cm^2), the average combinations with PI have a lower overpotential regardless of with which membrane the catalyst layer was used (Figure 44 Left). One potential explanation might be that the Pajarito Powder retained a high BET of 603 m^2/g surface area after integration into the CL with PI compared to the original BET surface area of Pajarito Powder itself (675 m^2/g) (Figure 45 d)). Therefore, there might be more active sites still accessible at higher current densities. The best performance at high current

densities was not achieved by a pair of the same ACP family, but by PI combined with SM. Referring back to the introduction of this chapter where it was outlined that the same AEP as membrane and ionomer might not be the ideal solution due to different requirement for membranes and ionomer. As SM was the membrane, which gave the best combination at high current densities, a combination of unmodified Nafion™ ionomer with Pajarito Powder and SM membrane was also measured (Figure A8). Despite the fact that Nafion™'s molecular structure is designed for proton transport, it showed a comparable performance as FI. Nafion™ has been also used as a binder in a AEMFC, thus, it can be suspected that the water channels might be responsible for the hydroxide transport in the catalyst layer at the high relative humidity (RH).[319] The worst performance at high current densities on average is the combination of FI and FM. Among 5 measurements, 4 showed bubble formation in the upper cell compartment opening above the membrane potentially as a result of damage to the membrane at high current densities. Even though the FI might not be the most suitable choice at high current densities, FI in combination with PM demonstrated repeatedly superior performances at lower current densities between 50 and 250 mA/cm^2 (Figure 44 right). With exception for PI/SM, FI represented the preferential choice for low current density operation.

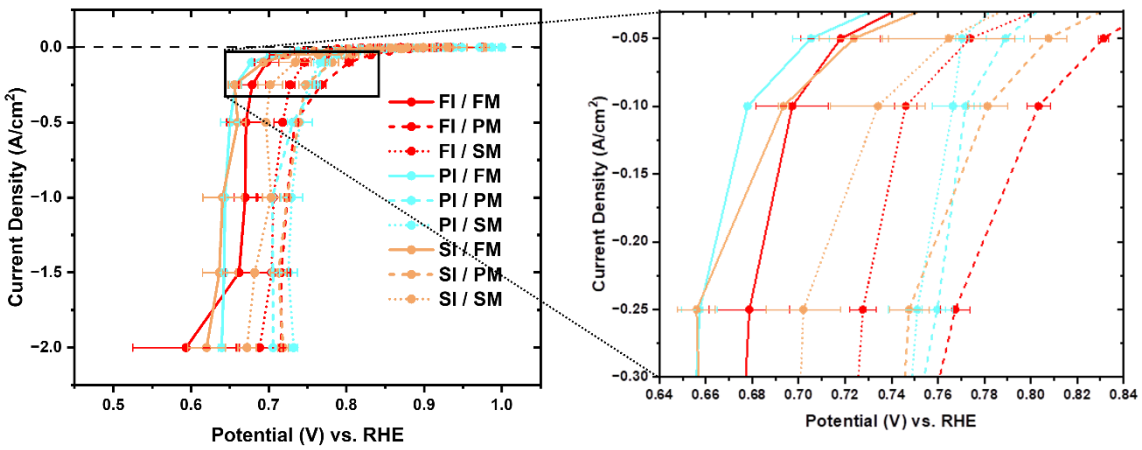


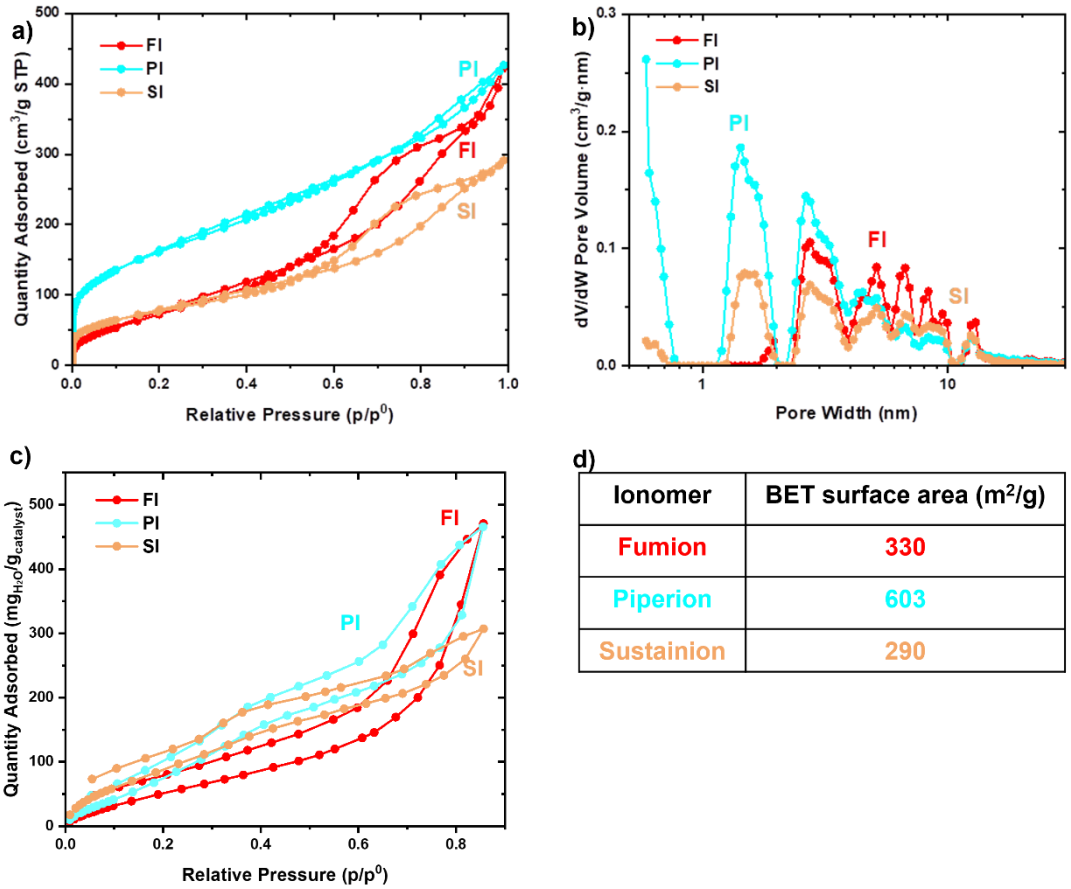
Figure 44. Left: Oxygen reduction reaction measurement with GEIS protocol with data plotted to emphasize the effect of the ionomer. Right: Zoom in at lower current density range.

Further conclusions about the interaction of the ionomer with the catalysts were drawn from nitrogen sorption (Figure 45 a), b), d)). The pore size distribution of the catalyst layers indicated that Fumion and Sustainion block the micropores of Pajarito Powder. Consequently, the total

BET surface area was reduced significantly by ~50%. In contrast, Piperion granted still access to the micropores of the catalyst. However, the quantity of mesopores with sizes between 5 nm and 10 nm were filled for the interaction of Piperion with Pajarito Powder. As opposed to Fumion, the catalyst layer structure had the largest amount of mesopores in the catalyst still accessible.

6.3.5. Effect of the AEI on the water vapor sorption capabilities of Fe-N-C catalyst layers

As water is a reactant at the cathode in AEMFC, cathodes are inclined to dry out at high current densities. In the GDE setup, a bubbler was used to set the relative humidity to 100%. Insights into water sorption behavior of the catalyst layers and the interaction of water with the ionomer and pore structure are important to optimize the performance. The water sorption isotherms of all AEIs normalized to the catalyst mass in the respective catalyst layer were assigned to type 3 isotherms with little sorption at low RH and an exponential sorption at high RH range[320] (Figure 45 c)).



Ionomer	BET surface area (m^2/g)
Fumion	330
Piperion	603
Sustainion	290

Figure 45. a) BET Isotherm of the catalyst layers sprayed on aluminum foil b) Pore size distribution c) Water Sorption Isotherms d) Table of BET surface areas.

The prevalence of strong adsorbate-adsorbate interactions over weak adsorbate-adsorbent interactions is characteristic for type 3 isotherms. As a consequence of the hydrogen bonds between the water molecules in the vapor, strong intermolecular gas interactions can be expected. In addition, the weak water-adsorbent interaction implies a rather hydrophobic nature of the catalyst layers with regards to the ionomer and catalyst itself. Below 40% RH, the adsorption is controlled by hydrophilic functional groups in the catalyst layer.[321] As opposed to the formation of monolayer as in the case of nonpolar adsorbent such as nitrogen, water molecules adsorb first on the hydrophilic sites of the catalyst such as pyridinic nitrogen species[322] and AEI. As FI/CL took up a smaller water quantity at low RH, Fumion behaves more hydrophobically. The SI/CL was more willing to adsorb water at low RH and therefore, Sustainion is more hydrophilic. In the intermediate range of RH, 30% to 80% RH), water molecules form multilayers around hydrophilic sites due to hydrogen bonding and, when these localized clusters of water are saturated, they coalescence.[321] This merging of water clusters causes capillary condensations.[323] The lower the relative pressure at which the rise begins, indicates the smaller the capillaries, as the onset of condensation shifts to higher pressure with increasing pore size. The upturn of water adsorption for PI at lower relative pressure compared to FI is in agreement with the PSD from N_2 sorption data (Figure 45 b)), in which PI/CL had more mesopores with 3 nm pore width compared to FI/CL.[324] Between 5 and 10 nm, FI/CL has a higher proportion of mesopores than PI/CL. A steep isotherm at RH higher than 80% implies that secondary pores are filled with water.[325] FI and PI based catalyst layers have their secondary pores proportionally more filled with water than SI/CL which is associated with a higher risk of blocking the gas transport in the pores at higher RH for FI/CL and PI/CL. The similar hysteresis for all AEI/CLs points towards similar water retention capacities. After reducing the relative humidity in the backward scan, Sustainion retained the highest amount of water compared to the other AEIs. The water adsorption isotherm of a catalyst layer with Pajarito Powder and QAPF-4 ionomer (wt%/wt% 0.43 I/C) has been reported with a similar type 3 isotherm.[326] The water adsorption capacity of ~470 mg_{H2O}/g_{cat} (QAPF-4/CL) compares to 471 mg_{H2O}/g_{cat} (FI/CL), 466 mg_{H2O}/g_{cat} (PI/CL) and 307 mg_{H2O}/g_{cat} (SI/CL). While, an investigation of the AEI content onto the water sorption is beyond the scope of this work, the effect of ionomer content onto water vapor adsorption has been investigated in previous studies with Nafion ionomer and Pt/C catalyst in PEMFC community. Water uptake has been found to increase with higher Nafion ionomer loading, as concomitant with increase of hydrophilic sulfonic acid groups.[321] However, there are no sulfonic structures present in the AEIs investigated in this study.

6.3.6. Effect of the membrane on the ORR overpotential in the GDE

To make the comparison between the membranes fair, the thickness was chosen to be as close as possible with dry thicknesses between 40 and 55 µm. The alkaline activation protocols recommended by the respective manufacturer have been followed as described in the Experimental part. At low and high current densities of the ORR, stark differences of 150 mV in overpotential are observed. The potentials range from 0.395 V to 0.533 V at a current density of -0.05 A/cm^2 and from 0.493 V to 0.705 V and from 0.525 V to 0.737 V at -2 A/cm^2. After exploring the effect of the AEI, the impact caused by choice of the membrane is elucidated in this section. By grouping the AEI tested according to the membrane (Figure 46 a)), it becomes obvious that AEI tested with FM membrane in general have a higher overpotential. A color mapping indicates that even though a clear separation of both FM and SM performances can be found, both show huge overpotential ranges depending on the AEI.

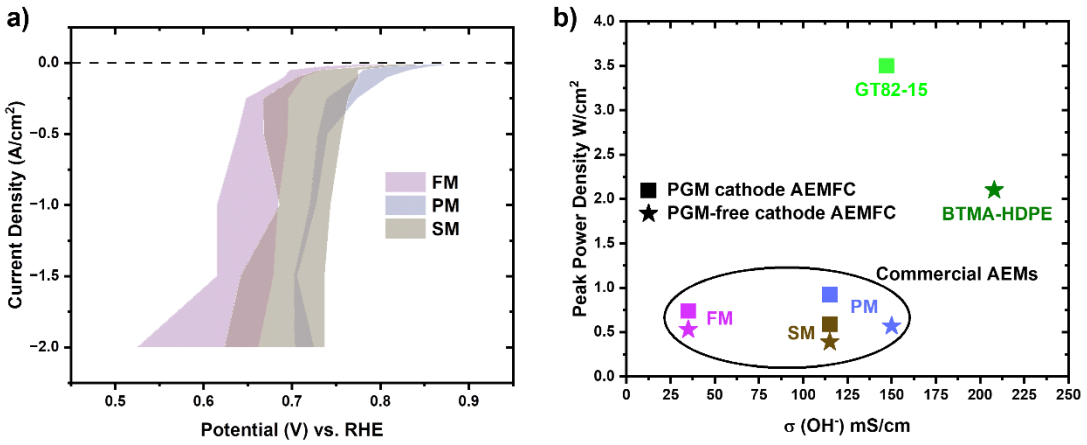


Figure 46. a) Colour scheme of membrane performances. b) Peak power densities versus hydroxide conductivities of commercial AEMs and best performing AEMs in best reported AEMFCs with PGM- (square) and PGM-free- (star) based cathodes.

Therefore, it can be concluded that the effect of the AEI is pronounced on the overpotential. In contrast for PM, the overpotentials irrespective of the AEI fall into a rather small segment. The hydroxide conductivities σ(OH^-) of the respective membranes might explain the differences in ORR between the membranes. The σ(OH^-) of FM at 25°C has been reported to be 21 mS/cm at 25°C, the temperature conditions in this study, in contrast to 50 mS/cm at 70°C relevant for AEMFC studies.[327] The σ(OH^-) of SM is reported to be 64 mS/cm at room temperature[328] in a similar range as the σ(OH^-) of PM is 66 mS/cm at 25°C.[329] This trend of hydroxide conductivities correlates to the AEM overpotential segments, with higher hydroxide

conductivities of the AEM associated with lower overpotentials. Apart from the membrane properties, the adhesion of CL to the membrane has an influence on interfacial resistance between CL and membrane.[330] Another factor could be the water transport at the interface of CL and AEM.[326] To put the GDE studies in context with AEMFCs results, the commercial membranes at higher temperature in AEMFCs don't fall into the high performance class of the research lab produced AEMs for both PGM- and PGM-free cathode catalysts (Figure 46 b)), Table A5).

6.3.7. The effect of AEI on O_2 mass-transport in the catalyst layer

Due to their thickness with the Fe-N-C based cathodes with ~40µm (for 1.2 $mg_{Fe\text{-}N\text{-}C}$) in this study compared to Pt/C (~ 10 µm)[331], O_2 transport limitations are much more likely in Fe-N-C cathodes. As already observed during ORR measurements in the RDE setup, the diffusion limiting currents in thin film electrodes with AEIs were lower compared to Nafion™ implying a poor O_2 permeability of the AEIs. Despite the reduction of the weight fraction of AEI in the CLs for the GDE studies to reduce the effect of excessive ionomer blockage on oxygen diffusion, gas-phase-transport might be still impeded to a different degree depending on the AEI in the CL. Limiting current measurement enable to explore the effect of the AEI on the oxygen transport capabilities of the CL. For the sake of simplicity, the AEI is combined with their respective brand membrane (FI/FM, PI/PM, SI/SM) and in the set of experiments for the evaluation of the O_2 mass transport. Limiting current measurements are widely applied technique to determine the oxygen transport resistance in MEAs in PEMFC.[332,333,334] Nevertheless, the study of oxygen transport in AEMFC is still little explored. Only recently, a protocol was developed to study the O_2 mass transport in large GDE (GDE-L) setups.[135] The authors reported an increase in O_2 transport resistance with increasing I/C for Nafion and Pt/C based CLs in acidic environment. They concluded that voltages losses at high current densities for high I/C CLs originate from oxygen transport limitations. Adapting the protocol to the GDE-S setup, the recommended O_2 concentration of 2.5% and the galvanostatic step of 20 mA/cm^2 in 5 seconds has been included. The oxygen limiting current measurement is sensitive to design of flow field[335], number of carbon papers[332] (H23 and H23C8) as gas-diffusion medium. Therefore, a quantitative comparison of the mass transport values between GDE in this study and GDE-L was not possible. As illustrated for the FI/FM (Figure 47 a)), the potential decreased with increasing current, consuming the oxygen present in the catalyst layer. At a certain current all oxygen in the catalyst layer has reacted, concomitant with a sudden potential jump.

Corresponding to the definition of the limiting current, changes in potential do not change the current any further ($\partial i/\partial E = 0$).[332] In this study, the limiting current was determined as the value of the current step before the potential jump (black circles in Figure 47 a)).

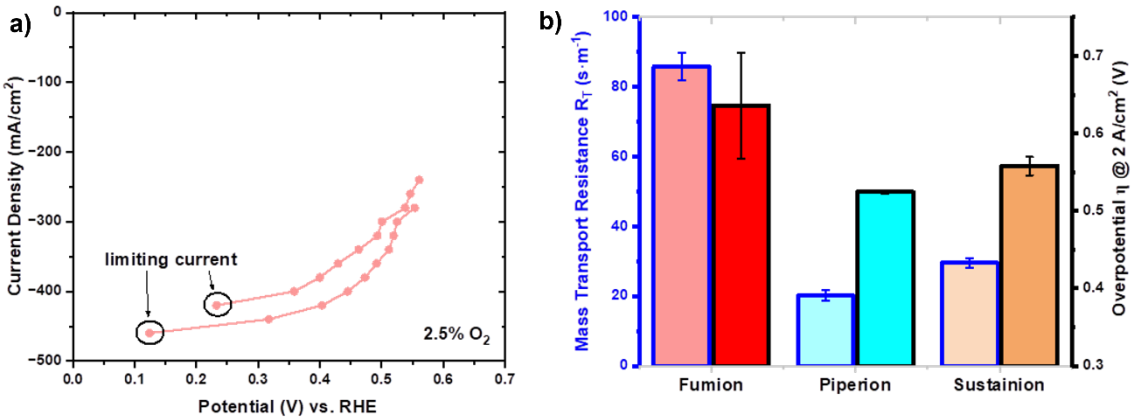


Figure 47. a) Limiting current measurement for Fumion ionomer at 2.5% O_2. b) Mass Transport Resistance R_T of the catalyst layers with different ionomers at 2.5% O_2 (blue border) besides the potential at 2 A/cm^2 at 100% O_2 (black border).

Taking the value of the limiting currents, the O_2 mass transport resistance (R_T) was calculated. (Eq. 3) FI based CL had the highest mass transport resistance, followed by SI based CLs (Figure 47 b)). The lowest mass-transport resistance was measured for the PI based catalyst layer. Mass-transfer losses are expected become dominant at high current in the GEIS measurement. Therefore, the overpotentials at 2 A/cm^2 were correlated to the mass transport resistance values. The overpotentials at high current densities measured with a concentration of 100% O_2 in GDE followed the same trend as the R_T values (Figure 44 a)). It can be concluded that the type of ionomer is impacting the oxygen transport in the Fe-N-C CL and thus, the performance at current densities with high oxygen consumption.

6.4. Conclusion

This study is a starting point into the separate optimization of cathode catalyst layer for AEMFCs with half-cell GDE setups. The RDE screening of Fe-N-C catalysts in alkaline medium is recommended to be extended beyond Nafion, to actually involve AEIs, which are integrating the Fe-N-C catalyst into the MEA cathode. As reduced oxygen permeability has been observed for all AEI in comparison with Nafion, future developments for new AEIs might shift away from using a molecular structure that fulfil the requirements for AEM towards a

more AEI-functional design with regard to high oxygen flux and permeability.[316,336] The oxygen diffusion limiting current in RDE is an easy accessible value to check the oxygen transport on new developed AEIs. The RDE studies could be extended to quantify the mass-transport by parameters such as diffusion coefficient and solubility of O_2 in the AEI.[337] Blending AEIs with catalyst affect the mesopore and micropore structure of the catalyst material, with FI and SI blocking the accessibility of micropores. While the lack of micropores might not be relevant at low current densities in the case of FI, at high current densities the PI based catalyst layer with the highest BET surface area shows the best performance. Despite similar amounts of water present as a reactant in the FI and PI catalyst layers at 100% RH, the restricted oxygen transport capabilities limit the performance at high current densities for FI. The hydration of the catalyst layer can be further optimized by tailoring the hydrophilic / hydrophobic properties via the polymer chemistry of the AEI.[338] This study confirmed that the membrane's hydroxide conductivity correlates with the performance of the AEM/AEI combination. As the chosen I/C ratio might not be the optimal for each of the AEIs investigated, future work can focus on optimizing the I/C ratio[339,340] in the catalyst layer for an individual AEI and also take the solvent composition[331,341] into account for the adjustment of the pore network of the CL. Ongoing developments in half-cell setups are going to enable to study temperature[127] and RH effects on the cathode catalyst layer performance. The market of commercial AEIs and AEMs has still space for new improved products. This opportunity should inspire and motivate young scientists to commercialize their discoveries.

7. Conclusive remarks

In the final chapter, the light is shone from all perspectives onto the thesis in order to place it in the context of existing literature and academic as well as industrial relevance. First, the value and successes of the thesis, two parameters that often remain in the background in discussions and meetings, which are focused on the shortcomings and current obstacles in the projects, have to be acknowledged. Then, of course, there is always blind spots, which in hindsight are easily identified. In the tunnel of chasing the next results, certain mistakes often are outside of the awareness, and only become conscious when pointed out from an outside observer or at the end of the thesis writing when a distanced perspective is taken. In addition, there is always new ideas on the journey of the PhD, which cannot be looked into due to lack of time, but are valuable research directions for the next generation of PhD students. At the end, a blunt prediction of the future of the field of PGM-free catalysts with regards to their application in FCEVs rounds off the thesis.

7.1. Value generated in this thesis

Chapter 4: For the first time, the theoretical concept of ideal fuel cell electrode, proposed by Middleman, is demonstrated with vertically-aligned oriented macro-sized tubular carbon tubes for Fe-N-C catalysts. A successful transfer of the aligned carbon tubes with a length of 50 µm on a Nafion membrane as a platform for the tubes, overcomes the issue in previous works, where loose aggregates of bundles of tubes formed during the etching process of the AAO template. In addition, short-chain ionomer is used to infiltrate the macropores of the carbon tubes, which are not accessible for larger-sized Nafion agglomerates.

Chapter 5: Polystyrene nanospheres are applied for the first time as a template for a freestanding carbon film based on mesophase pitch and PVA. The optimization process of chemical composition, optimization of the template to carbon precursor ratio, and heating rate, yields a carbon film with unprecedented material properties including excellent bendability and interconnected open pore network. The value of replacing the silica template, which requires an etching process of three days, with PS spheres, which can be dissolved after the stabilization step or burn off during carbonization, is industrially relevant. Considering the nanoporous carbon scaffold on the market[342], the film developed in this PhD represents an advancement. From academic perspective, the investigation of the macroporous film as a support for

molecular Fe-N-C catalyst in the GDE testified the suitability of the film's mass transport properties as alternative for conventional powder-based catalyst at high current densities.

Chapter 6: The gap of a ORR study involving all accessible commercial alkaline ionomers is filled by a liquid half-cell study in RDE complemented by GDE application at ambient conditions. The reason for the lack of a benchmark alkaline ionomer of the ORR in liquid half-cell is attributed to their functional deficit in oxygen permeability in contrast to proton-conducting ionomer Nafion. In addition, the interaction of the AEI with commercial PGM-free Fe-N-C significantly influences the pore size distribution and water uptake of the catalyst layer, with the catalyst layer with the highest BET surface area showing the best performance at high current densities. A oxygen limiting current measurement protocol was established to analyse the oxygen transport properties of the catalyst layers with alkaline ionomers.

7.2. Retrospective blind spots of the research in this thesis

- A numerical model to analyse the mass transport of order-structured PGM-free catalyst layer architectures could have provided strong data-founded directions. Due to the lack of a model, the thicknesses of the CL and size of the macroporous channels were rather chosen empirically. The design parameters such as pore size to make a certain BET surface area with a defined number of active sites could have elucidated that the normal AAO template yield a too low BET surface area support.

- Relying on the cell design of a previous a PhD student for 2 years before implementing the improved design with reduced uncompensated resistance necessitated the repetition of a lot of measurements. Such advanced nanoarchitecture materials can only be reliably measured when a scrutinized and benchmarked system is well established.

Chapter 4:

The lack of efficient etching protocol cost a lot of time. Initially, the etching container was glass, which was etched in competition with the actual template. At the end, a Teflon container was used for reliable etching, which introduces fewer contaminations. In addition, the process of realization was slow that the phase transition of the AAO at 900°C towards an etching-resistant phase and that a thin carbon film might cover the whole AAO sample. A lot of time was invested in exploring pyrolysis procedures with dissolving the AAO template at low temperatures, before a second pyrolysis, which lead to the formation of small nanotubes instead of the macrotubes.

Chapter 5:

The research was overly focused on materials development of carbon materials for carbon support neglecting the application of them in the GDE. It could have been expanded towards integrating more nitrogen-precursor despite one attempt included poly allyl amine instead of PVA, which didn't give a film. A lot of time was spent on adjusting the slurry and figuring out the coating substrate. Also, the ionomer distribution in the film is not clear yet. Nano-CT with labelling of the ionomer could help to reveal the ionomer intrusion into the film. Laser cutting of the samples for GDE testing is a delicate process.

Chapter 6:

As conductivity of AEMs and AEIs strongly is dependent on the temperature, the room temperature measurements don't actually reflect their real performance in an AEMFC at elevated temperatures, limiting the predictability of the conclusions in this chapter. In addition, the ionomer to catalyst ratio was not optimized for the specific catalyst. Dynamic light scattering and rheology studies are not the most useful for inks that are sprayed as in this study, but more relevant for inks that are coated with doctor blade.

7.3. Prospective research directions outgoing from this thesis

Materials development

Addressing the inherent lack of nitrogen to coordinate iron sites in the macroporous carbon film opens up several possibilities. Nitrogen-containing molecules can either be introduced as precursors into the slurry or deposited on the structure of the film. In the first case, it is not guaranteed that the nitrogen-functionalities will be on the surface. Nevertheless, chitosan might be a candidate fitting in the overall research theme of sustainability of the research group. Previously, chitosan and PVA-based film have been reported for other applications.[343] In the second case, either aniline could be electrodeposited[291] onto the porous carbon film or a chemical vapour deposition of a nitrogen-containing carbon compound could also uniformly cover the porous carbon film. The initial work on mesopore template as reported in thesis could be expanded with regards to mesopore template content to maximize the surface area and thus of the accessible active sites.

Electrochemical GDE half-cells

The electrochemical GDE half-cell has further potential for development to create conditions in the catalyst layer as close as possible to the conditions in a real fuel cell catalyst layer. The effect of temperature and pressure on the performance of the catalyst layer are crucial and should be adjustable parameters in the next generation of GDE half-cell.[125] In addition, the rudimentary humidifier in form of a simple bubbler could be replaced by a low flow humidification system to be able to set the humidity accurately.

7.4. The destiny of PGM-free Fe-N-C catalysts

The future success of PGM-free Fe-N-C depends on several factors, foremost in meeting the MEA performance (> 1000 mW/cm^2) target (H_2-air) and durability targets. On the catalyst level, the previous limits of iron loadings below 1 wt% have been surpassed by CVD and decoupled Fe coordination approaches.[65] However, despite the higher loading of atomically dispersed iron sites, the utilisation of Fe sites in RDE liquid electrolyte ex situ measurement has been shown to be fairly low.[63] Integration of the catalysts into catalyst layers with solid electrolyte is expected to be associated with even lower utilization due to reduced triple-phase boundary as observed in PGM-free catalysts.[344] Therefore, the engineering of catalyst layers with high utilization of the active sites is the next major hurdle for Fe-N-C catalysts in PEMFCs. Apart from utilization, the mass transport in the catalyst layer of thick Fe-N-C catalyst is a main topic to be addressed especially for operation in H_2-air. The thesis contributed and explored innovative design concepts of freestanding cathode catalyst support films for mass-transport tailored cathode design. A topic, that was not addressed much in this thesis is the durability. The low stability of the most durable Fe-N-C catalysts, loss of 50% of current density within first 200 hours.[40] Far away from the 2025 target for transportation application of 8000 hours with less than 10% loss of performance.[345] Surely, Fe-N-C materials remain a topic for academia, but they are a quantum leap away from industrial relevance. Despite, this pessimistic prognosis, a single commercial MEA product based on Fe-N-C cathode from a collaboration between Ballard Power System and Nisshinbo Holdings might be small spark of hope on the dark horizon.[346]

Further consolation is found in the recent progress in AEMFC technologies due to the availability of AEM with high OH^- conductivity and durability.[347] The basic pH environment benefits the activity and durability of PGM-free for promising applications outside of the harsh

acid environment.[348] In this context, the thesis contributed to the foundation by presenting a cathode catalyst layer testing platform for commercial alkaline ionomers in combination with a commercial Fe-N-C catalyst with the option to cover the catalyst layer with an AEM.

Appendix

Appendix Chapter 4

Reference	Material	Temperature	Etching agent + conditions
194	Polyacrylnitrile (PAN)	600°C	1 M NaOH
195	Ethylenediamine	600°C	2 M NaOH, 4 h, 40°C
196	CVD of acetylene	620°C	5 M NaOH, 48 h
197	Furaldehyde	750°C	conc. H_3PO_4, 65°C
162	CVD of acetonitrile	800°C	HF + HCl mixture, 70°C, 12 h
198	CVD of propylene	800°C	46% HF
185	N,N-DMF, Pyrridine	850°C	5 wt% HF
199	Glucose	900°C	HF
200	CVD of acetylene	900°C	0.5 wt% HF (not successful)
204	CVD of methane	900°C	40% HF, 22 h
201	CVD of propylene	900°C	HF
202	HBC-PhC_{12}	900°C	3 M NaOH (partial etching)
203	Polymer precursors: polyphenylacetylene (PPA), poly(4-vinylpyridine) (P4VP), poly(3-methylpyrrole) (PMPy), poly(2-methyl-1-vinylimidazole) (PMVI), and poly(*p*-pyridazine-3,6-diyl) (PPP)	900°C	6 M NaOH
205	CVD of methane	920°C	40% HF/H_2O, 24 h 25% $HClO_4$/EtOH, 24 h

Table A1: Etching of AAO to release carbonized 1D structure arrays.

Appendix Chapter 5

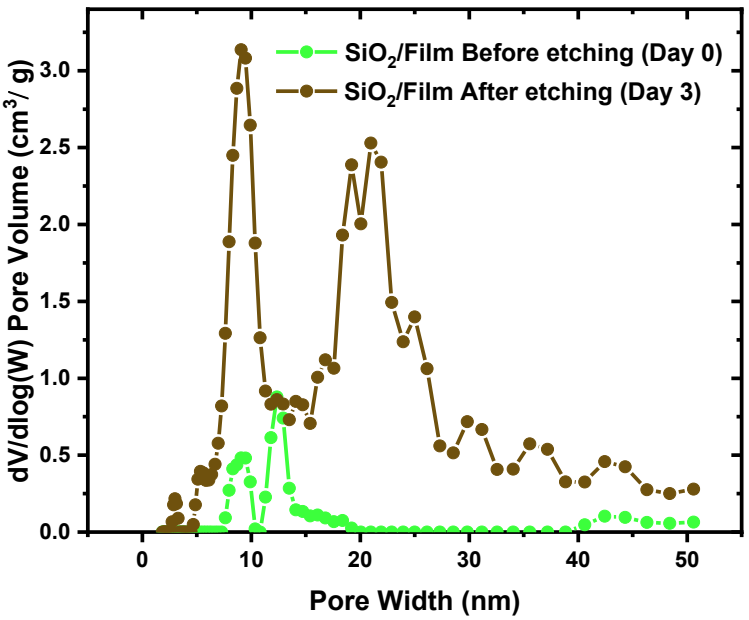
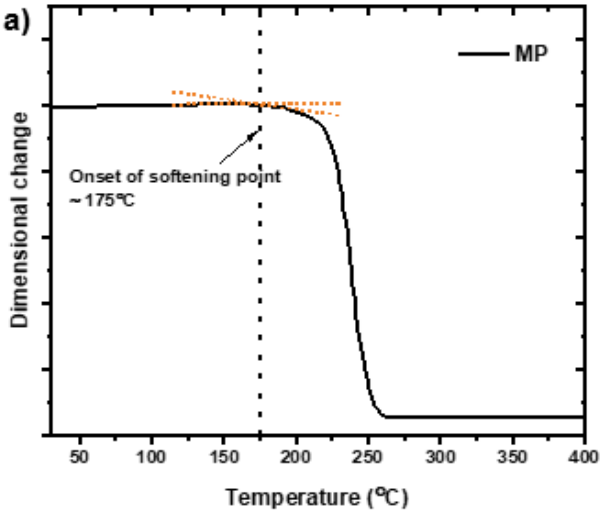


Figure A1. Pore size distribution of SiO_2 templated carbon films before and after etching.

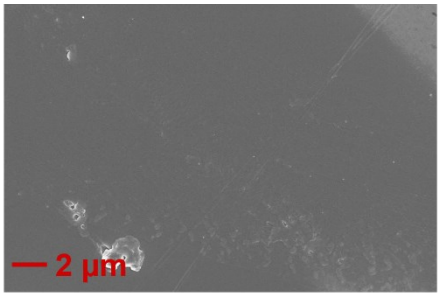


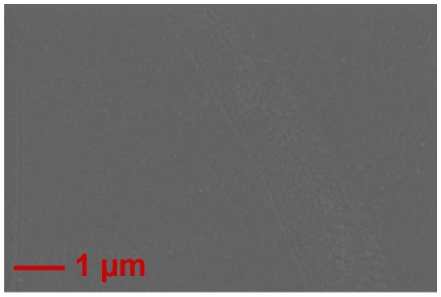
b)

Element	wt%
Fe	0.014
Na	0.077
Mg	0.010
Al	0.026
Ni	0.001
Cu	0.002

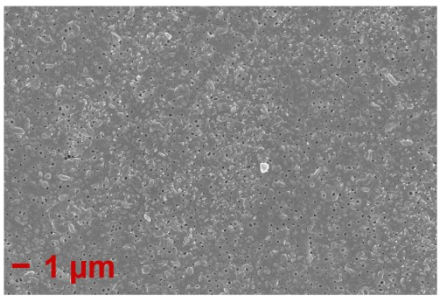
Figure A2. a) Thermomechanical analysis of mesophase pitch. b) Elemental contamination of the mesophase pitch with elements listed that deviate by 10% from the blank sample in ICP-MS.

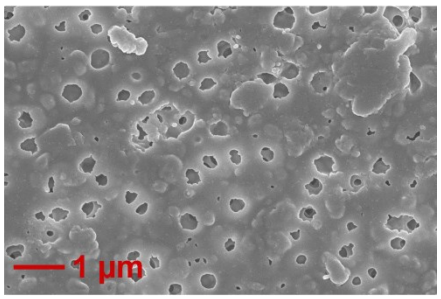
0 g PS



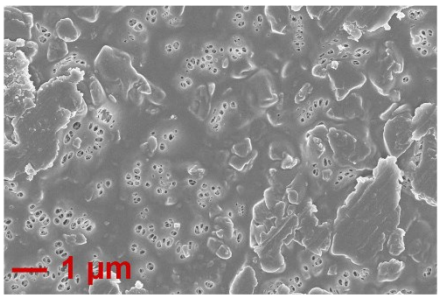


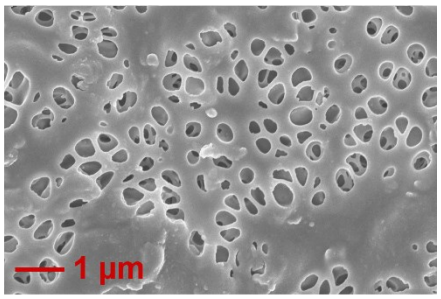
0.25 g PS





0.63 g PS





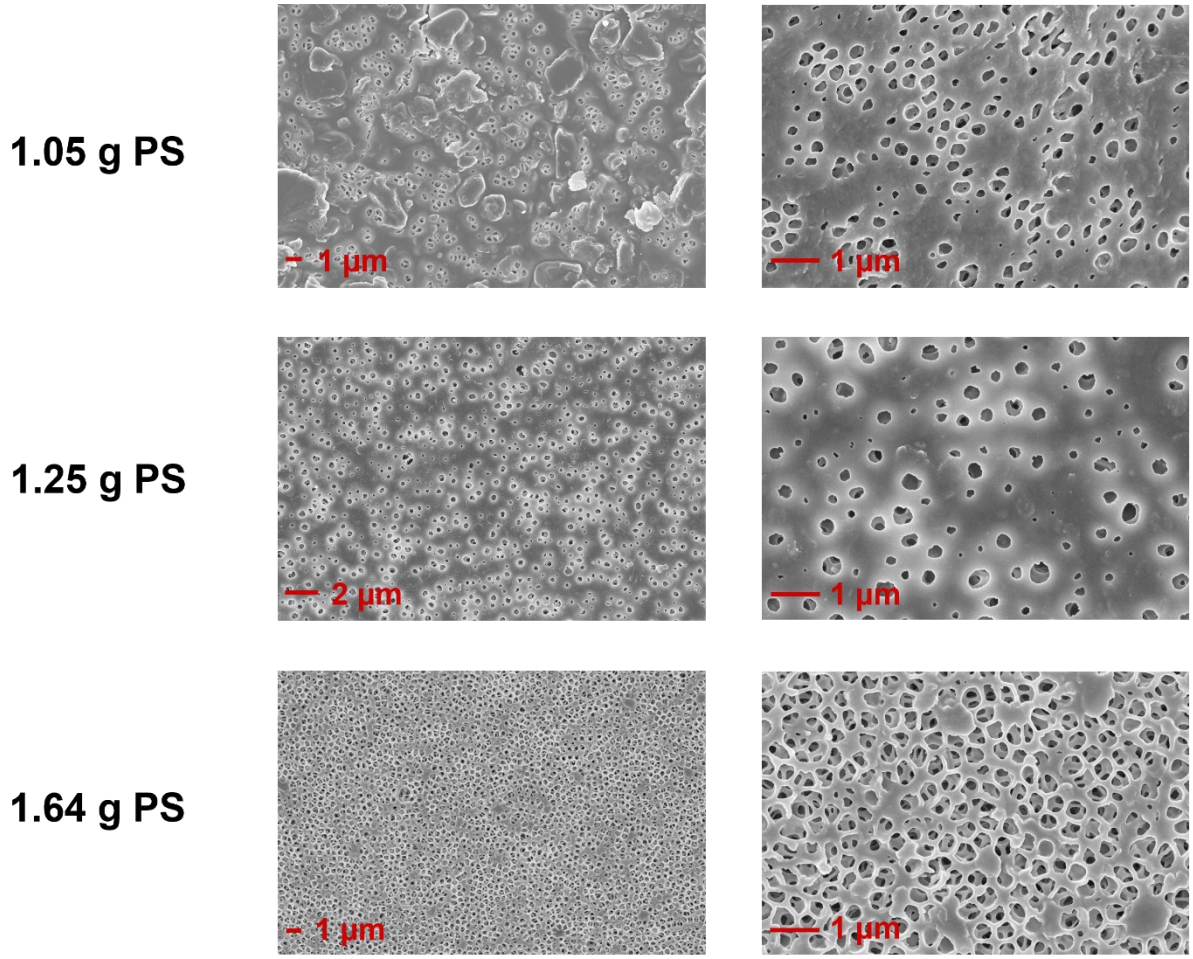


Figure A3. Optimization of the PS loading in the film.

	Pristine MP film	Oxidative stabilized film (210°C)	Carbonized film (900°C)
Conductivity (S/m)	4.02×10^{-6}	2.14×10^{-6}	3.02

Table A2. Conductivity measurements of the film at stages in preparation sequence.

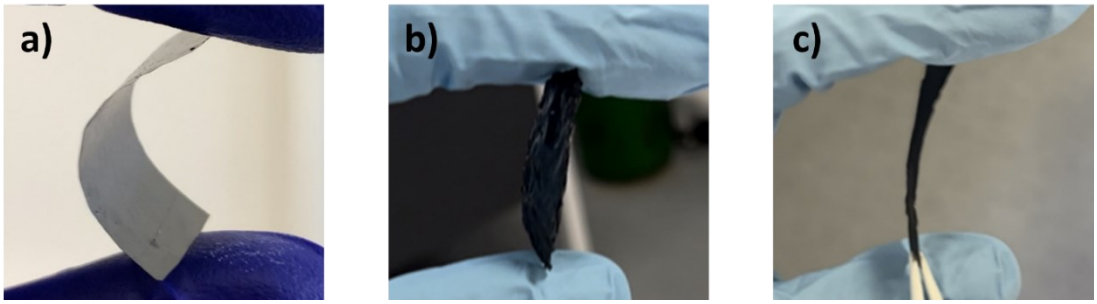


Figure A4. Effect of the heating rate on the brittleness of the macroporous carbon film at 0.1°C/min (a), 0.5°C/min (b), 1°C/min (c). (Snapshot at maximum bending from video recording)

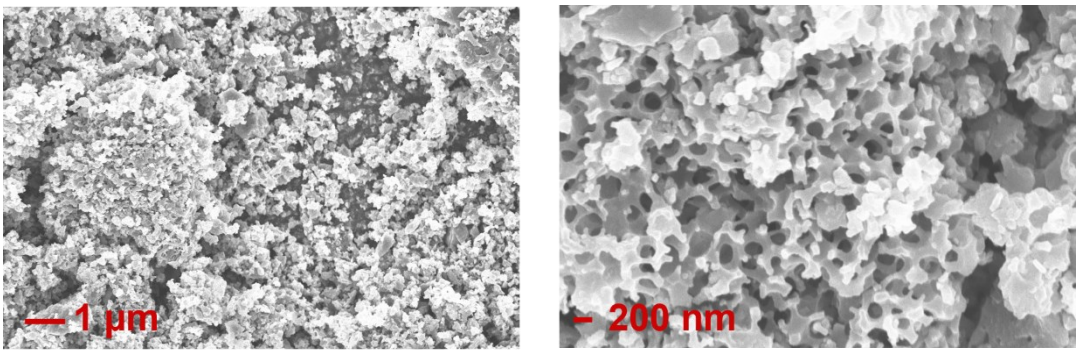


Figure A5. SEM images of ball milled BM-Film-N_2.

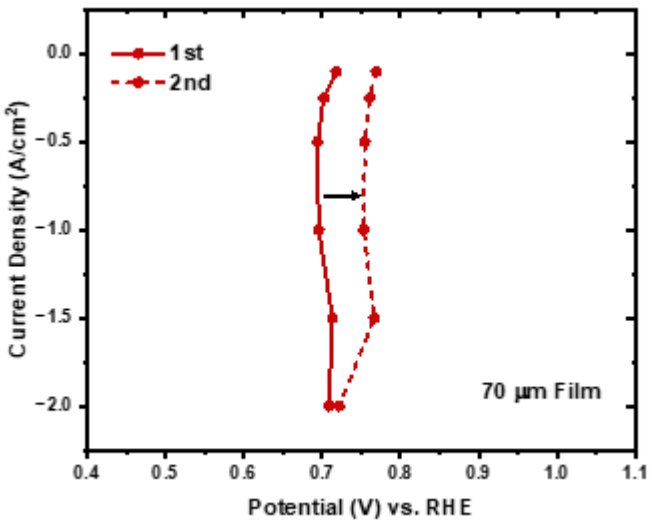


Figure A6. First GEIS polarization curve and second repetition of GEIS protocol for the high current density steps. In both it is stepped from lower current densities to higher current densities.

Appendix Chapter 6

Reference	AEM / AEI	Anode / Cathode	PPD	Operating conditions
349	AEM: BTMA-HDPE AEI: BTMA-ETFE BTMA = Benzyltrimethylammonium ETFE = Poly(ethylene-coptetrafluoroethylene) HDPE = high density polyethylene	Anode: PtRu/C (0.4 mg_{Pt}/cm^2) Cathode: Pt/C (0.4 mg_{Pt}/cm^2)	2.5 W/cm^2	80°C (H_2-O_2) 92% RH Flow rate: 1 L/min No back pressure
350	AEM: PTFE-reinforced poly(norborene) GT64-15 AEI: BTMA-ETFE	Anode: PtRu/C (0.7 mg/cm^2) Cathode: Pt/C (0.6 mg/cm^2)	3.4 W/cm^2	80°C (H_2-O_2) Anode / Cathode dew points: 67°C / 74°C
306	AEM: GT82-15* AEI: ETFE-g-poly(VBTMAC) *Poly(norborene)-based	Anode: PtRu/C (0.7m mg/cm^2) Cathode: Pt/C (0.6 mg/cm^2)	3.5 W/cm^2	80°C (H_2-O_2) Anode / Cathode dew points: 66°C / 75°C Anode / Cathode back pressure: 0.05 MPa / 0.1 MPa
338	AEM: GT64-15* AEI: Anode: GT78*/ Cathode: GT32* *Poly(norborene)-based	Anode: PtRu/C (0.7 mg/cm^2) Cathode: Pt/C (0.6 mg/cm^2)	3.2 W/cm^2	80°C (H_2-O_2)
347	AEM: PFBP-14 AEI: PFTP-13 PFBP = Poly(fluorene N,N-dimethylpipiridinium-co-nonfluoride) PFTP = Poly(fluorne-co-terphenyl N,N'-dimethylpiperidinium)	Anode: PtRu/C (0.42 mg/cm^2) Cathode: Pt/C (0.33 mg/cm^2)	2.3 W/cm^2	80°C (H_2-O_2) Flow rate: 1 L/min Anode / Cathode RH: 75% / 100%
351	AEM: PDTP-25 AEI: PFBP PDTP = Poly(diphenyl-terphenylpiperidinium)	Anode: PtRu/C (0.39 mg/cm^2) Cathode: Pt/C (0.26 mg/cm^2)	2.6 W/cm^2	80°C (H_2-O_2) Anode / Cathode RH: 75% / 100% Anode / Cathode back pressure: 1.3 bar / 1.3 bar
352	AEM: b-PTP-2.5** AEI: PFBP PFBP = Poly(fluorenyl-co-biphenyl piperidinium) **Branched poly(aryl piperidinium)	Anode: PtRu/C (0.6 mg/cm^2) Cathode: (0.4 mg/cm^2)	2.3 W/cm^2	80°C (H_2-O_2) Anode / Cathode RH: 75% / 100% Anode / Cathode back pressure: 1.3 bar / 1.3 bar
353	AEM: b-PDTP-Trip-5*** AEI: b-PFBP-Trip-3.5*** ***Triptycene-branched poly(arylpiperidinium)	Anode: PtRu/C (0.39 mg/cm^2) Cathode: Pt/C (0.26 mg/cm^2)	2.5 W/cm^2	80°C (H_2-O_2) Anode / Cathode RH: 75% / 100% Anode / Cathode back pressure: 1.3 bar / 1.3 bar

Table A3. PGM-based cathodes in AEMFC with peak power densities (PPD) > 2.0 W/cm^2.

Reference	AEM / AEI	Anode / Cathode	PPD	Operating conditions
50	AEM: BTMA-HDPE AEI: BTMA-ETFE	Anode: PtRu/C (0.6 mg/cm^2) Cathode: Fe-N-C Pajarito Powder (1 mg/cm^2)	2.1 W/cm^2	80°C (H_2-O_2) Anode / Cathode dew points: 70°C / 75°C Anode / Cathode back pressure: 200 kPa
296	AEM: no information AEI: BTMA-ETFE	Anode: PtRu/C (0.6 mg/cm^2) Cathode: Fe-N-C $Fe_{0.5}$-NH_3 (0.9 mg/cm^2)	1.4 W/cm^2	65°C (H_2-O_2) Anode / Cathode dew points: 55°C / 60°C
49	AEM: BTMA-HDPE AEI: BTMA-ETFE	Anode: PtRu/C (0.6 mg/cm^2) Cathode: Fe-N-C $Fe_{0.5}$-dry (0.91 mg/cm^2)	1.8 W/cm^2	80°C (H_2-O_2) Anode / Cathode dew points: 71°C / 77°C Anode / Cathode back pressure: 0.05 MPa / 0.1 MPa
354	AEM: PVA-0.8PQVBC40% AEI: Nafion	Anode: PtRu/C (0.3 mg/cm^2) Cathode: Fe-N-C FeN_x-CNTs (4.0 mg/cm^2)	1.2 W/cm^2	60°C (H_2-O_2) Anode / Cathode back pressure 2 bar / 2 bar
355	AEM: PVA-1.8PVBMP AEI: QPPO QPPO = quaternized poly(2,6-dimethyl-1,4-phenylene) oxide	Anode: PtRu/C (0.4 mg/cm^2) Cathode: Fe-N-C FeN_xCNTs (2 mg/cm^2)	1.2 W/cm^2	60°C (H_2-O_2) Flow rate: 400 mL/min Anode / Cathode back pressure 0.1 MPa / 0.1 MPa
356	AEM: Xion Pention-72-15CL AEI: Pention D35	Anode: PtRu/C (0.6 mg_{Cat}/cm^2) Cathode: Fe-N-C Fe-N-PDC-HA (1 mg/cm^2)	1.1 W/cm^2	80°C (H_2-O_2) Anode / Cathode dew points: 71°C / 77°C Anode / Cathode flow rate: 500 mL/min / 1000 mL/min Cathode back pressure 0.1 MPa
357	AEM: Poly(norobene) tetra block copolymer AEI: Poly(norobene) tetra block copolymer	Anode: CST-PtRu/NC (0.05 mg/cm^2) Cathode: Fe-N-C Pajarito Powder (1.0 mg/cm^2)	1.2 W/cm^2	80°C (H_2-O_2) Anode / Cathode dew points: 70°C / 75°C

Table A4. Fe-N-C-based cathodes in AEMFC with PPD > 1.0 W/cm^2.



Figure A7. The macroscopic images of the sprayed samples for BET sorption experiments.

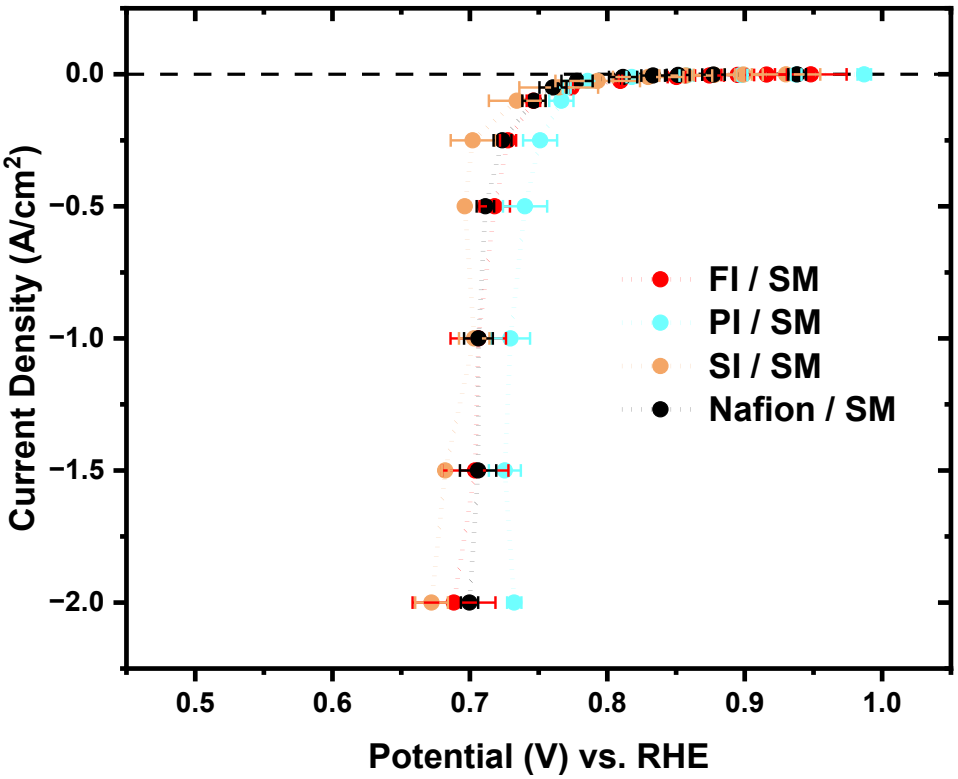


Figure A8. ORR GEIS polarization curves of AEIs and Nafion combined with SM membrane.

Reference	AEM / AEI	Anode / Cathode	PPD/ $\sigma(OH^-)$	Operating conditions
327 358	AEM: FAA-3-50 AEI: FAA-3	PGM Anode: PtRu/C (0.4 mg/cm^2) Cathode: Pt/C (0.4 mg/cm^2)	PPD: 0.74 W/cm^2 $\sigma(OH^-)$: 35 mS/cm (T = 60°C)	60°C (H_2-O_2) Anode: 0.8 L/min / Cathode: 1.0 L/min
359 358	AEM: FAA-3-50 AEI: FAA-3	PGM-free cathode Anode: Pt/C (0.5 mg$_{Pt}$/cm^2) Cathode: FeNC-4000 (0.5 mg/cm^2)	PPD: 0.53 W/cm^2 $\sigma(OH^-)$: 35 mS/cm (T = 60°C)	60°C (H_2-O_2) Anode: 0.8 L/min / Cathode: 1.0 L/min Anode / Cathode RH: 80% / 90% Back pressure: 1.5 bar
360 361	AEM: Sustainion X37-50 AEI: Sustainion	PGM Anode: Pt/C (0.76 mg$_{Pt}$/cm^2) Cathode: Pt/C (0.76 mg$_{Pt}$/cm^2)	PPD: 0.59 W/cm^2 $\sigma(OH^-)$: 115 mS/cm (T = 60°C)	60°C (H_2-O_2) Anode: 500 sccm Cathode: 1000 sccm
362 361	AEM: Sustainion X37-50 Grade RT AEI: Sustainion	PGM-free cathode Anode: Pt/C (0.76 mg$_{Pt}$/cm^2) Cathode: FeCo-N-C (0.70 mg/cm^2)	PPD:0.39 W/cm^2 $\sigma(OH^-)$: 115 mS/cm (T = 60°C)	60°C (H_2-O_2) Anode: 500 sccm Cathode: 1000 sccm Anode / Cathode RH: 93% / 93%
363 364	AEM: PiperION AEI: PiperION	PGM Anode: PtRu/C (0.4 mg/cm^2) Cathode: Pt/C (0.4 mg/cm^2)	PPD: 0.92 W/cm^2 $\sigma(OH^-)$: 115 mS/cm (T = 60°C)	60°C (H_2-O_2) Anode: 1000 sccm Cathode: 1000 sccm
365 364	AEM: PiperION AEI: PiperION	PGM-free cathode Anode: PtRu/C (0.4 mg/cm^2) Cathode: Co/Fe-N-C (2mg/cm^2)	PPD: 0.57 W/cm^2 $\sigma(OH^-)$: 150 mS/cm (T = 80°C)	80°C (H_2-O_2) Anode: 0.2 L/min / Cathode: 0.4 L/min Anode / Cathode RH: 70% / 100% Back pressure: 100 kPa
306	AEM: GT82-15* AEI: ETFE-g-poly(VBTMAC) *Poly(norborene)-based	Anode: PtRu/C (0.7m mg/cm^2) Cathode: Pt/C (0.6 mg/cm^2)	PPD: 3.5 W/cm^2 $\sigma(OH^-)$: 147 mS/cm (T = 80°C)	80°C (H_2-O_2) Anode / Cathode dew points: 66°C / 75°C Anode / Cathode back pressure: 0.05 MPa / 0.1 MPa
50	AEM: BTMA-HDPE AEI: BTMA-ETFE	PGM-free cathode Anode: PtRu/C (0.6 mg/cm^2) Cathode: Fe-N-C Pajarito Powder (1 mg/cm^2)	PPD: 2.1 W/cm^2 $\sigma(OH^-)$: 208 mS/cm (T = 80°C)	80°C (H_2-O_2) Anode / Cathode dew points: 70°C / 75°C Anode / Cathode back pressure: 200 kPa

Table A5. Commercial AEMs vs. lab-scale AEMs: PPDs and hydroxide conductivities $\sigma(OH^-)$

References

1 https://www.goodreads.com/quotes/272021-the-significant-problems-we-have-cannot-be-solved-at-the

2 F. S. Wyczalek, D. L. Frank, G. E. Smith, 1968, A Vehicle Fuel Cell System, *SAE Transactions*, **76**, 1008-1028

3 C. E. Winters, W. L. Morgen, 1967, THE HYDROGEN-OXYGEN THIN ELECTRODE FUEL CELL MODULE", *SAE Technical Paper*, 670182

4 K. Kordesch, V. Hacker, K. Reichmann, M. Cifrain, T. Hejze, 2008, *ECS Trans.*, **11**, 167-185

5 https://www.gm.com/heritage/archive
(Retrieved 10.04.2024)

6 https://iea.blob.core.windows.net/assets/dacf14d2-eabc-498a-8263-9f97fd5dc327/GEVO2023.pdf
(Retrieved 10.04.2024)

7 https://www.statista.com/statistics/1026719/number-of-hydrogen-fuel-stations-by-country/
(Retrieved 10.04.2024)

8 https://afdc.energy.gov/fuels/hydrogen-locations#/find/nearest?fuel=HY
(Retrieved 10.04.2024)

9 https://hydrogen-central.com/shell-abandons-hydrogen-refuelling-stations-in-california/
(Retrieved 10.04.2024)

10 K. Kodama, T. Nagai, A. Kuwaki, R. Jinnouchi, Y. Morimoto, 2021, Challenges in applying highly active Pt-based nanostructured catalysts for oxygen reduction reactions to fuel cell vehicles, *Nat. Nanotechnol.*, **16**, 140-147

11 B. K. Hong, S. H. Kim, 2018, Recent Advances in Fuel Cell Electric Vehicle Technologies of Hyundai, *ECS Trans.*, **86**, 3-11

12 T. Yoshizumi, H. Kubo, M. Okumura, 2021, Development of High-Performance FC Stack for the New MIRAI, *SAE Tech. Pap.*, 2021-01-0740

13 R. O'Hayre, S. W. Cha, W. Colella, F. B. Prinz, 2016, Fuel cell fundamentals, Wiley

14 L. Fan, H. Deng, Y. Zhang, Q. Du, D. Y. C. Leung, Y. Wang, K. Jiao, 2023, Towards ultralow platinum loading proton exchange membrane fuel cells, *Energy Environ. Sci.*, **16**, 1466-1479

15 K. Jiao, J. Xuan, Q. Du, Z. Bao, B. Xie, B. Wang, Y. Zhao, L. Fan, H. Wang, Z. Hou, S. Huo, N. P. Brandon, Y. Yin, M. D. Guiver, 2021, Designing the next generation of proton-exchange membrane fuel cells, *Nature*, **595**, 361-369

16 S. T. Thompson, B. D. James, J. M. Huya-Kouadio, C. Houchins, D. A. DeSantis, R. Ahluwalia, A. R. Wilson, G. Kleen, D. Papageorgopoulos, 2018, Direct hydrogen fuel cell electric vehicle cost analysis: System and high volume manufacturing description, validation and outlook, *J. Power Sources*, **399**, 304-313

17 B. D.James, Fuel Cell Cost and Performance Analysis. 2022 DOE Hydrogen and Fuel Cells Program Annual Merit Review and Peer Evaluation Meeting Presentation, 2022, https://www.hydrogen.energy.gov/pdfs/review22/fc353_james_2022_o.pdf
(Retrieved 10.04.2024)

18 https://www.reuters.com/article/us-platinum-week-bosch-fuelcells-exclusi-idUSKCN1SJ0FG/ (Retrieved: 10.04.2024)

19 M. David, S. M. Lyth, R. Lindner, G. F. Harrington, 2021, Critical Raw Materials in Polymer Electrolyte Fuel Cells, *Future-Proofing Fuel Cells*

20 S. Mizuno, T. Hayashi, H. Kubo, M. Okumura, T. Kurihara, K. Mori, 2021, Development of the Fuel Cell Stack for the Second-Generation Mirai, *TTR*, **66**, 22-27

21 Y. Kim, H. E. Bae, D. Lee, J. Kim, E. Lee, S. Oh, J.-H. Jang, Y.-H. Cho, M. Karuppannan, Y.-E. Sung, T. Lim, O. J. Kwon, 2022, High-performance long-term driving proton exchange membrane fuel cell implemented with chemically ordered Pt-based alloy catalyst at ultra-low Pt loading, *J. Power Sources*, **533**, 231378

22 H. A. Gasteiger, S. S. Kocha, B. Sompalli, F. T. Wagner, 2005, Activity benchmarks and requirements for Pt, Pt-alloy, and non-Pt oxygen reduction catalysts for PEMFCs, *Appl. Catal., B*, **56**, 9-35

23 L. Osmieri, A. H. A. Monteverde Videla, P. Ocón, S. Specchia, 2017, Kinetics of Oxygen Electroreduction on Me-N-C (Me = Fe, Co, Cu) Catalysts in Acidic Medium: Insights on the Effect of the Transition Metal, *J. Phys. Chem. C*, **121**, 17796-17817

24 J. Masa, A. Zhao, W. Xia, M. Muhler, W. Schuhmann, 2014, Metal-free catalysts for oxygen reduction in alkaline electrolyte: Influence of the presence of Co, Fe, Mn and Ni inclusion *Electrochim. Acta*, **128**, 271278

25 C. Zhu, Q. Shi, B. Z. Xu, S. Fu, G. Wan, C. Yang, S. Yao, J. Song, H. Zhou, D. Du, S. P. Beckman, D. Su, Y. Lin, 2018, Hierarchically porous M-N-C (M =Co and Fe) single-atom electrocatalysts with robust MNx active moieties enable enhanced ORR performance, *Adv. Energy Mater.*, **8**, 1801956

26 L. Wang, X. Wan, S. Liu, L. Xu, J. Shui, 2019, Fe-N-C catalysts for PEMFC: Progress towards the commercial application under DOE reference, *J. Energy Chem.*, **39**, 77-87

27 S. T. Thompson, A. R. Wilson, P. Zelenay, D. J. Myers, K. L. More, K. C. Neyerlin, D. Papageorgopoulos, 2018, ElectroCat: DOE's approach to PGM-free catalyst and electrode R&D, *Solid State Ion.*, **319**, 68-76

28 Y. He, G. Wu, 2022, PGM-Free Oxygen-Reduction Catalyst Development for Proton-Exchange Membrane Fuel Cells: Challenges Solutions, and Promises, *Acc. Mater. Res.*, **3**, 224-236

29 X. Zhang, L. Truong-Phuoc, T. Asset, S. Pronkin, C. Pham-Huu, 2022, Are Fe-N-C Electrocatalysts an Alternative to Pt-based Electrocatalysts for the Next Generation of Proton Exchange Membrane Fuel Cells?, *ACS Catal.*, **12**, 13853-13875

30 A. M. Damjanovic, B. Koyutürk, Y.-S. Li, D. Menga, C. Eickes, H. A. El-Sayed, H. A. Gasteiger, T.-P. Fellinger, M. Piana, 2021, Loading Impact of a PGM-Free Catalyst on the Mass Activity in Proton Exchange Membrane Fuel Cells, *J. Electrochem. Soc.*, **168**, 114518

31 F. Barbir, 2005, PEM Fuel Cells Theory and Practice, Elsevier, p. 115-145

32 T. Takahashi, T. Ikeda, K. Murata, O. Hotaka, S. Hasegawa, Y. Tachikawa, M. Nishihara, J. Matsuda, T. Kitahara, S. M. Lyth, A. Hayashi, K. Sasaki, 2022, Accelerated Durability Testing of Fuel Cell Stacks for Commercial Automotive Applications: A Case Study, *J. Electrochem. Soc.*, **169**, 044523

33 A. Mehmood, M. Gong, F. Jaouen, A. Roy, A. Zitolo, A. Khan, M.-T. Sougrati, M. Primbs, A. Martinez Bonastre, D. Fongalland, G. Drazic, P. Strasser, A. Kucernak, 2022, High loading of single atomic iron sites in Fe-NC oxygen reduction catalysts for proton exchange membrane fuel cells, *Nat. Catal.*, **5**, 311-323

34 A. J. Bard and L. R. Faulkner, 1980, Electrochemical methods: fundamentals and applications, Wiley

35 Z. Li, Z. Zheng, L. Xu, X. Lu, 2019, A review of the applications of fuel cells in microgrids: opportunities and challenges, *BMC Energy*, **1**, 8

36 J. Durst, A. Siebel, C. Simon, F. Hasche, J. Herranz, H. A. Gasteiger, 2014, New insights into the electrochemical hydrogen oxidation and evolution reaction mechanism, *Energy Environ. Sci*, **7**, 2255-2260

37 M. Fikry, Á. García-Padilla, J. Herranz, P. Khavlyuk, A. Eychmüller, T. J. Schmidt, 2024, A Comprehensive Analysis of the Overpotential Losses in Polymer Electrolyte Fuel Cells, *ACS Catal*., **14**, 1903-1913

38 T. Takahashi, T. Ikeda, K. Murata, O. Hotaka, S. Hasegawa, Y. Tachikawa, M. Nishihara, J. Matsuda, T. Kitahara, S. M. Lyth, A. Hayashi, K. Sasaki, 2022, Accelerated Durability Testing of Fuel Cell Stacks for Commercial Automotive Applications: A Case Study, *J. Electrochem. Soc.*, **169**, 044523

39 S. T. Thompson and D. Papageorgopoulos, 2019, Platinum group metal-free catalysts boost cost competitiveness of fuel cell vehicles, *Nat. Catal.*, **2**, 558–561

40 Y. Zeng, C. Li, B. Li, J. Liang, M. J. Zachman, D. A. Cullen, R. P. Hermann, E. E. Alp, B. Lavina, S. Karakalos, M. Lucero, B. Zhang, M. Wang, Z. Fen, G. Wang, J. Xie, D. J. Myers, J.-P. Dodelet, G. Wu, 2023, Tuning the thermal activation atmosphere breaks the activity-stability trade-off of Fe-N-C oxygen reduction fuel cell catalysts, *Nat. Catal.*, **6**, 1215-1227

41 R. K. Ahluwalia, X. Wang, L. Osmieri, J.-K. Peng, H. T. Chung, K. C. Neyerlin, 2019, Performance of Polymer Electrolyte Fuel Cell Electrodes with Atomically Dispersed (AD) Fe-C-N ORR Catalyst, *J. Electrochem. Soc.*, **166**, F1096-F1104

42 S. Favero, I. E. L. Stephens, M.-M. Titirici, 2024, Anion Exchange Ionomers: Design Considerations and Recent Advances – An Electrochemical Perspective, *Adv. Mater.*, **36**, 2308238

43 Y. Zhang, F. Zhang, L. Wu, X. Ge, T. Xu, 2024, An Overview of Commercial and Non-commercial Anion Exchange Membranes, Alkaline Anion Exchange Membranes for Fuel Cells: From Tailored Materials to Novel Applications, Wiley

44 S. T. Thompson, D. Peterson, D. Ho, D. Papageorgopoulos, 2020, Perspective – The Next Decade of AEMFCs: Near Term Targets to Accelerate Applied R&D, *J. Electrochem. Soc.*, **167**, 084514

45 T. J. Omasta, L. Wang, X. Peng, C. A. Lewis, J. R. Varcoe, W. E. Mustain, 2018, Importance of balancing membrane and electrode water in anion exchange membrane fuel cells, *J. Power Sources*, **375**, 205-213

46 P. G. Santori, F. D. Speck, J. Li, A. Zitolo, Q. Jia, S. Mukerjee, S. Cherevko, F. Jaouen, 2019, Effect of Pyrolysis Atmosphere and Electrolyte pH on the Oxygen Reduction Activity, Stability and Spectroscopic Signature of FeNx Moieties in Fe-N-C Catalysts, *J. Electrochem. Soc.*, **166**, F3311-F3320

47 S. Rojas-Carbonell, K. Artyushkova, A. Serov, C. Santoro, I. Matanovic, P. Atanassov, 2018, Effect of pH on the Activity of Platinum Group Metal-Free Catalysts in Oxygen Reduction Reaction, *ACS Catal.*, **8**, 3041-3953

48 A. Mehmood, B. Ali, M. Gong, M. G. Kim, J.Y. Kim, H.-H. Bae, A. Kucernak, Y.-M. Kang, K.-W. Nam, 2021, Development of a highly active Fe-N-C catalyst with the preferential formation of atomic iron sites for oxygen reduction in alkaline and acidic electrolytes, *J. Colloid Interface Sci.*, **596**, 148-157

49 H. Adabi, P. G. Santori, A. Shakouri, X. Peng, K. Yassin, I. G. Rasin, S. Brandon, D. R. Dekel, N. U. Hassan, M.-T. Sougrati, A. Zitolo, J. R. Varcoe, J. R. Regalbuto, F. Jaouen, W. E. Mustain, 2021, Understanding how single-atom site density drives the performance and durability of PGM-free Fe-N-C cathodes in anion exchange membrane fuel cells, *Mater. Today Adv.*, **12**, 100179

50 H. Adabi, A. Shakouri, N. U. Hassan, J. R. Varcoe, B. Zulevi, A. Serov, J. R. Regalbuto, W. E. Mustain, 2021, High-performing commercial Fe-N-C cathode electrocatalyst for anion-exchange membrane fuel cells, *Nat. Energy*, **6**, 834-843

51 G. W., K. L. More, C. M. Johnston, P. Zelenay, 2011, High-Performance Electrocatalysts for Oxygen Reduction Derived from Polyaniline, Iron, and Cobalt, *Science*, **332**, 443-447

52 E. Proietti, F. Jaouen, M. Lefèvre, N. Larouche, J. Tian, J. Herranz, J.-P. Dodelet, 2011, Iron-based cathode catalyst with enhanced power density in polymer electrolyte membrane fuel cells, *Nat. Commun.*, **2**, 416

53 D. E. Beltrán, S. Litster, 2019, Half-Wave Potential or Mass Activity? Characterizing Platinum Group Metal-Free Fuel Cell Catalysts by Rotating Disk Electrodes, *ACS Energy Lett.*, **4**, 1158-1161

54 F. Jaouen, D. Jones, N. Coutard, V. Artero, P. Strasser, A. Kucernak, 2018, Toward Platinum Group Metal-Free Catalysts for Hydrogen/Air Proton-Exchange Membrane Fuel Cells, *Johns. Matthey Technol. Rev.*, **62**, 231-255

55 Y. Li, Q. Li, H. Wang, L. Zhang, D. P. Wilkinson, J. Zhang, 2019, Recent progresses in oxygen reduction reaction electrocatalysts for electrochemical energy applications, *EER*, **2**, 518-538, 2019

56 C.-X. Zhao, B.-Q. Li, J.-N. Liu, Q. Zhang, 2021, Intrinsic electrocatalytic activity regulation of M-N-C single-atom catalysts for the oxygen reduction reaction, *Angew. Chem. Int. Ed.*, **60**, 4448-4463

57 D. Malko, A. Kucernak, T. Lopes, 2016, In situ electrochemical quantification of active sites in Fe-N/C non-precious metal catalysts, *Nat. Commun.*, **7**, 13285

58 Z. Chen, D. Higgins, A. Yu, L. Zhang, J. Zhang, 2011, A review on non-precious metal electrocatalysts for PEM fuel cells, *Energy Environ. Sci.*, **4**, 3167-3192

59 X. X. Wang, M. T. Swihart, G. Wu, 2019, Achievements, challenges, and perspectives on cathode catalysts in proton exchange membrane fuel cells for transportation, *Nat. Catal.*, **2**, 578-589

60 F. Luo, C. H. Choi, M. J. M. Primbs, W. Ju, S. Li, N. D. Leonard, A. Thomas, F. Jaouen, P. Strasser, 2019, Accurate evaluation of active-site density (SD) and turnover frequency (TOF) of PGM-free metal-nitrogen-doped carbon (MNC) electrocatalysts using CO Cryo Adsorption, *ACS Catal.*, **9**, 4841-4852

61 M. Primbs, Y. Sun, A. Roy, D. Malko, A. Mehmood, M.-T. Sougrati, P.-Y. Blanchard, G. Granozzi, T. Kosmala, G. Daniel, P. Atanassov, J. Sharman, C. Durante, A. Kucerank, D. Jonas, F. Jaouen, P. Strasser, 2020, Establishing reactivity descriptors for platinum group metal (PGM)-free Fe-N-C catalysts for PEM fuel cells, *Energy Environ. Sci.*, **13**, 2480-2500

62 R. Z. Snitkoff-Sol, A. Friedman, H. C. Honig, Y. Yurko, A. Kozhushner, M. J. Zachman, P. Zelenay, A. M. Bond, L. Elbaz, 2022, Quantifying the electrochemical active site density of precious metal-free catalysts in situ in fuel cells, *Nat. Catal.*, **5**, 163-170

63 J. Barrio, A. Pedersen, S. Ch. Sarma, A. Bagger, M. Gong, S. Favero, C.-X. Zhao, R. Garcia-Serres, A. Y. Li, Q. Zhang, F. Jaouen, F. Maillard, A. Kucernak, I. E. L. Stephens, M.-M. Titirici, 2023, FeNC Oxygen Reduction Electrocatalyst with High Utilization Penta-Coordinated Sites, *Adv. Mater.*, **35**, 2211022

64 A. Mehmood, J. Pampel, G. Ali, H. Y. Ha, F. Ruiz-Zepeda, T.-P. Fellinger, 2018, Facile Metal Coordination of Active Site Imprinted Nitrogen Doped Carbons for the Conservative Preparation of Non-Noble Metal Oxygen Reduction Electrocatalysts, *Adv. Energy Mater.*, **8**, 17011771

65 L. Jiao, J. Li, L. LaRochelle, Richard, Q. Sun, T. Stracensky, E. Liu, M.-T. Sougrati, Z. Zhao, F. Yang, S. Zhong, H. Xu, S. Mukerjee, Y. Huang, D. A. Cullen, J. H. Park, M. Ferrandon, D. J. Myers, F. Jaouen, Q. Jia, 2021, Chemical vapour deposition of Fe-N-C oxygen reduction catalysts with full utilization of dense Fe-N_4 sites, *Nat. Mater.*, **20**, 1385-1391

66 Z. W. Seh, J. Kibsgaard, C. F. Dickens, I. Chorkendorff, J. K. Norskov, T. F. Jaramillo, 2017, Combining theory and experiment in electrocatalysis: Insights into materials design, *Science*, **355**, eaad4998

67 Y. Xie, X. Chen, K. Sun, J. Zhang, W.-H. Lai, H. Liu, G. Wang, 2023, Direct Oxygen-Oxygen Cleavage through Optimizing Interatomic Distances in Dual Single-atom Electrocatalysts for Efficient Oxygen Reduction Reaction, *Angew. Chem. Int. Ed.*, **62**, e202301833

68 A. Kulkarni, S. Siahrostami, A. Patel, J. K. Nørskov, 2018, Understanding Catalytic Activity Trends in the Oxygen Reduction Reaction, *Chem. Rev.*, **118**, 2302-2312

69 H. Xu, D. Cheng, D. Cao, X. C. Zeng, 2024, Revisiting the universal principle for the rational design of single-atom electrocatalysts, *Nat. Catal.*, **7**, 207-218

70 N. Zhang, T. Zhou, M. Chen, H. Feng, R. Yuan, C. Zhong, W. Yan, Y. Tian, X. Wu, W. Chu, C. Wu, Y. Xie, 2020, High-purity pyrrole-type FeN_4 sites as a superior oxygen reduction electrocatalyst, *Energy Environ. Sci.*, **13**, 111-118

71 Y. Sun, L. Han, P. Strasser, 2020, A comparative perspective of electrochemical and photochemical approaches for catalytic H_2O_2 production, *Chem. Soc. Rev.*, **49**, 6605-6631

72 F. Luo, A. Roy, L. Silvioli, D. A. Cullen, A. Zitolo, M. T. Sougrati, I. C. Oguz, T. Mineva, D. Teschner, S. Wagner, J. Wen, F. Dionigi, U. I. Kramm, J. Rossmeisl, F. Jaouen, P. Strasser, 2020, P-block single-metal-site tin/nitrogen-doped carbon fuel cell cathode catalyst for oxygen reduction reaction, *Nat. Mater.*, **19**, 1215-1223

73 Y. Sun, L. Silvioli, N. R. Sahraie, W. Ju, J. Li, A. Zitolo, S. Li, A. Bagger, L. Arnarson, X. Wang, T. Moeller, D. Bernsmeier, J. Rossmeisl, F. Jaouen, P. Strasser, 2019, Activity-selectivity trends in the electrochemical production of hydrogen peroxide over single-site metal-nitrogen-carbon catalysts, *J. Am. Chem. Soc.*, **141**, 12372-12381, 2019

74 F. Calle-Vallejo, J. I. Martinez, J. Rossmeisl, 2011, Density functional studies of functionalized graphitic materials with late transition metals for oxygen reduction reactions, *Phys. Chem. Chem. Phys.*, **13**, 15639 15643

75 H. A. Hansen, V. Viswanathan, J. K. Nørskov, 2014, Unifying Kinetic and Thermodynamic Analysis of 2 e^- and 4 e^- Reduction of Oxygen on Metal Surfaces, *J. Phys. Chem. C*, **117**, 6706-6718

76 S. Liu, C. Li, M. J. Zachman, Y. Zeng, H. Yu, B. Li, M. Wang, J. Braaten, J. Liu, H. M. Meyer III, M. Lucero, A. J. Kropf, E. E. Alp, Q. Gong, Q. Shi, Z. Feng, H. Xu, G. Wang, D. J. Myers, J. Xie, D. A. Cullen, S. Litster, G. Wu, 2022, Atomically dispersed iron sites with a nitrogen-carbon coating as highly active and durable oxygen reduction catalysts for fuel cells, *Nat. Energy*, **7**, 652-663

77 Y. Wu, X. Wang, B. Tian, W. Shuang, Z. Bai, L. Yang, 2023, Optimizing reaction intermediate adsorption by engineering the coordination structure of single-atom Fe-N_5-C electrocatalysts for efficient oxygen reduction, *Inorg. Chem. Front.*, **10**, 4209-4220

78 L. Osmieri, Q. Meyer, 2022, Recent advances in integrating platinum group metal-free catalysts in proton exchange membrane fuel cells, Curr. Opin. Electrochem., 31, 100847

79 M. Qiao, M.-M. Titirici, 2018, Engineering the Interface of Carbon Electrocatalysts at the Triple Point for Enhanced Oxygen Reduction Reaction, Chem. Eur. J., 24, 18374-18384

80 G. Yang, C. H. Lee, X. Qiao, S. Komini Babu, U. Martinez, J. S. Spendelow, 2024, Advanced Electrode Structures for Proton Exchange Membrane Fuel Cells: Current Status and Path Forward, *EER*, **7**, 9

81 H. Ge, N. Bibent, K. Teixeira Santos, K. Kumar, J. Jaxel, M.-T. Sougrati, A. Zitolo, M. Dupont, F. Lecoeur, M. Mermoux, V. Martin, L. Dubau, F. Jaouen, F. Maillard, S. Berthon-Fabry, 2023, Modulating the FeN_4 Active Site Content By Nitrogen Source in Fe-N-C Aerogel Catalysts for Proton Exchange Membrane Fuel Cell, *ACS Catal.*, **13**, 1149-1163

82 S. Komini Babu, H. T. Chung, P. Zelenay, S. Litster, 2016, Resolving Electrode Morphology's Impact on Platinum Group Metal-Free Cathode Performance Using Nano-CT of 3D Hierarchical Pore and Ionomer Distribution, *ACS Appl. Mater. Interfaces*, **8**, 32764-32777

83 G. Wang, L. Osmieri, A. G. Star, J. Pfeilsticker, K. C. Neyerlin, 2020, Elucidating the Role of Ionomer in the Performance of Platinum Group Metal-free Catalyst Layer via in situ Electrochemical Diagnostics, *J. Electrochem. Soc.*, **167**, 044519

84 S. Ünsal, M. Bozzetti, U.-C. Chen, R. Girod, A. Berger, J. S. Diercks, S. Gialamoidou, J. Lyu, M. Medarde, H. A. Gasteiger, 2023, Catalyst Aggregate Size Effect on the Mass Transport Properties of Non-Noble Metal Catalyst Layers for PEMFC Cathodes*, J. Electrochem. Soc.*, **170**, 074502

85 S. Raso, M. T. Sougrati, M. Käärik, M. Merisau, Mihkel Rähn, V. Kisand, A. Kikas, P. Paiste, J. Leis, V. Sammelselg, F. Jaouen, K. Tammeveski, 2019, Effect of Ball-Milling on the Oxygen Reduction Reaction Activity of Iron and Nitrogen Co-doped Carbide-Derived Carbon Catalysts in Acid Media, *ACS Appl. Energy Mater.*, **2**, 7952-7962

86 C. Li, S. Liu, Y. Zeng, Y. Liu, G. W, D. A. Cullen, J. Xie, 2021, Effects of Ink Formulation on the Structure and Performance of PGM-Free Catalyst Layer in PEMFCs, *ECS Trans.*, **104**, 327-333

87 J. Li, S. Brüller, D. C. Sabarirajan, N. Ranjbar-Sahraie, M. T. Sougrati, S. Cavaliere, D. Jones, I. V. Zenyuk, A. Zitolo, F. Jaouen, 2019, Designing the 3D Architecture of PGM-Free Cathodes for H_2/Air Proton Exchange Membrane Fuel Cells, *ACS Appl. Energy Mater.*, **2**, 7211-7222

88 S. Kabir, S. Medina, G. Wang, G. Bender, S. Pylypenko, K. C. Neyerlin, 2020, Improving the bulk gas transport of Fe-N-C platinum group metal-free nanofiber electrodes via electrospinning for fuel cell applications, *Nano Energy*, **73**, 104791

89 V. Yarlagadda, M. K. Carpenter, T. E. Moylan, R. S. Kukreja, R. Koestner, W. Gu, L. Thompson, A. Kongkanand, 2018, Boosting Fuel Cell Performance with Accessible Carbon Mesopores, *ACS Energy Lett.*, **3**, 618-621

90 https://www.osti.gov/biblio/1440415 (Retrieved: 10.04.2024)

91 https://www.energy.gov/eere/fuelcells/doe-technical-targets-polymer-electrolyte-membrane-fuel-cell-components (Retrieved: 10.04.2024)

92 https://www.hydrogen.energy.gov/pdfs/review21/fc303_xie_2021_o.pdf (Retrieved: 10.04.2024)

93 P. Zelenay, L.A.N. Laboratory, ElectroCat 2.0 (Electrocatalysis Consortium), (n.d.) 54.

94 L. Osmieri, G. Wang, F. C. Cetinbas, S. Khandavalli, J. Park, S. Medina, S. A. Mauger, M. Ulsh, S. Pylypenko, D. J. Myers, K. C. Neyerlin, 2020, Utilizing ink composition to tune bulk-electrode gas transport, performance, and operational robustness for a Fe-N-C catalyst in polymer electrolyte fuel cell, *Nano Energy*, **75**, 104943

95 T. Reshetenko, M. Odgaard, G. Randolf, K. K. Ohtaki, J. P. Bradley, B. Zulevi, X. Lyu, D. A. Cullen, C. J. Jafta, A. Serov, A. Kulikovsky, 2022, Design of PGM-free cathodic catalyst layers for advanced PEM fuel cells, *Appl. Cat. B: Environm.*, **312**, 121424

96 S. Komini Babu, H. T. Chung, P. Zelenay, S. Litster, 2017, Modeling Electrochemical Performance of the Hierarchical Morphology of Precious Group Metal-Free Cathode for Polymer Electrolyte Fuel Cell, *J. Electrochem. Soc.*, **164**, F1037-F1049

97 P. Urbina, T. Asset, M. Secanell, P. Atanssov, J. Barralet, J. T. Gostick, 2023, Insights on designing non-PGM catalyst layers at low humidity, *J. Power Sources*, **562**, 232741

98 Y. Kim, T. Asset, F. Weo, P. Atanassov, M. Secanell, J. Barralet, J. T. Gostick, 2021, Fabrication of platinum group metal-free catalyst layer with enhanced mass transport characteristics via an electrospraying technique, *Mater. Today Energy*, **20**, 100641

99 H. Zhang, H. T. Chung, D. A. Cullen, S. Wagner, U. I. Kramm, K. L. More, P. Zelenay, G. Wu, 2019, High-performance fuel cell cathodes exclusively containing atomically dispersed iron active sites, *Energy Environ. Sci.*, **12**, 2548-2558

100 S. M. Rao, Y. Xing, 2008, Simulation of nanostructured electrodes for polymer electrolyte membrane fuel cells, *J. Power Sources*, **185**, 1094-1100

101 M. M. Hussain, D. Song, Z.-S. Liu, Z. Xie, 2011, Modeling an ordered nanostructured cathode catalyst layer for proton exchange membrane fuel cells, *J. Power Sources*, **196**, 4533-4544

102 P. Z. Lin, J. Sun, M. C. Wu, T. S. Zhao, 2022, A multiscale model for proton exchange membrane fuel cells with order-structured catalyst layers, *Int. J. Heat Mass Transf.*, **195**, 123092

103 L. Liang, Y. Wei, X. Zhang, S. Chen, F. Yu, Z. Q. Tian, P. K. Shen, 2020, 3D Model of an Order-Structured Cathode Catalyst Layer with Vertically Aligned Carbon Nanotubes for PEM Fuel Cells under the Water Flooding Condition, *ACS Sustainable Chem.*, **8**, 695-705

104 B. Batton, L. Mishchenko, S. Davis, J. Aizenberg, 2010, Assembly of large-area, highly ordered, crack-free inverse opal films, *PNAS*, **107**, 10354-10359

105 M. Lai, D. J. Riley, 2008, Templated electrosynthesis of nanomaterials and porous structures, *J. Colloid Interface Sci.*, **323**, 203-212

106 O. H. Kim, Y. H. Cho, S. H. Kang, H. Y. Park, M. Kim, J. W. Lim, D. Y. Chung, M. J. Lee, H. Choe, Y. E. Sung, 2013, Ordered macroporous platinum electrode and enhanced mass transfer in fuel cells using inverse opal structure, *Nat. Commun.*, **4**, 1-9

107 M. Qiao, Y. Wang, Q. Wang, G. Hu, X. Mamat, S. Zhag, S. Wang, 2020, Hierarchically Ordered Porous Carbon with Atomically Dispersed FeN_4 for Ultraefficient Oxygen Reduction Reaction in Proton-Exchange Membrane Fuel Cells, *Angew. Chem. Int. Ed.*, **59**, 2688-2694

108 S. Qin, S. Zhang, M. Chen, L. Wu, 2022, Electrochemical fabrication of long-range ordered macro-microporous metal-organic framework films, *J. Mater. Chem. A*, **10**, 0407-9505

109 T. Lazaridis, B. M. Stühmeier, H. A. Gasteiger, H. A. El-Sayed, 2022, Capabilities and limitations of rotating disk electrodes versus membrane electrode assemblies in the investigation of electrocatalysts, *Nat. Catal.*, **5**, 363-373

110 S. Zaman, X. Tian, B. Y. Xia, 2023, Bridging oxygen reduction performance gaps in half and full cells: challenges and perspectives, *Mater. Chem. Front.*, **7**, 4605-4612

111 E. Luo, Y. Chu, J. Liu, Z. Shi, S. Zhy, L. Gong, J. Ge, C. H. Choi, C. Li, W. Xing, 2021, Pyrolyzed M-N_x catalysts for oxygen reduction reaction: progress and prospects, *Energy Environ. Sci.*, **14**, 2158-2185

112 S. Xu, Y. Kim, D. Higgins, M. Yusuf, T. F. Jaramillo, F. B. Prinz, 2017, Building upon the Koutecky-Levich Equation for Evaluation of Next-Generation Oxygen Reduction Reaction Catalysts, *Electrochim. Acta*, **255**, 99-108

113 G. Zhong, S. Xu, L. Liu, C. Z. Zheng, J. Dou, F. Wang, X. Fu, W. Liao, H. Wang, 2020, Effect of Experimental Operations on the Limiting Current Density of Oxygen Reduction Reaction Evaluated by Rotating-Disk Electrode, *ChemElectroChem*, **7**, 1107-1114

114 X. Cheng, J. You, S. Shen, G. Wie, X. Yan, C. Wang, J. Zhang, 2022, An ingenious design of nanoporous nafion film for enhancing the local oxygen transport in cathode catalyst layers of PEMFCs, *J. Chem. Eng.*, **439**, 135387

115 C. Wang, X. Cheng, J. Lu, S. Shen, X. Yan, J. Yin, G. Wie, J. Zhang, 2017, The Experimental Measurement of Local and Bulk Oxygen Transport Resistances in the Catalyst Layer of Proton Exchange Membrane Fuel Cells, *J. Phys. Chem. Lett.*, **8**, 5848-5852

116 J. Shui, C. Chen, L. Grabstanowicz, D. Zhao, D.-J. Liu, 2015, Highly efficient nonprecious metal catalyst with metal-organic framework in a continuous carbon nanofibrous network, P*NAS*, **112**, 10629-10634

117 Q. Liu, X. Liu, L. Zheng, J. Shui, 2018, The Solid-Phase Synthesis of an Fe-N-C Electrocatalyst for High-Power Proton-Exchange Membrane Fuel Cells, *Angew. Chem. Ind Ed.*, **57**, 1204-1208

118 C. M. Zalitis, D. Kramer, A. R. Kucernak, 2013, Electrocatalytic performance of fuel cell reactions at low catalyst loading and high mass transport, *Phys. Chem. Chem. Phys.*, **15**, 4329-4340

119 B. A. Pinaud, A. Bonakdarpour, L. Daniel, J. Sharman, D. P. Wilkinson, 2017, Key Considerations for High Current Fuel Cell Catalyst Testing in an Electrochemical Half-Cell, *J. Electrochem. Soc.*, **164**, F321-F327

120 K. Ehelebe, D. Seeberger, M. T. Y. Paul, S. Thiele, K. J. J. Mayrhofer, S. Cherevko, 2019, Evaluating Electrocatalysts at Relevant Currents in a Half-Cell: The Impact of Pt Loading on Oxygen Reduction Reaction, *J. Electrochem. Soc*., **166**, F1259-F1268

121 N. Schmitt, M. Schmidt, G. Hübner, B. J. M. Etzold, 2022, Oxygen reduction reaction measurements on platinum electrocatalysts in gas diffusion electrode half-cells: Influence of electrode preparation, measurement protocols and common pitfalls, *J. Power Sources*, **539**, 231530

122 G. K. H. Wiberg, M. Fleige, M. Arenz, 2015, Gas diffusion electrode setup for catalyst testing in phosphoric acid at elevated temperatures, *Rev. Sci. Instrum.*, **86**, 024102

123 M. Inaba, A. W. Jensen, G. W. Sievers, M. Escudero-Escribano, A. Zana, M. Arenz, 2018, Benchmarking high surface area electrocatalysts in a gas diffusion electrode: measurement of oxygen reduction activities under realistic conditions, *Energy Environ. Sci.*, **11**, 988-994

124 K. Ehelebe, N. Schmitt, G. Sievers, A. W. Jensen, A. Hrnjić, P. C. Jiménez, P. Kaiser, M. Geuß, Y.-P. Ku, P. Jovanovič, K. J. J. Mayrhofer, B. Etzold, N. Hodnik, M. Escudero-Escribano, M. Arenz, S. Cherevko, 2022, Benchmarking Fuel Cell Electrocatalysts Using Gas Diffusion Electrodes: Inter-lab Comparison and Best Practices, *ACS Energy Lett.*, **7**, 816-826

125 G. K. H. Wiberg, S. Nösberger, M. Arenz, 2022, Evolution of a GDE setup: Beyond ambient conditions, *Curr. Opin. Electrochem.*, **36**, 101129

126 S. Alinejad, J. Quinson, J. Schröder, J. J. K. Kirkensgaard, M. Arenz, 2020, Carbon-Supported Platinum Electrocatalysts Probed in a Gas Diffusion Setup with Alkaline Environment : How Particle Size and Mesoscopic Environment Influence the Degradation Mechanism, *ACS Catal.*, **10**, 13040-13049

127 V. Gridin, J. Du, S. Haller, P. Theis, K. Hofmann, G. K. H. Wiberg, U. I. Kramm, M. Arenz, 2023, GDE vs RDE: Impact of operation conditions on intrinsic catalytic parameters of FeNC catalyst for the oxygen reduction reaction, *Electrochim. Acta*, **444**, 142012

128 K. Xiao, L. Chen, L. Jiang, M. Antonietti, 2020, Carbon nitride nanotube for ion transport based photo-rechargeable electric energy storage, *Nano Energy*, **67**, 104230

129 https://www.fuelcellstore.com/spec-sheets/fumapem-faa-3-50-technical-specifications.pdf

130 https://www.fuelcellstore.com/versogen-piperion-aem-mechanically-reinforced-15um-73800004

131 https://dioxidematerials.com/product/sustainion-anion-exchange-membrane/

132 A. Kusoglu, A. Kwong, K. T. Clark, H. P. Gunterman, A. Z. Weber, 2012, Water Uptake of Fuel-Cell Catalyst Layers, *J. Electrochem. Soc.*, **159**, F530-F535

133 J. Rouquerol, F. Rouquerol, K. S. W. Sing, P. Llewellyn, and G. Maurin, "Adsorption by powders and porous solids: principles." Methodology and Applications (Academic, New York) (2014)

134 K. Kawashima, R. A. Márquez, Y. J. Son, C. Guo, R. R. Vaidyula, L. A. Smith, C. E. Chukwuneke, C. B. Mullins, 2023, Accurate Potentials of Hg/HgO Electrodes: Practical Parameters or Reporting Alkaline Water Electrolysis Overpotentials, *ACS Catal.*, **13**, 1893-1898

135 P. Lauf, V. Lloret, M. Geuß, C. C. Collados, M. Thommes, K. J. J. Mayrhofer, K. Ehelebe, S. Cherevko, 2023, Characterization of Oxygen and Ion Mass Transport Resistance in Fuel Cell Catalyst Layers in Gas Diffusion Electrode Setups, J. *Electrochem. Soc.*, **170**, 064509

136 G. Wang, L. Zou, Q. Huang, Z. Zou, H. Yang, 2019, Multidimensional nanostructured membrane electrode assemblies for proton exchange membrane fuel cell applications, *J. Mater. Chem. A*, **7**, 9447-9477

137 Y. Lu, S. Du, R. Steinberger-Wilckens, 2016, One-dimensional nanostructured electrocatalysts for polymer electrolyte membrane fuel cells-a review, *Appl. Catal. B.: Environ.*, **199**, 292-314

138 S. Du, 2021, Recent advances in electrode design based on one-dimensional nanostructure arrays for proton exchange membrane fuel cell applications, *Engineering*, **7**, 33-49

139 A. Baricci, A. Bisello, A. Serov, M. Odgaard, P. Atanassov, A. Casalegno, 2019, Analysis of the effect of catalyst layer thickness on the performance and durability of platinum group metal-free catalysts for polymer electrolyte membrane fuel cells, *Sustain. Energy Fuels*, **3**, 3375-3386

140 Y. Sun, S. Polani, F. Luo, S. Ott, P. Strasser, F. Dionigi, 2021, Advancements in cathode catalyst and cathode layer design for proton exchange membrane fuel cells, *Nat. Commun.*, **12**, 5984

141 S. Stariha, K. Artyushkova, M. J. Workman, A. Serov, S. Mckinney, B. Halevi, P. Atanassov, 2016, PGM-free Fe-NC catalysts for oxygen reduction reaction: Catalyst layer design, *J. Power Sources*, **326**, 43-49

142 E. Middelman, 2002, Improved PEM fuel cell electrodes by controlled self-assembly, *Fuel Cells Bull.*, **2022**, 9-12

143 S. Galbiati, A. Morin, N. Pauc, 2015, Nanotubes array electrodes by Pt evaporation: Half-cell characterization and PEM fuel cell demonstration, *Appl. Catal. B: Environ.*, **165**, 149-157

144 S. Galbiati, A. Morin, N. Pauc, 2014, Supportless platinum nanotubes array by atomic layer deposition PEM fuel cell electrode, *Electrochim. Acta*, **125**, 107-116

145 D. C. Sabarirajan, T. Y. George, J. Vlahakis, R. D. White, I. V. Zenyuk, 2019, Atomic layer deposition of Pt nanoelectrode array for polymer electrolyte fuel cells, *J. Electrochem. Soc.*, **166**, F3081-F3088

146 T. Hatanakaa, H. Nakanishib, S. Matsumotob, Y. Morimoto, 2006, PEFC Electrodes Based on Vertically Oriented Carbon Nanotubes, *ECS Trans.*, **3**, 277-284

147 W. Zhang, A. I. Minett, M. Gao, J. Zhao, J. M. Razal, G. G. Wallace, T. Romeo, J. Chen, 2011, Integrated High-Efficiency Pt/Carbon Nanotube Arrays for PEM Fuel Cells, *Adv. Energy Mater.*, **1**, 671-677

148 W. Zhang, J. Chen, A. I. Minett, G. F. Swiegers, C. O. Too, G. G. Wallace, 2010, Novel ACNT arrays based MEA structure-nano-Pt loaded ACNT/Nafion/ACNT for fuel cell applications, *Chem. Commun.*, **46**, 4824-4826

149 Z. Q. Tian, S. H. Lim, C. K. Poh, Z. Tang, Z. Xia, Z. Luo, P. K. Shen, D. Chua, Y. P. Feng, Z. Shen, J. Lin, 2011, A highly order-structured membrane electrode assembly with vertically aligned carbon nanotubes for ultra-low Pt loading PEM fuel cells, *Adv. Energy. Mater.*, **1**, 1205-1214

150 X. Meng, X. Deng, L. Zhou, B. Hu, W. Tan, W. Zhou, M. Liu, Z. Shao, 2021, A highly ordered hydrophilic-hydrophobic janus bi-functional layer with ultralow Pt Loading and Fast Gas/Water Transport for Fuel Cells, *Energy Environ. Mater.*, **4**, 126-133

151 Q. H. Meng, C. Hao, B. Yan, B. Yang, J. Liu, P. K. Shen, Z. Q. Tian, 2022, High-performance proton exchange membrane fuel cell with ultra-low loading Pt on vertically aligned carbon nanotubes as integrated catalyst layer, *J. Energy Chem.*, **71**, 497-506

152 S. Murata, M. Imanishi, S. Hasegawa, R. Namba, 2014, Vertically aligned carbon nanotube electrodes for high current density operating proton exchange membrane fuel cells, *J. Power Sources*, **253**, 104-113

153 P. A. Cirkel, T. Okada, S. Kinugasa, 1999, Equilibrium aggregation in perfluorinated ionomer solutions, *Macromol.*, **32**, 531-533

154 C.-H. Ma, T. L. Yu, H.-L. Lin, Y.-T. Huang, Y.-L. Chen, U.-S. Jeng, Y.-H. Lai, Y.-S. Sun, 2009, Morphology and properties of Nafion membranes prepared by solution casting, *Polymer*, **50**, 1764-1777

155 M. S. Saha, R. Li, X. Sun, 2008, High loading and monodispersed Pt nanoparticles on multiwalled carbon nanotubes for high performance proton exchange membrane fuel cells, *J. Power Sources*, **177**, 314-322

156 A. A. Zasypkina, N. A. Ivanova, D. D. Spasov, R. M. Mensharapov, O. K. Alekseeva, E. A. Vorobyeva, E. V. Kukueva, V. N. Fateev, 2023, Electrode with a Carbon Nanotube Array for a Proton Exchange Membrane Fuel Cell, *Inorganics*, **11**, 219

157 Q. Guo, D. Zhao, S. Liu, S. Chen, M. Hanif, H. Hou, 2014, Free-standing nitrogen-doped carbon nanotubes at electrospun carbon nanofibers composite as an efficient electrocatalyst for oxygen reduction, *Electrochim. Acta*, **138**, 318-324

158 P. Mardle, X. Ji, J. Wu, S. Guan, H. Dong, S. Du, 2020, Thin film electrodes from Pt nanorods supported on aligned N-CNTs for proton exchange membrane fuel cells, *Appl. Catal. B.: Environ.*, **260**, 118031

159 Y. Pei, W. Zhu, R. Yue, L. Wang, R. Li, J. Zhang, Y. Yin, 2024, Controllable construction of Pt/CNT catalyst layers to improve Pt utilization in PEMFCs, *J. Mater. Chem. A*, **12**, 739

160 R. Liu, W. Zhou, W. Ling, S. Li, F. Li, 2021, Performance optimization of ultra-low platinum loading membrane electrode assembly prepared by electrostatic spraying, *Int. J. Hydrog. Energy*, **46**, 10457-10467

161 J. Yang, D.-J. Liu, N. N. Kariuki, L. X. Chen, 2008, Aligned carbon nanotubes with built-in FeN4 active sites for electrocatalytic reduction of oxygen, *Chem. Commun.*, **2008**, 329-331

162 J.-C. Li, P.-X. Hou, C. Shi, S.-Y. Zhao, D.-M. Tang, M. Cheng, C. Liu, H.-M. Cheng, 2016, Hierarchically porous Fe-N-doped carbon nanotubes as efficient electrocatalyst for oxygen reduction, *Carbon*, **109**, 632-639

163 G. C.-K. Liu, J. R. Dahn, 2008, Fe-NC oxygen reduction catalysts supported on vertically aligned carbon nanotubes, *Appl. Catal. A: Gen.*, **347**, 43-49

164 K. Gong, F. Du, Z. Xia, M. Durstock, L. Dai, 2009, Nitrogen-doped carbon nanotube arrays with high electrocatalytic activity for oxygen reduction, *Science*, **323**, 760-764

165 Z. Mo, S. Liao, Y. Zheng, Z. Fu, 2012, Preparation of nitrogen-doped carbon nanotube arrays and their catalysis towards cathodic oxygen reduction in acidic and alkaline media, *Carbon*, **50**, 2620-2627

166 H. Masuda, K. Fukuda, 1995, Ordered metal nanohole arrays made by a two-step replication of honeycomb structures of anodic alumina, *Science*, **268**, 1466-1468

167 O. Jessensky, F. Müller, U. Gösele, 1998, Self-organized formation of hexagonal pore arrays in anodic alumina, *Appl. Phys. Lett.*, **72**, 1173-1175

168 B. Koyuturk, E. M. Farber, F. E. Wagner, T.-P. Fellinger, D. Eisenberg, 2022, A simple decagram-scale synthesis of an atomically dispersed, hierarchically porous Fe-N-C catalyst for acidic ORR, *J. Mater. Chem. A*, **10**, 19859

169 S. Liu, M. Wang, X. Yang, Q. Shi, Z. Qiao, M. Lucero, Q. Ma, K. L. More, D. A. Cullen, Z. Feng, G. Wu, 2020, Chemical vapor deposition for atomically dispersed and nitrogen coordinated single metal site catalysts, *Angew. Chem. Int. Ed.*, **59**, 21698-21705

170 Y. Ji, Y. Song, Y. Huang, H. Zhu, C. Yue, F. Liu, J. Zhao, 2022, One-Step Synthesis of Ultrathin Zeolitic Imidazole Framework-8 (ZIF-8) Membrane on Unmodified Porous Support via Electrophoretic Deposition, *Membranes*, **12**, 1062

171 R. Li, B. Lu, Z. Xie, J. Zhai, 2019, The Confinement Effect of Angstrom-Sized Pores in Asymmetrical Membrane Constructed by Zeolitic Imidazolate Frameworks: Partially Dehydrated Ion Transport Performance, *Small*, **15**, 1904866

172 Y. Guo, H. Huang, Z. Li, X. Wang, P. Li, Z. Deng, X. Peng, 2019, Sulfonated sub-nanochannels in a robust MOF membrane: Harvesting salinity gradient power, *ACS Appl. Interfaces*, **11**, 35496-35500

173 A. Ronte, P. Wagle, G. Mahmodi, M. Chevula, S. Dangwal, M. R. Saeb, J. S. Lee, D. N. McIlroy, S.-K. Kim, 2023, High-flux ZIF-8 membranes on ZnO-coated supports for propane/propylene separation, *Energy Fuels*, **37**, 8456-8464

174 S. Öztürk, N. Taşaltin, N. Kilinç, Z. Z. Öztürk, 2009, Fabrication of ZnO nanotubes using AAO template and sol-gel method, *J. Optoelectron. Biomed. Mater.*, **1**, 15-19

175 S. Yue, Z. Yan, Y. Shi, G. Ran, 2013, Synthesis of zinc oxide nanotubes within ultrathin anodic aluminum oxide membrane by sol-gel method, *Mater. Lett.*, **98**, 246-249

176 I. Stassen, M. Styles, G. Grenci, H. Van Gorp, W. Vanderlinden, S. De Feyter, P. Falcaro, D. De Vos, P. Vereecken, R. Ameloot, 2016, Chemical vapour deposition of zeolitic imidazolate framework thin films, *Nat. Mater.*, **15**, 304-310

177 H. Bahadur, A. Srivastava, R. Sharma, S. Chandra, 2007, Morphologies of sol-gel derived thin films of ZnO using different precursor materials and their nanostructures, *Nanoscale Res. Lett.*, **2**, 469-475

178 C. Yuanqing, Y. Fuxue, Z. Gaoyang, W. Zhezhe, 2011, Photosensitive sol-gel preparation and direct micro-patterning of c-oriented ZnO film, *Appl. Surf. Sci.*, **257**, 6817-6820

179 E. Hosono, S. Fujihara, T. Kimura, J. Imai, 2004, Growth of layered basic zinc acetate in methanolic solutions and its pyrolytic transformation into porous zinc oxide films, *J. Colloid Interface Sci.*, **272**, 391-398

180 J. Li, D. Yang, X. Zhu, 2017, Effects of aging time and annealing temperature on structural and optical properties of sol-gel ZnO thin films, *AIP Advances*, **7**, 065213

181 L. Znaidi, 2010, Sol-gel-deposited ZnO thin films: A review, *Mater. Sci. Eng. B.*, **174**, 18-30

182 W.-C. Wang, J. Wang, Y. Liao, L. Zhang, B. Cao, G. Song, X. She, 2010, Surface initiated ATRP of acrylic acid on dopamine-functionalized AAO membranes, *J. Appl. Polym. Sci.*, **117**, 534-541

183 X. She D. Yang, D. Jing, F. Yuan, W. Yang, L. Guo, Y. Che, 2014, Nitrogen-doped one-dimensional (1D) macroporous carbonaceous nanotube arrays and their application in electrocatalytic oxygen reduction reactions, *Nanoscale*, **6**, 11057-11061

184 K. Ghosh, M. Kumar, T. Maruyama, Y. Ando, 2010, Controllable growth of highly N-doped carbon nanotubes from imidazole: a structural, spectroscopic and field emission study, *J. Mater. Chem.*, **20**, 4128-4134

185 M. Alsawat, T. Altalhi, A. Santos, D. Losic, 2016, Facile and controllable route for nitrogen doping of carbon nanotubes composite membranes by catalyst-free chemical vapour deposition, *Carbon*, **106**, 295-305

186 A. J. Maeland, R. Rittenhouse, W. Lahar, P. V. Romano, 1974, Infrared reflection-absorption spectra of anodic oxide films on aluminum, *Thin Solid Films*, **21**, 67-72

187 A. H. A. Rahim, S. R. Majid, 2023, Ni/Co-based zeolitic-imidazolate framework pseudocapacitance in symmetrical cells, *J. Appl. Electrochem.*, **53**, 1727-1737

188 H. Zhang, M. Zhao, Y. Yang, Y. S. Lin, 2019, Hydrolysis and condensation of ZIF-8 in water, *Microporous Mesoporous Mat.*, **288**, 109568

189 Y. Zhang, Y. Jia, M. Li, L. Hou, 2018, Influence of the 2-methylimidazole/zinc nitrate hexahydrate molar ratio on the synthesis of zeolitic imidazolate framework-8 crystals at room temperature, *Sci. Rep.*, **8**, 9597

190 S. Wang, S. Zhang, 2017, Study on the structure activity relationship of ZIF-8 synthesis and thermal stability, *J. Inorg. Organomet. Polym.*, **27**, 1317-1322

191 B. Hachuła, M. Nowak, K. Kusz, 2010, Crystal and molecular structure analysis of 2-methylimidazole, *J. Chem Crystallogra.*, **40**, 201-206

192 G. Hu, H. Zhang, W. Di, T. Zhao, 2009, Study on Wet Etching of AAO Template, *Appl. Phys. Res.*, **1**, 78-82

193 C.-W. Lee, H.-S. Kang, Y.-H. Chang, Y.-M. Hahm Korean, 2000, Thermotreatment and chemical resistance of porous alumina membrane prepared by anodic oxidation, *J. Chem. Eng.*, **17**, 266-272

194 J. Guo, Y. Xu, C. Wang, 2011, Sulfur-Impregnated Disordered Carbon Nanotubes Cathode for Lithium-Sulfur Batteries, *Nano Lett.*, **11**, 4288-4292

195 S.-W. Bian, Z. Ma, W.-G. Song, 2009, Preparation and characterization of carbon nitride nanotubes and their applications as catalyst supporter, *J. Phys. Chem. C*, **113**, 8668-8672

196 E. Fleming, F. Du, E. Ou, L. Dai, L. Shi, 2019, Thermal conductivity of carbon nanotubes grown by catalyst-free chemical vapor deposition in nanopores, *Carbon*, **145**, 195-200

197 S. Kubo, I. Tan, R. J. White, M. Antonietti, M.-M. Titirici, 2010, Template synthesis of carbonaceous tubular nanostructures with tunable surface properties, *Chem. Mater.*, **22**, 6590-6597

198 T. Kyotani, L. Tsai, A. Tomita, 1996, Preparation of ultrafine carbon tubes in nanochannels of an anodic aluminum oxide film, *Chem. Mater.*, **8**, 2109-2113

199 Z. Wen, Q. Wang, J. Li, 2008, Template synthesis of aligned carbon nanotube arrays using glucose as a carbon source: Pt decoration of inner and outer nanotube surface for fuel-cell catalysts, *Adv. Funct. Mater.*, **18**, 959-964

200 A. M. Lindo, E. Pellicer, M. A. Zeeshan, R. Grisch, F. Qiu, J. Sort, M. S. Sakar, B. J. Nelson, S. Pané, 2015, The biocompatibility and anti-biofouling properties of magnetic core-multishell Fe@ C NWs-AAO nanocomposite, *Phys. Chem. Chem. Phys.*, **17**, 13274-13279

201 G. L. Hornyak, A. C. Dillon, P. A. Parilla, J. J. Schneider, N. Czap, K. M. Jones, F. S. Fasoon, A. Mason, M. J. Heben, 1999, Template synthesis of carbon nanotubes, *Nanostructured Materials*, **12**, 83-88

202 L. Zhi, J. Wu, J. Li, U. Kolb, K. Müllen, 2005, Carbonization of Disclike Molecules in Porous Alumina Membranes: Toward Carbon Nanotubes with Controlled Graphene-Layer Orientation, *Angew. Chem. Int. Ed.*, **44**, 2120-2123

203 C. Venkateswara Rao, C. R. Cabrera, Y. Ishikawa, 2010, In search of the active site in nitrogen-doped carbon nanotube electrodes for the oxygen reduction reaction, *J. Phys. Chem. Lett.*, **1**, 2622-2627

204 H. Zhan, D. J. Garrett, N. V. Apollo, K. Ganesan, D. Lau, S. Prawer, J. Cervenka, 2016, Direct fabrication of 3D graphene on nanoporous anodic alumina by plasma-enhanced chemical vapor deposition, *Sci. Rep.*, **6**, 19822

205 M. Aramesh, K. Fox, D. W. M. Lau, J. Fang, K. Ostrikov, S. Prawer, J. Cervenka, 2014, Multifunctional three-dimensional nanodiamond-nanoporous alumina nanoarchitectures, *Carbon*, **75**, 452-464

206 H. Liu, Z.-Z. Pan, A. Aziz, R. Tang, W. Lv., H. Nishihara, 2023, Nanoporous membrane electrodes with an ordered array of hollow giant carbon nanotubes, *Adv. Funct. Mater.*, **33**, 2303730

207 M. Golshadi, L. Nguyen, I. M. Dickerson, M. G. Schrlau, 2021, Template-Based Farbication of Vertically Aligned Carbon Nanotube Arrays, *JMEST*, **8**, 13358-13369

208 A. Yin, H. Chik, J. Xu, 2004, Postgrowth processing of carbon nanotube arrays-enabling new functionalities and applications, *IEEE TNANO*, **3**, 147-151

209 P. P. Mardilovich, A. N. Govyadinov, N. I. Mazurenko, R. Paterson, 1995, New and modified alumina membranes part II. Comparison of solubility of amorphous (normal) and polycrystalline anodic alumina membranes, *J. Membr. Sci.*, **98**, 143-155

210 I. V. Roslyakov, I. V. Kolesnik, E. E. Levin, N. S. Katorova, P. P. Pestrikov, T. Y. Kardash, L. a. Solovyov, K. S. Napolskii, 2020, Annealing induced structural and phase transitions in anodic aluminum oxide prepared in oxalic acid electrolyte, *Surf. Coat. Technol.*, **381**, 125159

211 I. V. Gasenkova, N. I. Mukhurov, S. P. Zhvavyi, E. E. Kolesnik, A. P. Stupak, 2017, Photoluminescent properties of nanoporous anodic alumina doped with manganese ions, *J. Lumin.*, **185**, 298-305

212 L. Kovarik, M. Bowden, J. Szanyi, 2021, High temperature transition aluminas in δ-Al_2O_3/θ-Al_2O_3 stability range: Review, *J. Catal.*, **393**, 357-368

213 C. Y. Han, Z.-L. Xiao, H. H. Wang, X.-M. Lin, S. Trasobares, R. E. Cook, 2009, Facile synthesis of highly aligned multiwalled carbon nanotubes from polymer precursor, *J. Nanomater.*, **2009**, 562376

214 R. Gloukhovski, V. Freger, Y. Tsur, 2016, A novel composite nafion/anodized aluminum oxide proton exchange membrane, *Fuel Cells*, **16**, 434-443

215 Z. Yang, J. Li, Q. Zhang, Y. Ling, X. Yu, W. Cai, 2017, High durability and performance of a platinum electrocatalyst supported on sulfonated macromolecules coated carbon nanotubes, *ChemCatChem*, **9**, 4005-4012

216 T. Fugigaya, N. Nakashima, 2013, Fuel Cell Electrocatalyst Using Polybenzimidazole-Modified Carbon Nanotubes As Support Materials, *Adv. Mater.*, **25**, 1666-1681

217 Y. Ju, O. Kwon, O. S. Jeon, S. Yim, Y. Jeon, Y.-G. Shul, 2023, Effective single web-structured electrode for high membrane electrode assembly performance in polymer electrolyte membrane fuel cell, *Sci. Adv.*, **9**, eadf4863

218 J. W. Elam, D. Routkevitch, P. P. Mardilovich, S. M. George, 2003, Conformal coating on ultrahigh-aspect-ratio nanopores of anodic alumina by atomic layer deposition, *Chem. Mater.*, **15**, 3507-3517

219 H. Deng, Q. Li, J. Liu, F. Wang, 2017, Active sites for oxygen reduction reaction on nitrogen-doped carbon nanotubes derived from polyaniline, *Carbon*, **112**, 219-229

220 Y. Xia, R. Mokaya, 2006, Synthesis of ordered mesoporous carbon and nitrogen-doped carbon materials with graphitic pore walls via a simple chemical vapor deposition method, *Adv. Mater.*, **16**, 1553-1558

221 Z. Mo, S. Liao, Y. Zheng, Z. Fu, 2012, Preparation of nitrogen-doped carbon nanotube arrays and their catalysis towards cathodic oxygen reduction in acidic and alkaline media, *Carbon*, **50**, 2620-2627

222 D. Geng, H. Liu, Y. Chen, R. Li, X. Sun, S. Ye, S. Knights, 2011, Non-noble metal oxygen reduction electrocatalysts based on carbon nanotubes with controlled nitrogen contents, *J. Power Sources*, **196**, 1795-1801

223 Z. Chen, D. Higgins, Z. Chen, 2010, Nitrogen doped carbon nanotubes and their impact on the oxygen reduction reaction in fuel cells, *Carbon*, **48**, 3057-3065

224 D. Mattia, M. P. Rossi, B. M. Kim, G. Korneva, H. H. Bau, Y. Gogotsi, 2006, Effect of graphitization on the wettability and electrical conductivity of CVD-carbon nanotubes and films*, J. Phys. Chem. B*, **110**, 9850-9855

225 W. Ding, Z. Wei, S. Chen, X. Qi, T. Yang, J. Hu, D. Wang, L.-J. Wan, S. F. Alvi, L. Li, 2013, Space-confinement-induced synthesis of pyridinic-and pyrrolic-nitrogen-doped graphene for the catalysis of oxygen reduction, *Angew. Chem.*, **125**, 11971-11975

226 J. Shui, M. Wang, F. Du, L. Dai, 2015, N-doped carbon nanomaterials are durable catalysts for oxygen reduction reaction in acidic fuel cells, *Sci. Adv.*, **1**, e1400129

227 H. Hasimoto, S. Kojima, T. Sasaki, H. Asoh, 2018, α-Alumina membrane having a hierarchical structure of straight macropores and mesopores inside the pore wall, *J. Eur. Ceram. Soc.*, **38**, 1936-1840

228 F. Han, O. Qian, G. Meng, D. Lin, G. Chen, S. Zhang, Q. Pan, X. Zhang, X. Zhu, B. Wie, 2022, Structurally integrated 3D carbon tube grid-based high-performance filter capacitor, *Science*, **377**, 1004-1007

229 Q. Pan, Y. Wang, B. Chen, X. Zhang, D. Lin, S. Yan, F. Han, H. Zhao, G. Meng, 2024, Pt Single-Atoms on Structurally-Integrated 3D N-Doped Carbon Tubes Grid for Ampere-Level Current Density Hydrogen Evolution, *Small*, **2024**, 2309067

230 L. Fan, H. Deng, Y. Zhang, Q. Du, D. Y. C. Leung, Y. wang, K. Jiao, 2023, Towards ultralow platinum loading proton exchange membrane fuel cells, *Energy Environ. Sci.*, **16**, 1466-1479

231 Y. Deng, J. Luo, B. Chi, H. Tang, J. Li, X. Qiao, Y. Shen, Y. Yang, C. Ja, P. Rao, S. Liao, X. Tian, 2021, Advances atomically dispersed metal-nitrogen-carbon catalysts toward cathodic oxygen reduction in PEM fuel cells, *Adv. Energy Mater.*, **11**, 2101222

232 M. M. Hossen, M. S. Hasan, M. R. I. Sardar, J. bin Haider, Mottakin, K. Tammeveski, P. Atanassov, 2023, State-of-the-art and developmental trends in platinum group metal-free cathode catalyst for anion exchange membrane fuel cell (AEMFC), *Appl. Catal. B: Environ.*, **325**, 121733

233 M. Gong, A. Mehmood, B. Ali, K.-W. Nam, A. Kucernak, 2023, Oxygen Reduction Reaction Activity in Non-Precious Single-Atom (M-N/C) Catalysts – Contribution of Metal and Carbon/Nitrogen Framework-Based Site, *ACS Catal.*, **13**, 6661-6674

234 X. Zhang, L. Truong-Phuoc, T. Asset, S. Pronkin, C. Pham-Huu, 2022, Are Fe-N-C electrocatalysts an alternative to Pt-based electrocatalysts fort he next generation of proton exchange membrane fuel cells?, *ACS Catal.*, **12**, 13853-13975

235 T. Lopes, A. Kucernak, D. Malko, E. A. Ticianelli, 2016, Mechanistic insights into the oxygen reduction reaction on metal-N-C electrocatalysts under fuel cell conditions, *ChemElectroChem*, **3**, 1580-1590

236 X. Yang, Y. Wang, G. Zhang, L. Du, L. Yang, M. Markiewicz, J. Choi, R. Chenitz, S. Sun, 2020, SiO2-Fe/N/C catalyst with enhanced mass transport in PEM fuel cells, *Appl. Cat. B.: Environ.*, **264**, 118523

237 X. Wan, X. Liu, Y. Li, R. Yu, L. Zheng, W. Yan, H. Wang, M. Xu, J. Shui, 2019, Fe-N-C electrocatalyst with dense active sites and efficient mass transport for high-performance proton exchange membrane fuel cells, *Nat. Catal.*, **2**, 259-268

238 C. Shao, S. Zhuang, H. Zhang, Q. Jiang, X. Xu, J. Ye, B. Li, X. Wang, 2021, Enhancement of Mass Transport for Oxygen Reduction Reaction Using Petal-Like Porous Fe-NC Nanosheet, *Small*, **17**, 2006178

239 S.-H. Park, D.-H. Park, J.-H. Byeon, M.-H. Kim, Y. Gu, D.-M. Lim, J.-H. Kim, J.-S. Jang, C.-E. Hong, D.-G. Seo, J.-I. Han, K.-W. Park, 2024, Tri-doped mesoporous carbon nanostructures prepared via template method for enhanced oxygen reduction reaction, *Carbon*, **218**, 2024, 118666

240 S. Chen, S. Xiang, Z. Tan, H. Li, X. Yan, J. Yin, S. Shen, J. Zhang, 2023, Exploration of the oxygen transport behavior in non-precious metal catalyst-based cathode catalyst layer for proton exchange membrane fuel cells, *Front. Energy*, **17**, 123-133

241 A. G. Star, G. Wang, S. Medina, S. Pylypenko, K. C. Neyerlin, 2020, Mass transport characterization of platinum group metal-free polymer electrolyte fuel cell electrodes using a differential cell with an integrated electrochemical sensor, *J. Power Sources*, **450**, 227655

242 A. Serov, A. D. Shum, X. Xiao, V. De Andrade, K. Artyushkova, I. V. Zenyuk, P. Atanassov, 2018, Nano-structured platinum group metal-free catalysts and their integration in fuel cell electrode architectures, *Applied. Cat. B: Environ.*, **237**, 1139-1147

243 M. Atwa, X. Li, Z. Wang, S. Dull, S. Xu, X. Tong, R. Tang, H. Nishihara, F. Prinz, V. Birss, 2021, Scalable nanoporous carbon films allow line-of-sight 3D atomic layer deposition of Pt: towards a new generation catalyst layer for PEM fuel cells, *Mater. Horiz.*, **8**, 2451-2462

244 S. Kumar, M. Srivastava, 2015, Mesophase formation behavior in petroleum residues, *Carbon Lett.*, **16**, 171-182

245 S. Lee, Y. Eom, B. J. Kim, I. Mochida, S. H. Yoon, B. C. Kim, 2015, The thermotropic liquid crystalline behavior of mesophase pithcees with different chemical structures, *Carbon*, **81**, 694-701

246 J. D. Brooks, G. H. Taylor, 1965, The formation of graphitizing carbons from the liquid phase, *Carbon*, **3**, 185-186

247 Z. Li, M. Jaroniec, 2001, Colloidal imprinting: a novel approach tot he synthesis of mesoporous carbos, *J. Am. Chem. Soc.*, **123**, 9208-9209

248 X. Li, D. Banham, F. Feng, F. Forouzandeh, S. Ye, D. Y. Kwok, V. Birss, 2015, Wettability of colloid-imprinted carbons by contact angle kinetics and water vapor sorption measurements, *Carbon*, **87**, 44-60

249 H. Yang, Y., Y. Liu, F. Zhang, R. Zhang, Y. Y. Meng, M. Li, S. Xie, B. Tu, D. Zhao, 2004, A simple melt impregnation method to synthesize ordered mesoporous carbon and carbon nanofiber bundles with graphitized structure from pitches, *J. Phys. Chem. B*, **108**, 17320-17328

250 P. Adelhelm, K. Cabrera, B. M. Smarsly, 2012, On the use of mesophase pitch for the preparation of hierarchical porous carbon monoliths by nanocasting, *Sci. Technol. Adv. Mater.*, **13**, 015010

251 G. Gupta, D. A. Slanac, P. Kumar, J. D. Wiggings-Camacho, J. Kim, R. Ryoo, K. J. Stevenson, K. P. Johnston, 2010, Highly stable Pt/ordered graphitic mesoporous carbon electrocatalysts for oxygen reduction, *J. Phys. Chem. C*, **114**, 10796-10805

252 A. Serov, K. Artyushkova, P. Atanassov, 2014, Fe-N-C oxygen reduction fuel cell catalyst derived from carbendazim: synthesis, structure, and reactivity, *Adv. Energy. Mater.*, **4**, 1301735

253 C. Janson, A. E. C. Palmqvist, 2019, Improved oxygen reduction activity of transition metal-chelating ordered mesoporous carbon fuel cell catalysts by milder template removal, *Catal. Lett.*, **149**, 1297-1304

254 J. Zou, C. Chen, Y. Zhu, Q. Cheng, L. Zou, Z. Zou, H. Yang, 2022, Facile steam-etching approach to increase the active site density of an ordered porous Fe-N-C catalyst to boost oxygen reduction reaction, *ACS Catal.*, **12**, 4517-4525

255 M. Qiao, Y. Wang, Q. Wang, G. Hu, X. Mamat, S. Zhang, S. Wang, 2020, Hierarchically Ordered Porous Carbon with Atomically Dispersed FeN4 for Ultraefficient Oxygen Reduction Reaction in Proton-Exchange Membrane Fuel Cells, , *Angew. Chem. Int. Ed.*, **59**, 2688-2694

256 G. He, Q. Pan, 2004, Synthesis of polystyrene and polystyrene/poly(methyl methacrylate) nanoparticles, *Macromol. Rapid Commun.*, **17**, 1545-1548

257 I. Milošević, V. Mauroy, H. Dabboue, S. Serieye, F. Warmont, J.-P. Salvetat, M.-L. Saboungi, S. Guillot, 2009, Synthesis and size control of polystyrene nanoparticles via "liquid crystalline" nanoemulsion, *Microporous Mesoporous Mat.*, **120**, 7-11

258 A. B. D. Nandiyanto, N. Hagura, F. Iskandar, K. Okuyama, 2010, Design of a highly ordered and uniform porous structure with multisized pores in film and particle forms using a template-driven self-assembly technique, *Acta Mater.*, **58**, 282-289

259 K. Abitaev, Y. Qawasmi, P. Atanasova, C. Dargel, J. Bill, T. Hellweg, T. Sottman, 2021, Adjustable polystyrene nanoparticle templates for the production of mesoporous foams and ZnO inverse opals, *Colloid Polym. Sci.*, **299**, 243-258

260 S. Homaeigohar, R. Kabir, M. Elhbahri, 2020, Size-Tailored Physicochemical Properties of Monodisperse Polystyrene Nanoparticles and Nanocomposites Made Thereof, *Sci. Rep.*, **10**, 5191

261 P. Sieira, C. Guimarães, A. Braga, C. E. L. dos Santos, M. H. Pereira, L. E. Pizarro Borges, Stabilization time and temperature influence on the evolution of the properties of mesophase pitch stabilized fibers and carbon fibers, *J. Ind. Eng. Chem.*, 2024

262 T. Senda, Y. Yamada, M. Morimoto, N. Nono, T. Sogabe, S. Kubo, S. Sato, 2019, Analyses of oxidation process for isotropic pitch-based carbon fibers using model compounds, *Carbon*, **142**, 311-326

263 J. Drbohlav, W. T. K. Stevenson, 1995, The oxidative stabilization and carbonization of a synthetic mesophase pitch, part I : The oxidative stabilization process, *Carbon*, **33**, 693-711

264 G. Yuan, X. Li, X. Xiong, Z. Dong, A. Westwood, B. Li, C. Ye, G. Ma, Z. Cui, Y. Cong, J. Zhang, Y. Li, 2017, A comprehensive study on the oxidative stabilization of mesophase pitch based tape-shaped thick fibers with oxygen, *Carbon*, **115**, 59-76

265 A. Sandi, A. Sawitri, A. Rajak, A. Zulfi, D. Edikresnha, M. M. Munir, K. Khairurrijal, 2018, Fabrication and characterization of monodisperse polystyrene latex (PSL) with various diameters, *Mater. Sci. Eng.*, **367**, 012015

266 O.Larue, F. Vorobiev, C. Vu, B. Durand, 2003, Electrocoagulation and coagulation by iron of latex particles in aqueous suspensions, *Sep. Purif. Technol.*, **31**, 177-192

267 T. Qin, J. Zhao, R. Shi, C. Ge, Q. Li, 2020, Ionic liquid derived active atomic iron sites anchored on hollow carbon nanospheres for bifunctional oxygen electrocatalysis, *Chem. Eng. J.*, **399**, 125656

268 X. Yang, G. Sun, F. Wang, X. Li, Z. Zhang, Y. Zhen, D. Wang, X. Gao, F. Fu, R. Chi, 2023, Rational design of dense microporous carbon derived from coal tar pitch towards high mass loading supercapacitors, J. Colloid Interface Sci., **646**, 228-237

269 B. Fathollahi, P. C. Chau, J. L. White, 2005, Injection and stabilization of mesophase pitch in the fabrication of carbon-carbon composites: Part II. Stabilization process, *Carbon*, **43**, 135-141

270 V. Birss, X. Li, D. Banham, D. Y. Kwok, Porous carbon films, Patent: US20170014780A1

271 Z.-M. Wang, N. Yamashita, Z.-X. Wang, K. Hoshinoo, H. Kanoh, 2004, Air oxidation effects on microporosity, surface property, and CH4 adsorptivity of pitch-based activated carbon fibers, *J. Colloid Interface Sci.*, **276**, 143-150

272 J. Wang, S. Kaskel, 2012, KOH activation of carbon-based materials for energy storage, *J. Mater. Chem.*, **22**, 23710-23725

273 E. Desimoni, G. I. Casella, A. M. Salvi, T. R. I. Catladi, A. Morone, 1992, XPS investigation of ultra-high-vacuum storage effects on carbon fibre surfaces, *Carbon*, **30**, 527-531

274 X. Chen, X. Wang, D. Fang, 2020, Fuller Nanotub, *Carbon Nanostructures*, **28**, 1048-1058

275 J. Guo, H. He, D. Chu, R. Chen, 2012, OH^--Binding Effects on Metallophthalocyanine Catalysts for O_2 Reduction Reaction in Anion Exchange Membrane Fuel Cells, *Electrocatal.*, **3**, 252-264

276 T. Marshall-Roth, N. J. Libretto, A. T. Wrobel, K. J. Anderton, M. L. Pegis, N. D. Ricke, T. Van Voorhis, J. T. Miller, Y. Surendranath, 2020, A pyridinic Fe-N4 macrocycle models the active sites in Fe/N-doped carbon electrocatalysts, *Nat. Commun.*, **11**, 5283

277 S. Baranton, C. Coutanceau, C. Roux, F. Hahn, J.-M. Léger, 2005, Oxygen reduction reaction in acid medium at iron phthalocyanine dispersed on high surface area carbon substrate: tolerance to methanol, stability and kinetics, *J. Electroanal. Chem.*, **577**, 223-234

278 H. C. Honig, L. Elbaz, 2023, Degradation Mechanisms of Platinum Group Metal-Free Oxygen Reduction Reaction Catalyst based on Iron Phthalocyanine, *ChemElectroChem*, **10**, e202300042

279 G. Lalande, G. Faubert, R. Côté, D. Guay, J. P. Dodelet, L. T. Weng, P. Bertrand, 1996, Catalytic activity and stability of heat treated iron phthalocyanines for electroreduction of oxygen in polymer electrolyte fuel cells, *J. Power Sources*, **61**, 227-237

280 H. A. Miller, M. Bellini, W. Oberhauser, X. Deng, H. Chen, Q. He, M. Passaponti, M. Innocenti, R. Yang, F. Sun, Z. Jiang, F. Vizza, 2016, Heat treated carbon supported iron(II)phthalocyaine oxygen reduction catalysts: elucidation of the structure-activity relationship using X-ray absorption spectroscopy, *Phys. Chem. Chem. Phys.*, **18**, 33142-33151

281 M. Mubyuddin, E. Berretti, S. A. Mirshokraee, J. Orsilli, R. Lorenzi, L. Capozzoli, F. D'Acapito, E. Murphy, S. Guo, P. Atanassov, A. Lavacchi, C. Santoro, 2024, Formation of the active site structures during pyrolysis transformation of Fe-phthalocyanine into Fe-N_x-C electrocatalysts for the oxygen reduction reaction, *Appl. Cat. B.: Environ.*, **343**, 123515

282 M. A. C. de Oliveira, V. C. A. Ficca, R. Gokhale, C. Santoro, B. Mecheri, A. D'Epifanio, S. Licoccia, P. Atanassov, 2021, Iron(II)phthalocyanine (FePc) over carbon support for oxygen reduction reaction electrocatalysts operating in alkaline electrolyte, *J. Solid State Electrochem.*, **25**, 93-104

283 J. Yang, J. Tao, T. Isomura, H. Yanagi, I. Moriguchi, N. Nakashima, 2019, A comparative study of iron phthalocyanine electrocatalysts supported on different nanocarbons for oxygen reduction reaction, *Carbon*, **145**, 565-571

284 Y. Jiang, Y. Lu, X. Lv, D. Han, Q. Zhang, L. Niu, W. Chen, 2013, Enhanced catalytic performance of Pt-free iron phthalocyanine by graphene support for efficient oxygen reduction reaction, *ACS Catal.*, **3**, 1263-1271

285 K. Chen, K. Liu, P. An, H. Li, Y. Lin, J. Hu, C. Jia, J. Fu, H. Li, H. Li, H. Liu, Z. Lin, W. Li, J. Li, Y.-R. Lu, T.-S. Chan, N. Zhang, M. Liu, 2020, Iron phthalocyanine with coordination induced electronic localization to boost oxygen reduction reaction, *Nat. Commun.*, **11**, 4173, 2020

286 Y. Hong, L. Li, B. Huang, X. Tang, W. Zhai, T. Hu, K. Yuan, Y. Chen, 2021, Molecular control of carbon-based oxygen reduction electrocatalysts through metal macrocyclic complexes functionalization, *Adv. Energy Mater.*, **11**, 2100866

287 R. Chen, H. Li, D. Chu, G. Wang, 2009, Unraveling oxygen reduction reaction mechanisms on carbon-supported Fe-phthlocyanine and Co-phthalocyanine catalysts in alkaline solutions, *J. Phys. Chem. C*, **113**, 20689-20697

288 A. Friedman, M. Mizrahi, N. Levy, N. Zion, M. Zachman, L. Elbaz, 2021, Application of molecular catalysts for the oxygen reduction reaction in alkaline fuel cells, *ACS Appl. Mater. Interfaces*, **13**, 58532-58538

289 S. Akula, M. Mooste, B. Zulevi, S. McKinney, A. Kikas, H.-M. Piirsoo, M. Rähn, A. Tamm, V. Kisand, A. Serov, E. B. Creel, D. A. Cullen, K. C. Neyerlin, H. Wang, M. Odgaard, T. Reshetenko, K. Tammeveski, 2022, Mesoporous textured Fe-NC electrocatalysts as highly efficient cathodes for proton exchange membrane fuel cells, *J. Power Sources*, **520**, 230819

290 T. von Graberg, P. Hartmann, A. Rein, S. Gross, B. Seelandt, C. Roeger, R. Zieba, A. Trau, M. Wark, J. Janek, B. M. Smarsly, 2011, Mesoporous tin-doped indium oxide thin films: effect of mesostructure on electrical conductivity, *Sci. Technol. Adv. Mater.*, **12**, 1-12

291 C. Ai, I. V. Chernyshova, E. L. Gawron, S. Ponnurangam, V. I. Birss, 2022, Electrochemistry of new generation conformal polyaniline/carbon scaffolds with monodispersed nanopores and high capacitance, J. *Mater. Chem. C*, **10**, 2271-2280

292 T. Reshetenko, A. Serov, A. Kulikovsky, P. Atanassov, 2020, Impedance spectroscopy characterization of PEM fuel cells with Fe-NC-based cathodes, *J. Electrochem. Soc.*, **166**, F653-F660

293 S. Slade, S. A. Campbell, T. R. Ralph, F. C. Walsh, 2002, Ionic conductivity of an extruded Nafion 1100 EW series of membranes, *J. Electrochem. Soc.*, **149**, A1556-A1564

294 X.Z. Lim, 2023, Could the world go PFAS-free? Proposal to ban 'forever chemicals' fuels debate, *Nature*, **620**, 24

295 J. Hyun, H.-T. Kim, 2023, Powering the hydrogen future: current status and challenges of anion exchange membrane fuel cells, *Energy Environ. Sci*., **16**, 5633-5662

296 H. A. Firouzjaie, W. E. Mustain, 2020, Catalytic advantages, challenges, and priorities in alkaline membrane fuel cells, *ACS Catal.*, **10,** 225-234

297 N. Ramaswamy, S. Mukerjee, 2012, Fundamental mechanistic understanding of electrocatalysis of oxygen reduction on Pt and non-Pt surfaces: acid versus alkaline media, *Adv. Phys. Chem.*, **2012,** 491604

298 A. García, L. Pascual, P. Ferrer, D. Gianolio, G. Held, D. C. Grinter, M. A. Peña, M. Retuerto, S. Rojas, 2021, Study of the evolution of FeN_xC_y and Fe_3C species in Fe/N/C catalysts during the oxygen reductio reaction in acid and alkaline electrolyte, *J. Power Sources*, **490**, 229487

299 N. Chen, Y. M. Lee, 2021, High-performance anion exchange membrane water electrolyzers with a current density of 7.68 A cm^{-2} and durability of 1000 hours, *Prog. Polym.*, **113**, 101345

300 Y. Yang, P. Li, X. Zheng, W. Sun, S. X. Dou, T. Ma, H. Pan, 2022, Anion-exchange membrane water electrolyzers and fuel cells, *Chem. Soc. Rev.*, **51**, 9620-9694

301 Y. Zhao, Y. Yang, S. Wang, T. Wang, C. Liu, S. Cheng, H. Wie, Y. Ding, 2023, Rational design protocols to tune the morphology and conductivity of poly(arylene alkylene)-based anion exchange membranes, *J. Membr. Sci.*, **88**, 122132

302 J. Wang, Y. Zhao, B. P. Setzler, S. Rojas-Carbonell, C. B. Yehuda, A. Amel, M. Page, L. Wang, K. Hu, L. Shi, S. Gottesfeld, B. Xu, Y. Yan, 2019, Poly (aryl piperidinium) membranes and ionomers for hydroxide exchange membrane fuel cells, *Nat. Energy*, **4**, 392

303 W. Song, X. Zhang, C. Yang, Z. Yang, L. Wu, X. Ge, T. Xu, 2023, Alkaline membranes toward electrochemical energy devices: recent development and future perspectives, *ACS Cent. Sci.*, **9**, 1538

304 T. Wang, L. Shi, J. Wang, Y. Zhao, B. P. Setzler, S. Rojas-Carbonell, Y. Yan, 2019, High-performance hydroxide exchange membrane fuel cells through optimization of relative humidity, backpressure and catalyst selection, *J. Electrochem. Soc.*, **166**, F3305-F3310

305 X. Wu, N. Chen, H.-A. Klok, Y. M. Lee, X. Hu, 2022, Branched poly (aryl piperidinium) membranes for anion-exchange membrane fuel cells, *Angew. Chem. Int. Ed.*, **61**, e202114892

306 M. Mandal, G. Huang, N. U. Hassan, X. Peng, T. Gu, A. H. Brooks-Starks, B. Bahar, W. E. Mustain, P. A. Kohl, 2020, The importance of water transport in high conductivity and high-power alkaline fuel cells, *J. Electrochem. Soc.*, **167**, 054501

307 C. Han, W. Shi, M. Huang, Q. Wang, J. Yang, J. Chen, R. Ding, X. Yin, 2024, Solvent Effects on the Catalyst Ink and Layer Microstructure for Anion Exchange Membrane Fuel Cells, *ACS Appl. Mater. Interfaces*, **16**, 4550-4560

308 K. Ehelebe, T. Ashraf, S. Hager, D. Seeberger, S. Thiele, S. Cherevko, 2020, Fuel cell catalyst layer evaluation using a gas diffusion electrode half-cell: Oxygen reduction reaction on Fe-NC in alkaline media, *Electrochem. Commun.*, **116**, 106761

309 L. Mazzoli, A. Pedersen, S. Kellner, R. D. Hunter, R. Cai, M. Wang, K. Sivula, S. J. Haigh, J. Barrio, 2024, Inducing Porosity in Xylose-derived FeNC Electrocatalysts for Alkaline Oxygen Reduction, *Green Chem.*

310 M. M. Hossen, K. Artyushkova, P. Atanassov, A. Serov, 2018, Synthesis and characterization of high performing Fe-NC catalyst for oxygen reduction reaction (ORR) in Alkaline Exchange Membrane Fuel Cells, *J. Power Sources*, **375**, 214-221

311 L. Peng, J. Yang, Y. Yang, F. Qian, Q. Wang, D. Sun-Waterhouse, L. Shang, T. Zhang, G. I. N. Waterhouse, 2022, Mesopore-Rich Fe-N-C Catalyst with FeN4-O-NC Single-Atom Sites Delivers Remarkable Oxygen Reduction Reaction Performance in Alkaline Media, *Adv. Mater.*, **34**, 2202544

312 P. G. Santori, A. N. Mondal, D. R. Dekel, F. Jaouen, 2020, The critical importance of ionomers on the electrochemical activity of platinum and platinum-free catalysts for anion-exchange membrane fuel cells, *Sustain. Energy Fuels*, **3**, 3300-3307

313 N. Daems, T. Breugelsman, I. F. J. Vankelecom, P. P. Pescarmona, 2018, Influence of the Composition and Preparation of the Rotating Disk Electrode on the Performance of Mesoporous Electrocatalysts in the Alkaline Oxygen Reduction Reaction, *ChemElectroChem*, **5**, 119-128

314 G. Zhong, S. Xu, L. Liu, C. Z. Zheng, J. Dou, F. Wang, X. Fu, W. Liao, H. Wang, 2020, Effect of Experimental Operations on the Limiting Current Density of Oxygen Reduction Reaction Evaluated by Rotating-Disk Electrode, *ChemElectroChem*, **7**, 1107-1114

315 R. K. Singh, R. Devivaraprasad, T. Kar, A. Chakraborty, M. Neergat, 2015, Electrochemical Impedance Spectroscopy of Oxygen Reduction Reaction (ORR) in a Rotating Disk Electrode Configuration: Effect of Ionomer Content and Carbon-Support, *J. Electrochem. Soc.*, **162**, F489-F498

316 W. Yu, Y. Xu, X. Shen, X. Yang, Z. Liu, H. Wang, X. Liang, X. Ge, M. D. Guiver, L. Wu, T. Xu, 2024, Ionomer boosts catalyst layer oxygen transport and membrane ion conductio for fuel cells, *Next Energy*, **3**, 100104

317 https://www.bwt.com/en/-/media/bwt/fumatech/datasheets/new/fumion/fumion-faa-3-shredded-film.pdf?rev=35904cd7e67944a38279064513d904ff

318 S. Khandavalli, R. Iyer, J. H. Park, D. J. Myers, K. C. Neyerlin, M. Ulsh, S. A. Mauger, 2020, Effect of Dispersion Medium Composition and Ionomer Concentration on the Microstructure and Rheology of Fe-N-C Platinum Group Metal-free Catalyst Inks for Polymer Electrolyte Membrane Fuel Cells, *Langmuir*, **36**, 12247-12260

319 Q. He, L. Zeng, J. Wang, J. Jiang, L. Zhang, J. Wang, W. Ding, Z. Wei, 2021, Polymer-coating-induced synthesis of FeN_x enriched carbon nanotubes as cathode that exceeds 1.0Wcm^{-2} peak power in both proton and anion exchange membrane fuel cells, *J. Power Sources*, **489**, 229499

320 L. Liu, S. J. Tan, T. Horikawa, D. D. Do, D. Nicholson, J. Liu, 2017, Water adsorption on carbon-A review, *Adv. Colloid Interface Sci.*, **250**, 64-78

321 T. Soboleva, K. Malek, Z. Xie, T. Navessin, S. Holdcroft, 2011, PEMFC Catalyst Layers: The Role of Micropores and Mesopores on Water Sorption and Fuel Cell Activity, *ACS Appl. Mater. Interfaces*, **3**, 1827-1837

322 M. J. Dzara, K. Artyushkova, M. T. Sougrati, C. Ngo, M. A. Fitzgerald, A. Serov, B. Zulevi, P. Atanassov, F. Jaouen, S. Pylypenko, 2020, Characterizing Complex Gas-Solid Interfaces with in Situ Spectroscopy: Oxygen Adsorption Behavior on Fe-N-C Catalysts, *J. Phys. Chem C*, **124**, 16529-16543

323 C. Piece, N. R. Smith, J. W. Wiley, H. Cordes, 1951, Adsorption of Water by Carbon, *J. Am. Chem. Soc.*, **73**, 4551-4557

324 M. Thommes, J. Morell, K. A. Cychosz, M. Fröba, 2013, Combining Nitrogen, Argon, and Water Adsorption for Advanced Characterization of Ordered Mesoporous Carbons (CMKs) and Periodic Mesoporous Organosilicas (PMOs), *Langmuir*, **29**, 14893-14902

325 T. Mashio, K. Sato, A. Ohma, 2014, Analysis of Water Adsorption and Condensation in Catalyst Layers for Polymer Electrolyte Fuel Cells, *Electrochim. Acta*, **140**, 238-249

326 K. Otsuji, Y. Shirase, T. Asakawa, N. Yokota, K. Nagase, W. Xu, P. Song, S. Wang, D. A. Tryk, K. Kakinuma, J. Inukai, K. Miyatake, M. Uchida, 2022, Effect of water management in membrane and cathode catalyst layers on suppressing the performance hysteresis phenomenon in anion-exchange membrane fuel cells, *J. Power Sources*, **522**, 230997

327 M. S. Cha, J. E. Park, S. Kim, S.-H. Han, S.-H. Shin, S. H. Yang, T.-H. Kim, D. M. Yu, S. So, Y. T. Hong, S. J. Yoon, S.-G. Oh, S. Y. Kang, O.-H. Kim, H. S. Park, B. Bae, Y.-E. Sung, Y.-H. Cho, J. Y. Lee, 2020, Poly (carbazole)-based anion-conducting materials with high performance and durability for energy conversion devices, *Energy Environ. Sci.*, **13**, 3633-3645

328 Z. Liu, H. Yang, R. Kutz, R. I. Masel, 2018, CO_2 Electrolysis to CO and O_2 at High Selectivity, Stability and Efficiency Using Sustainion Membranes, *J. Electrochem. Soc.*, **165**, J3371-J3377

329 J. E. Chae, J. Choi, S. Lee, C. Park, S. Kim, 2023, Effects of fabrication parameters of membrane-electrode assembly for high-performance anion exchange membrane fuel cells, *J. Ind. Eng. Chem.*, **133**, 255-262

330 C. Hu, H. W. Kang, S. W. Jung, X. Zhang, Y. J. Lee, N. Y. Kang, C. H. Park, Y. M. Lee, 2024, Stabilizing the Catalyst Layer for Durable and High Performance Alkaline Membrane Fuel Cells and Water Electrolyzers, *ACS Cent. Sci.*, **10**, 603-614

331 B. Britton, S. Holdcroft, 2016, The Control and Effect of Pore Size Distribution in AEMFC Catalyst Layers, *J. Electrochem. Soc.*, **163**, F353-F358

332 U. Beuscher, 2006, Experimental Method to Determine the Mass Transport Resistance of a Polymer Electrolyte Fuel Cell, *J. Electrochem. Soc*., **153**, A1788-A1793

333 N. Nonoyama, S. Okazaki, A. Z. Weber, Y. Ikogi, T. Yoshida, 2011, Analysis of Oxygen-Transport Diffusion Resistance in Proton-Exchange-Membrane Fuel Cells, *J. Electrochem. Soc.*, **158**, B416-B423

334 D. R. Baker, D. A. Caulk, K. C. Neyerlin, M. W. Murphy, 2009, Measurement of Oxygen Transport Resistance in PEM Fuel Cells by Limiting Current Methods, *J. Electrochem Soc.*, **156**, B991-B1003

335 T. Reshetenko, O. Polevaya, 2021, Determination of oxygen mass transport resistance in proton exchange membrane fuel cells with an open flow field architecture, *Electrochim. Acta*, **387**, 138529

336 W. Yu, J. Zhang, D.-M. Huang, X. Liang, K. Zhang, Y. Xu, H. Zhang, B. Ye, X. Ge, T. Xu, L. Wu, 2023, Molecular-Level Control over Oxygen Transport and Catalyst-Ionomer Interaction by Designing Cis-Trans Isomeric Ionomers, *ACS Energy Lett.*, **8**, 790-799

337 P. S. Khadke, U. Krewer, 2014, Mass-Transport Characteristics of Oxygen at Pt/Anion Exchange Ionomer Interface, *J. Phys. Chem. C*, **118**, 11215-11223

338 N. U. Hassan, M. Mandal, G. Huang, H. A. Firouzjaie, P. A. Kohl, W. E. Mustain, 2020, Achieving High-Performance and 2000 h Stability in Anion Exchange Membrane Fuel Cells by Manipulating Ionomer Properties and Electrode Optimization, *Adv. Energy. Mater.*, **10**, 2001986

339 Y. Zhou, H. Yu, F. Xie, Y. Zhao, X. Sun, D. Yao, G. Jiang, J. Geng, Z. Shao, 2023, Improving cell performance for anion exchange membrane fuel cells with FeNC cathode by optimizing ionomer content, *J. Int. Hydrog. Energy*, **48**, 5266-5275

340 A. Carlson, P. Shapturenka, B. Eriksson, G. Lindbergh, C. Lagergren, R. W. Lindström, 2018, Electrode parameters and operating conditions influencing the performance of anion exchange membrane fuel cells, *Electrochim. Acta*, **277**, 151-160

341 C. Han, W. Shi, M. Huang, Q. Wang, J. Yang, J. Chen, R. Ding, X. Yin, 2024, Solvent Effects on the Catalyst Ink and Layer Microstructure for Anion Exchange Membrane Fuel Cells, *ACS Appl. Mater. Interfaces*, **16**, 4550-4560

342 momentummaterials.ca (retrieved: 10.04.2024)

343 N. Stachowiak, J. Kowalonek, J. Kozlowska, 2020, Effect of plasticizer and surfactant on the properties of poly(vinyl alcohol)/chitosan films, *Int. J. Biol. Macromol.*, **164**, 2100-2107

344 A. Ly, T. Asset, P. Atanassov, 2020, Integrating nanostructured Pt-based electrocatalysts in proton exchange membrane fuel cells, *J. Power Sources*, **478**, 228516

345 https://www.energy.gov/eere/vehicles/articles/us-drive-fuel-cell-technical-team-roadmap (Retrieved 10.04.2024)

346 https://www.ballard.com/about-ballard/newsroom/news-releases/2017/09/13/ballard-to-offer-world-s-first-pem-fuel-cell-product-using-non-precious-metal-catalyst (Retrieved 10.04.2024)

347 N. Chen, H. H. Wang, S. P. Kim, H. M. Kim, W. H. Lee, C. Hu, J. Y. Bae, E. S. Sim, Y.-C. Chung, J.-H. Jang, S. J. Yoo, Y. Zhuang, Y. M. Lee, 2021, Poly(fluorenyl aryl piperidinium) membranes and ionomers for anion exchange membrane fuel cells, *Nat. Commun.*, **12**, 2367

348 G. Bae, M. W. Chung, S. Gu, F. Jaouen, C. H. Choi, 2020, pH Effect on the H_2O_2-Induced Deactivation of Fe-N-C Catalysts, *ACS Catal.*, **10**, 8485-8495

349 K. Wang, X. Peng, W. E. Mustain, J. R. Varcoe, 2019 Radiation-grafted anion-exchange membranes: the switch from low-to high density polyethylene leads to remarbably enhanced fuel cell performance, *Energy Environ. Sci.*, **12**, 1575-1579

350 G. Huang, M. Mandal, X. Peng, A. C. Yang-Neyerlin, B. S. Pivovar, W. E. Mustain, P. A. Kohl, 2019, Composite Poly (norbornene) Anion Conducting Membranes for Achieving Durability, Water Management and High Power (3.4 W/cm^2) in Hydrogen/Oxygen Alkaline Fuel Cells, *J. Electrochem. Soc.*, **166**, F637-F644

351 N. Chen, C. Hu, H. H. Wang, S. P. Kim, H. M. Kim, W. H. Lee, J. Y. Bae, J. H. Park, Y. M. Lee, *Angew. Chem. Int. Ed.*, **60**, 7710 (2021)

352 X. Wu, N. Chen, H.-A. Klok, Y. M. Lee, X. Hu, 2022, Poly(Alkyl- Terphenyl Piperidinium) Ionomers and Membranes with an Outstanding Alkaline-Membrane Fuel-Cell Performance of 2.58 Wcm^{-2}, *Angew. Chem. Int. Ed.*, **61**, e202114892

353 C. Hu, N. Y. Kang, H. W. Kang, J. Y. Lee, X. Zhang, Y. J. Lee, S. W. Jung, J. H. Park, M.-G. Kim, S. J. Yoo, S. Y. Lee, C. H. Park, Y. M. Lee, 2024, Triptycene Branched Poly (aryl-co-aryl piperidinium) Electrolytes for Alkaline Anion Exchange Membrane Fuel Cells and Water Electrolyzers, *Angew. Chem. Int. Ed.*, **63**, e202316697

354 Q. He, L. Zeng, J. Wang, J. Jiang, L. Zhang, J. Wang, W. Ding, Z. Wei, 2021, Polymer-coating-induced synthesis of FeNx enriched carbon nanotubes as cathode that exceeds 1.0 Wcm^{-2} peak power in both proton and anion exchange membrane fuel cells, *J. Power Sources*, **489**, 229499

355 L. Zeng, Q. He, Y. Liao, S. Kuang, J. Wang, W. Ding, Q. Liao, Z. Wei, 2020, Anion Exchange Membrane Based on Interpenetrating Polymer Network with Ultrahigh Ion Conductivity and Excellent Stability for Alkaline Fuel Cell, *AAAS*, **2020**, 4794706

356 P. Teppor, R. Jäger, M. Koppel, O. Volobujeva, R. Palm, M. Månsson, E. Härk, Z. Kuchovski, J. Aruväli, K. Kooser, S. Granroth, T. Käämbre, J. Nerut, E. Lust, 2024, Unlocking the porosity of Fe-N-C catalysts using hydroxyapatite as a hard template en route to eco-friendly high-performance AEMFCs, *J. Power Sources*, **591**, 233816

357 H. Adabi, A. Shakouri, A. Zitolo, T. Asset, A. Khan, J. Bohannon, R. Chattot, C. Williams, F. Jaouen, J. R. Regalbuto, W. E. Mustain, 2023, Multi-atom Pt and PtRu catalysts for high performance AEMFCs with ultra-low PGM content, *Appl. Cat. B: Environ.*, **325**, 122375

358 A. Zhegur-Khais, F. Kubannek, U. Krewer, D. R. Dekel, 2020, Measuring the true hydroxide conductivity of anion exchange membranes, *J. Membr. Sc.*, **612**, 118461

359 M.-J. Kim, S. Kim, J. E. Park, C.-C. Hwang, S. Lee, S. Y. Kang, D. Jung, Y.-H. Cho, J. Kim, K-S. Lee, Y.-E. Sung, 2020, Controlling active sites of Fe-N-C electrocatalysts for oxygen electrocatalysis, *Nano Energy*, **78**, 105395

360 J. Calderon, N. Huq, M. Zheng, Y. Zhou, 2022, Power Enhancement of Anion Exchange Membrane Fuel Cells (AEMFCs) Through Spray-Coating of Membrane With Partially Reduced Graphene Oxide, *J. Undergrad. Chem. Eng. Res.*, **75**

361 Z. Liu, S. D. Sajjad, Y. Gao, H. Yang, J. J. Kaczur, R. I. Masel, 2017, The effect of membrane on an alkaline water electrolyzer, *Int. J. Hydrog. Energy*, **42**, 29661-29665

362 A. Raut, H. Fang, Y.-C. Lin, S. Fu, D. Sprouster, R. Shimogawa, A. I. Frenkel, C. Bae, J. C. Douglin, J. Lillojad, K. Tammeveski, Z. Zeng, S. Bliznakov, M. Rafailovich, D. R. Dekel, 2023, Migration and Precipitation of Platinum in Anion Exchange Membrane Fuel Cells, *Angew. Chem. Int. Ed.*, **62**, e202306754

363 J. Hyun, D. W. Lee, E. Oh, H. Bae, J. Park, G. Doo, H.-T. Kim, 2023, Manufacturing and structural control of slurry-cast catalyst layers for AEMFC, *J. Power Sources*, **573**, 233161

364 J. E. Chae, J. Choi, S. Lee, C. Park, S. Kim, 2024, Effects of fabrication parameters of membrane-electrode assembly for high-performance anion exchange membrane fuel cells, *J. Ind. Eng. Chem.*, **133**, 255-262

365 Y. Pei, W. Zhu, R. Yue, J. Yao, X. Liu, L. Wang, J. Zhang, Y. Yin, M. D. Guiver, 2023, Fine adjustment of catalyst agglomerate for the controllable construction of Co/Fe-N-C catalyst layers, *J. Power Sources*, **566**, 232904